



THE HONG KONG  
POLYTECHNIC UNIVERSITY

香港理工大學

Pao Yue-kong Library

包玉剛圖書館

---

## Copyright Undertaking

This thesis is protected by copyright, with all rights reserved.

**By reading and using the thesis, the reader understands and agrees to the following terms:**

1. The reader will abide by the rules and legal ordinances governing copyright regarding the use of the thesis.
2. The reader will use the thesis for the purpose of research or private study only and not for distribution or further reproduction or any other purpose.
3. The reader agrees to indemnify and hold the University harmless from and against any loss, damage, cost, liability or expenses arising from copyright infringement or unauthorized usage.

### IMPORTANT

If you have reasons to believe that any materials in this thesis are deemed not suitable to be distributed in this form, or a copyright owner having difficulty with the material being included in our database, please contact [lbsys@polyu.edu.hk](mailto:lbsys@polyu.edu.hk) providing details. The Library will look into your claim and consider taking remedial action upon receipt of the written requests.

**THERMO-MECHANICAL BEHAVIOUR OF ENERGY PILES IN  
UNSATURATED SILT**

**CUI SHEQIANG**

PhD

The Hong Kong Polytechnic University

2023

The Hong Kong Polytechnic University

Department of Civil and Environmental Engineering

**Thermo-Mechanical Behaviour of Energy Piles in Unsaturated Silt**

CUI Sheqiang

A thesis submitted in partial fulfilment of the requirements for the degree of

Doctor of Philosophy

September 2022

## **Certificate of originality**

I hereby declare that this thesis is my own work and that, to the best of my knowledge and belief, it reproduces no material previously published or written, nor material that has been accepted for the award of any other degree or diploma, except where due acknowledgement has been made in the text.

Signature: \_\_\_\_\_

Name of Student: CUI Sheqiang  
\_\_\_\_\_

## Abstract

Energy pile is an environment-friendly and efficient technology for harvesting shallow geothermal energy. It has received much attention during the past two decades. Most of the previous studies focused on the thermo-mechanical behaviour of energy piles in saturated soils. However, water tables are very deep in many regions. Energy piles in the unsaturated ground have been widely reported worldwide, such as Beijing in China, Melbourne in Australia and Colorado in the United States. An in-depth study is needed to understand the behaviour of energy piles in unsaturated soils.

Given this background, the major objectives of this study are to (i) reveal and model the coupled effects of soil moisture and stress state on the thermal conductivity of saturated and unsaturated soils, which is an important input in the analysis of pile thermal performance; (ii) investigate the coupled effects of temperature and suction on the soil-pile interface behaviour and develop an advanced constitutive model for it; (iii) study the thermo-mechanical performance of energy piles in different roughness and suction conditions through physical model tests. To meet these objectives, four interrelated investigations were carried out.

A new apparatus based on the thermal needle probe was developed for testing thermal conductivity. It was used to conduct a comprehensive test program for revealing the influence of porosity, degree of saturation, stress level and soil type. Particularly, the understanding of the influence of stress has been improved. With a stress increase from 0 to 1200 kPa, the thermal conductivity increases by 60% for kaolin clay, 25% for silt (completely decomposed granite) with 85% degree of compaction (DOC), 20% for the silt with 95% DOC, 10% for Toyoura sand with an initial void ratio of 0.76 and 7.5% for the sand with an initial void ratio of 0.60. The observed increase in thermal conductivity is attributed to different mechanisms, including a reduction of the void ratio and a change in inter-particle contact. These two mechanisms are relatively more important for clay and sand, respectively.

Based on the thermal conductivity results, a semi-empirical equation was newly proposed to model the thermal conductivity of saturated and unsaturated soils. It considers stress effects on the void ratio and inter-particle contacts. As compared to existing models, it

has two major improvements: (i) it can well capture the influence of stress on thermal conductivities of various soils; (ii) it is able to capture the hysteresis of stress-thermal conductivity relation during the loading and unloading processes. It was then utilized in a finite element code to compute the heat exchange rate between the energy pile and the ground. The computed results indicate that the heat exchange rate is underestimated if stress effects on soil thermal conductivity are not considered. Taking energy pile of 0.6 m in diameter and 50 in aspect ratio as one example, the underestimation is up to 18%, 13% and 2% for the clay, silt and sand grounds, respectively.

To study the thermo-mechanical behaviour of the soil-pile interface, a new temperature- and suction-controlled direct shear device was developed. Two types of tests (i.e., constant-temperature shearing and constant-stress heating-cooling) were carried out at various temperatures, net normal stresses and suctions. The results show that temperature can have a minor impact on the friction angle, whose value at 42°C is smaller by about 2.2° than that at 8 °C, likely because heating can increase the void ratio in the shear zone. More importantly, the interface strength increases nonlinearly with increasing suction, and the incremental rate is temperature-dependent. Heating the interface at a net normal stress of 50 kPa reduces this incremental rate due to surface tension reduction. In contrast, this incremental rate increases at a net normal stress of 150 kPa with the same temperature increment, probably because the heated specimen has more small-size pores due to thermal contraction and more menisci water lenses, whose influence outweighs the effects of surface tension. For the constant-stress heating and cooling tests, irreversible relative movement occurs during cooling. This is most likely due to the thermally induced contraction of soil particles, which could lead to the collapse of force chains.

A thermo-mechanical constitutive model was newly developed based on the bounding surface plasticity framework to predict the thermo-mechanical behaviour of saturated and unsaturated interfaces. Some new formulations were proposed to model the critical state void ratio and shear strength. Comparisons between measured and computed results suggest that

this model can well capture the coupled effects of temperature, suction and net normal stress on the shear behaviour of interfaces at various suctions, stresses and temperatures.

Furthermore, a small-scale physical model was set up to investigate the thermo-mechanical behaviour of energy piles. Several series of tests were carried out with considering the effects of soil suction and interface roughness. It is observed that the bearing capacity of an energy pile increase with increasing suction and roughness but decreasing temperature. A suction increment can increase both shaft and toe resistance, while temperature and roughness mainly affect the shaft resistance. During cyclic heating and cooling, suction and roughness increment reduces the irreversible pile head settlement, due to the increment of shaft resistance. These findings are explained based on the results of thermal conductivity and interface shear behaviour, obtained from the above tests.

It is anticipated that the experimental and theoretical results from this study are useful for researchers and engineers to investigate the thermal efficiency and mechanical performance of energy piles in different ground conditions.

## Publications Arising from the Thesis

### Journal paper:

- (1) **Sheqiang Cui**, Chao Zhou\*, Qingyi Mu, Huafu Pei and Jianhua Yin (2022), “Coupled Effects of Temperature and Suction on the Shear Behaviour of Saturated and Unsaturated Silt-Structure Interfaces”, manuscript submitted to *Géotechnique* (in review).
- (2) **Sheqiang Cui** and Chao Zhou\* (2022), “Coupled effects of stress state and void ratio on thermal conductivity of saturated soils”, *Géotechnique Letters* **12(2)**:1-6.
- (3) **Sheqiang Cui**, Chao Zhou\* and Junhui Zhang (2022), “Experimental Investigations on the State-Dependent Thermal Conductivity of Sand-Rubber Mixtures”, *Journal of Materials in Civil Engineering*, 34(3).
- (4) **Sheqiang Cui**, Chao Zhou\* and Jinquan Liu, “Stress Effects on Thermal Conductivity of Soils and Thermal Efficiency of Energy Piles under Saturated and Unsaturated Conditions”, (under preparation).
- (5) **Sheqiang Cui** and Chao Zhou\*, “Thermally-induced Relative Movement at Saturated and Unsaturated Silt-Structure Interfaces”, (under preparation).
- (6) **Sheqiang Cui** and Chao Zhou\*, “A Thermo-Mechanical Model for Saturated and Unsaturated Soil-Structure Interfaces”, (under preparation).
- (7) **Sheqiang Cui** and Chao Zhou\*, “Physical Modelling of the Thermo-Mechanical Behaviour of Energy Piles in Saturated and Unsaturated Silts”, (under preparation).

### Conference paper:

- (1) **Sheqiang Cui** and Chao Zhou (2023), “Investigation of thermal effects on the shear behaviour of saturated silt-structure interface”, IS-PORTO 2023: 8th International Symposium on Deformation Characteristics of Geomaterials. (in review)

## **Acknowledgements**

I wish to take this opportunity to thank the following people, who gave me lots of support throughout my study period.

First of all, I would like to express my heartiest gratitude to my chief supervisor, Dr. Chao ZHOU, for his patient encouragement and constructive guidance. His academic criticism in my research work helped me develop a good habit, which will be beneficial to my future career. His kindly personality made our communication easier and helped me relieve lots of pressure in my daily life.

I would also like to extend my thanks to my co-supervisor, Prof. Jianhua YIN, for providing the advanced test devices in our soil lab. Many thanks to Prof. Limin ZHANG from Hong Kong University of Science and Technology, Prof. Annan ZHOU from Royal Melbourne Institute of Technology, and Prof. Zhenyu YIN from Hong Kong Polytechnic University for their precious time and great efforts as the external examiners and the committee chairman.

I appreciate the help from my previous and current research colleagues for their constructive suggestions on my research in various ways. I also want to thank the laboratory technicians, Mr. Kwok-man Leung and Mr. David LEUNG, for their heartfelt and professional assistance in my laboratory tests.

Last but not least, I would like to express my deepest gratitude to my parents and my fiancée, for their selfless love and support throughout my whole study period.

# Table of Contents

<b>Certificate of originality .....</b>	<b>I</b>
<b>Abstract.....</b>	<b>II</b>
<b>Publications Arising from the Thesis.....</b>	<b>V</b>
<b>Acknowledgements .....</b>	<b>VI</b>
<b>Table of Contents .....</b>	<b>VII</b>
<b>List of tables.....</b>	<b>XIV</b>
<b>List of figures.....</b>	<b>XV</b>
<b>Chapter 1: Introduction .....</b>	<b>1</b>
1.1 Research background .....	1
1.2 Research objectives and strategy .....	5
1.3 Structure of the thesis.....	6
<b>CHAPTER 2: Literature Review .....</b>	<b>10</b>
2.1 Thermal conductivity of soils .....	10
2.1.1 Thermal conductivity of soil in various states .....	10
2.1.2 Existing models for calculating soil thermal conductivity .....	13
2.2 Thermal efficiency of energy piles .....	16
2.2.1 Effects of pipe configuration on the thermal efficiency .....	17
2.2.2 Effects of soil thermal conductivity on the thermal efficiency.....	18
2.3 Thermo-mechanical behaviour of saturated and unsaturated interfaces.....	19
2.3.1 Shear behaviour of saturated interfaces .....	20
2.3.2 Shear behaviour of unsaturated interfaces .....	21
2.4 Constitutive models for saturated and unsaturated interfaces.....	23

2.4.1 Modeling temperature effect on the shear behaviour of interfaces.....	23
2.4.2 Modeling suction effect on the shear behaviour of interfaces .....	24
2.5 Thermo-mechanical behaviour of energy piles.....	26
2.5.1 Full-scale tests on the behaviour of energy piles .....	26
2.5.2 Physical model tests on the behaviour of energy piles .....	29
2.5.3 Effects of roughness on the pile’s behaviour at room temperature .....	32
2.6 Summary .....	32

**CHAPTER 3: Experimental Investigation of The State-Dependent Thermal Conductivity**  
 .....50

3.1 Test apparatus and its working principle.....	50
3.2 Test materials and specimen preparation .....	52
3.2.1 Test materials .....	52
3.2.2 Specimen preparation.....	53
3.3 Test program and procedures .....	55
3.3.1 Tests at zero stress .....	56
3.3.2 Tests with consideration of stress effects.....	56
3.4 Interpretations of experimental results.....	57
3.4.1 Effects of void ratio on the thermal conductivity .....	57
3.4.2 Effects of moisture condition on the thermal conductivity.....	60
3.4.3 Effects of stress on the thermal conductivity of sand, silt and clay .....	62
3.4.4 Effects of stress on the thermal conductivity of sand-rubber mixtures .....	64
3.4.5 Comparisons of stress effects at various degrees of saturation.....	66
3.4.6 Hysteresis in the thermal conductivity-stress relation .....	68

3.5 Summary .....	69
<b>CHAPTER 4: A New Model for Soil Thermal Conductivity and Its Applications for Analyzing the Thermal Efficiency of Energy Pile.....</b>	<b>90</b>
4.1 A new model for the thermal conductivity of soil.....	90
4.1.1 Evaluation of existing models for considering stress effects.....	90
4.1.2 A new semi-empirical equation for thermal conductivity of saturated soil....	91
4.1.3 Extension of the new equation from saturated to unsaturated soils.....	93
4.2 A numerical model for analysing the thermal efficiency of energy piles .....	95
4.2.1 Governing equations for the water flow in soils and piles.....	95
4.2.2 Governing equations for the heat transfer in soils and piles.....	97
4.2.3 Governing equations for the water flow and heat transfer inside pipes.....	98
4.2.4 Model implementation and verification.....	100
4.3 Numerical parametric studies .....	101
4.4 Interpretations of numerical results .....	103
4.4.1 Typical temperature distributions around energy piles.....	103
4.4.2 Thermal efficiency of energy piles with different dimensions .....	105
4.4.3 Thermal efficiency of energy piles at different flow conditions in pipes.....	107
4.4.4 Stress effects on the thermal efficiency of energy piles in different soils ....	110
4.4.5 Coupled effects of stress and unsaturation on pile thermal responses.....	110
4.5 Summary.....	111
<b>CHAPTER 5: Coupled Effects of Temperature and Suction on the Shear Behaviour of Interfaces .....</b>	<b>139</b>
5.1 A new suction- and temperature-controlled apparatus for testing soil-structure	

interfaces .....	139
5.2 Test soil and specimen preparation .....	142
5.3 Test program and procedures .....	143
5.3.1 Constant-temperature direct shear tests .....	143
5.3.2 Constant-stress heating and cooling tests .....	144
5.4 Repeatability of the test results .....	145
5.5 Interpretations of constant-temperature shear test results.....	146
5.5.1 Thermally induced soil deformation before shearing .....	146
5.5.2 Temperature effects on the shear behaviour of saturated interfaces.....	147
5.5.3 Temperature effects on the friction angle of saturated interfaces.....	149
5.5.4 Coupled effects of temperature and suction on the shear strength of unsaturated interfaces .....	150
5.5.5 Suction and temperature effects on dilatancy .....	154
5.6 Interpretations of constant-stress heating and cooling test results.....	155
5.6.1 Tangent and normal displacements during heating and cooling.....	155
5.6.2 Effects of stress and suction on the irreversible tangent displacement.....	157
5.7 Summary .....	158
<b>CHAPTER 6: A Thermo-Mechanical Model For Saturated and Unsaturated Soil- structure Interfaces.....</b>	<b>187</b>
6.1 Mathematical formulations .....	187
6.1.1. Constitutive stress variables.....	187
6.1.2. Critical state shear strength.....	189
6.1.3. Critical state void ratio and state parameter.....	190

6.1.4. Elasto-plasticity.....	192
6.1.5 Bounding and yield surfaces.....	194
6.1.6. Condition of consistency.....	195
6.2 Calibration of model parameters.....	196
6.3 Model validation.....	198
6.3.1. Shear behaviour of unsaturated interfaces at the isothermal condition .....	198
6.3.2. Shear behaviour of saturated interfaces at different temperatures.....	200
6.3.3. Shear behaviour of unsaturated interfaces at different temperatures.....	201
6.4 Summary.....	203
<b>CHAPTER 7: Physical Modelling of Energy Piles in Saturated and Unsaturated Silts</b> .....	<b>222</b>
7.1 Experimental program .....	222
7.2 Model energy piles.....	223
7.3 Model setup and instrumentation.....	225
7.4 Test soil and model preparation .....	227
7.5 Test procedures .....	228
7.6 Interpretations of the results of constant-temperature pile load tests .....	230
7.6.1 Load-settlement relationship and bearing capacity.....	230
7.6.2 Mobilization of the shaft and toe resistances.....	232
7.7 Interpretations of the results of constant-load heating and cooling tests.....	234
7.7.1 Typical responses of energy pile to cyclic heating and cooling .....	234
7.7.2 Accumulation of irreversible pile settlement during cyclic heating and cooling .....	234

7.7.3 Distribution of soil temperature .....	237
7.7.4 Thermal effects on the axial load distribution and neutral plane.....	238
7.7.5 Effects of suction and roughness on the thermally induced axial load.....	240
7.7.6 Axial displacement of piles subjected to heating and cooling .....	242
7.8 Summary .....	243
<b>CHAPTER 8: Conclusions and Future Work .....</b>	<b>265</b>
8.1 Major conclusions .....	265
8.1.1 State-dependent thermal conductivity of soil .....	265
8.1.2 A new model for the soil thermal conductivity and its application in the analysis of pile thermal performance .....	266
8.1.3 Shear behaviour of saturated and unsaturated interfaces at different temperatures .....	266
8.1.4 Constitutive modelling of thermo-mechanical behaviour of unsaturated interface.....	267
8.1.5 Physical modelling of energy piles in saturated and unsaturated silts.....	268
8.2 Future work.....	269
8.2.1 Suggestions for experimental work .....	269
8.2.2 Suggestions for constitutive modelling.....	270
8.2.3 Suggestions for numerical simulation.....	271
<b>Appendix: some formulations for the model in Chapter 6.....</b>	<b>272</b>
Elastic moduli .....	272
Plastic modulus .....	272
Dilatancy .....	272

**References.....274**

## List of tables

Table 2.1 Some of equations for calculating soil thermal conductivity.....	35
Table 3.1. Basic properties of the test materials. ....	72
Table 3.2. Physical properties of the sand-rubber mixtures.....	73
Table 3.3. Summary of the tests at zero stress (42 tests in total with three replicates for each test).....	74
Table 3.4. Summary of the tests with a loading-unloading cycle (13 tests in total with three replicates for each condition).....	75
Table 3.5. Value of model parameters in equation (3-2).....	76
Table 4.1. Model parameters of the soils used in the study. ....	113
Table 4.2. Pipe and heat flow parameters used to simulate the field test (Abdelaziz, 2013). 114	
Table 4.3. Pile and ground parameters used to simulate the field test (Abdelaziz, 2013). ....	115
Table 4.4. Values of input parameters for numerical parametric studies. ....	116
Table 4.5. Soil parameters for numerical parametric studies.....	117
Table 4.6. Numerical program for parametric studies at saturated condition (90 cases in total). .....	118
Table 4.7. Numerical program for parametric studies at unsaturated condition. (6 cases in total) .....	119
Table 5.1. Basic properties of the soil used in the chapter. ....	161
Table 5.2. Summary of the constant-temperature direct shear tests at zero suction (24 tests in total). ....	162
Table 5.3. Summary of the constant-temperature direct shear tests at different suctions (12 tests in total). ....	163
Table 5.4. Summary of constant-stress heating and cooling tests. (12 tests in total).....	164
Table 6.1. Summary of parameters for the current model and their values for the various soil-structure interfaces. ....	205
Table 7.1. Summary of constant-temperature pile load tests. ....	246
Table 7.2. Summary of constant-load heating and cooling tests.....	246

## List of figures

Figure 1.1. Working principle of energy pile (Suryatriyastuti et al., 2012).	8
Figure 1.2. Schematic diagram of an energy pile.	8
Figure 1.3. Research methodology and layout of this study.	9
Figure 2.1. The relationship between thermal conductivity and porosity (Chen 2008).	36
Figure 2.2. The relationship between thermal conductivity and degree of saturation (Chen 2008).	37
Figure 2.3. Conceptual sketches (Likos 2014): (a) soil-water characteristic curve (SWCC); (b) thermal conductivity dryout curve (TCDC) for coarse-grained soil.	38
Figure 2.4. The relationship between thermal conductivity and effective vertical stress (Roshankhah and Santamarina 2014).	39
Figure 2.5. Effects of pipe numbers on the thermal efficiency of energy piles (Cecinato and Loveridge, 2015).	40
Figure 2.6. Energy pile configurations (Fadejev et al., 2017).	40
Figure 2.7. Effects of water table depth on the thermal efficiency of energy piles (Choi et al., 2011): $h_c$ is the depth of water table; L is the pile length.	41
Figure 2.8. Results for saturated sand-structure interface under constant normal load conditions (Maghsoodi et al., 2020).	42
Figure 2.9. Results for saturated clay-structure interface under constant normal load conditions (Maghsoodi et al., 2020).	43
Figure 2.10. Thermo-mechanical loading paths in the field tests of Laloui et al. (2006).	44
Figure 2.11. Irreversible displacement after one heating and cooling cycle (Laloui et al., 2006).	44
Figure 2.12. Responses of energy piles under different thermal loading (Amatya et al., 2012).	45
Figure 2.13. Effects of soil restraint on the energy responses (Bourne-Webb et al., 2013).	46
Figure 2.14. Layout of physical model in the study of Yavari et al. (2014).	47
Figure 2.15. Pile head displacement during heating and cooling (Wang et al., 2016).	48

Figure 2.16. The pile load-settlement curves in the centrifuge modelling tests of Ng et al. (2015). .....	49
Figure 3.1. A test apparatus for measuring thermal conductivity modified with stress control and deformation measurement: (a) schematic diagram; (b) photo.....	77
Figure 3.2. Typical response curve of the temperature in a thermal conductivity test. ....	78
Figure 3.3. Particle size distribution of the test rubber, Toyoura sand, silt (CDG) and kaolin clay. ....	78
Figure 3.4. Thermal conductivity of saturated specimens with various void ratios at zero net stress (results of D1-D3 tests). ....	79
Figure 3.5. Thermal conductivity of dry specimens with various void ratios and rubber contents under zero net stress (results of D4-D6 tests). ....	79
Figure 3.6. Influence of degree of saturation on the soil thermal conductivity under zero net stress (results of M1-M4 tests).....	80
Figure 3.7. Influence of degree of saturation on the normalized thermal conductivity $\lambda/\lambda_{dry}$ under zero stress (results of M1-M4 tests).....	80
Figure 3.8. The behaviour of soil specimens in series S1-S5 during loading-unloading: (a) void ratio-stress relation; (b) evolution of thermal conductivity.....	81
Figure 3.9. Thermal conductivity-void ratio relation during the loading-unloading process..	82
Figure 3.10. Comparisons between measured and calculated results: (a) Toyoura sand with an initial void ratio of 0.76; (b) Toyoura sand with an initial void ratio of 0.6; (c) CDG silt with an initial void ratio of 0.63; (d) CDG silt with an initial void ratio of 0.48; (e) Kaolin clay with an initial void ratio of 1.93.....	84
Figure 3.11. Test results of silt with initial $S_r = 25\%$ and $50\%$ (results of S6-S7 tests): (a) void ratio-stress relation; (b) thermal conductivity-stress relation.....	85
Figure 3.12. Test results of dry sand-rubber mixtures (results of S8-S9 tests): (a) void ratio- stress relation; (b) thermal conductivity-stress relation. ....	86
Figure 3.13. Test results of sand-rubber mixtures with initial $S_r = 50\%$ (results of S10-S11 tests): (a) void ratio-stress relation; (b) thermal conductivity-stress relation. ....	87

Figure 3.14. Test results of saturated sand-rubber mixtures (results of S12-S13 tests): (a) void ratio-stress relation; (b) thermal conductivity-stress relation.....	88
Figure 3.15. Influence of initial degree of saturation and rubber content on $\lambda_{600}$ ( $\lambda_{600}$ and $\lambda_0$ are the thermal conductivities at net stresses of 600 and 0 kPa, respectively). .....	89
Figure 3.16. Increase in the thermal conductivity induced by a loading and unloading cycle ( $H = \lambda_0 * -\lambda_0 \lambda_0 * +\lambda_0 2$ , where $\lambda_0$ is the initial thermal conductivity, and $\lambda_0 *$ is the thermal conductivity after a loading-unloading cycle).....	89
Figure 4.1. Comparisons between measured and calculated thermal conductivities of saturated soils: (a) Toyoura sand with initial void ratio of 0.76; (b) Toyoura sand with initial void ratio of 0.6; (c) CDG with initial void ratio of 0.63; (d) CDG with initial void ratio of 0.48; (e) Kaolin clay with initial void ratio of 1.93. ....	121
Figure 4.2. The relationship between parameter $b$ and degree of saturation. ....	122
Figure 4.3. Comparisons between measured and calculated thermal conductivities of unsaturated CDG with initial void ratio of 0.63.....	122
Figure 4.4. Comparisons between measured and calculated relations between thermal conductivity and net stress for saturated and unsaturated sand-rubber mixtures.....	123
Figure 4.5. Comparison between measured and calculated thermal conductivities with considering coupled effects of stress, void ratio and degree of saturation.....	123
Figure 4.6. Model setup based on the Virginia Tech field test site (after Ozudogru et al. (2015)). .....	124
Figure 4.7. Comparison between computed and measured results.....	125
Figure 4.8. Finite element mesh of the numerical model for parametric studies.....	126
Figure 4.9. Temperature distribution in the horizontal direction at the mid-height of pile (unit: °C).....	127
Figure 4.10. Contour of temperature during heating (pile diameter: 0.9 m; pile aspect ratio: 30; soil: kaolin clay; unit: °C). ....	128
Figure 4.11. Typical contour of temperature inside pipe (pile diameter: 0.6 m; soil: kaolin clay): (a) (c) pile aspect: 10; (b) (d) pile aspect: 50. ....	129

Figure 4.12. Temperature distribution at different distances from the pile surface (pile diameter: 0.6 m; pile aspect ratio: 30; soil: kaolin clay): (a) 3 days; (b) 15 days; (c) 30 days. ....	130
Figure 4.13. Typical temperature distribution in the horizontal direction at the mid-height of pile (pile diameter: 0.6 m; pile aspect ratio: 30; soil: kaolin clay).....	131
Figure 4.14. Coupled effects of stress and aspect ratio on heat exchange rate at a typical condition (pile diameter: 0.6 m; soil: kaolin clay): (a) heat exchange rates with and without stress effects; (b) heat exchange rate with stress effects $Q_{stress}$ over that without stress effects $Q_0$ .....	132
Figure 4.15. Coupled effects of stress and pile diameter on the heat exchange rate at a typical condition (pile aspect ratio: 30; soil: kaolin clay): (a) heat exchange rates with and without stress effects; (b) the ratio $Q_{stress}/Q_0$ .....	133
Figure 4.16. Heat exchange rate at different flow rate conditions: (a) 3 days; (b) 15 days; (c) 30 days. ....	134
Figure 4.17. Coupled effects of stress and pile aspect ratio on the heat exchange rate at different flow rate conditions.....	135
Figure 4.18. Effects of flow rate on the difference between inlet and outlet temperatures. ..	135
Figure 4.19. Effects of stress on the heat exchange rate with inlet fluid temperatures of 38°C: (a) heat exchange rates with and without stress effects; (b) the ratio $Q_{stress}/Q_0$ . ....	136
Figure 4.20. Stress effects on the heat exchange rate for piles in different soils considering typical pile diameters and aspect ratios.....	137
Figure 4.21. Effects of water table locations on the heat exchange rate: (a) heat exchange rates with and without stress effects; (b) the ratio $Q_{stress}/Q_0$ . ....	138
Figure 5.1. Schematic diagram of the new suction- and temperature-controlled direct shear apparatus. ....	165
Figure 5.2. A photo of direct shear apparatus. ....	166
Figure 5.3. Typical temperature-time relation monitored at different locations of soil specimen subjected to heating/cooling.....	167
Figure 5.4. Calibration of the total frictional force, including the friction between lower and	

upper shear boxes and the friction between loading rod and chamber, at different temperatures and air pressures in the chamber. ....	167
Figure 5.5. CDG water retention curve (data from Hossain and Yin (2010)).....	168
Figure 5.6. Thermo-hydro-mechanical path of the direct shear tests: (a) constant-temperature shearing tests; (b) constant-stress heating and cooling tests. (Point A represents the initial state after soil saturation).....	169
Figure 5.7. Repeatability of test results: (a) stress-horizontal displacement relation; (b) shearing induced vertical deformation (positive value means contraction). ....	170
Figure 5.8. Thermal strain at various stresses and suctions (positive value means contraction): (a) zero suction; (b) various suctions. ....	171
Figure 5.9. Shear behaviour of saturated silt-structure interface at various temperatures and a net normal stress of 25 kPa: (a) stress-horizontal displacement relation; (b) shearing induced vertical deformation. ....	172
Figure 5.10. Shear behaviour of saturated silt-structure interface at various temperatures and a net normal stress of 50 kPa: (a) stress-horizontal displacement relation; (b) shearing induced vertical deformation. ....	173
Figure 5.11. Shear behaviour of saturated silt-structure interface at various temperatures and a net normal stress of 100 kPa: (a) stress-horizontal displacement relation; (b) shearing induced vertical deformation. ....	174
Figure 5.12. Shear behaviour of saturated silt-structure interface at various temperatures and a net normal stress of 150 kPa: (a) stress-horizontal displacement relation; (b) shearing induced vertical deformation. ....	175
Figure 5.13. Shear behaviour of saturated silt-structure interface at various temperatures and a net normal stress of 225 kPa: (a) stress-horizontal displacement relation; (b) shearing induced vertical deformation. ....	176
Figure 5.14. Shear behaviour of saturated silt-structure interface at various temperatures and a net normal stress of 300 kPa: (a) stress-horizontal displacement relation; (b) shearing induced vertical deformation. ....	177

Figure 5.15. Critical state shear strength of saturated CDG-structure interface at different temperatures. ....	178
Figure 5.16. Temperature effects on the critical state friction angle of different soil-structure interfaces. ....	178
Figure 5.17. Shear behaviour of unsaturated CDG-structure interface at various temperatures and a net normal stress of 50 kPa: (a) stress-horizontal displacement relation; (b) shearing induced vertical deformation.....	179
Figure 5.18. Shear behaviour of unsaturated CDG-structure interface at various temperatures and a net normal stress of 100 kPa: (a) stress-horizontal displacement relation; (b) shearing induced vertical deformation.....	180
Figure 5.19. Shear behaviour of unsaturated CDG-structure interface at various temperatures and a net normal stress of 150 kPa: (a) stress-horizontal displacement relation; (b) shearing induced vertical deformation.....	181
Figure 5.20. Critical state shear strength of unsaturated CDG-structure interface in the plane of: shear strength versus suction. ....	182
Figure 5.21. Dilatancy of CDG-structure interface at different suctions, temperatures and net normal stresses .....	182
Figure 5.22. Shear behaviour of saturated CDG-structure interface during heating and cooling: (a), (b), (c) normalized tangent displacement; (d), (e), (f) volumetric strain.....	183
Figure 5.23. Shear behaviour of unsaturated CDG-structure interface during heating and cooling: (a), (b), (c) normalized tangent displacement; (d), (e), (f) volumetric strain.....	184
Figure 5.24. Irreversible tangent displacement induced by one thermal cycle: (a) effects of net normal stress; (b) effects of suction. ....	185
Figure 5.25. Influence of shear stress on the irreversible tangent displacement induced by one thermal cycle. ....	186
Figure 6.1. Comparisons between the measured (Hossain and Yin, 2012) and computed critical state shear strengths $\tau_c$ using different formulations for normal skeleton stress.....	206
Figure 6.2. Definition of the state parameter ( $\psi$ ) in equation (6-11). ....	206

Figure 6.3. Schematic diagram of two bounding surfaces and one yield surface.....	207
Figure 6.4. Calibration of the parameters: $rM$ and $r\Gamma$ .....	208
Figure 6.5. Calibration of the parameters: $a_0$ , $c_0$ ,.....	209
Figure 6.6. Comparisons between measured (Hossain and Yin, 2012) and computed shear behaviour of a soil-cement interface at a net normal stress of 100 kPa and suctions of 0, 50 and 100 kPa: (a) and (b) for the current model; (c) and (d) for the model of (Zhou et al., 2020). .....	210
Figure 6.7. Comparisons between measured (Hossain and Yin, 2012) and computed shear behaviour of a soil-cement interface at zero suction and effective normal stresses of 50, 100 and 300 kPa: (a) and (b) for the current model; (c) and (d) for the model of (Zhou et al., 2020). .....	211
Figure 6.8. Comparisons between measured (M) (Di Donna et al., 2016) and computed (C) shear behaviour of saturated soil-concrete interfaces at various normal stresses and temperatures (the numbers after letters N and T denote the normal stress (unit: kPa) and temperature (unit: °C), respectively).....	212
Figure 6.9. Comparisons between measured (M) (Chapter 5) and computed (C) shear behaviour of saturated soil-steel interfaces at 8°C: (a) stress-horizontal displacement relation; (b) shearing induced vertical displacement (the number after S denotes suction (unit: kPa)). ..	213
Figure 6.10. Comparisons between measured (M) (Chapter 5) and computed (C) shear behaviour of saturated soil-steel interfaces at 20°C: (a) stress-horizontal displacement relation; (b) shearing induced vertical displacement.....	214
Figure 6.11. Comparisons between measured (M) (Chapter 5) and computed (C) shear behaviour of saturated soil-steel interfaces at 42°C: (a) stress-horizontal displacement relation; (b) shearing induced vertical displacement.....	215
Figure 6.12. Comparisons between measured (M) (Chapter 5) and computed (C) shear behaviour of unsaturated soil-steel interfaces at 50 kPa net stress and 20°C: (a) stress-horizontal displacement relation; (b) shearing induced vertical displacement. ....	216
Figure 6.13. Comparisons between measured (M) (Chapter 5) and computed (C) shear	

behaviour of unsaturated soil-steel interfaces at 100 kPa net stress and 20°C: (a) stress-horizontal displacement relation; (b) shearing induced vertical displacement. ....	217
Figure 6.14. Comparisons between measured (M) (Chapter 5) and computed (C) shear behaviour of unsaturated soil-steel interfaces at 150 kPa net stress and 20°C: (a) stress-horizontal displacement relation; (b) shearing induced vertical displacement. ....	218
Figure 6.15. Comparisons between measured (M) (Chapter 5) and computed (C) shear behaviour of unsaturated soil-steel interfaces at 50 kPa net stress and 42°C: (a) stress-horizontal displacement relation; (b) shearing induced vertical displacement. ....	219
Figure 6.16. Comparisons between measured (M) (Chapter 5) and computed (C) shear behaviour of unsaturated soil-steel interfaces at 100 kPa net stress and 42°C: (a) stress-horizontal displacement relation; (b) shearing induced vertical displacement. ....	220
Figure 6.17. Comparisons between measured (M) (Chapter 5) and computed (C) shear behaviour of unsaturated soil-steel interfaces at 150 kPa net stress and 42°C: (a) stress-horizontal displacement relation; (b) shearing induced vertical displacement. ....	221
Figure 7.1. Model piles with different degrees of roughness. ....	247
Figure 7.2. Schematic diagram of the experimental set-up: (a) elevation view; (b) side view. ....	248
Figure 7.3. Layout of the physical model test.....	249
Figure 7.4. Overview of the calibration tests.....	250
Figure 7.5. Calibration results of the fibers at different thermo-mechanical loading paths: (a) mechanical loading at different temperatures; (b) thermal loading without mechanical loads. ....	251
Figure 7.6. Installation of thermocouples and tensiometers. ....	252
Figure 7.7. Thermo-mechanical loading paths for constant-load heating and cooling tests..	253
Figure 7.8. Load-settlement relationships of model piles at various conditions of suction, temperature and roughness.....	254
Figure 7.9. Evolution of axial load distributions during the loading process at various suctions, temperatures and degrees of roughness.....	255

Figure 7.10. Evolution of shaft resistance and pile toe resistance at various suctions, temperatures and degrees of roughness.....	256
Figure 7.11. Typical response curves: (a) fluid temperature inside piles and soil temperature; (b) pile head settlement during heating and cooling. ....	257
Figure 7.12. Pile head displacement during thermo-mechanical loads: (a) effects of suction, roughness and working load; (b) effects of thermo-mechanical paths. ....	258
Figure 7.13. Measured soil temperature at different suctions: (a) heating phase; (b) cooling phase.....	259
Figure 7.14. Axial load distributions at various stress levels and suctions: (a), (c), (e) heating phase; (b), (d), (f) cooling phase. ....	260
Figure 7.15. Variations of neutral plane locations: (a) at end of 5 <sup>th</sup> heating; (b) at end of 5 <sup>th</sup> cooling.....	261
Figure 7.16. Thermally induced axial load: (a), (b), (c) heating phase; (d), (e), (f) cooling phase. ....	262
Figure 7.17. Axial displacement of model piles at various stress levels and suctions: (a), (b), (c) heating phase; (d), (e), (f) cooling phase.....	263
Figure 7.18. Axial displacement distributions of piles head and toe at various suctions, temperatures roughnesses and vertical loads: (a), (b) heating phase; (c), (d) cooling phase. ....	264

## **Chapter 1: Introduction**

### **1.1 Research background**

Population growth has increased the energy consumption demand throughout the world. Currently, space heating and cooling account for about 25% of the total energy produced in the world (Patel and Bull, 2011). Energy pile is considered a new solution to reduce the energy used in space heating and cooling. Figure 1.1 shows the working principle of an energy pile which has two major functions: providing mechanical support and exchanging heat between buildings and the ground. The latter relies on the fact that the Earth's temperature at a certain depth remains fairly constant throughout the year (i.e., not affected by seasonal variation of air temperature) (Brandl, 2006). In summer, hot fluid is pumped into an energy pile and heat is expelled to the ground. Similarly, in winter, cold fluid is circulated in an energy pile and heat is extracted from the ground. Through the utilization of energy piles, both energy consumption and carbon dioxide emissions can be reduced by about 60% and 50%, respectively (Patel and Bull, 2011). Hence, energy pile is one environment-friendly and efficient technology for harvesting shallow geothermal energy.

Energy piles have received much attention during the past two decades (Brandl, 2006; Suryatriyastuti et al., 2012; Laloui and Di Donna, 2013; Fadejev et al., 2017; Han and Yu, 2018). Most of the previous studies focused on the thermo-mechanical performance of energy piles (e.g., the heat exchange rate between the ground and pile, bearing capacity and thermally induced settlement of pile) in saturated soils. However, water tables are very deep in many regions. For instance, the average groundwater table in Beijing was 24.3m below the ground

surface in 2012, and this level keeps dropping due to the underground water over-exploitation which is very common in northern China (Wang et al., 2015b). In the literature, energy piles in the unsaturated ground have been widely reported, from many locations of the world such as Beijing, China (You et al., 2016), Melbourne, Australia (Faizal et al., 2019a) and Colorado, US (Murphy et al., 2015). Moreover, some preliminary results in the literature suggest that the variation of soil moisture has a significant influence on the thermo-mechanical performance of energy piles. For instance, McCartney (2013) observed that an energy pile in the unsaturated ground showed continuous settlement under thermal cycles, probably due to the consolidation and drying of surrounding unsaturated soils. To better improve the understanding and analysis of energy piles in unsaturated ground, more experimental and theoretical studies are needed.

Concerning the heat transfer function of energy piles, soil thermal conductivity ( $\lambda$ ) is the key parameter (Brandl, 2006), because heat transfer is mainly dependent on conduction in the ground (Haigh, 2012). So far, soil thermal conductivity has been investigated via many laboratory tests. The thermal conductivity of a specific soil reduces with increasing voids ratio but decreasing degree of saturation (Kersten, 1949; Woodside and Messmer, 1961; Johansen, 1977; Chen, 2008; Tarnawski et al., 2011; Tarnawski et al., 2009; Zhang et al., 2017; Likos, 2014; Smits et al., 2010). Based on these experimental observations, some semi-empirical equations have been developed for soil thermal conductivity under different moisture and porosity conditions. Furthermore, a few studies were also conducted to investigate thermal conductivity under different stresses. Yun and Santamarina (2008) found the influence of stress on the thermal conductivity of aluminium-bronze spheres under dry conditions, while Yao et

al. (2019) investigated the influence of stress on the thermal conductivity of pure sand. It is postulated in both studies that the increase in thermal conductivity was due to a reduction in void ratio and an increase in the inter-particle contact area. However, the contribution from these two different mechanisms was not analyzed in detail. There is also no study of stress effects on the thermal conductivity of unsaturated soils. The coupled effects of stress and other factors, including porosity and moisture conditions, have not been investigated. More experimental and theoretical studies are needed to understand and model the state-dependent thermal conductivity of unsaturated soils.

Given the above research gap about soil thermal conductivity, previous studies on the thermal efficiency of energy piles did not incorporate stress effects on the heat exchange rate. The influence of soil moisture condition on the pile thermal performance is not clear either. Some comprehensive and in-depth experimental and theoretical studies are needed to improve the understanding of heat exchange rate of energy piles in unsaturated soils.

On the other hand, heat exchange would affect the mechanical response of energy piles. Therefore, the design of energy piles is more challenging and complex than that of conventional piles. The soil-pile interaction is greatly affected by the thermo-mechanical behaviour of soils and soil-pile interfaces (Bourne-Webb et al., 2009). The thermo-mechanical behaviour of soils has been extensively studied (Ng and Zhou, 2014; Sultan et al., 2002; Alsherif and McCartney, 2015; Uchaipichat and Khalili, 2009; Romero et al., 2003; Hueckel et al., 2009). Only recently, some researchers have investigated the temperature influence on the mechanical behaviour of saturated soil-pile interfaces by conducting temperature-controlled direct shear tests (Di Donna

et al., 2016; Yavari et al., 2016a; Maghsoodi et al., 2020; Li et al., 2019). They found that thermal effects on the shear strength of sand-pile interfaces were negligible, but no general conclusion was drawn for clay-pile interfaces. More importantly, it should also be pointed out that all of these studies focused on fully saturated sand and clay. There is no study of the thermal effect on unsaturated soil-pile interfaces. To the best of the author's knowledge, there is no theoretical model for the thermo-mechanical behaviour of unsaturated interfaces.

Through field monitoring, physical model tests and theoretical analysis, some previous researchers have shown that the variation of temperature can affect the mechanical behaviours of energy piles, such as pile settlement under thermal loads (Murphy et al., 2015; Laloui et al., 2006; Pasten and Santamarina, 2014; Stewart and McCartney, 2014; Ng et al., 2015; Yavari et al., 2016b; Liu et al., 2019). Most of them, however, focused on dry and saturated conditions. Only several field tests and centrifuge modelling tests were conducted under unsaturated conditions. Each study considered a single value of initial water content, so suction/moisture effects cannot be revealed. In addition, no study has been conducted to investigate the roughness effects on the behaviour of energy piles.

In summary, it is important to study the coupled thermal and mechanical behaviour of soil-pile interfaces and their influence on the performance of energy piles. To be more specific, some grand scientific challenges should be addressed, as shown in Figure 1.2. Firstly, how does stress affect the thermal conductivity of soils and thus the heat exchange rate of energy piles under saturated and unsaturated conditions? Secondly, how does temperature affect the mechanical behaviour at the soil-pile interfaces and thus the mechanical performance of energy

piles? Thirdly, how should the state-dependent thermal conductivity of soils and thermo-mechanical behaviour of interfaces be modelled?

## 1.2 Research objectives and strategy

The major objectives of this study are as follows:

(i) To understand and model the coupled effects of soil moisture and stress state on the thermal conductivity of saturated and unsaturated soils.

(ii) To compare the thermal efficiency of energy piles with and without considering stress effects on soil thermal conductivity in different ground conditions.

(iii) To explore the coupled effects of temperature and suction on the soil-pile interface behaviour.

(iv) To develop a constitutive model for simulating the thermo-hydro-mechanical behaviour of saturated and unsaturated soil-pile interfaces.

(iii) To reveal the thermo-mechanical behaviour of energy piles in different roughness and suction conditions through physical model tests.

To meet the above objectives, experimental study and theoretical modelling are carried out in this study. The research strategy is shown in Figure 1.3. Three testing apparatuses/systems were developed, including an apparatus for measuring stress-dependent thermal conductivity based on the thermal needle method, a temperature- and suction-controlled direct shear apparatus for testing saturated and unsaturated interfaces, a small-scale physical model (1 m × 0.6 m × 0.8 m) for testing energy pile. By using these apparatuses/systems, extensive tests were carried out. Firstly, 58 thermal conductivity tests were conducted to study the

thermal conductivity of saturated and unsaturated soils in different states. Based on the experimental results, a semi-empirical equation for soil thermal conductivity with consideration of stress effects was proposed. It was then applied in numerical simulations to study the thermal efficiency of energy piles at different stress levels. To investigate the coupled effects of temperature and suction on the interface behaviour, 46 groups of direct shear tests were carried out on a steel-silt interface along two different thermo-mechanical paths, including the constant-temperature direct shear test and constant-stress heating and cooling tests. Furthermore, a new constitutive model was developed to predict the thermo-hydro-mechanical behaviour of saturated and unsaturated interfaces. Finally, a series of physical model tests were conducted to study the bearing capacity and thermally-induced settlement of energy pile at different suctions and roughnesses. The results of soil thermal conductivity and interface shear behaviour are applied to interpret the data of physical model tests.

### **1.3 Structure of the thesis**

Experimental and theoretical results are analyzed and reported in this thesis. The outline of the thesis is as follows:

Chapter 1 provides a brief description of the background, scientific challenges, objectives, research content, and layout of this thesis.

Chapter 2 reviews the thermal and mechanical behaviours of soils and interfaces, and the performance of energy piles in saturated and unsaturated grounds.

Chapter 3 introduces the experimental study of soil thermal conductivity, including the development of a new apparatus, test method and results. The coupled effects of void ratio, degree of saturation and stress state on thermal conductivity are discussed in detail.

In Chapter 4, a semi-empirical equation is proposed for calculating the state-dependent thermal conductivity of soils. The new equation was utilized in the numerical code to study the thermal efficiency of energy piles.

Chapter 5 presents the details and results of direct shear tests on saturated and unsaturated interfaces through a new temperature- and suction-controlled direct shear apparatus.

In Chapter 6, an advanced constitutive model is proposed for the thermo-mechanical behaviour of saturated and unsaturated interfaces. Mathematical formulations, parameter calibration and model validation are reported.

Chapter 7 describes small-scale physical model tests on energy piles in saturated and unsaturated soils. The suction and roughness effects on the thermo-mechanical behaviour of energy piles are analyzed.

Chapter 8 summarizes the major conclusions of this study and gives some recommendations for future studies in this area.

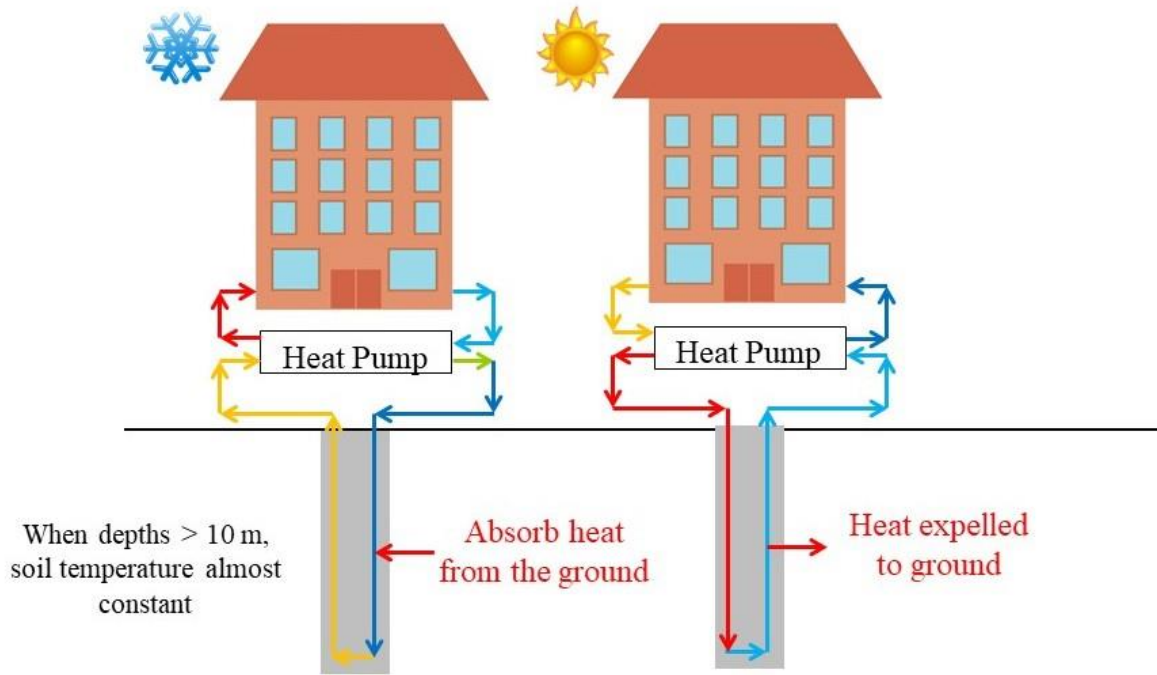


Figure 1.1. Working principle of energy pile (Suryatriyastuti et al., 2012).

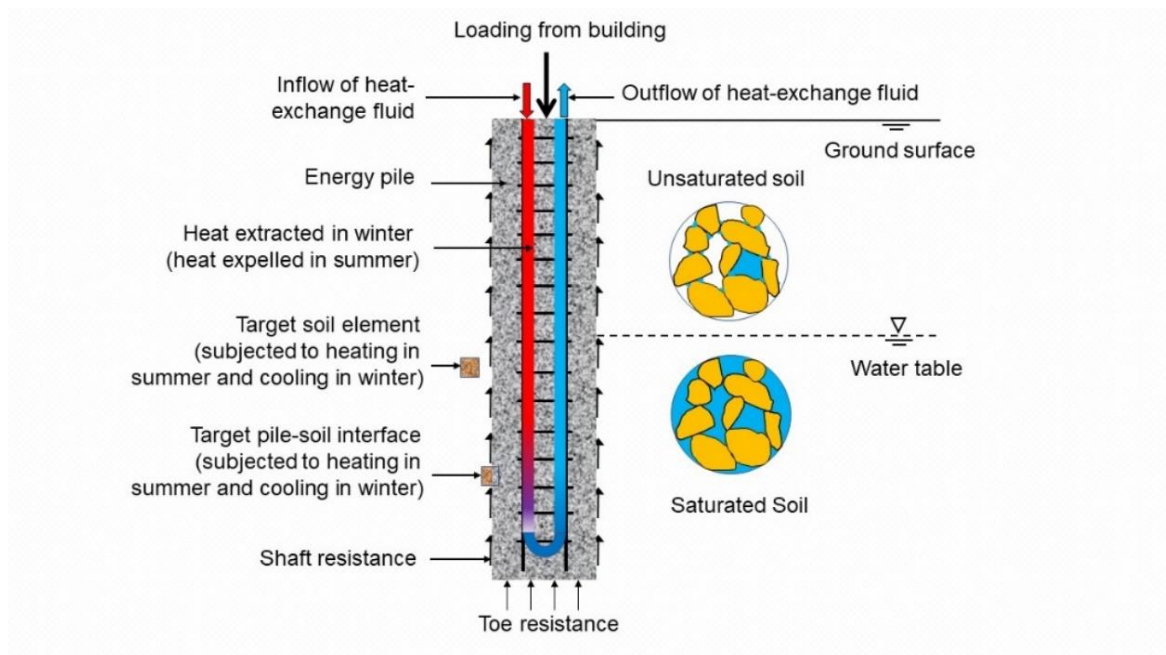


Figure 1.2. Schematic diagram of an energy pile.

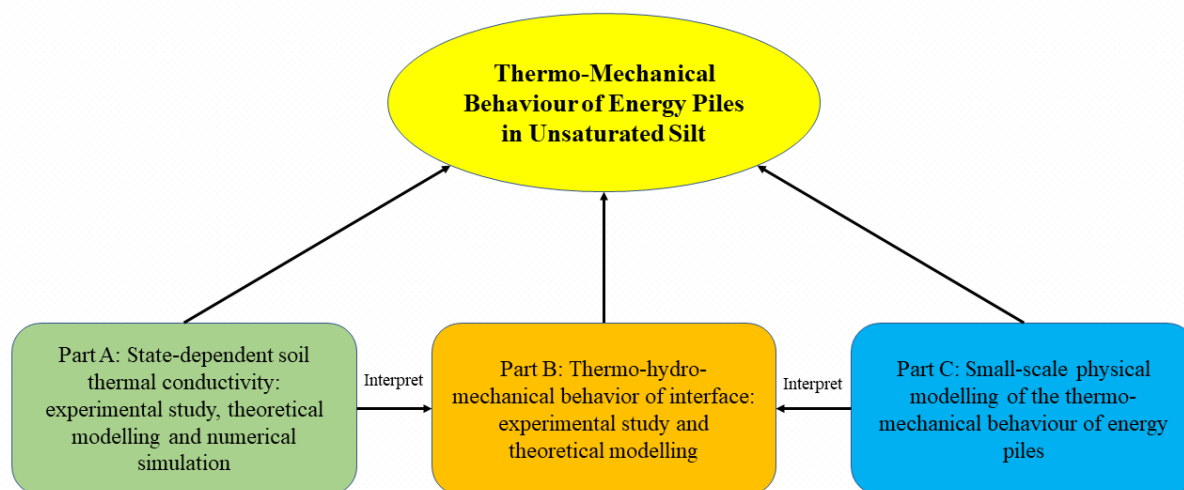


Figure 1.3. Research methodology and layout of this study.

## **CHAPTER 2: Literature Review**

This chapter starts with a review of soil thermal conductivity, including experimental investigation and theoretical modelling. Following that, the influencing factors on the thermal efficiency of energy piles are presented. The soil-structure interface behaviours are reviewed. Then, constitutive models for saturated and unsaturated soil-structure interfaces are discussed. Finally, the thermal and mechanical responses of energy piles are introduced through field tests and physical model tests.

### **2.1 Thermal conductivity of soils**

To analyze the thermal performance of energy geostructures such as energy piles and borehole heat exchangers, soil thermal conductivity is one of the most crucial parameters (Sani and Singh, 2020; Haigh, 2012; McCartney et al., 2016). This is because heat transport in most soils is mainly through heat conduction, even though heat convection may be important for some soils with large permeability such as gravels. In this section, the thermal conductivity of soils is reviewed, with a focus on the influence of soil state (e.g., porosity, moisture and stress) and existing theoretical or semi-empirical models.

#### **2.1.1 Thermal conductivity of soil in various states**

Many laboratory studies of soil thermal conductivity have been reported in the literature. It is generally concluded that apart from the mineral composition, soil thermal conductivity is strongly dependent on soil states. Woodside and Messmer (1961) measured the thermal conductivity of quartz sand under dry and saturated conditions by using the transient heat source method. For both dry and saturated specimens, the thermal conductivity

consistently decreased with increasing porosity. This is because the thermal conductivities of air and water are generally much smaller than that of solid particles. This finding has been confirmed by a lot of researchers (Johansen, 1977; Clauser and Huenges, 1995; Côté and Konrad, 2005; Tang et al., 2008a; Chen, 2008). In particular, Chen (2008) designed a comprehensive test program, considering four kinds of quartz sands and different initial degrees of saturation. The key results from his study are shown in Figure 2.1. The sand thermal conductivity consistently decreased with increasing porosity, regardless of the initial degree of saturation. Similar observations were reported by some other researchers (Tarnawski et al., 2009; Tarnawski et al., 2011; Johansen, 1975; Zhang et al., 2017; Xiao et al., 2018; Yao et al., 2019).

Apart from sands, the thermal conductivity of silts and clays was also measured at different densities (Liu et al., 2020; Zhen et al., 2019; Tang et al., 2008a; Hotz and Ge, 2010). For example, Tang et al. (2008a) used the transient heat source method to detect the thermal conductivity of compacted bentonites, while the remoulded and undisturbed loess was tested by Zhen et al. (2019) through the same technology. Similar to the results of sand, the thermal conductivities of silt and clay decreased with increasing porosity.

Recently, some researchers conducted laboratory tests to explore porosity effects on the thermal conductivities of soil-rubber mixtures (Roshankhah et al., 2021; Xiao et al., 2020; Xiao et al., 2019). Roshankhah et al. (2021) observed a reduction in the thermal conductivity of sand-silt mixtures with increasing porosity. The same conclusion was drawn on sand-rubber mixtures by Xiao et al. (2019).

The degree of saturation is another important factor influencing soil thermal conductivity. Many experimental tests were carried out to investigate its effects on soil thermal conductivity. For example, Chen (2008) presented the variation of thermal conductivity with the degree of saturation based on the experimental results of four different quartz sands. As shown in Figure 2.2. When the degree of saturation increased from 0 to 1, the soil thermal conductivity can increase by 10-15 times. The sand thermal conductivity increased sharply with the degree of saturation at the initial stage but slightly when the degree of saturation was larger than 20%. Similar experimental observations were also found by Zhang et al. (2017) who conducted a comprehensive test program on the thermal conductivity of kaolin clay. Other researchers also provided supportive data to reveal the same trends for soil thermal conductivity at different moisture conditions (Smits et al., 2010; Tai et al., 2020; Liu et al., 2020; Kersten, 1949; Likos, 2014; Likos, 2015). The increment of thermal conductivity resulting from the increasing degree of saturation is because the larger thermal conductivity of water (i.e.,  $0.58 \text{ W}\cdot\text{m}^{-1}\cdot\text{K}^{-1}$ ) is much larger than that of air (i.e.,  $0.024 \text{ W}\cdot\text{m}^{-1}\cdot\text{K}^{-1}$ ) (Bristow et al., 2002; Clauser and Huenges, 1995; Mitchell and Soga, 2005). For the nonlinear relationship between thermal conductivity and degree of saturation, Likos (2014) attributed it to the different saturation regimes based on the soil-water retention curves, as shown in Figure 2.3. Grain-water-grain contact can be formed efficiently by adding a small amount of pore water, which would increase the contact area between two soil particles. Hence, the thermal conductivity is very sensitive to a change in the degree of saturation when the latter is relatively low.

In recent years, several experimental and numerical studies have been carried out to investigate stress effects on the thermal conductivity of porous materials (Yun and Santamarina, 2008; Roshankhah and Santamarina, 2014; Garrett and Ban, 2011; Choo et al., 2013; Yao et al., 2021; Roshankhah et al., 2021; Duc Cao et al., 2021). Yun and Santamarina (2008) firstly found the influence of stress on the thermal conductivity of dry aluminum-bronze spheres, while Yao et al. (2021) investigated stress effects on the thermal conductivity of sands. The typical relationship between thermal conductivity and stress is shown in Figure 2.4. The soil thermal conductivity increased with increasing vertical stress. They postulated qualitatively that the increase in thermal conductivity was due to a reduction in void ratio and an increase in the interparticle contact area, but the contribution from these two different mechanisms was not analyzed in detail.

### 2.1.2 Existing models for calculating soil thermal conductivity

For soils in saturated or dry conditions, the most important factor affecting their thermal conductivity is the porosity. As discussed above, thermal conductivity consistently increases with decreasing porosity (Zhang et al., 2017; Sani and Singh, 2020; Xiao et al., 2018; Lu and Dong, 2015; Chen, 2008). To simulate porosity effects on the thermal conductivity of saturated and dry soils, the theoretical series and parallel models were adopted in the heat transfer analysis (Woodside and Messmer, 1961). They can be expressed as follows:

$$\text{Parallel model: } \lambda = \lambda_s \cdot (1 - n) + \lambda_f \cdot n \quad (2-1)$$

$$\text{Series model: } \frac{1}{\lambda} = \frac{1-n}{\lambda_s} + \frac{n}{\lambda_f} \quad (2-2)$$

where  $\lambda$  is the overall thermal conductivity of a two-phase material (i.e. completely dry or fully saturated soils);  $\lambda_s$  is the solid particle thermal conductivity;  $\lambda_w$  is the thermal conductivity of pore fluid inside soil skeleton (either water or air);  $n$  is soil porosity. These two theoretical models are classical, but they are unable to provide accurate predictions because they do not consider the complexity of soil structure (Dong et al., 2015). As a result, the series and parallel models were modified by many researchers to give better predictions (Tarnawski and Leong, 2012; Gori and Corasaniti, 2002; Woodside and Messmer, 1961). Some semi-empirical equations have also been proposed (Hopmans and Dane, 1986; Chen, 2008; Zhang et al., 2017; Johansen, 1977). Some of the existing equations are presented in Table 2.1. One of the examples, which was proposed and verified by Chen (2008), is described here:

$$\ln \lambda = n \cdot a_s + \ln \lambda_s \quad (2-3)$$

where  $a_s$  is a fitting parameter to describe the sensitivity of thermal conductivity to a change in porosity.

Different from saturated and dry conditions, the soil thermal conductivity under unsaturated conditions is greatly dependent on the degree of saturation, as shown in Figures 2.2 and 2.3. To quantify effects of the degree of saturation on soil thermal conductivity, many semi-empirical models were proposed (Zhang et al., 2017; Liu et al., 2020; Chen, 2008; Johansen, 1977). Johansen (1977) proposed a semi-empirical equation to calculate soil thermal conductivity:

$$\lambda = \left( \lambda_w^n \lambda_s^{1-n} - \frac{0.137\rho_d + 64.7}{2650 - 0.947\rho_d} \right) (0.7 \log S_r + 1) + \frac{0.137\rho_d + 64.7}{2650 - 0.947\rho_d} \quad (2-4)$$

where  $\rho_d$  is the dry density of soil ( $\text{kg}\cdot\text{m}^{-3}$ ). In this model, the soil thermal conductivity is logarithmically dependent on  $S_r$ , which implies that equation (2-4) is not applicable for very dry conditions (e.g.,  $S_r$  lower than 5% (Haigh, 2012)). To address this problem, Côté and Konrad (2005) developed a new model based on the work of Johansen (1977):

$$\lambda = (\lambda_w^n \lambda_s^{1-n} - \chi^{10^{-\eta n}}) \left[ \frac{AS_r}{1+(a-1)S_r} \right] + \chi^{10^{-\eta n}} \quad (2-5)$$

where  $\chi$ ,  $\eta$  and  $A$  are fitting parameters. However, the modified model of Côté and Konrad (2005) is still not suitable for the dry condition.

After analyzing 80 needle-probe tests on four soils ranging from silt to sand (at four porosities and five saturation ratios for each soil), a model was developed by Chen (2008):

$$\ln \lambda = na(Sr) + \ln \lambda_0 \quad (2-6)$$

$$a(S_r) = c \ln[(1 - b)S_r + b] + \ln d \quad (2-7)$$

where  $b$ ,  $c$  and  $d$  are fitting parameters. This model is widely used because it is able to well capture the influence of porosity and degree of saturation on the thermal conductivity of unsaturated soils.

More recently, Lu and Dong (2015) proposed a theoretical equation based on the soil-water retention curve (SWRC), as follows:

$$\frac{\lambda - \lambda_{dry}}{\lambda_{sat} - \lambda_{dry}} = 1 - \left[ 1 + \left( \frac{S_r}{S_r^f} \right)^m \right]^{\frac{1}{m} - 1} \quad (2-8)$$

where  $\lambda_{dry}$  and  $\lambda_{sat}$  are the thermal conductivities of dry and saturated soils, respectively;  $S_r^f$  is the degree of saturation at which the funicular regime occurs; and  $m$  is a model parameter, similar to the pore-size parameter in van Genuchten's SWRC model. More equations about the thermal conductivity of unsaturated soils are given in Table 2.1.

In addition to porosity and degree of saturation, it was recently observed that stress also has an impact on soil thermal conductivity. Two semi-empirical equations were recently proposed for stress effects (Duc Cao et al., 2021; Roshankhah and Santamarina, 2014; Roshankhah et al., 2021). Both of them assume a logarithmic function between thermal conductivity and stress. The equation of Roshankhah and Santamarina (2014) is shown here as one example:

$$\lambda = \lambda_1 \left[ 1 + \beta \log \left( \frac{\sigma'}{1 \text{ kPa}} \right) \right] \quad (2-9)$$

where  $\lambda_1$  is the thermal conductivity at a reference effective stress of 1 kPa;  $\beta$  is a soil parameter. This equation has not been verified by extensive data. Moreover, it is obvious that this equation assumes a unique relationship between thermal conductivity and stress, so the hysteresis during loading-unloading cannot be described.

Although the previous studies improved the understanding and modelling of thermal conductivity at various porosities, moisture conditions and stress states, further studies on this topic are still required. The calculation of soil thermal conductivity is possible by using the previous equations, but the coupled effects of stress, void ratio and degree of saturation were not considered.

## **2.2 Thermal efficiency of energy piles**

Energy piles not only provide structural support for buildings but also facilitate heat exchange between the ground and buildings. To meet the second objective, pipes are installed in piles and connected to a geothermal heat pump that provides a circulating heat-exchange fluid through the pipes. The pile would absorb heat from the ground in winter or expel heat to

the ground in summer (Suryatriyastuti et al., 2012), as shown in Figure 1.1. During this process, geothermal energy can be utilized. This technology provides an energy-efficient and environmentally friendly space cooling and heating (Sawhney and Mahajan, 1994; Jacovides and Mihalakakou, 1995; Gauthier et al., 1997; Ozgener et al., 2005).

The thermal efficiency of energy piles has attracted much attention in the last decades since an optimized design can reduce the cost and harvest more energy. The thermal efficiency of energy piles in the short term, as well as the long term, has been analysed via experimental, analytical and numerical studies. It has been found that the thermal efficiency of energy piles is governed by many factors, including the pipe condition (e.g., water flow velocity in pipes, pipe shape, pipe distributions), soil thermal conductivity, pile thermal resistance, heat pump working mode and so on (Fadejev et al., 2017; McCartney et al., 2019; Cecinato and Loveridge, 2015; Choi et al., 2011; Thomas and Rees, 2009; Loveridge and Powrie, 2013; Ozudogru et al., 2014). The first three factors are reviewed in the following sections because (i) they are important; (ii) they can vary greatly and hence significantly affect the thermal performance of energy piles; (iii) they are closely relevant to civil engineering.

### 2.2.1 Effects of pipe configuration on the thermal efficiency

Brandl (2006) investigated the influence of pile size on the heat exchange rate between soil and energy piles. He concluded that piles with a larger diameter could provide more thermal output due to a larger surface area. However, the increment of pile diameter could probably alter the pile thermal resistance, which has a significant influence on the thermal response of energy piles (Loveridge et al., 2013). To investigate factors governing the thermal

resistance of energy piles, Loveridge and Powrie (2014) conducted a comprehensive numerical analysis. They concluded that the thermal resistance is mainly dependent on the pipe arrangement and pipe number. Increasing the number of pipes and the distance between the pipe and pile center can reduce the thermal resistance and hence improve the soil-pile heat exchange rate. Cecinato and Loveridge (2015) also developed a 3-D numerical model and proved that increasing the number of pipes can bring beneficial effects on the thermal efficiency of energy piles, as shown in Figure 2.5.

The shape of pipes is another factor that can change the heat transfer rate between piles and soils, based on previous studies (Gao et al., 2008; Ozudogru et al., 2014; Zhao et al., 2016). By conducting in-suit tests and numerical simulations, Gao et al. (2008) found that parallel U-pipes were slightly more efficient than series U-pipes. Zhao et al. (2016) observed that the spiral-shaped pipes have a better performance by comparing with U-shaped and W-shaped pipes in a transient 3-D heat transfer model. The current pipe shapes used in energy piles were summarized by Fadejev et al. (2017), as shown in Figure 2.6. For the effects of fluid conditions inside pipes, faster heat flows can also increase the heat transfer rate between soil and piles (Gao et al., 2008; Cecinato and Loveridge, 2015).

### 2.2.2 Effects of soil thermal conductivity on the thermal efficiency

Soil thermal conductivity is a key factor in the assessment of the thermal efficiency of energy piles (Sani and Singh, 2020; Haigh, 2012; McCartney et al., 2016). Several researchers investigated the heat exchange rate at different ground moisture conditions (Thomas and Rees, 2009; Choi et al., 2011; Akrouch et al., 2016). For example, Thomas and Rees (2009) built a

1-D and 2-D slab to estimate the variations of the heat transfer rate from the slab to soils with different water contents. Similarly, Choi et al. (2011) also studied the energy transfer between piles and ground by changing groundwater table depths. They all found that the heat exchange rate decreases with decreasing water table, shown in Figure 2.7. To study the effects of soil moisture on the thermal performance of energy piles, Akrouch et al. (2016) conducted a comprehensive research program, including experimental, analytical and numerical investigations. They confirmed the variations of heat exchange induced by varying soil saturations. Besides, Morais et al. (2020) observed the different thermal responses of energy piles in different seasons in Brazilia. The most important factor is the varying gravimetric water content. In these previous studies, no one considered the effects of stress on the heat exchange between soil and energy piles.

### **2.3 Thermo-mechanical behaviour of saturated and unsaturated interfaces**

As supported by existing theoretical and experimental studies, the variation of temperature can affect the engineering properties of soils and soil-structure interfaces, and hence alter the settlement and bearing capacity of piles (Murphy et al., 2015; Laloui et al., 2006; Pasten and Santamarina, 2014; Stewart and McCartney, 2014; Ng et al., 2015; Yavari et al., 2016b; Liu et al., 2019). Thus, it is crucial to understand the thermal and mechanical behaviours of soils and interfaces for properly analyzing the performance of energy piles. The thermo-mechanical behaviour of soils has been extensively studied (Ng and Zhou, 2014; Sultan et al., 2002; Alsherif and McCartney, 2015; Uchaipichat and Khalili, 2009; Romero et al., 2003; Hueckel et al., 2009). Only recently, some researchers have investigated the temperature

influence on the mechanical behaviour of saturated soil-pile interfaces by conducting temperature-controlled direct shear tests (Di Donna et al., 2016; Yavari et al., 2016a; Maghsoodi et al., 2020; Li et al., 2019). Hence, the current studies focus on interface behaviour and they are reviewed in the following paragraphs.

### 2.3.1 Shear behaviour of saturated interfaces

In recent years, a few investigations have been conducted on the thermo-mechanical behaviour of saturated sand-structure and clay-structure interfaces (Maghsoodi et al., 2020; Li et al., 2019; Yavari et al., 2016a; Di Donna et al., 2016; Yazdani et al., 2019; Maghsoodi et al., 2021). The results present negligible thermal effects on saturated sand-structure interfaces. The saturated clay-structure interfaces display a temperature-dependent response, and different trends are reported in the literature. Di Donna et al. (2016) observed that the interface shear strength increases with the increase of temperature via conducting some direct shear tests on an illite clay-structure interface. They postulated that such an increment is induced by the volumetric contraction of soil during heating (i.e., thermal hardening). However, Yazdani et al. (2019) reported that the elevation of temperature reduces the shear strength of a kaolin clay-structure interface, which is considered to be attributed to the variation of interparticle force under thermal loads. Some other researchers stated that the thermally induced variations of shear strength are within 5% based on tests on red/kaolin clay-structure interfaces (Maghsoodi et al., 2020; Li et al., 2019; Yavari et al., 2016a), as shown in Figure 2.9.

Effects of thermal cycles on the interface shear behaviour were also investigated (Yazdani et al., 2019; Ravera et al., 2021; Li et al., 2019). For instance, Li et al. (2019)

conducted a series of tests on a saturated red clay-structure interface subjected to two thermal cycle numbers. They observed negligible variations of the interface shear strength after two thermal cycles. Based on the test results, they postulated that the viscous adhesion force at the clay–structure interface is governed by temperature variations. Yazdani et al. (2019) concluded that the net normal stress and soil consolidated state are the dominant factors controlling the shear behaviour of the clay-structure interface. A similar conclusion was drawn in the study of Ravera et al. (2021).

The above results suggested that thermal effects on the interface shear strength are probably associated with soil types since temperature could affect shear strength through different mechanisms. So far, no experimental investigation has been conducted on the shear behaviour of saturated silt-structure interface with considering temperature effects.

### 2.3.2 Shear behaviour of unsaturated interfaces

As discussed in Chapter 1, energy piles in unsaturated ground have been widely reported from many locations of the world. To understand the performance of energy piles in unsaturated ground, it is necessary to investigate the shear behaviour of unsaturated interfaces subjected to different temperatures. To the best knowledge of the author, temperature effects on the mechanical behaviour of an unsaturated interface were only investigated by Xiao et al. (2014) through a simple test program. The measured shear strength increases with elevated temperature. Their study considered a single value of initial water content. Soil suction was not controlled, and it changed during heating and shearing. For these reasons, the coupled effects of suction, temperature and stress were not revealed.

In addition, some experimental results at room temperature have suggested that suction can alter the shear behaviour of unsaturated interfaces (Borana et al., 2018; Hamid and Miller, 2009; Hossain and Yin, 2012; Hamid and Miller, 2008). For example, Hamid and Miller (2009) observed that suction increment can increase interface shear strength and dilatancy, by conducting a series of suction-control direct shear tests on a silt-steel interface. The median diameter of tested soil, which was sampled from Oklahoma, is 0.05 mm, while the maximum vertical distance between the highest peak and lowest trough on the steel counterface is 0.38 mm. In their tests, the axis-translation technique was used to control three different suctions (i.e., 20, 50 and 100 kPa). In the study of Hossain and Yin (2012), a wider range of suctions (0, 50, 100, 200 and 300 kPa) were applied on a silt-cement interface. A modified direct shear device was also developed to control soil suction by using the axis-translation technique. The tested soil is CDG from Hong Kong. Based on the experimental results, Hossain and Yin (2012) concluded that both the interface shear strength and dilative deformation increase with increasing suction. Similar observations were obtained in other researches (Borana et al., 2018; Khoury et al., 2011; Hamid and Miller, 2008). In the literature, it is generally concluded that suction increment can enhance strength and dilation because suction not only changes the average skeleton stress but also supplies additional bonding forces at inter-particle contact/soil-structure interfaces (Karube, 1994; Wheeler et al., 2003a). The changes in skeleton stress and interparticle contact are highly likely related to the change in temperature since the water surface tension is affected by temperature. Hence, it is necessary to investigate the mechanical behaviour of interfaces under different temperature and suction conditions.

## 2.4 Constitutive models for saturated and unsaturated interfaces

The shear behaviour of interfaces is one of the key aspects affecting the thermo-mechanical performance of energy piles. As stated in Section 2.3, the interface behaviour is influenced by soil suction and temperature. Therefore, it is necessary to propose a constitutive model to evaluate the coupled effects of suction and temperature on the shear behaviour of soil-pile interfaces.

### 2.4.1 Modeling temperature effect on the shear behaviour of interfaces

In the literature, there are many constitutive models for saturated soil-structure interfaces at room temperature (Georgiadis et al., 2005; Lashkari, 2013; Liu et al., 2006; Samtani et al., 1996; Desai and Ma, 1992; Clough and Duncan, 1971; Fakharian and Evgin, 2000; Gennaro and Frank, 2002; Ghionna and Mortara, 2002; Mortara et al., 2002; Shahrour and Rezaie, 1997). These existing models were developed based on different theoretical frameworks. For example, classical elastoplasticity was used by Lashkari (2013) to develop an interface model combined with critical state theory. The prediction of this interface model was well verified by experimental tests, considering different degrees of interface roughness and soil properties. Hu and Pu (2004) proposed another interface model with ten model parameters on the basis of damage mechanics. The computed results by using their model were well matched with the results of the direct shear tests on a steel-sand interface under the dry condition. Based on the generalized plasticity, Liu et al. (2006) developed a new interface model, coupling with the critical state soil mechanics. Some published experimental data were used to validate their model. It was confirmed that the model was able to capture the strain-

hardening, strain-softening and dilatancy. Furthermore, some other theoretical frameworks were also used to develop interface models in the literature, such as viscoplasticity (Samtani et al., 1996), hyperbolic formulation (Clough and Duncan, 1971) and disturbed-state concept (Desai and Ma, 1992). However, these mentioned models are designed for dry and saturated interfaces at room temperature.

As far as the author is aware, so far, there are only two interface models considering temperature effects on interface behaviour under dry and saturated conditions (Stutz et al., 2016; Maghsoodi et al., 2021). Based on the hypoplasticity, Stutz et al. (2016) developed a new interface model by preserving the previous tensorial notations (Mašín and Khalili, 2012; Mašín and Khalili, 2011) and using reduced stress and strain. Without comparing the computed results using their model and the measured results in the literature, they presented the possibility of their model for future application. Recently, Maghsoodi et al. (2021) developed a new one in the framework of classical elastoplasticity combined with critical state soil mechanics. To capture the variations of critical state void ratio at different temperatures, a modified equation was developed as follows:

$$e = e_{cs} [1 - \exp(-\xi W)] + (e_{cs} - \alpha \cdot \Delta T) \exp(-\xi W) - \frac{k_1}{1+K/k_2} W \exp(-\xi W) \quad (2-10)$$

where  $e$  is the current void ratio;  $e_{cs}$  is the critical state void ratio;  $\alpha$  is the material-dependent parameter;  $W$  is shear displacement;  $K$  is normal stiffness at the interface;  $\xi$ ,  $k_1$  and  $k_2$  are model fitting parameters. However, the above two interface models (Maghsoodi et al., 2021; Stutz et al., 2016) are only suitable for dry and saturated interfaces.

#### 2.4.2 Modeling suction effect on the shear behaviour of interfaces

For unsaturated soil-structure interfaces, a few constitutive models were developed (Hamid and Miller, 2008; Lashkari and Kadivar, 2016; Lashkari and Torkanlou, 2016; Zhou et al., 2020). On the basis of the disturbed-state concept, Hamid and Miller (2008) proposed an interface model by extending the work of Desai and Ma (1992) from the saturated condition to unsaturated conditions. To quantify the effect of the degree of saturation, most of the model parameters are described by soil suction in their new model. It implies that more experimental tests are needed to calibrate model parameters. Lashkari and Kadivar (2016) presented another unsaturated interface model by modifying the previous one (Lashkari, 2013). The effective stress and modified soil suction were used as the major stress variables in the interface model of Lashkari and Kadivar (2016). Also, the effects of suction on the critical state line were captured by using the bonding variable, based on the study of Gallipoli et al. (2003). Following that, Lashkari and Torkanlou (2016) presented another new one by generalizing the previous interface model from dry/saturated condition (Lashkari, 2013) to unsaturated condition. Based on the previous work (Gallipoli et al., 2003; Wan and Guo, 1998; Lashkari, 2009; Been and Jefferies, 1985), some additional modifications were made for the effective stress and critical state lines in unsaturated conditions. Both of the models (Lashkari and Torkanlou, 2016; Lashkari and Kadivar, 2016) have been vitrified by a number of experimental results. Zhou et al. (2020) developed a new interface model, based on the theoretical framework of bounding surface plasticity. The model was also verified by the experimental results of direct shear tests on different interfaces at unsaturated conditions. However, all the existing constitutive models

for unsaturated interfaces were developed at room temperature without considering the coupled effects of temperature and suction.

## **2.5 Thermo-mechanical behaviour of energy piles**

Energy piles are designed with dual functions: structural support and geothermal supply (Brandl, 2006; Mimouni and Laloui, 2014; Olgun et al., 2014; Sani et al., 2019; de Moel et al., 2010). During geothermal operations, energy piles and surrounding soils are always subjected to thermal loadings. The thermal and mechanical behaviour are coupled. As mentioned in the previous sections, the mechanical stress would influence the heat transfer between soils and piles (see Sections 2.1 and 2.2), while temperature variations during the heat transfer process affect the mechanical behaviour of soil-pile interfaces (see Sections 2.3 and 2.4). Therefore, it is crucial to understand the coupled thermo-mechanical behaviour of energy piles.

### **2.5.1 Full-scale tests on the behaviour of energy piles**

In the last two decades, a number of field tests were conducted on full-scale energy piles (Laloui, 2011; Bourne-Webb et al., 2009; Faizal et al., 2019b; Faizal et al., 2019a; Laloui et al., 2006; Moradshahi et al., 2021; Akrouch et al., 2014; Wang et al., 2015a; Rotta Loria and Laloui, 2018; You et al., 2016; Mimouni and Laloui, 2015).

Laloui et al. (2006) presented a detailed investigation of an instrumented energy pile, which was constructed at the Swiss Federal Institute of Technology in Lausanne. In their in-situ tests, the thermal loading was applied at the end of the construction for each building story, and the temperature gradient was controlled as 21°C for test 1 and 15°C for others. The thermo-mechanical loading history was presented in Figure 2.10. By using optical fibers and

extensometers, the pile head settlement was obtained, as shown in Figure 2.11. It can be seen that the irreversible settlement occurred after the temperature recovered to the initial value. This is probably related to the thermally induced variations of interaction between soil and pile.

Bourne-Webb et al. (2009) conducted another full-scale test in the Clapham Centre of Lambeth College in South London, where two instrumented energy piles with a 0.6 m diameter and 23 m length were tested under different thermo-mechanical loading paths. Although the permanent pile settlement after cyclic thermal loading was not obtained in their tests, they still observed the changes in the axial strain and stress during the heating and cooling phases.

A full-scale energy pile embedded in highly plastic clay was tested at the NGES at Texas A&M University (Akrouch et al., 2014). They heated the pile for 4 hours at five different vertical loads (i.e., 40, 100, 150, 200 and 256 kN) and control the temperature increment by 10-15°C. The measured data indicated that there was a significant pile head settlement when the thermal loading induced some variations of the axial strain and stress.

Several instrumented energy piles were constructed at Monash University, Melbourne, Australia and tested under different thermo-mechanical loading paths to investigate variations of axial and radial strains (Faizal et al., 2018; Faizal et al., 2019b; Faizal et al., 2019a). All the tested piles were 0.6 m in diameter and 16.1 m in length. The soil profile consists of 1.5 m-depth fill material, 1 m-depth sandy clay and 13.6 m-depth sand. Vibrating wire strain gauges and O-cells were used to measure strains and load. In their first study (Faizal et al., 2018), monotonic and cyclic thermal loadings were applied to energy piles without mechanical loads. The measured data presented that the axial strain is significantly dependent on the temperature

variations, while the thermal loading has a negligible influence on the radial strain. There was also no irreversible axial settlement after each thermal cycle. Following that, the authors applied the energy piles to cyclic thermal loading, coupling with the mechanical load that is equal to 52% of the pile ultimate capacity (Faizal et al., 2019b). Similar conclusions were also drawn from the results: the thermally-induced variations of radial strain were considerably smaller than that in the axial strain. Different from the above two thermo-mechanical loading paths, the same energy piles were subjected to only one thermal cycle with the same mechanical loads (i.e., 52% of the pile ultimate capacity) in their next study (Faizal et al., 2019a). The same observation was also obtained in this study, probably due to the same mechanical loads and soil state.

In the in-situ tests of Mimouni and Laloui (2015), four tested piles, which were 0.9 m in diameter and 28 m long, were constructed on the campus of the Swiss Federal Institute of Technology in Lausanne, Switzerland. Compared to the above studies (Faizal et al., 2018; Faizal et al., 2019b; Faizal et al., 2019a), one of the major differences is the soil profile, which mainly consists of a 0-15.7 m depth soft soil layer and 15.7-28 m depth stiff soil layer in the study of Mimouni and Laloui (2015). Therefore, the thermal and mechanical responses of energy piles in the radial direction are different. This comparison suggests that the soil properties, such as soil stiffness, could probably affect the soil-pile interaction. This speculation is also partially confirmed by the study of Moradshahi et al. (2021) through numerical simulations. Mimouni and Laloui (2015) also observed that the changes in the radial strain

during the heating phase could probably have a significant impact on the contact pressure applied to the soil-pile interface.

Based on data from the above field tests, it is generally concluded that thermal loading may result in non-negligible building settlement due to pile-ground interaction. Based on the measured results (Bourne-Webb et al., 2009; Laloui et al., 2006), some researchers carried out some simplified theoretical analyses. Amatya et al. (2012) proposed some mechanisms for energy piles under thermo-mechanical loading paths, as shown in Figure 2.12. It can be seen that the pile shaft resistance is greatly affected by the applied thermal loadings. When temperature increases, the pile expands and negative skin friction could easily occur at the pile's upper part. During the cooling phase, the potential negative skin friction shows up in the pile's lower part. Following that, Bourne-Webb et al. (2013) presented a modified mechanism, considering the variations of restraint from surrounding soils, as shown in Figure 2.13. The changing properties of surrounding soils, such as soil stiffness, would lead to a variation in soil-pile interactions. This conclusion implies that energy piles could show different responses in the unsaturated ground.

### 2.5.2 Physical model tests on the behaviour of energy piles

To improve the understanding of the thermo-mechanical behaviour of energy piles, some researchers carried out different physical model tests on small-scale energy piles (Ng et al., 2015; Yavari et al., 2016b; Liu et al., 2019; Nguyen et al., 2017; Yavari et al., 2014; Wang et al., 2011; Ng et al., 2016; Wang et al., 2016). Some of them observed that thermal cycles would result in irreversible settlement when the pile was under a given vertical load. For

example, Yavari et al. (2014) manufactured a small-scale energy pile by using an end-closed aluminium tube, which had a length of 800 mm, an inner diameter of 18 mm and an outer diameter of 20 mm. A small-scale physical model was developed, as shown in Figure 2.14, through which they conducted a series of physical model tests in dry Fontainebleau sand. The applied temperatures varied between 5 and 35 °C with an increment or decrement of 5 °C, and each temperature was maintained for 2 hours. Six different vertical loads were considered (i.e., 0, 100, 150, 200, 250 and 300 N). At each vertical load, two thermal cycles were applied. An irreversible settlement was observed after each thermal cycle. They attributed this observation to the variations of the mobilized skin friction induced by thermal loadings. By using the same instrumentations, Yavari et al. (2016b) conducted another small-scale model test on the model pile in saturated kaolin clay. A similar thermo-mechanical path was applied in the tests. The thermal cycles still resulted in an irreversible pile settlement that was more significant under a larger vertical load. It was speculated that the changes in mobilized shaft resistance resulted in an irreversible settlement. Furthermore, a similar observation was obtained in the physical model test (Wang et al., 2016), shown in Figure 2.15.

To study the thermal effect on the bearing capacity of energy piles, Ng et al. (2015) conducted some centrifuge modelling tests in saturated Toyoura sand. The model pile used in their tests was also made of aluminium, which had a 13 mm inner diameter and a 19 mm outer diameter. The gravity was set equal to 40 g. A heating rod was used to control the temperature, hence there was only a heating phase but no cooling phase. The results indicated that the heating temperature led to an increase in the ultimate bearing capacity of energy piles, as shown

in Figure 2.16. Because the temperature elevation could increase shaft resistance at a reducing rate but enlarge toe resistance more rapidly.

Furthermore, a comprehensive small-scale physical model test program was conducted by Liu et al. (2019) to investigate the post-temperature effects on the bearing capacity of energy piles in dry and saturated sand. The material of the tested model pile was concrete. All the model piles were 1600 mm in length and 104 mm in diameter. Nanjing sand was chosen as the tested soil. The results indicated that the under both dry and saturated conditions, the bearing capacity reduced with increasing thermal cycles, which is attributed to the degradation of soil–pile interaction after each thermal cycle. In summary, the temperature variations influence the pile bearing capacity under dry and saturated conditions, based on the measured results in the above literature.

Different from the above physical model tests, Goode and McCartney (2015) studied the thermal and mechanical responses of energy piles under unsaturated conditions by conducting a series of centrifuge model tests on small-scale energy piles. The model pile, which was 533 mm in length and 50.8 mm in diameter, was made of concrete. Bonny silt with an initial water content of 14% was used in their tests. All the tests were performed in a gravimetric field with an acceleration of 24 g. Only the heating was applied in the tests. Goode and McCartney (2015) observed that heating a semi-floating energy pile resulted in an increment in bearing capacity. The increment may result from the drying of surrounding soils and the increase of shaft resistance. But all the existing studies were conducted through a single value

of initial water content. The suction effects were not revealed, and more studies need to be carried out.

### 2.5.3 Effects of roughness on the pile's behaviour at room temperature

Some experimental results at room temperature have suggested that pile surface roughness can alter the soil-pile interaction (Tehrani et al., 2016; Kim et al., 2020; Tovar-Valencia et al., 2018; Chen et al., 2015; DeJong et al., 2001). It is generally observed that roughness increment enhances soil-pile interface strength and dilation because larger roughness increases the thickness of the shear band surrounding the pile. For example, Tovar-Valencia et al. (2018) combined a chamber with digital image correlation (DIC). By using this developed chamber, they conducted a series of tensile load tests on model piles in dry sand. Six different surface roughnesses were considered in their tests. The results indicated that the shaft resistance of model piles increased with increasing roughness. Based on the definition of normalized roughness (Uesugi and Kishida, 1986), the pile surface roughness depends on the both pile surface and median diameter  $D_{50}$  of soil. Therefore, more studies are needed to explore roughness effects on the thermo-mechanical behaviour of energy piles.

## 2.6 Summary

Although previous studies improved the understanding and modelling of thermal conductivity at various void ratios, degrees of saturation and stress states, some scientific challenges need to be addressed. Firstly, the mechanism of stress effects has not been well understood, particularly at a quantitative level. Secondly, the hysteresis of the stress-thermal conductivity relation during the loading–unloading process has not been modelled. Thirdly, the

coupled effects of void ratio and stress before and after yielding are not clear. Finally, as far as the author knows, there is only one equation proposed to capture the effects of void ratio, degree of saturation and stress. The capability of this equation has not been well verified using experimental results, so more theoretical studies are needed.

The heat exchange rate between ground and energy pile is influenced by many factors, such as pipe configuration, pipe flow condition, pile thermal resistance and soil thermal conductivity. It is generally concluded that the heat transfer rate increases when the pipe fluid velocity is larger and U-shape pipes are replaced by spatial pipes. So far, only a few studies investigated the thermal efficiency of energy piles considering the effects of soil thermal conductivity on purpose. The coupled effects of stress, void ratio and degree of saturation on the thermal efficiency of energy piles are yet investigated.

The shear behaviour of saturated and unsaturated soil-structure interfaces at isothermal conditions has been reported in many previous studies. Recently, the behaviour of saturated interfaces under non-isothermal conditions was studied by several researchers. However, as far as the author is aware, no study was conducted to investigate coupled effects of temperature, suction and net normal stress on the interface behaviour.

Many constitutive models have been developed to model the behaviour of interfaces at isothermal conditions. So far, only two interface models have been reported to incorporate temperature effects under saturated conditions. There is no constitutive model for unsaturated interfaces under non-isothermal conditions.

Although the thermo-mechanical behaviour of energy piles in different conditions has been studied by a number of full-scale field tests and small-scale physical model tests. All the existing studies were conducted through a single value of initial water content. The effects of suction and roughness have not been well understood.

Table 2.1 Some of equations for calculating soil thermal conductivity

Models	Formulations
Series model	$\frac{1}{\lambda} = \frac{1-n}{\lambda_s} + \frac{n}{\lambda_f}$
Parallel model	$\lambda = \lambda_s \cdot (1-n) + \lambda_f \cdot n$
Woodside and Messmer (1961)	$\lambda = \lambda_s \cdot b + \lambda_f \cdot c + \frac{\lambda_s \lambda_f \cdot a}{\lambda_f \cdot d + \lambda_s \cdot (1-d)}$ , where: $\begin{cases} a + b + c = 1 \\ b + ad = 1 - n \end{cases}$
Geometric man model (Sass et al., 1971)	$\lambda = \lambda_s^{1-n} \cdot \lambda_f^n$
Johansen (1977)	$\lambda = \left( \lambda_w^n \lambda_s^{1-n} - \frac{0.137\rho_d + 64.7}{2650 - 0.947\rho_d} \right) (0.7 \log S_r + 1) + \frac{0.137\rho_d + 64.7}{2650 - 0.947\rho_d}$
Gori and Corasaniti (2002)	$\frac{1}{\lambda} = \frac{\beta-1}{\lambda_f \cdot \beta} + \frac{\beta}{\lambda_f \cdot (\beta^2-1) + \lambda_s}$ , where: $\beta = \left[ \frac{1}{1-n} \right]^{1/3}$
Côté and Konrad (2005)	$\lambda = (\lambda_w^n \lambda_s^{1-n} - \chi^{10^{-\eta n}}) \left[ \frac{aS_r}{1 + (a-1)S_r} \right] + \chi^{10^{-\eta n}}$
Lu et al. (2007)	$\lambda = [\lambda_s^{1-n} \cdot \lambda_f^n - (b - an)] \exp[\alpha(1 - S_r^{\alpha-1.33})] + (b - an)$
Chen (2008)	$\ln \lambda = ng(S_r) + \ln \lambda_0$ $g(S_r) = c \ln[(1-b)S_r + b] + \ln d$
Roshankhah and Santamarina (2014)	$\lambda = \lambda_1 \left[ 1 + \beta \log \left( \frac{\sigma'}{1 \text{ kPa}} \right) \right]$

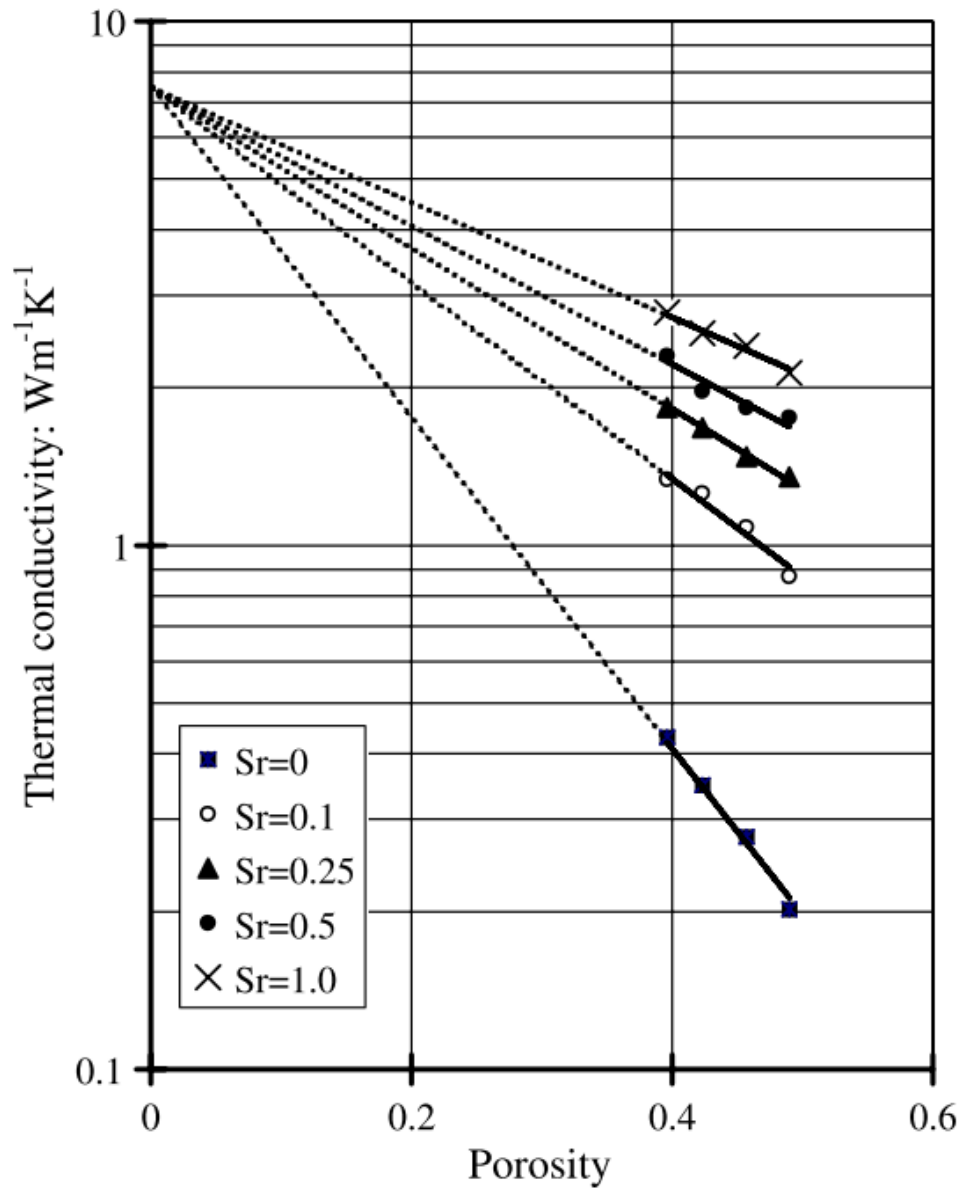


Figure 2.1. The relationship between thermal conductivity and porosity (Chen 2008).

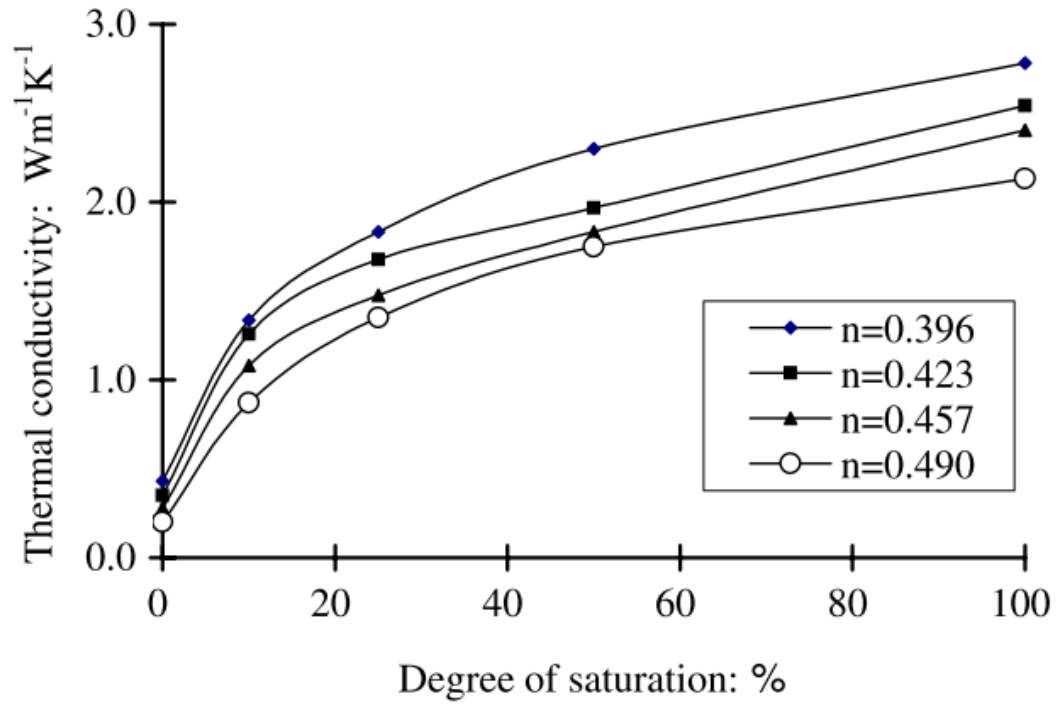


Figure 2.2. The relationship between thermal conductivity and degree of saturation (Chen 2008).

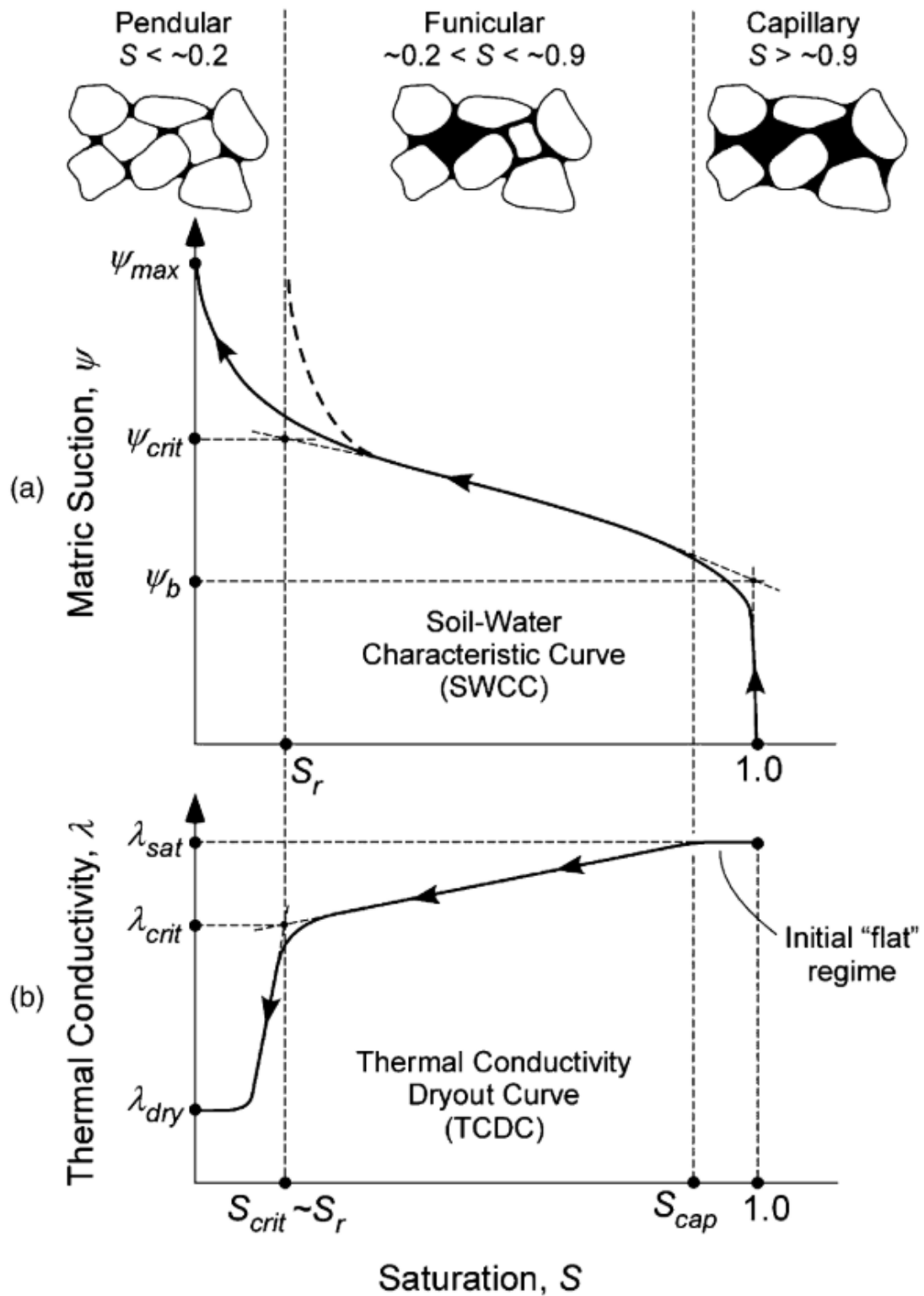


Figure 2.3. Conceptual sketches (Likos 2014): (a) soil-water characteristic curve (SWCC); (b) thermal conductivity dryout curve (TCDC) for coarse-grained soil.

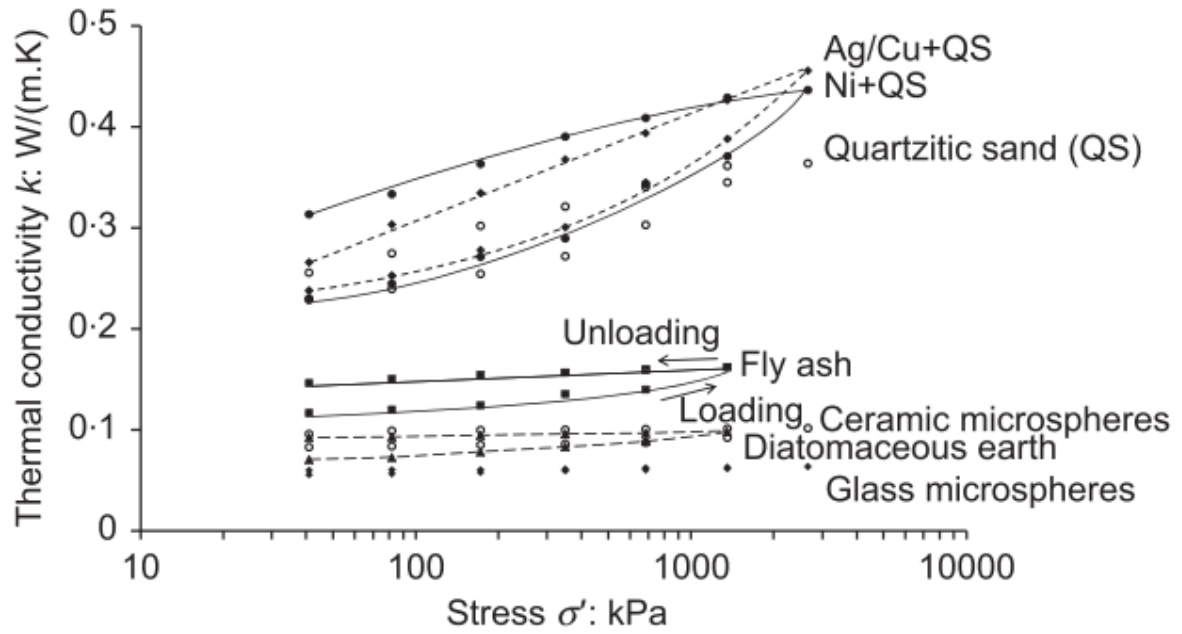


Figure 2.4. The relationship between thermal conductivity and effective vertical stress (Roshankhah and Santamarina 2014).

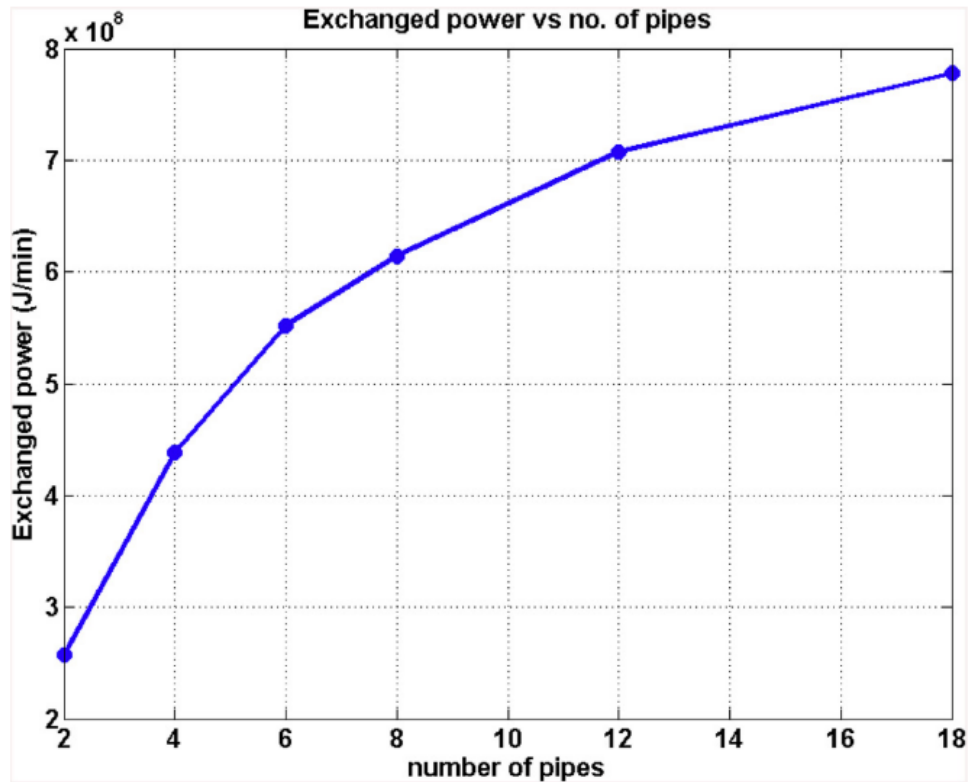


Figure 2.5. Effects of pipe numbers on the thermal efficiency of energy piles (Cecinato and Loveridge, 2015).

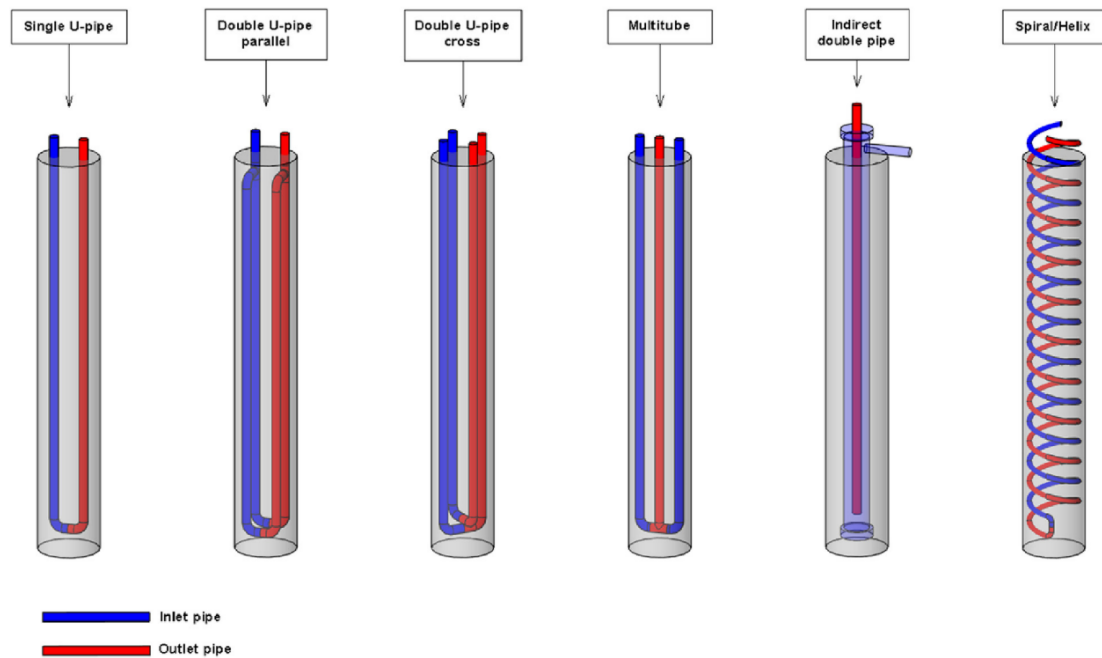


Figure 2.6. Energy pile configurations (Fadejev et al., 2017).

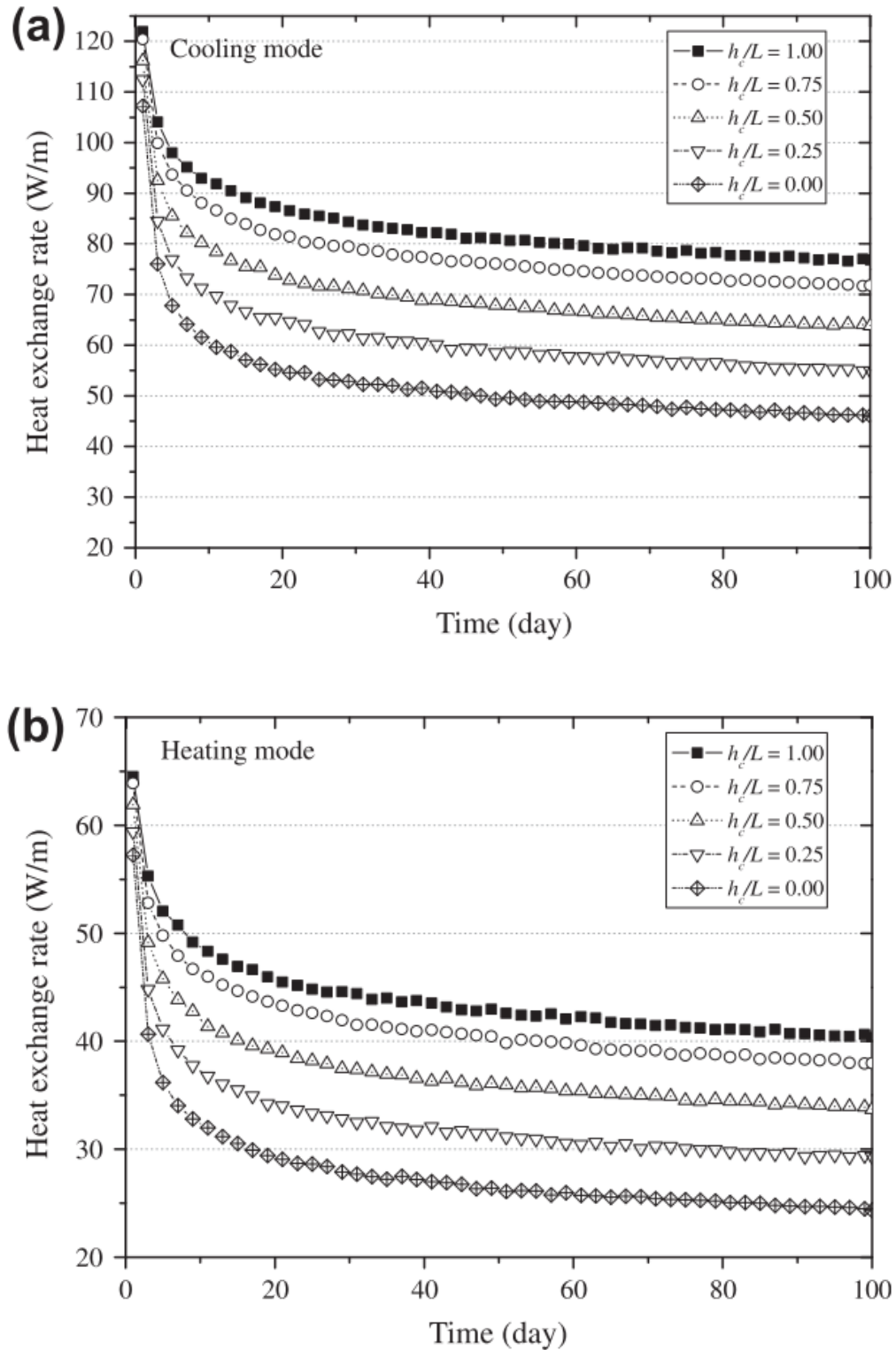


Figure 2.7. Effects of water table depth on the thermal efficiency of energy piles (Choi et al., 2011):  $h_c$  is the depth of water table;  $L$  is the pile length.

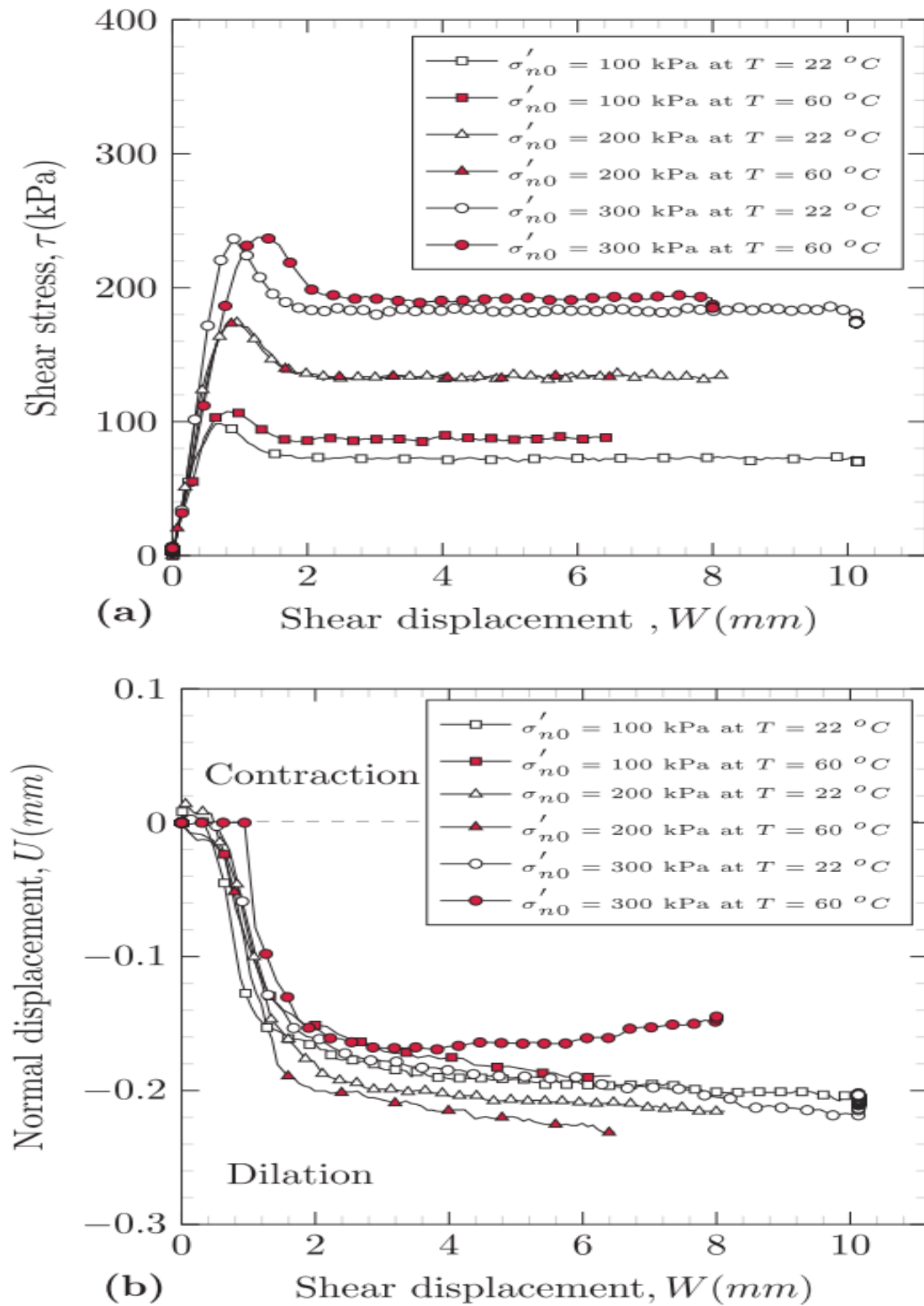


Figure 2.8. Results for saturated sand-structure interface under constant normal load conditions (Maghsoodi et al., 2020).

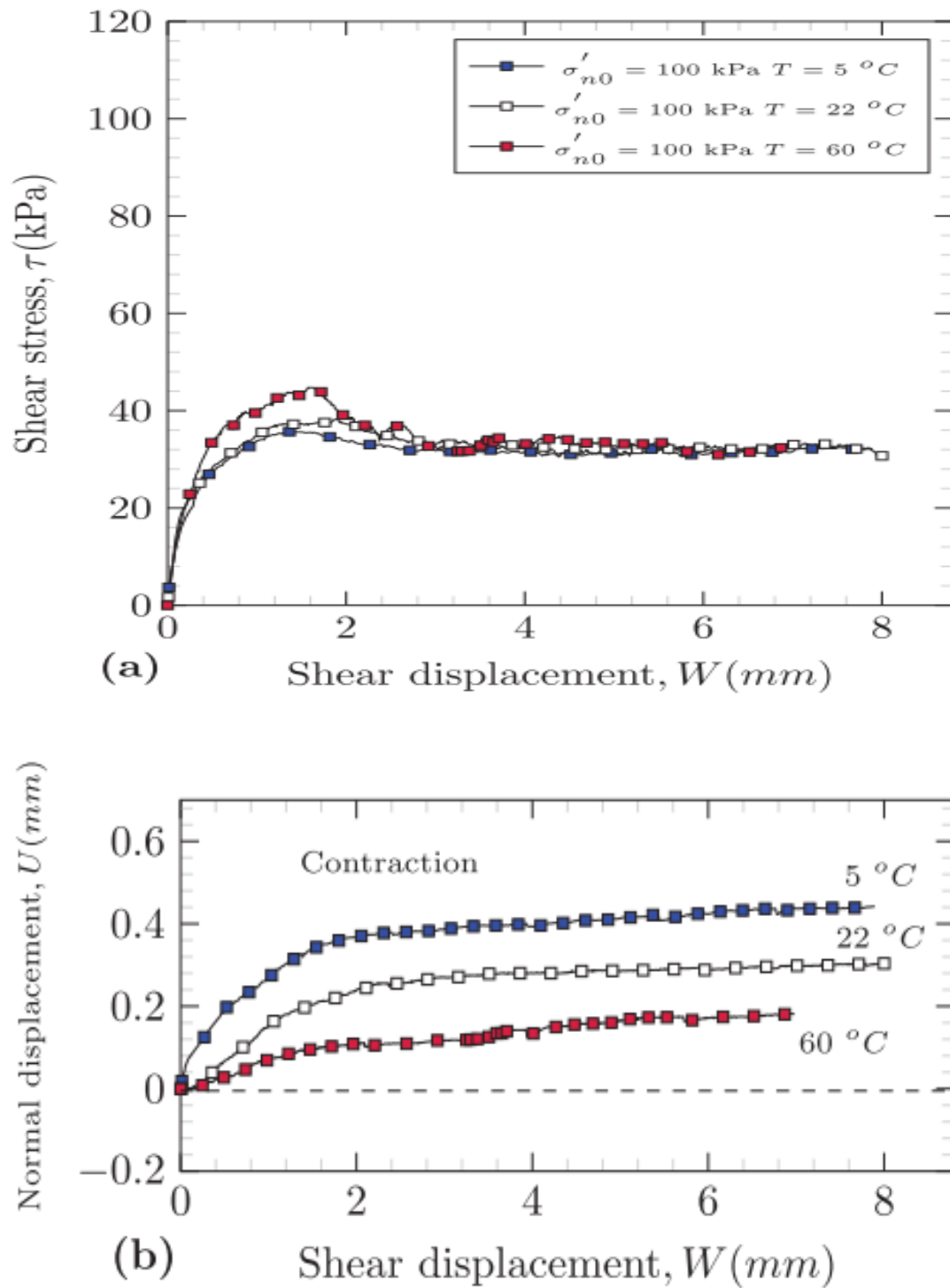


Figure 2.9. Results for saturated clay-structure interface under constant normal load conditions (Maghsoodi et al., 2020).

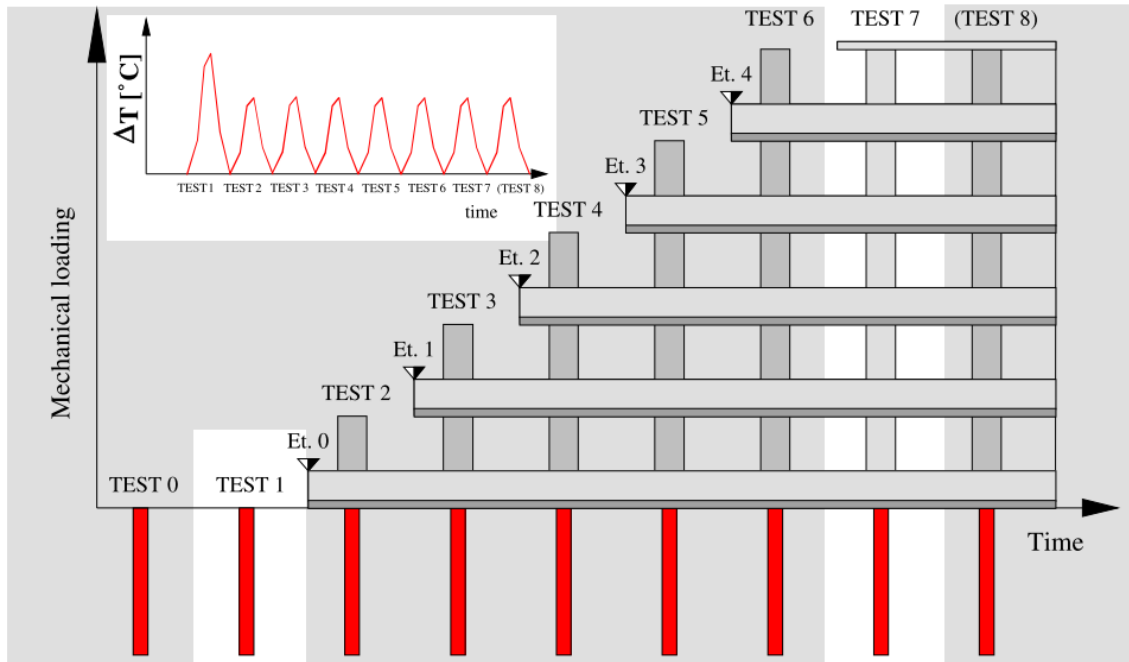


Figure 2.10. Thermo-mechanical loading paths in the field tests of Laloui et al. (2006).

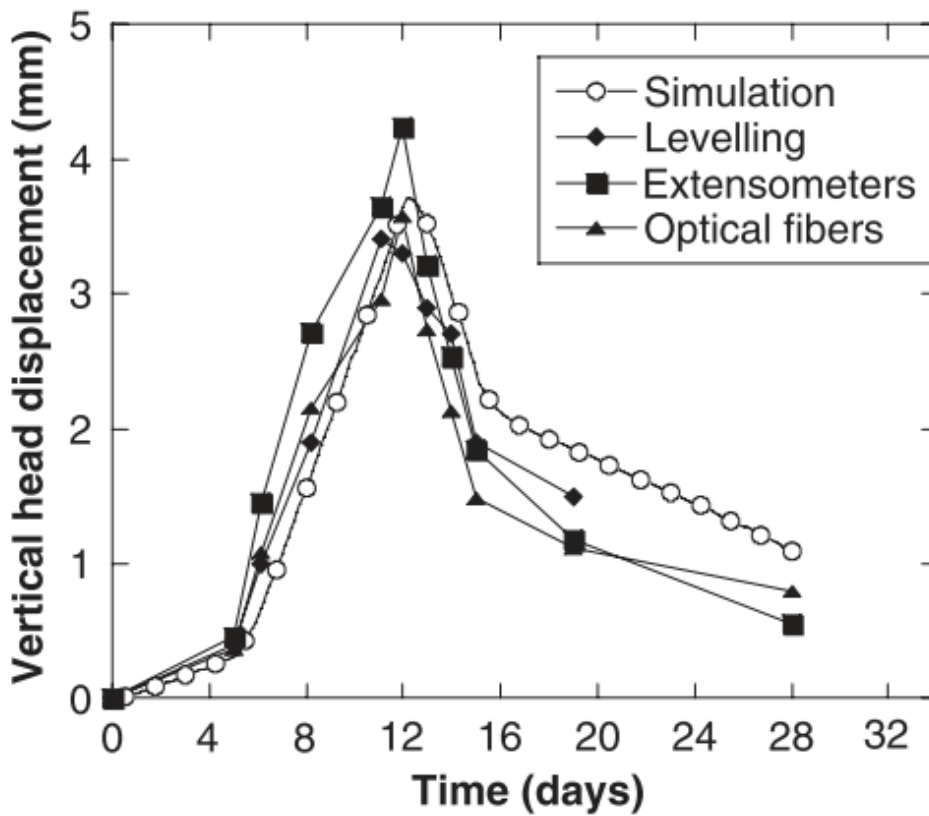
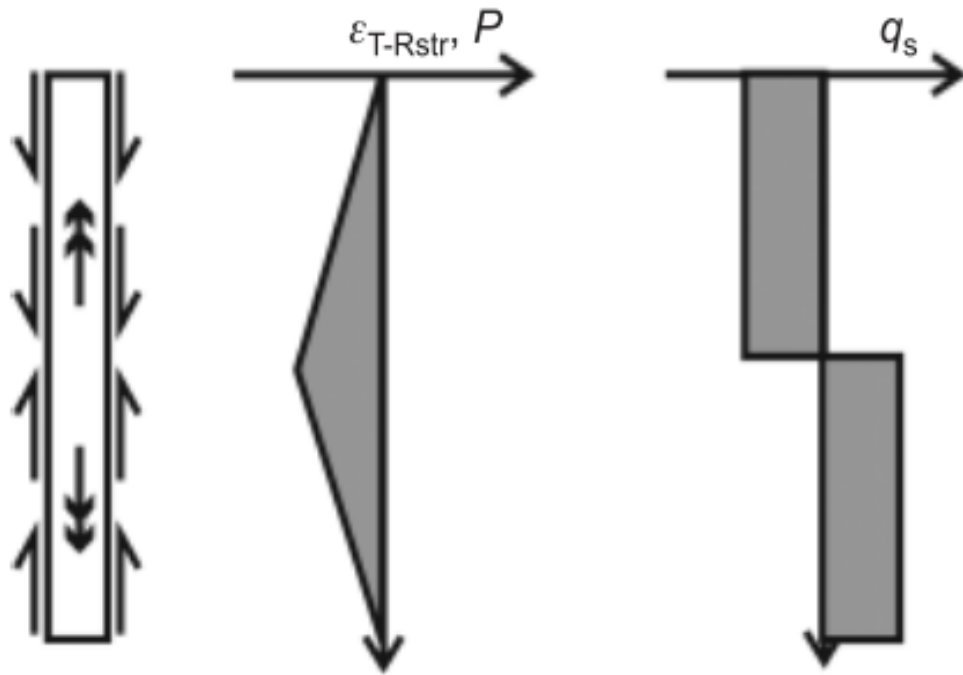
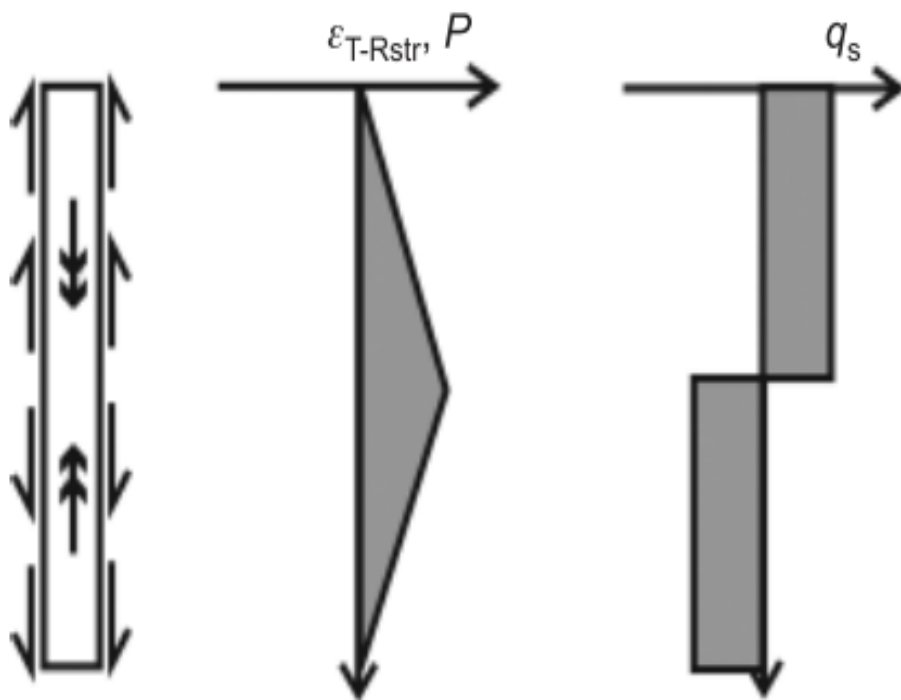


Figure 2.11. Irreversible displacement after one heating and cooling cycle (Laloui et al., 2006).

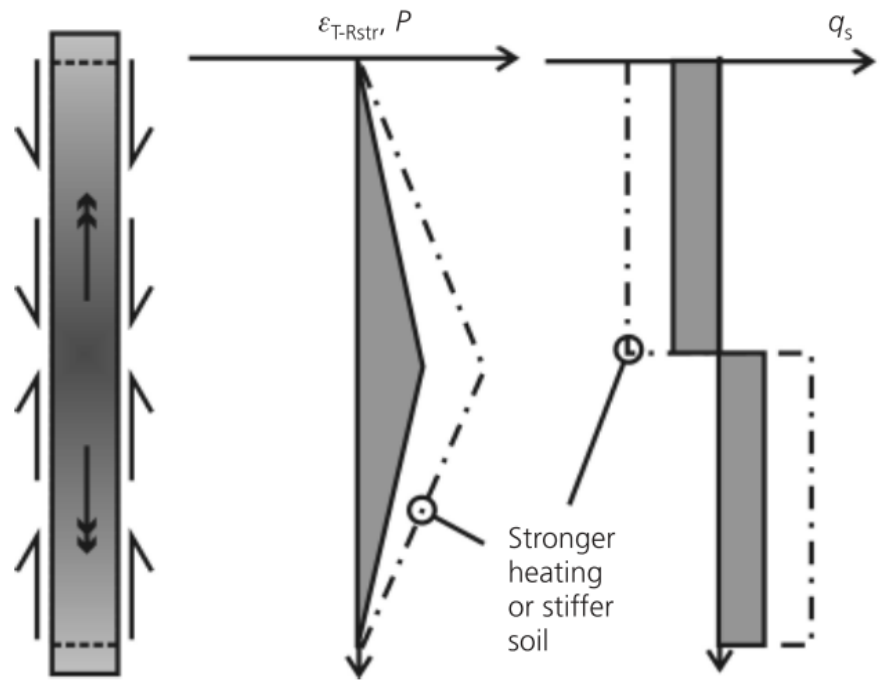


(a) heating

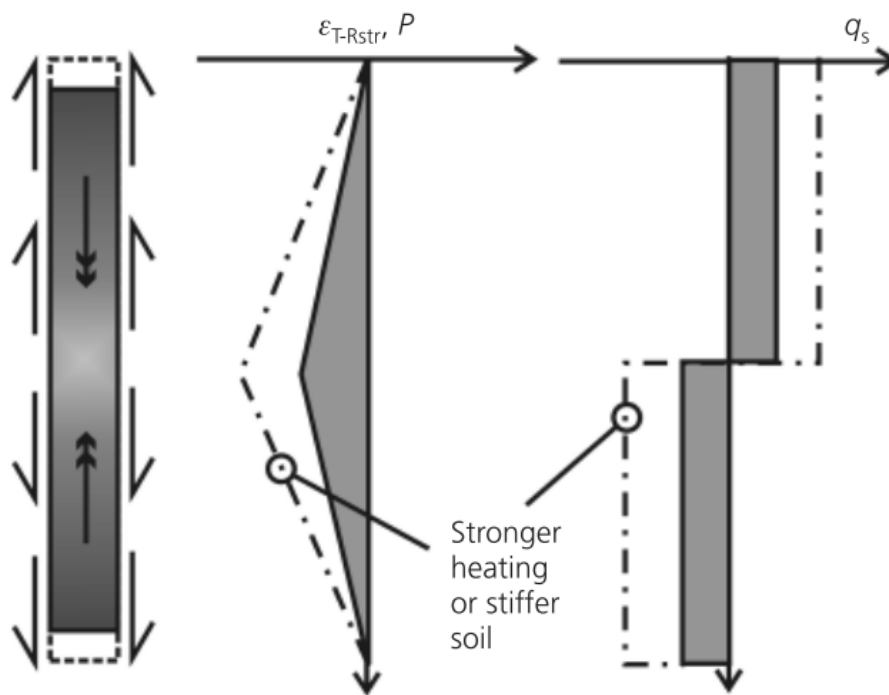


(b) cooling

Figure 2.12. Responses of energy piles under different thermal loading (Amatya et al., 2012).



(a) heating



(b) cooling

Figure 2.13. Effects of soil restraint on the energy responses (Bourne-Webb et al., 2013).

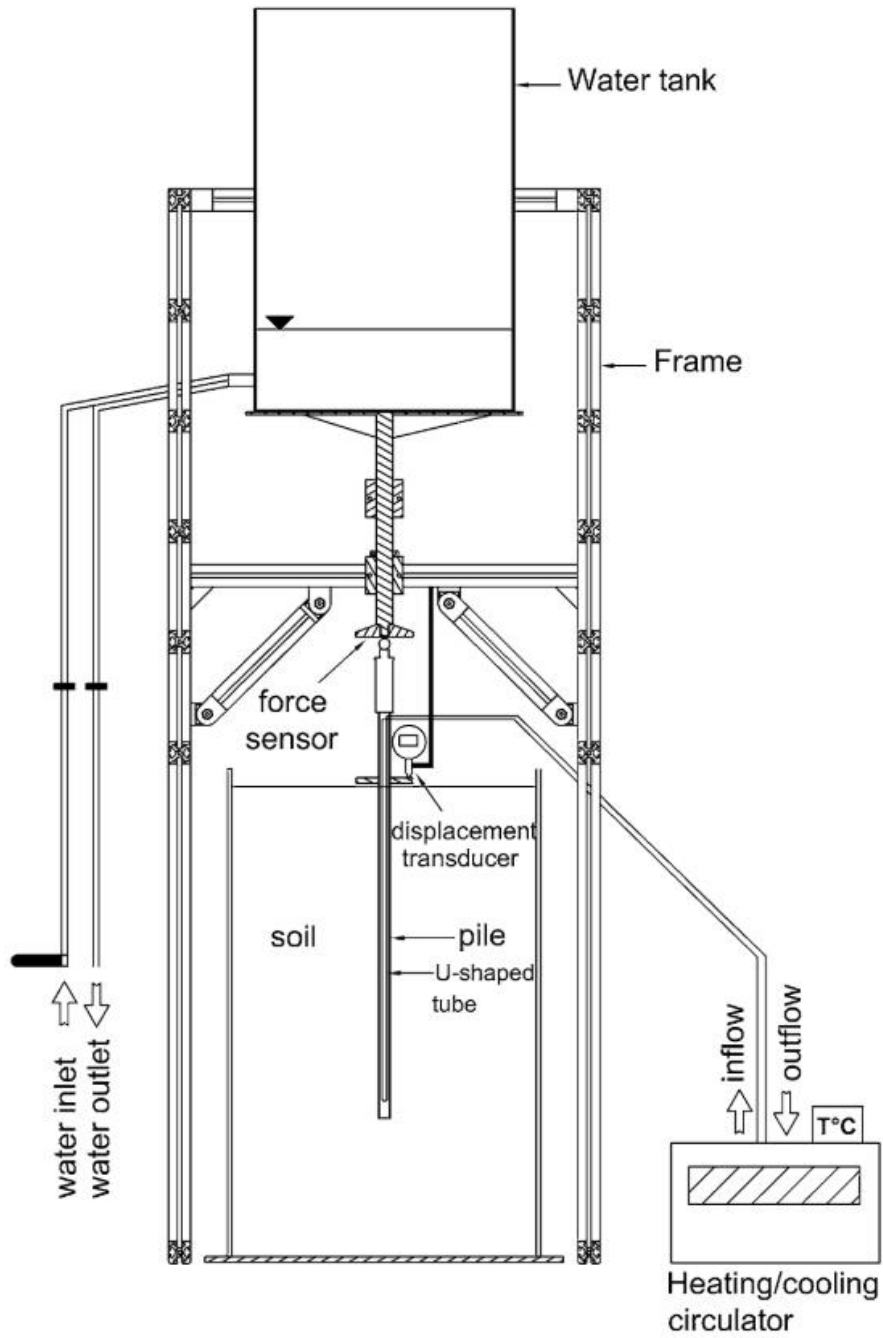


Figure 2.14. Layout of physical model in the study of Yavari et al. (2014).

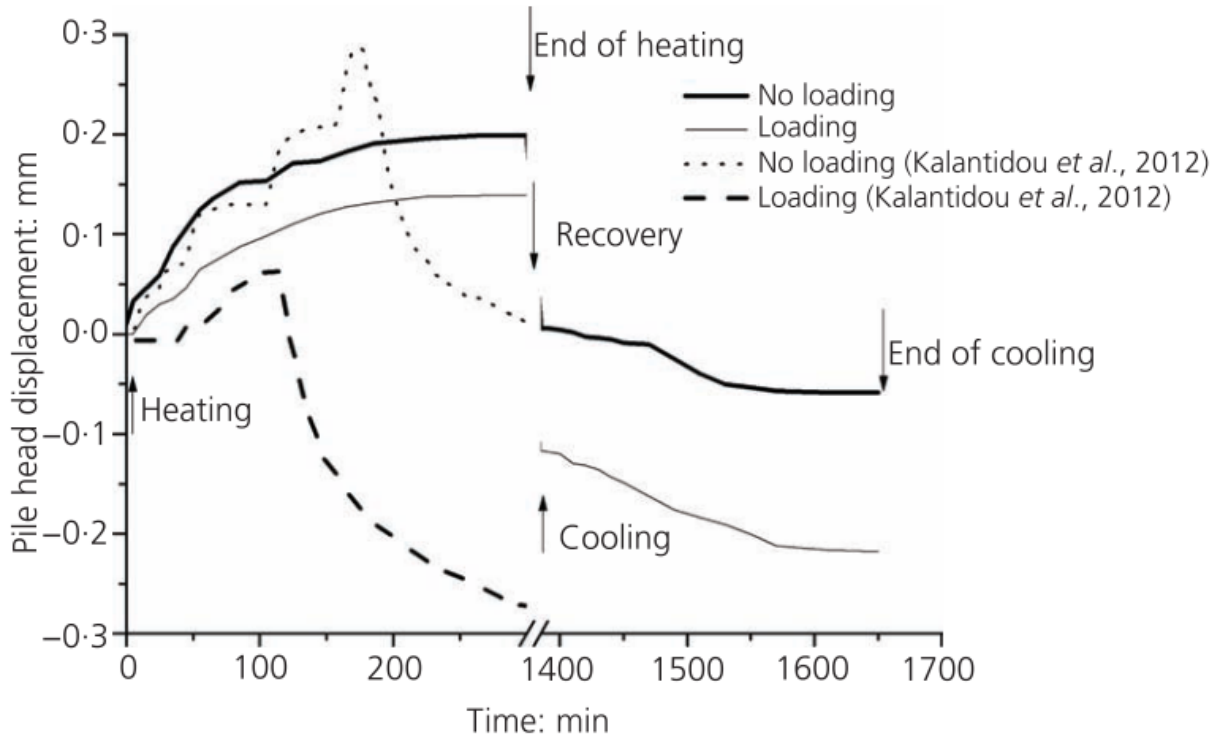


Figure 2.15. Pile head displacement during heating and cooling (Wang et al., 2016).

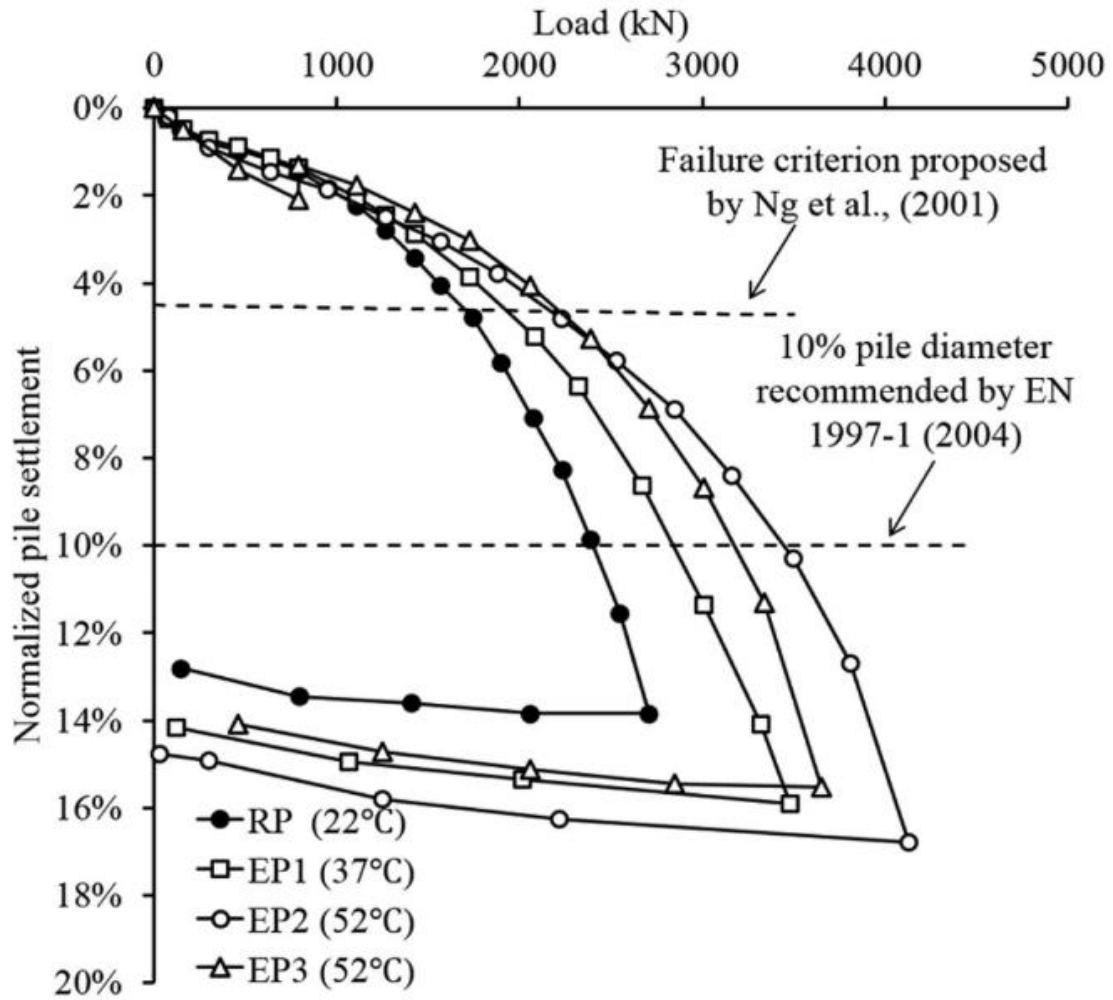


Figure 2.16. The pile load-settlement curves in the centrifuge modelling tests of Ng et al. (2015).

## **CHAPTER 3: Experimental Investigation of The State-Dependent Thermal Conductivity**

The principal objective of this chapter is to investigate the state-dependent thermal conductivity of different soils, with a consideration of the effects of stress, saturation and void ratio. To meet this objective, an apparatus based on the thermal needle probe technique was modified to control the stress and measure the deformation of a specimen. By using this new apparatus, comprehensive tests were conducted at various conditions of stress, initial degree of saturation, and void ratio. The experimental results are useful for improving the understanding of thermal conductivity, particularly in two aspects: (1) the mechanism of stress effects on the thermal conductivity (i.e., the relative contribution of decreasing the void ratio and increasing the inter-particle contacts); (2) the stress effects on thermal conductivity at different degrees of saturation.

### **3.1 Test apparatus and its working principle**

In this study, the non-steady-state probe (NSSP) method (i.e., transient state method) was used for thermal conductivity measurement. This method is widely used for soil testing, and it is also referred to as the transient line source, thermal needle, hot needle, heat pulse and hot wire techniques in the literature. Compared with steady state methods, the transient state method is less time-consuming. More importantly, some previous researchers found the transient state method more reliable, because it only imposes a very small temperature gradient in the specimen for a short period and hence minimizes soil moisture migration (Chen, 2008).

Along with the NSSP method, a new apparatus was developed and used. Its schematic diagram and photo are shown in Figure 3.1. The apparatus consists of a cylindrical container with 90 mm in length and 100 mm in diameter, a thermal needle probe (i.e., TP08 probe having a needle length of 70 mm and a diameter of 1.2 mm), a datalogger, a power-supply system for applying constant current, a computer, a loading system and a dial gauge. Different from the conventional apparatus in the ASTM D5334 (ASTM, 2014), the new one is able to control the vertical stress of soil specimen using dead load and measure the volume change using a dial gauge. The loading frame was modified based on a traditional oedometer device.

A TP08 probe manufactured by Hukseflus Thermal Sensors was used for the thermal conductivity measurement. The probe consists of a needle with a thermocouple located about 15 mm from the tip (the other junction located in the base) and a heating wire. During each test, heat is generated by imposing a DC through the heating wire. The temperature of the needle is monitored using the thermocouple. Figure 3.2 shows a typical result of the temperature-time relation, from which the thermal conductivity  $\lambda$  is computed using the following equation (ASTM, 2014):

$$\lambda = \frac{Q}{4\pi} \cdot \frac{\ln(t_2/t_1)}{(T_2 - T_1)} \quad (3-1)$$

where  $Q$  is the input heat per unit length of the heater ( $\text{W}\cdot\text{m}^{-1}$ );  $t_1$  and  $t_2$  are the time from the beginning of heating (s), and  $T_1$  and  $T_2$  are the corresponding temperatures (K). If the thermal conductivity of the specimen is larger, the rate of heat dissipation is higher. Consequently, the rate of the temperature increase detected by the thermocouple would be lower. It should be noted that the early portion of the temperature time series is affected by the needle-soil

coupling, while specimen boundaries perturb the long-time data. Following the suggestion of the ASTM standard, the thermal conductivity is obtained from the linear, central portion of the temperature versus log time plot, shown as the segment between  $t_1$  and  $t_2$  in Figure 3.2. Detailed descriptions of test procedures and calculation methods were reported in ASTM D5334 (ASTM, 2014).

Some trial tests were carried out to check the measurement repeatability and it was found that the variation of thermal conductivity was within  $\pm 0.03 \text{ W}\cdot\text{m}^{-1}\cdot\text{K}^{-1}$ . In addition, it was used to measure the thermal conductivity of Toyoura sand and the results agreed well with the data reported in the literature (Tarnawski et al., 2011).

In addition, a dial gauge from *Mitutoyo* (accuracy: 0.003 mm) was used to monitor the vertical deformation of soil specimen, which has a diameter of 100 mm and a height of 100 mm. The mould is made of aluminium with a thickness of up to 10 mm, so its lateral deformation should be negligible in the stress range considered in this study. Based on the above analysis, the change in void ratio can be determined accurately and the error should be less than 0.001.

## **3.2 Test materials and specimen preparation**

### **3.2.1 Test materials**

The new apparatus described in Section 3.1 was adopted to test three different soils, including the Toyoura sand, silt sampled from Hong Kong (i.e., completely decomposed granitic (CDG)) and the kaolin clay. Their particle size distributions and basic properties are

shown in Figure 3.3 and Table 3.1, respectively. Given their distinctly different properties, they are able to represent a wide range of soils.

Furthermore, the mixtures of tire shred and Toyoura sand were also tested at various rubber contents. The major objective is to investigate the state-dependent thermal conductivity of a wide range of materials, with various compressibilities, particle shapes, thermal conductivities of solid phase as well as degrees of wettability. The comprehensive data is useful for evaluating theoretical equations for thermal conductivity. The particle size distribution and basic properties of the rubber are included in Figure 3.3, Table 3.1 and Table 3.2, respectively. It can be seen that the mean size of the rubber particles is about 25 times larger than that of sand particles. The ratio was chosen based on the results of Xiao et al. (2019), who found that large-size rubbers are able to reduce the thermal conductivity efficiently and also it is more economic to manufacture larger rubber particles from waste tires. In addition, it should be noted that the determination of rubber density is very important because it is used in the calculation of void ratio. It is measured as  $1.26 \text{ g/cm}^3$  following ASTM C127 (ASTM, 2015), which falls in the range of  $1.13$  to  $1.36 \text{ g/cm}^3$  reported by Bosscher et al. (1997).

### 3.2.2 Specimen preparation

The unsaturated/dry specimens of sand and sand-rubber mixtures were prepared using the same method, which was proposed by Ladd (1978). Dry sand and rubber with a predefined mass ratio (i.e., rubber content of 0%, 10% and 20%) were firstly mixed. Distilled water was then mixed with the sand-rubber mixture (pure sand if the rubber content is 0%) slowly to reach the desired water content, which is a function of the predefined void ratio and initial degree of

saturation. The specimens in this study were able to retain a degree of saturation of up to 50%-60%, which is corresponding to suction of about 3 kPa, based on the water retention curve reported by Gallage et al. (2016). The moist sand-rubber mixture was then kept in a plastic bag for 24 hours to achieve uniform distribution of pore water (Zhang et al., 2015). During the specimen preparation, water loss may occur for different reasons, because some water evaporates or attach to the plastic bag. To determine the water content of soil accurately, some soil from the plastic bag was collected to measure its water content prior to the specimen compaction. In addition, the difference between this final water content and the initial water content is less than 0.3%. Then, the sand-rubber mixture was compacted in a cylindrical mould with 100 mm in diameter and 100 mm in height. Each specimen was prepared in five layers with the same mass. The under-compaction method proposed by Ladd (1978), in which the compaction dry density of the previous layer is 2% smaller than that of the subsequent layer, was used to eliminate the non-uniform density distribution along the specimen height. Sample compaction was obtained by repeatedly tapping the top wall of the shorter cylinder. To make sure the uniform distribution of water in unsaturated specimens, two sand-rubber specimens were used to check the water distribution, with different initial degrees of saturation (50% and 60%). Soils at different heights were sampled for moisture measurements. It was found that the initial degree of saturation is quite uniform along the height with a difference less than 4%.

To prepare unsaturated/dry silt specimens, the CDG was oven-dried at 105 °C and then broken up with a rubber pestle. After that, the soil particles were passed through a 2 mm sieve and the collected soil was mixed with distilled water to reach the target water content. Similar

to sand-rubber mixtures, the CDG specimen was also kept in a plastic bag for 24 hours to achieve uniform water distribution. After that, the moist silt was statically compacted in the same cylindrical by using a static compaction machine that can record the compaction pressure and control the compaction rate (i.e., 1 mm/min) during the process.

To prepare the fully saturated specimens of sand, sand-rubber mixtures and CDG, a dry specimen was firstly prepared using the above method. Then, two porous stones were put on the top and bottom of the cylindrical mould. After that, it was submerged in water and exposed to a vacuum of 10 kPa for 24 hours to remove air bubbles inside the specimen. This method was found able to saturate the specimen efficiently.

For the kaolin clay, reconstituted specimens were prepared. Firstly, dry kaolin clay was put in a cylindrical testing mould and then mixed with water, which was two times the liquid limit of kaolin clay by weight. To eliminate gas bubbles as much as possible, a stirrer was used to mix the clay and distilled water sufficiently. Then, a filter paper was placed on the top surface of the specimen before the loading cap was positioned. After setting up the loading device and dial gauge, the pressure was increased stepwise and maintained until equilibrium was reached. The maximum preloading pressure was 50 kPa and three loading pressures (12.5, 25 and 50 kPa) were adopted.

### **3.3 Test program and procedures**

In this chapter, three series of NSSP tests were carried out to investigate the effects of stress, degree of saturation, void ratio and creep on the thermal conductivity of different soils.

In total, 58 tests were carried out with three replicates at each condition. Details of the test program are given in Table 3.3 and Table 3.4.

### 3.3.1 Tests at zero stress

As shown in Table 3.3, tests in series D1 through D3 were carried out to study effects of void ratio on the thermal conductivity of three representative soils (Toyoura sand, CDG and kaolin clay) under the fully saturated condition.

Tests in the series D4 through D6 were carried out under the dry condition to study the effects of void ratio on the thermal conductivity of sand-rubber mixtures with various rubber contents. Rubber content of 0, 10% and 20%, which is defined as the ratio of rubber mass to total mass, were used. At each rubber content, the sand-rubber mixture was tested at various void ratios ranging from the maximum void ratio to the minimum one.

Tests in series M1 through M4 were conducted to study the effects of initial degree of saturation on the thermal conductivity of CDG, pure sand and sand-rubber mixtures. For each material, the full range of saturation (i.e., 0 to 100%) was considered.

### 3.3.2 Tests with consideration of stress effects

As shown in Table 3.3, tests in series S1 through S7 were conducted to investigate stress effects on the thermal conductivity of sand, silt and clay. Each specimen was subjected to a loading-unloading cycle stepwise in the stress range of 0 to 1200 kPa, which was chosen with reference to energy structures (10-50 meters long for energy piles and up to 200 meters long for borehole heat exchangers) (Fadejev et al., 2017). At each stress level, the loading duration is 24 hours to ensure the complete consolidation of specimens. The settlement was monitored

by the dial gauge and used to calculate the variation of void ratio. After that, the thermal conductivity under each stress level was measured. It should be noticed that the TP08 probe is made of stainless steel so that deformation of the probe under 1200 kPa normal stress can be negligible (Losertová et al., 2016).

Tests in series S8 through S13 were carried out to study the coupled effects of saturation and stress on the thermal conductivity of sand-rubber specimens. Each specimen was subjected to a loading and unloading cycle in the stress range of 0 to 600 kPa. Although sand-rubber mixture is unlikely encountered in the analysis of energy pile, sand-rubber mixtures could be used in the insulation layer beneath a large-scale underground thermal energy storage system (e.g., TTES and PTES), and that very high stress is generally used to compact soil during the construction.

For fully saturated specimens, during the loading and unloading process, they were submerged under water and expected to maintain fully saturated. For unsaturated specimens, the void ratio and hence the degree of saturation changed during the loading and unloading process. For the test conditions considered in this study, the change in degree of saturation is less than 3%.

### **3.4 Interpretations of experimental results**

#### **3.4.1 Effects of void ratio on the thermal conductivity**

Figure 3.4 presents the thermal conductivity of Toyoura sand, CDG silt and kaolin clay at saturated conditions, measured from the test series D1 to D3. An error bar is included for each condition based on the results of three replicates. The thermal conductivity consistently

reduces with an increase in void ratio, because the thermal conductivity of solid particles is generally higher than that of water. This has been widely reported by many researchers based on experimental results of various sands and other soils (Zhang et al., 2017; Chen, 2008; Côté and Konrad, 2005; Tarnawski et al., 2011).

In the literature, some previous researchers found that  $\ln \lambda$  and  $n$  follow a linear relationship, where  $\lambda$  and  $n$  are the thermal conductivity and porosity (equivalent to void ratio), respectively (Chen, 2008). Hence, their relationship can be described using the following equation:

$$\lambda_c = a * \exp \left( -b * \frac{e}{1+e} \right) \quad (3-2)$$

where  $\lambda_c$  is the calculated thermal conductivity using equation (3-2);  $a$  and  $b$  are soil parameters;  $e$  is the void ratio. Parameter  $a$  is the thermal conductivity with zero void ratio and therefore its value is governed by the thermal conductivity of the solid phase. Parameter  $b$  describes the sensitivity of thermal conductivity to void ratio. If the value of  $b$  is larger, the thermal conductivity reduces more significantly with increasing void ratio.

Equation (3-2) was applied to fit the results in Figure 3.4. The calculated results are included in the figure for comparison. It can be seen that the calculated and measured thermal conductivity are well matched. The equation can well capture the effects of void ratio. The values of parameters  $a$  and  $b$  were summarized in Table 3.5. The tested sand has a larger  $b$  value than the tested silt and clay, suggesting that the thermal conductivity of sand is more sensitive to a change in void ratio.

Figure 3.5 shows the influence of void ratio on the thermal conductivity of pure sand and sand-rubber mixtures under the dry condition (i.e.,  $S_r = 0$ ), obtained from series D4 through D6. Similarly, the thermal conductivity of each material decreases with increasing void ratio. At a given void ratio, the thermal conductivity of sand-rubber mixtures is smaller than that of pure sand. For instance, when the rubber content increases from 0 to 10% at a void ratio of 0.65, the thermal conductivity reduces by about  $0.025 \text{ W}\cdot\text{m}^{-1}\cdot\text{K}^{-1}$  which is corresponding to a percentage difference of about 10%. With a further increase of rubber content from 10% to 20%, the thermal conductivity also reduces by about 10%. The reduction is because rubber has a lower thermal conductivity ( $0.15 \text{ W}\cdot\text{m}^{-1}\cdot\text{K}^{-1}$ ) than sand ( $3 \text{ W}\cdot\text{m}^{-1}\cdot\text{K}^{-1}$ ) (Hannawi et al., 2010).

Equation (3-2) was applied to fit the results in Figure 3.5. The equation is able to fit the measured thermal conductivities at various void ratios. This suggests that equation (3-2) is also applicable for sand-rubber mixtures, even though it was originally proposed for pure soils. The values of parameters  $a$  and  $b$  are summarized in Table 3.5. The value of  $a$  decreases with increasing rubber content, mainly because rubber has a lower thermal conductivity than sand. More importantly, the same value of  $b$  can be used at different rubber contents, suggesting that the sensitivity to void ratio is almost identical for pure sand and sand-rubber mixtures. This is because this parameter is mainly affected by the particle shape, according to experimental results in the studies (Côté and Konrad, 2005; Xiao et al., 2019). Both the sand and rubber adopted in this study are sub-angular, resulting in the same  $b$  for specimens with different rubber contents. Furthermore, the tested sand has a larger  $b$  value than the tested silt and clay,

suggesting that the thermal conductivity of sand is more sensitive to a change in void ratio in terms of percentage difference.

### 3.4.2 Effects of moisture condition on the thermal conductivity

Figure 3.6 shows the variation of thermal conductivity with the degree of saturation for CDG, pure sand and sand-rubber mixtures. The results are obtained from tests in M1 to M4. It can be seen that the thermal conductivity increases with increasing degree of saturation for all specimens, consistent with the results of previous studies of pure soils (Hopmans and Dane, 1986; Zhang et al., 2015; Zhen et al., 2019; Haigh, 2012) and sand-rubber mixtures (Liu et al., 2020). This increase is mainly because the thermal conductivity of water and air is  $0.58 \text{ W}\cdot\text{m}^{-1}\cdot\text{K}^{-1}$  and  $0.024 \text{ W}\cdot\text{m}^{-1}\cdot\text{K}^{-1}$  at  $20^\circ\text{C}$ , respectively (Clauser and Huenges, 1995). Water is a much better heat conductor than air. Moreover, the relationship between thermal conductivity and degree of saturation is highly non-linear for both pure soils and sand-rubber mixtures. Taking the pure sand as an example, its thermal conductivity increases by about 6 times (i.e., from 0.23 to  $1.4 \text{ W}\cdot\text{m}^{-1}\cdot\text{K}^{-1}$ ) when the degree of saturation increases from 0 to 20%. The increase is only about 70% (i.e., from 1.4 to  $2.4 \text{ W}\cdot\text{m}^{-1}\cdot\text{K}^{-1}$ ), however, when the degree of saturation further increases from 20% to 100%. Similar observations were reported by some other researchers based on experimental studies of pure sands (Hopmans and Dane, 1986; Ochsner et al., 2001). The significant influence in the range of low degree of saturation (i.e.,  $S_r < 0.2$ ) is likely related to pore water distribution in specimens. Through X-ray computed tomography tests, Willson et al. (2012) found that pore water primarily distributes in a pendular form (i.e., bridging between the grains in the immediate vicinity or disconnected) when the degree of saturation is

below 20%. Grain-water-grain contacts can be formed efficiently by adding a small amount of pore water (Likos, 2014; Lu and Dong, 2015; Smits et al., 2010). As a consequence, the thermal conductivity increases greatly with an increase in the degree of saturation.

Compared to the mixture at 10% rubber content, the thermal conductivity at 20% rubber content is consistently smaller in the full range of degree of saturation, consistent with the findings in Figure 3.4. When the rubber content increases from 10% to 20%, the thermal conductivity decreases by about 19% in the dry state and by 28% in the fully saturated state. This phenomenon suggests that the effect of rubber content is more significant under full saturation.

To better understand effects of the degree of saturation for various soils,  $\lambda$  is normalized by the thermal conductivity under the dry condition  $\lambda_{dry}$ . Figure 3.7 shows the relationship between  $\lambda/\lambda_{dry}$  and degree of saturation. For CDG, the thermal conductivity increases by around 5 times when the degree of saturation increases from 0 to 100% (i.e.,  $\lambda_{sat}/\lambda_{dry}$  is equal to 5, where  $\lambda_{sat}$  is the thermal conductivity at the saturated condition). The increment for pure sand is 11 times. With the same change in the degree of saturation, the thermal conductivity increases by about 9 times and 8 times at 10% and 20% rubber contents, respectively. This comparison suggests that the thermal conductivity is less sensitive to the degree of saturation when the rubber content is larger, likely related to the microstructure of specimens. The series and parallel models are widely used in the study of thermal conductivity (Tarnawski and Leong, 2012). According to the series model, the ratio  $\lambda_{sat}/\lambda_{dry}$  is smaller when the thermal conductivity of solid particle  $\lambda_{solid}$  is lower. On the contrary, the parallel model would predict

a larger value for  $\lambda_{sat}/\lambda_{dry}$  at a smaller  $\lambda_{solid}$ . In the current study, the addition of rubber reduces the value of  $\lambda_{solid}$ . The results of  $\lambda_{sat}/\lambda_{dry}$  in Figure 3.7 are qualitatively consistent with the prediction of the series model. This finding implies that the series model is more relevant to sand-rubber mixtures, at least for the test conditions considered in the current study.

### 3.4.3 Effects of stress on the thermal conductivity of sand, silt and clay

From the tests in series S1 to S5, the void ratio and thermal conductivity of different saturated soils along a loading-unloading cycle were measured and shown in Figure 3.8. Based on the relationship between void ratio and vertical effective stress in Figure 3.8(a), the yielding stress of each specimen was determined using Casagrande's method. The yielding stresses are 100 kPa for the clay, 120 kPa for the silt with an initial void ratio of 0.63, 200 kPa for the silt with an initial void ratio of 0.48, 250 kPa for the sand with an initial void ratio of 0.76 and 300 kPa for the sand with an initial void ratio of 0.60.

According to Figure 3.8(b), the thermal conductivities of all specimens continuously increase during the loading process, agreeing well with some previous studies (Roshankhah et al., 2021; Yao et al., 2021; Cui and Zhou, 2022). The increases may be induced by various mechanisms, including two major mechanisms: (1) the reduction of void ratio; and (2) the increase in inter-particle contacts (Yun and Santamarina, 2008; Yao et al., 2019). The significance of each mechanism, however, has not been studied by previous researchers. It is analyzed later based on the new data.

Upon a loading from 0 to 1200 kPa, the thermal conductivity shows an increment of 60% for the clay, 25% for the loose silt, 20% for the dense silt, 10% for the sand with an initial

void ratio of 0.76 and 7.5% for the sand with an initial void ratio of 0.60. This observation suggests that when the specimen is more compressible, its thermal conductivity is more sensitive to the change in stress. Figure 3.8(b) also suggests that at the same stress state, soil specimen along the unloading path has a larger thermal conductivity than that along the loading path. This is probably because, for the compacted silt and sand, loading would increase the contact area and contact number between soil particles (Roshankhah et al., 2021; Cui and Zhou, 2022). For the reconstituted clay, the inter-particle contact is very different to that in granular soils and various repulsion/attraction forces from double-layers give rise to edge-to-face or face-to-face contacts. Loading-induced irreversible deformation may lead to the collapse of edge-to-face contact and result in more face-to-face contact (Pedrotti and Tarantino, 2018).

Figure 3.9 shows the relationship between thermal conductivity and void ratio during the loading-unloading path. The results from test series D1-D3 under zero stress are also included for comparison. At a given void ratio, the thermal conductivity along the loading-unloading path is larger than that measured without applying loading-unloading. Taking the silt with a void ratio of 0.63 as one example, the thermal conductivities are 2.19 and 2.01  $\text{W}\cdot\text{m}^{-1}\cdot\text{K}^{-1}$  under 300 and 0 kPa, respectively. The percentage difference is around 10% and it is mainly attributed to the loading-induced change of inter-particle contact, as discussed above.

To evaluate the contribution of void ratio changes to the thermal conductivity, equation (3-2) is used to calculate the thermal conductivity of saturated Toyoura sand, CDG and kaolin clay during a loading-unloading cycle. Figure 3.10 compares the measured and calculated thermal conductivity normalized by that at zero stress. The results of different soils consistently

suggest that equation (3-2) underestimates the influence of stress on thermal conductivity. This is because the loading-unloading can affect the thermal conductivity through two different mechanisms: (1) the reduction of void ratio; and (2) the increase in inter-particle contacts. Only the first mechanism can be considered by this equation. The percentage difference between measured and calculated results is the largest for the sand, implying that the second mechanism is the most important for this soil. For the kaolin clay, however, the first mechanism is more significant than the second one. Furthermore, there is an obvious hysteresis in the  $\lambda - \ln \sigma$  relation during the loading-unloading cycle. The calculated and measured hysteresis loops are comparable, implying that the hysteresis is mainly related to irreversible soil deformation (i.e., the first mechanism).

Figures 3.11 shows the variations of void ratio and thermal conductivity during a loading-unloading cycle for unsaturated CDG with a degree of saturation of 25% and 50%, respectively. The results are from tests S6 and S7. The measured results in these two figures are consistent with the results obtained in the fully saturated condition. Furthermore, the stress effects on the thermal conductivity are more significant at a 50% degree of saturation than at a 25% degree of saturation. This observation suggests that there are coupled effects of stress and moisture on thermal conductivity. The coupling effects between stress and degree of saturation are analyzed in detail later.

### 3.4.4 Effects of stress on the thermal conductivity of sand-rubber mixtures

Figure 3.12(a) shows the compression curves of dry sand-rubber mixtures subjected to a loading-unloading cycle, from tests S8 and S9. Taking the specimen with 10% rubber content

as an example, its void ratio decreases from 0.6 to 0.58 upon the loading from 0 to 600 kPa. During the subsequent unloading to 0 kPa, the void ratio increases to 0.59. The above data suggest that the loading and unloading process has induced slight and irreversible particle rearrangement. There is an obvious hysteresis in the relationship between void ratio and stress, mainly resulting in the irreversible response of sand-rubber mixtures. The irreversible deformation and hysteresis are more significant at lower stress. In addition, the specimen with 20% rubber content shows a much larger deformation than the specimen with 10% rubber content, mainly because the compressibility of rubber is higher than sand.

Figure 3.12(b) shows the measured thermal conductivities during the loading and unloading process. For both specimens with 10% and 20% rubber content, the thermal conductivity increases continuously during the loading process. To carry out a quantitative analysis, the thermal conductivity during the loading and unloading cycle is predicted using equation (3-2). Since this equation is able to well capture the influence of void ratio on sand-rubber mixtures (see Figure 3.7), the first mechanism could be considered using the parameters in Table 3.5. Figure 3.12(b) shows the comparison between measured and calculated results. It can be seen that the calculated thermal conductivity increases during the loading process and decreases during the unloading process, showing the same trend as the measured results. However, the measured thermal conductivity is significantly larger than the calculated one, confirming the observations in Figure 3.10. For example, when the specimen with 10% rubber content is compressed from 0 to 600 kPa, the measured thermal conductivity increases by about 30%, while the increase in the calculated value is only about 10%. As explained above, the

discrepancy between measured and calculated results implies that stress affects thermal conductivity through various mechanisms. If they are simplified as void ratio effects, the variation of thermal conductivity during the loading would be greatly underestimated. For example, when sand-rubber mixtures are used in the insulation layer beneath a seasonal energy storage system (e.g., TTES), the estimation of thermal conductivity only based on the density could underestimate the thermal conductivity and hence underestimate the thermal loss. Hence, the stress effects should be considered if a conservative design is required.

Figures 3.13 and 3.14 show the variations of void ratio and thermal conductivity during a loading-unloading cycle for specimens with an initial degree of saturation of 50% and 100%, respectively. The results are from tests S10 and S13. The measured and calculated results in these two figures confirm the major findings in Figure 3.12: (1) the thermal conductivity increases consistently with an increase in stress; (2) the void ratio effect cannot be simplified as the stress effect. This is because the change in void ratio accounts for less than 50% of the total change in thermal conductivity, as illustrated above.

### 3.4.5 Comparisons of stress effects at various degrees of saturation

To better understand the coupled effect of stress, degree of saturation and void ratio on the thermal conductivity. The results of sand-rubber mixtures are further analyzed in this section. The findings are qualitatively applicable to other materials like pure sand and CDG.

The measured  $\lambda_{600}$  (i.e. the thermal conductivity under a net stress of 600 kPa) is normalized by  $\lambda_0$  (i.e., the thermal conductivity at zero stress). Figure 3.15 shows the results of  $\lambda_{600}/\lambda_0$  at various initial degrees of saturation (0, 50% and 100%) and rubber contents (10%

and 20%). In both rubber contents, the relationship between  $\lambda_{600}/\lambda_0$  and degree of saturation follows a similar trend. Taking the case of 10% rubber content as an example, the value of  $\lambda_{600}/\lambda_0$  is 1.3 at the dry condition (i.e., the thermal conductivity increases by 30% due to compression). When the degree of saturation increases from 0 to 50%, the value of  $\lambda_{600}/\lambda_0$  decreases to about 1.17. In addition, the value of  $\lambda_{600}/\lambda_0$  increases slightly to 1.19. These observations suggest that stress effects are the most significant when the specimen is dry. This finding may be explained by the particle-level heat transfer mechanisms (Yun and Santamarina, 2008; Weidenfeld et al., 2004). For a dry specimen, heat conduction is mainly transmitted through the contact between solid particles (i.e., grain-grain conduction). Hence, the inter-particle contact area plays a very important role. Compression can increase the inter-particle contact area and hence the thermal conductivity significantly. When the degree of saturation is 50% and 100%, grain-water-grain conduction is dominant (i.e., heat is transmitted from solid particles to water, and then from water to neighbouring particles). The inter-particle contact area becomes less important, as water at the particle contacts contributes to the inter-particle heat transfer. Hence, the values of  $\lambda_{600}/\lambda_0$  at 50% and 100% saturation are smaller than that at the dry condition.

Figure 3.15 shows a significant difference between the measured and calculated thermal conductivities, similar to the findings from Figures 3.12(b), 3.11(b) and 3.14(b). More importantly, it is clear that the difference is much larger when the specimen is drier. Using the specimen with 10% rubber content as an example, the stress effects resulting from a larger contact area between solid particles during the loading-unloading cycle can account for about

80%, 79% and 68% increase in the thermal conductivity, when the degree of saturation is 0, 50% and 100%, respectively. In contrast, the contribution of changes in void ratio and moisture to the increment of thermal conductivity is only around 20%, 21% and 32%, respectively. This is likely because, in drier conditions, the inter-particle contact area plays an important role. A simplification of stress effects as void ratio effects would lead to an error of at least 68%. In addition, for both measured and calculated thermal conductivity, the  $\lambda_{600}/\lambda_0$  of 20% rubber content specimen is larger than that of 10% rubber content specimen. The major reason is that soil compressibility is larger with a higher rubber content, as shown in Figures 3.12(a), 3.13(a) and 3.14(a).

### 3.4.6 Hysteresis in the thermal conductivity-stress relation

As shown in Figures 3.8, 3.11, 3.12, 3.13 and 3.14, the relationship between thermal conductivity and net stress is not unique. At a given stress condition, there is a hysteresis between the loading and unloading curves. This hysteresis is likely attributed to the irreversible response of sand-rubber mixtures during the loading-unloading cycle. The irreversible deformation (i.e., the difference in the void ratio between the loading and unloading curves) can lead to an increase in the average number of inter-particle contacts (Lin and Ng, 1997). At a given stress condition, the contact area and hence the thermal conductivity is larger along the unloading process.

To further analyze the hysteresis induced by the stress history, the results of sand-rubber mixtures are further analyzed in this section. The findings could be qualitatively applicable to other materials like pure sand and CDG. A variable  $H = \frac{\lambda_0^* - \lambda_0}{(\lambda_0^* + \lambda_0)/2}$  is defined and used here,

where  $\lambda_0$  is the initial thermal conductivity before the loading, and  $\lambda_0^*$  is the thermal conductivity after a loading-unloading cycle in the stress range of 0 to 600 kPa. The value of  $H$  is larger when the stress history induced hysteresis is more significant. Figure 3.16 shows the values of  $H$  based on the measured and calculated thermal conductivities shown in Figures 3.12(b), 3.12(b) and 3.12(b). The hysteresis of the measured result is consistently larger than that of the calculated results. This implies that the hysteresis is induced by not only the decreasing void ratio but also the increasing contact area between solid particles. Furthermore, compared to the dry and fully saturated specimens, the specimen with an initial degree of saturation of 50% has a smaller hysteresis. This is because the higher suction under a 50% degree of saturation results in smaller compressibility. Similarly, the specimens with 20% rubber content have a larger hysteresis than the specimen with 10% rubber content, because the specimen compressibility is higher at a higher rubber content.

### 3.5 Summary

In this chapter, comprehensive tests were conducted to study the influence of net stress, void ratio, degree of saturation, rubber content and creep on the thermal conductivity of different soils. A widely-used equation is applied to fit the thermal conductivities during a loading-unloading cycle. Based on the measured and calculated results, some conclusions may be drawn as follows:

(1) Stress effects on the thermal conductivity are more significant when the soil specimen is more compressible. With a stress increase from 0 to 1200 kPa, the thermal conductivity increases by 60% for the clay, 25% for the silt with 85% DOC, 20% for the silt

with 95% DOC, 10% for the sand with an initial void ratio of 0.76 and 7.5% for the sand with an initial void ratio of 0.60. The observed increase in thermal conductivity is attributed to different mechanisms, including a reduction of the void ratio and a change in inter-particle contact. These two mechanisms seem relatively more important for the clay and sand, respectively. This finding implies that if stress effects are simplified as density effects in a heat transfer analysis, the thermal conductivity and hence heat transfer would be underestimated.

(2) For sand-rubber mixtures, the thermal conductivity also increases significantly with an increase in stress. For instance, at the dry condition (i.e.,  $S_r = 0$ ), the percentage increase is about 30% when the stress increases from 0 to 600 kPa. The former mechanism (i.e., a change in inter-particle contact) plays a dominant role, inducing about a 25% increase out of the 30% increase, whereas the reduction of void ratio plays a minor role, inducing the other 5%.

(3) Stress effects are more significant in the drier condition, where heat transfer is governed by inter-particle contacts. Taking the sand-rubber mixture as one example, at degrees of saturation of 0%, 50% and 100%, the thermal conductivity increase by about 30%, 17% and 19%, respectively, when the stress increases from 0 to 600 kPa.

(4) The  $\lambda - \ln \sigma'$  relation shows a clear bi-linearity, which is mainly attributed to yielding. Furthermore, during a loading and unloading cycle, there is an obvious hysteresis for the relationship between stress and thermal conductivity, due to the elastoplastic behaviour of soil specimens. At the same stress, soil specimen has a larger thermal conductivity along the unloading path than that along the loading path. This is most probably because loading-induced plastic deformation increases the average contact area between soil interparticle.

(5) The thermal conductivity increases consistently with increasing degree of saturation for each material. For sand-rubber mixtures, the rate of increase is affected by rubber content. When the test materials change from the dry to saturated condition, the thermal conductivity increases by about 11, 9 and 8 times at rubber content of 0, 10% and 20%, respectively. This finding implies that the addition of rubber shows a greater influence in the saturated condition than in the dry condition. When the rubber content increases from 10% to 20%, the thermal conductivity decreases by about 19% and 28% in dry and saturated conditions, respectively.

Table 3.1. Basic properties of the test materials.

Property	Toyoura sand	Silt (CDG)	Kaolin clay	Rubber
Unified soil classification system (ASTM D2487, 2011)	SP	ML	CH	—
Specific gravity	2.63	2.59	2.65	1.257
Liquid limit (%)	—	31	59	—
Plastic limit (%)	—	21	35	—
Plasticity index (%)	—	10	27	—
Maximum dry density (kg/m <sup>3</sup> )	1646	1840	1264	—
Optimum moisture content (%)	—	13.4	36.2	—
Minimum void ratio	0.65	—	—	—
Maximum void ratio	0.93	—	—	—

Table 3.2. Physical properties of the sand-rubber mixtures.

Test material	$\lambda_p$ (W·m <sup>-1</sup> ·K <sup>-1</sup> )	Grain size (mm)	d <sub>50</sub> (mm)	$G_s$	$e_{min}$	$e_{max}$
Toyoura sand	5	0.1-0.2	0.16	2630	0.65	0.93
Rubber	0.15	3-6	4.2	1257	-	-
Sand-rubber mixture A (rubber content: 10%)	-	0.1-6	3.79	2493	0.52	0.67
Sand-rubber mixture B (rubber content: 20%)	-	0.1-6	3.39	2355	0.45	0.62

Notes:  $\lambda_p$  is the thermal conductivity of sand/rubber particles (Côté and Konrad, 2005; Hannawi et al., 2010);  $d_{50}$  is the median diameter of all sand/rubber particles;  $G_s$  is the specific gravity which is the density of particles over the density of water;  $e_{min}$  is the minimum void ratio,  $e_{max}$  is the maximum void ratio. Rubber content is defined as the ratio of rubber mass and total mass in the soil-rubber mixtures.

Table 3.3. Summary of the tests at zero stress (42 tests in total with three replicates for each test).

Series ID	Soil type	Void ratio	Initial degree of saturation $S_r$
D1	Sand	0.6, 0.65, 0.70, 0.76	100%
D2	Silt	0.48, 0.56, 0.66, 0.76	100%
D3	Clay	2.35, 1.94, 1.61, 1.47	100%
D4	Sand	0.65, 0.71, 0.81, 0.93	0
D5	90% sand-10% rubber	0.52, 0.55, 0.58, 0.6, 0.67	0
D6	80% sand-20% rubber	0.45, 0.5, 0.55, 0.6, 0.62	0
M1	Silt	0.75	0, 25%, 50%, 100%
M2	Sand	0.7	0, 20%, 60%, 100%
M3	90% sand-10% rubber	0.6	0, 25%, 50%, 100%
M4	80% sand-20% rubber	0.6	0, 25%, 50%, 100%

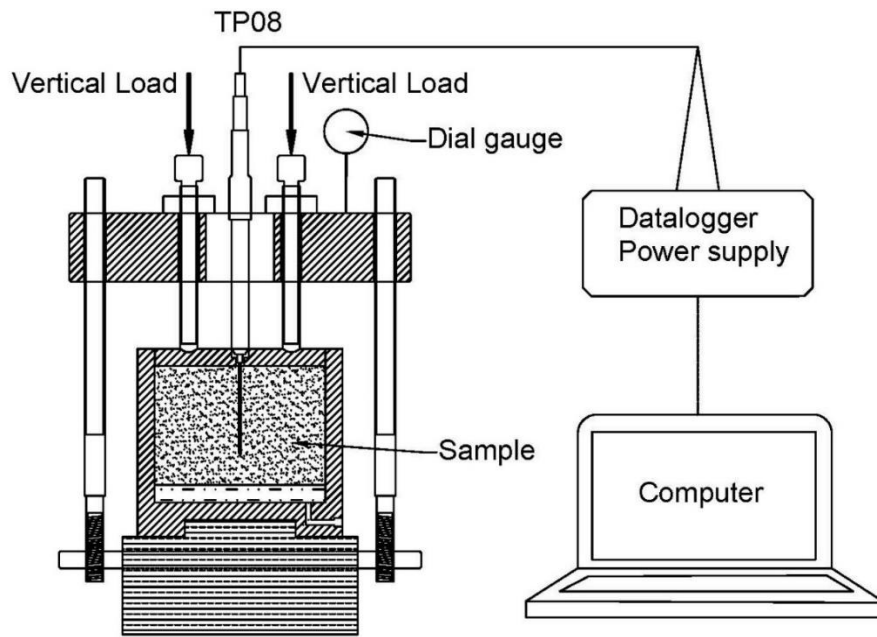
Table 3.4. Summary of the tests with a loading-unloading cycle (13 tests in total with three replicates for each condition).

Series ID	Soil type	Initial void ratio	Initial degree of saturation $S_r$	Net stress (kPa)
S1	Sand	0.6	100%	0-1200*
S2	Sand	0.76	100%	0-1200*
S3	Silt	0.48	100%	0-1200*
S4	Silt	0.63	100%	0-1200*
S5	Clay	1.93	100%	0-1200*
S6	Silt	0.63	25%	0-600*
S7	Silt	0.63	50%	0-600*
S8	90% sand-10% rubber	0.6	0	0-600*
S9	80% sand-20% rubber	0.6	0	0-600*
S10	90% sand-10% rubber	0.6	50%	0-600*
S11	80% sand-20% rubber	0.6	50%	0-600*
S12	90% sand-10% rubber	0.6	100%	0-600*
S13	80% sand-20% rubber	0.6	100%	0-600*

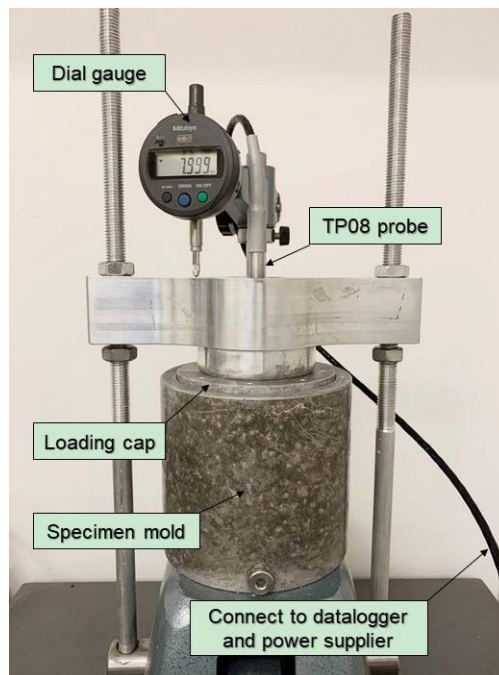
Note: \*Each specimen was subjected to a loading-unloading cycle. When the stress range is 0 to 1200 kPa, the stress path is 0→150→300→600→1200→600→300→150→0. If the stress range is 0 to 600 kPa, the stress path is 0→150→300→600→300→150→0. The duration of each stress stage is 1 day.

Table 3.5. Value of model parameters in equation (3-2).

Test material	$S_r$	a	b
Silt	100%	3.26	1.5
Clay	100%	2.89	1.2
Sand	0	6.3	7.5
	0	5.7	7.5
Sand-rubber mixture A (rubber content: 10%)	50%	5.7	3.4
	100%	5.7	2.6
	0	5.1	7.5
Sand-rubber mixture B (rubber content: 20%)	50%	5.1	3.7
	100%	5.1	2.9



(a)



(b)

Figure 3.1. A test apparatus for measuring thermal conductivity modified with stress control and deformation measurement: (a) schematic diagram; (b) photo.

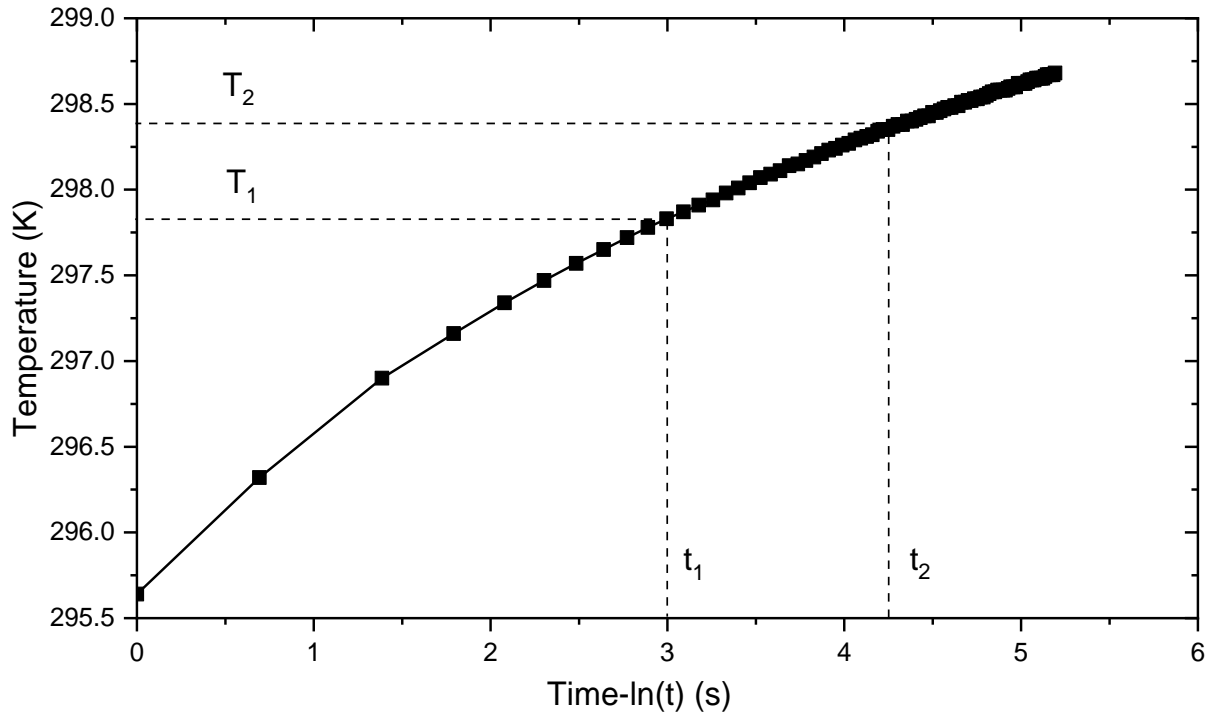


Figure 3.2. Typical response curve of the temperature in a thermal conductivity test.

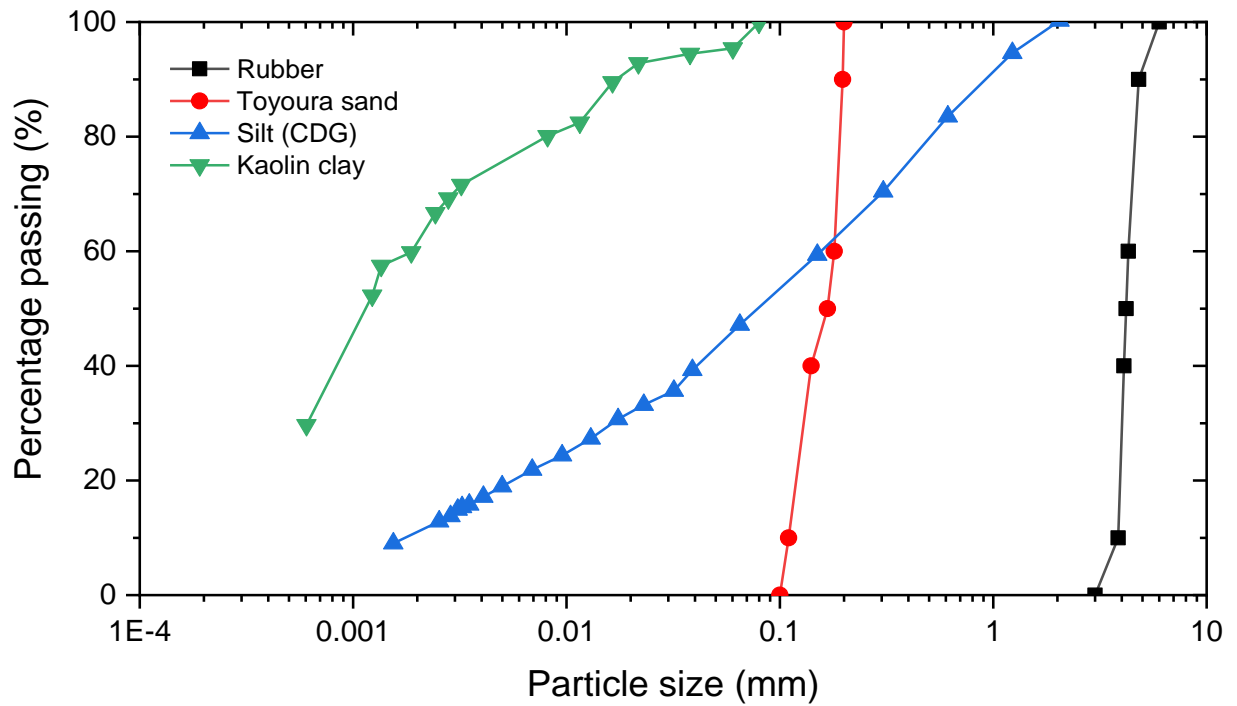


Figure 3.3. Particle size distribution of the test rubber, Toyoura sand, silt (CDG) and kaolin clay.

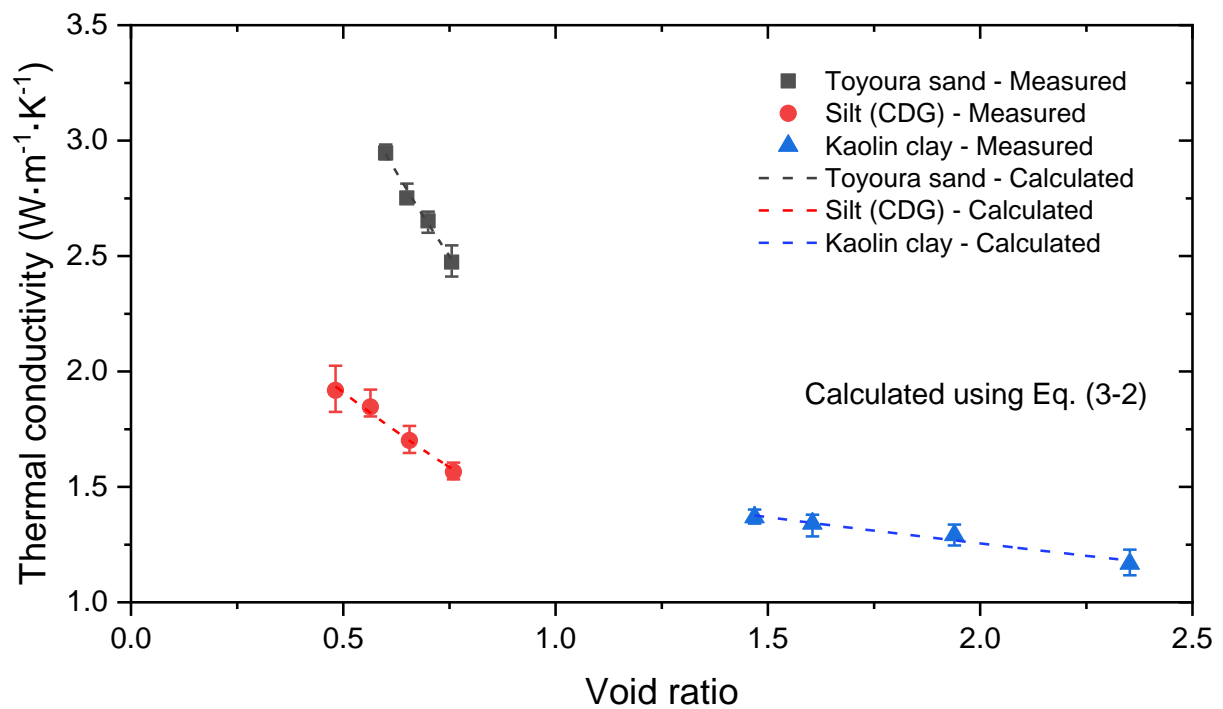


Figure 3.4. Thermal conductivity of saturated specimens with various void ratios at zero net stress (results of D1-D3 tests).

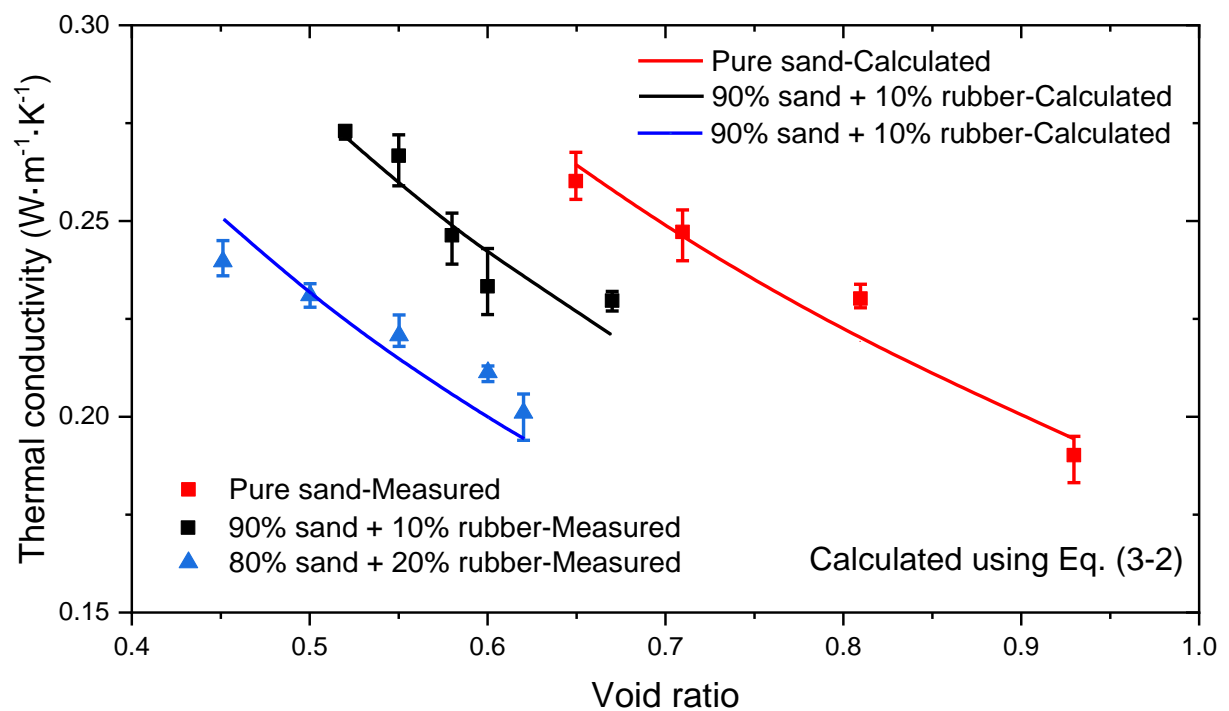


Figure 3.5. Thermal conductivity of dry specimens with various void ratios and rubber contents under zero net stress (results of D4-D6 tests).

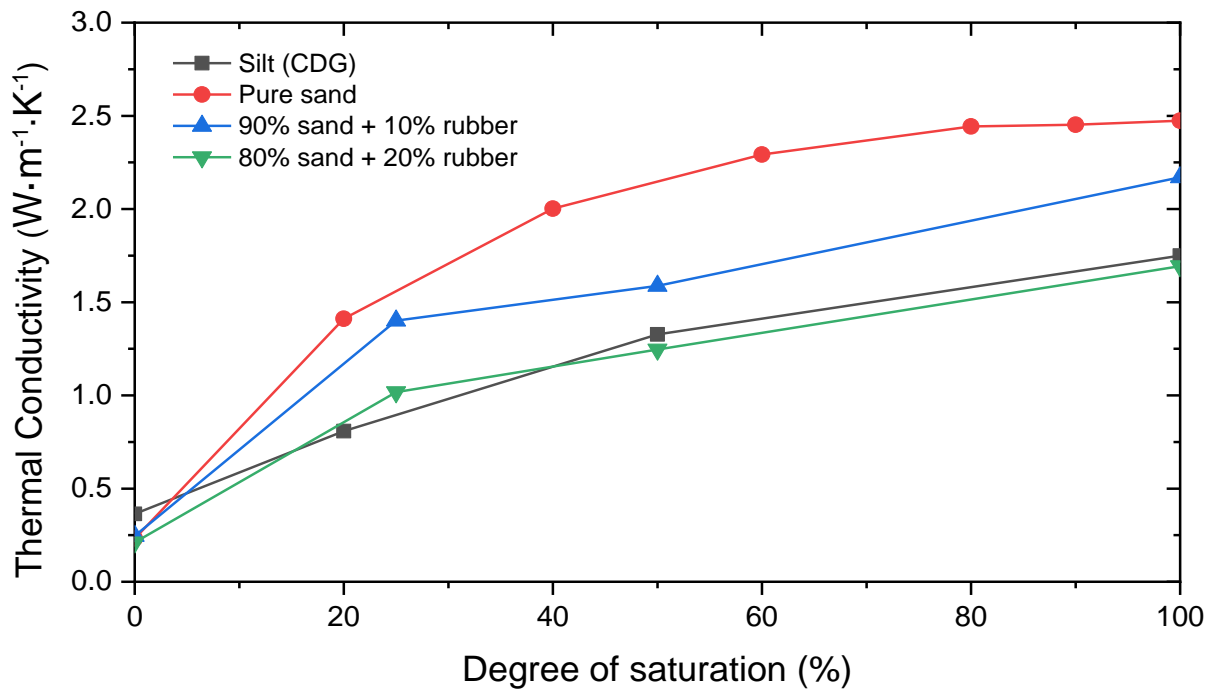


Figure 3.6. Influence of degree of saturation on the soil thermal conductivity under zero net stress (results of M1-M4 tests).

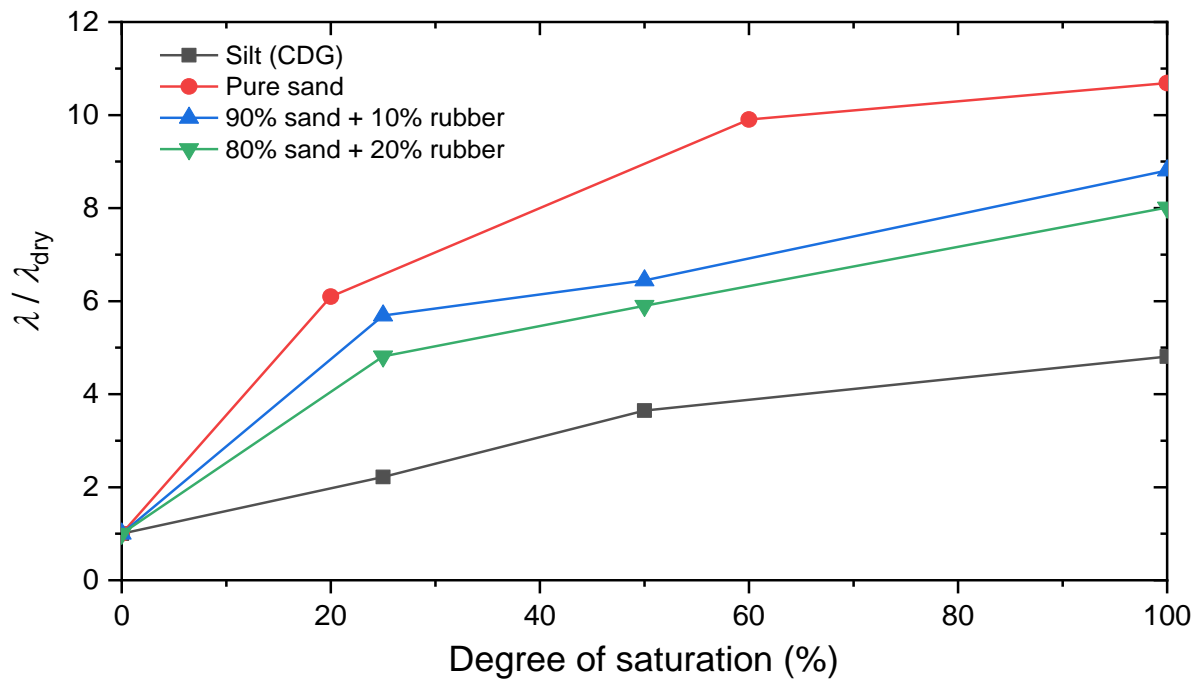
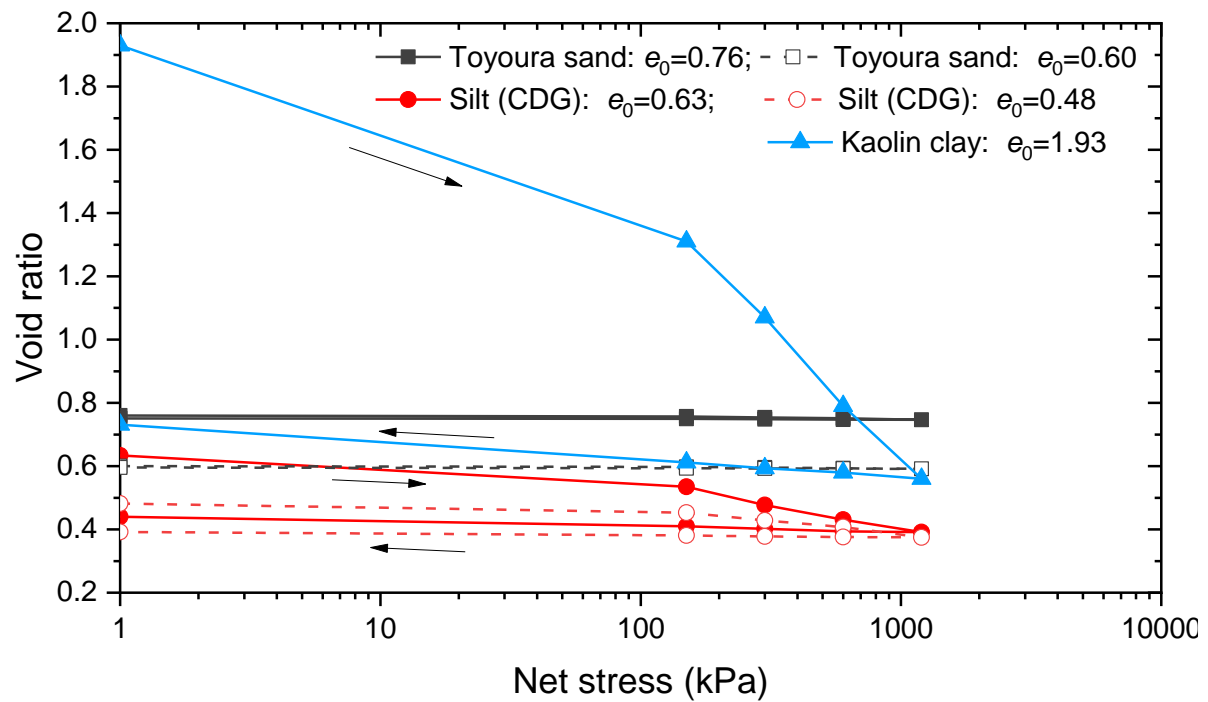
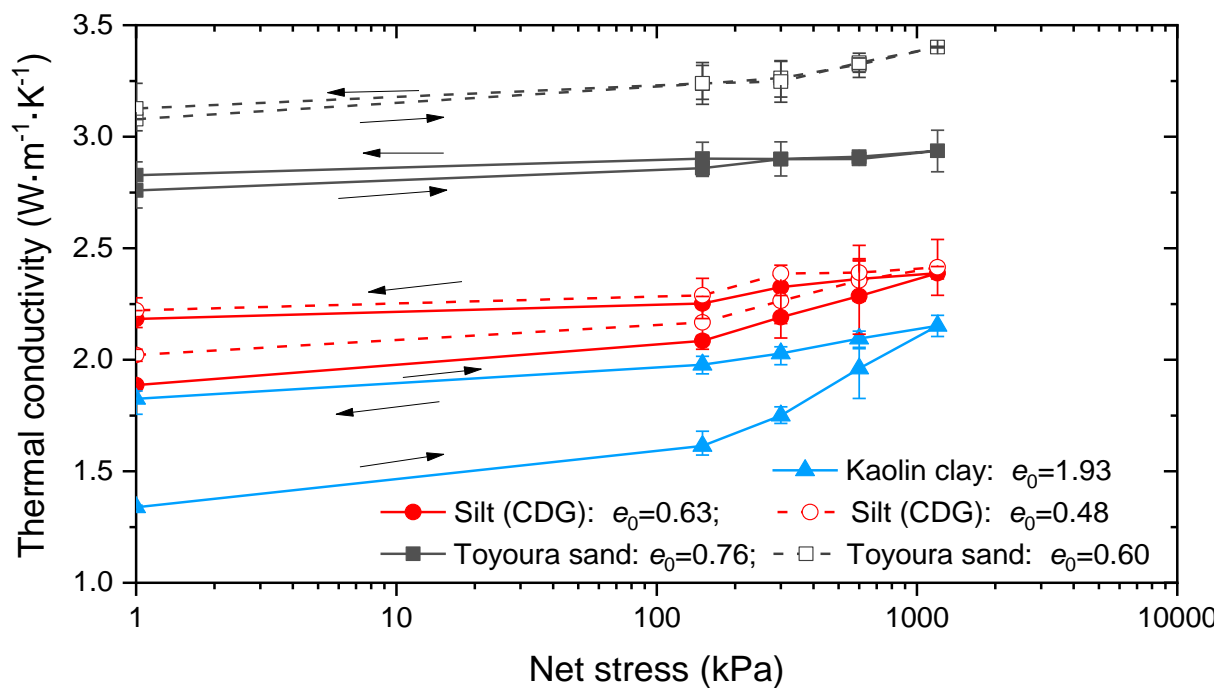


Figure 3.7. Influence of degree of saturation on the normalized thermal conductivity  $\lambda / \lambda_{dry}$  under zero stress (results of M1-M4 tests).



(a)



(b)

Figure 3.8. The behaviour of soil specimens in series S1-S5 during loading-unloading: (a) void ratio-stress relation; (b) evolution of thermal conductivity.

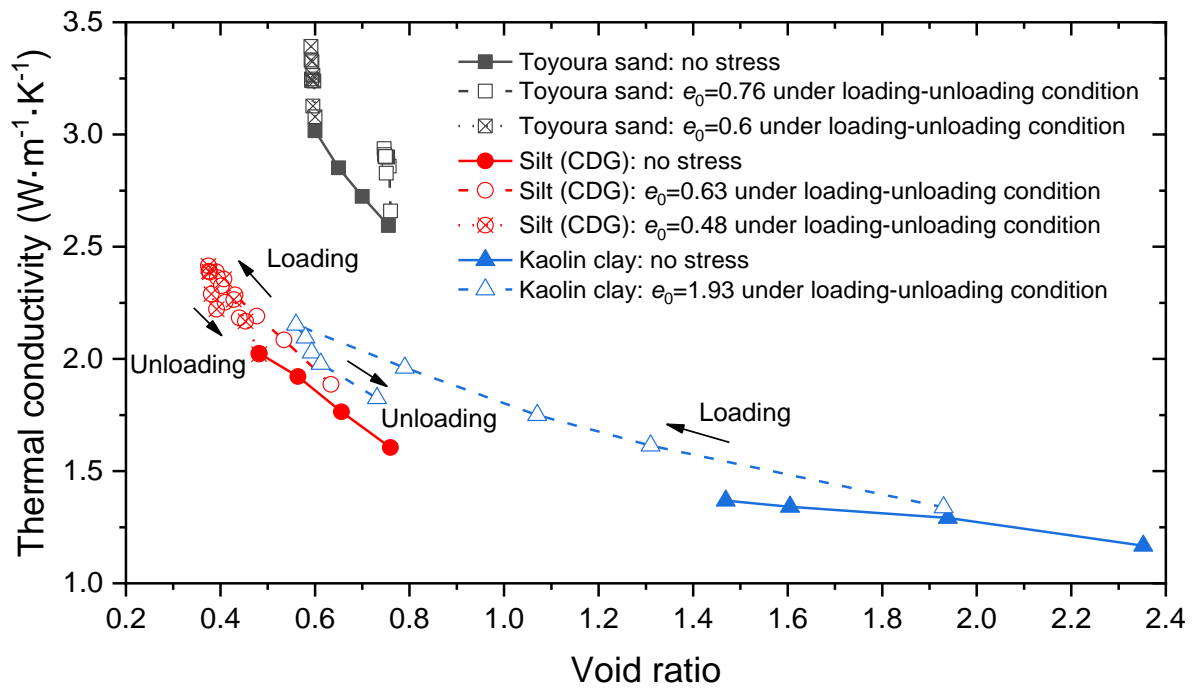
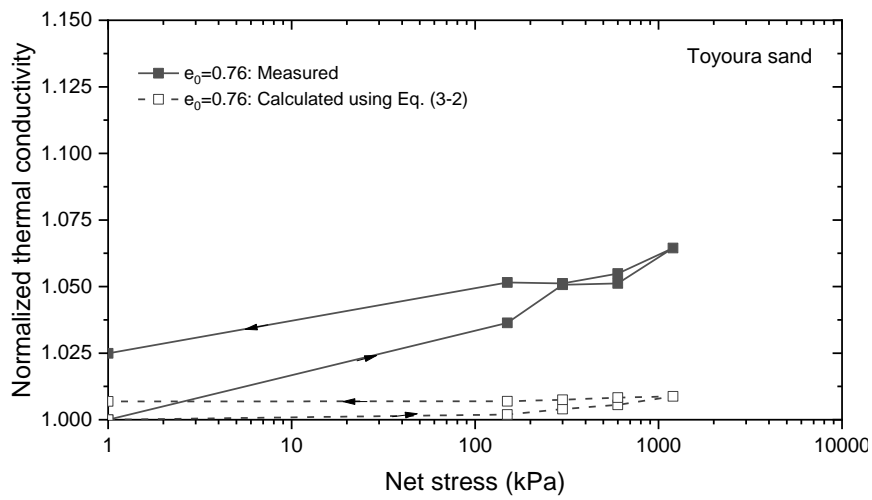
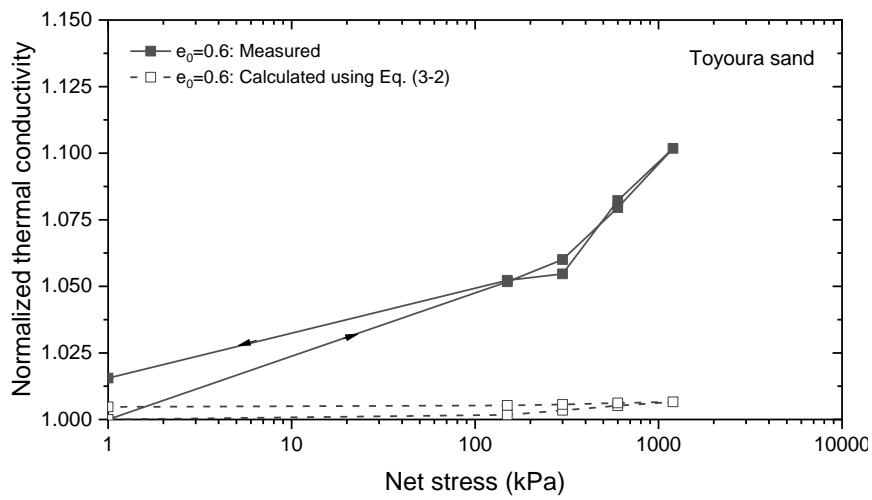


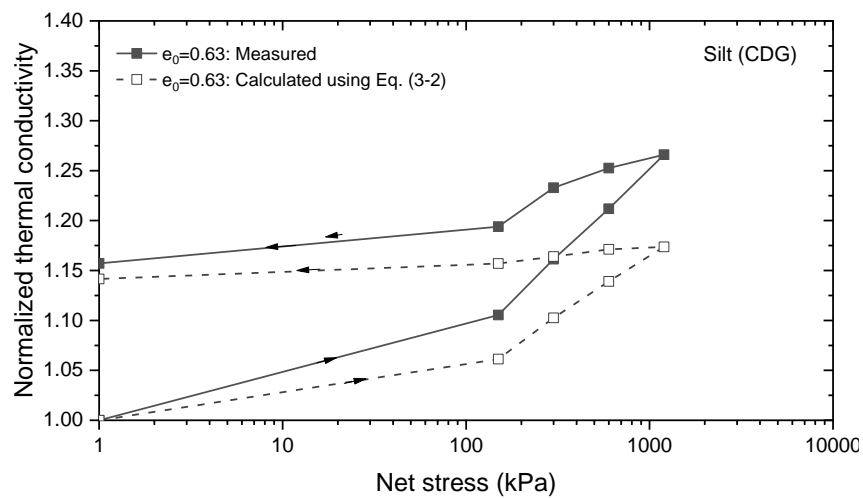
Figure 3.9. Thermal conductivity-void ratio relation during the loading-unloading process.



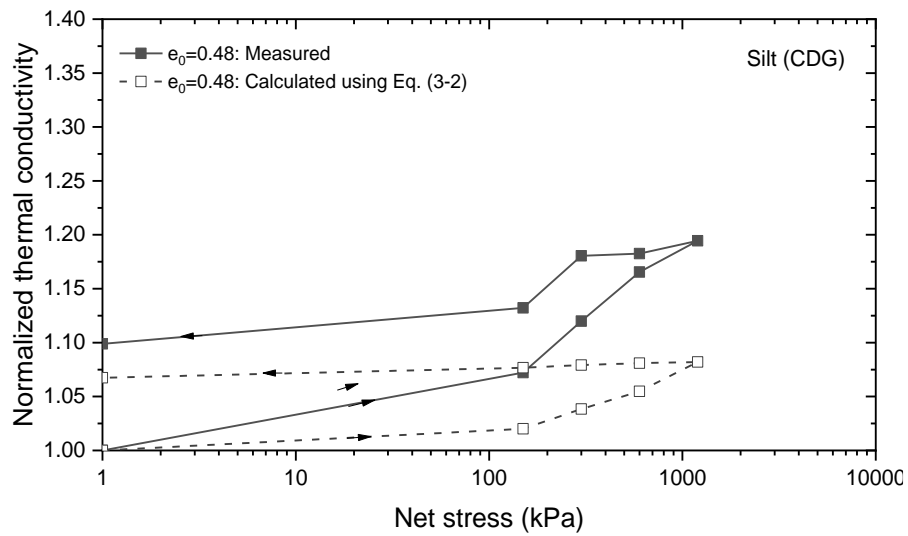
(a)



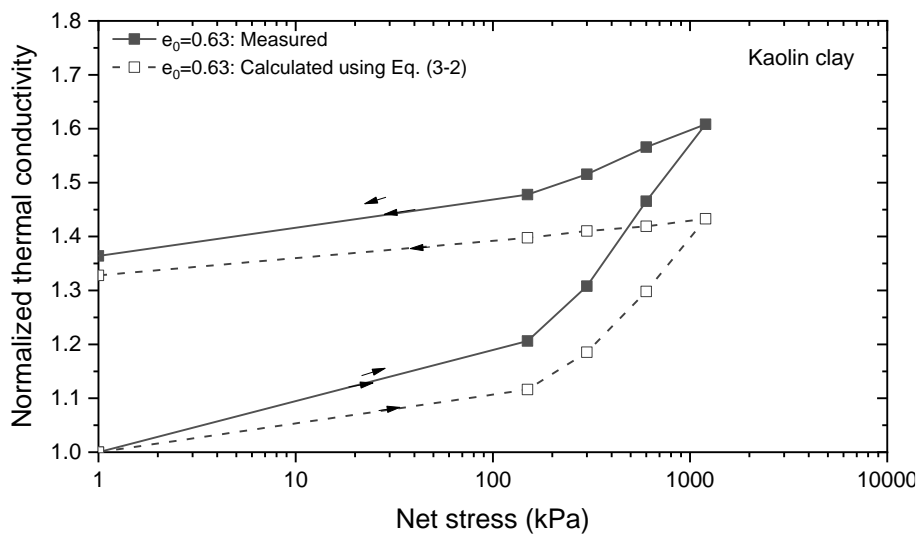
(b)



(c)

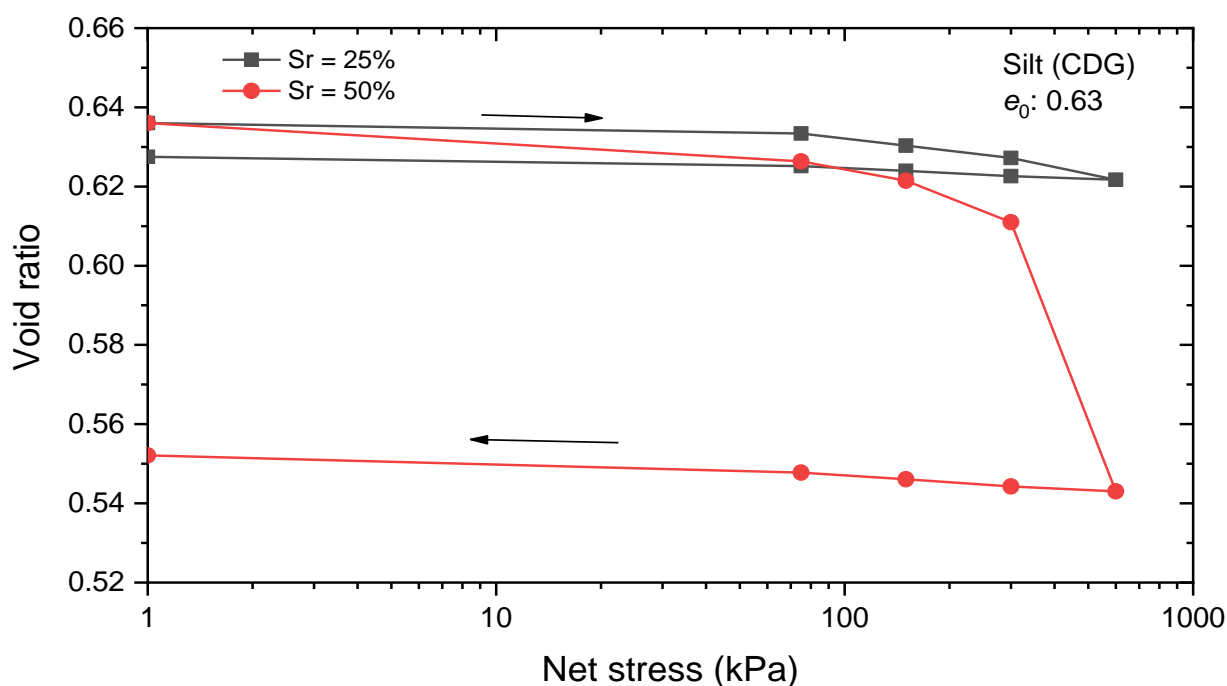


(d)

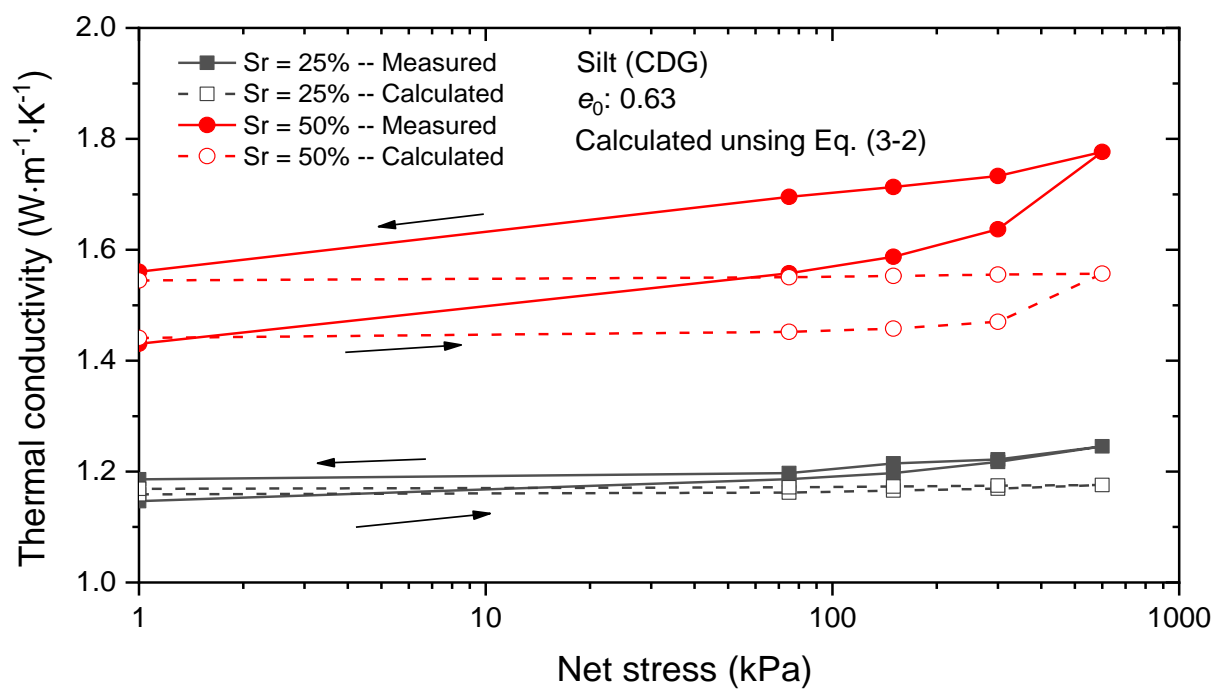


(e)

Figure 3.10. Comparisons between measured and calculated results: (a) Toyoura sand with an initial void ratio of 0.76; (b) Toyoura sand with an initial void ratio of 0.6; (c) CDG silt with an initial void ratio of 0.63; (d) CDG silt with an initial void ratio of 0.48; (e) Kaolin clay with an initial void ratio of 1.93.

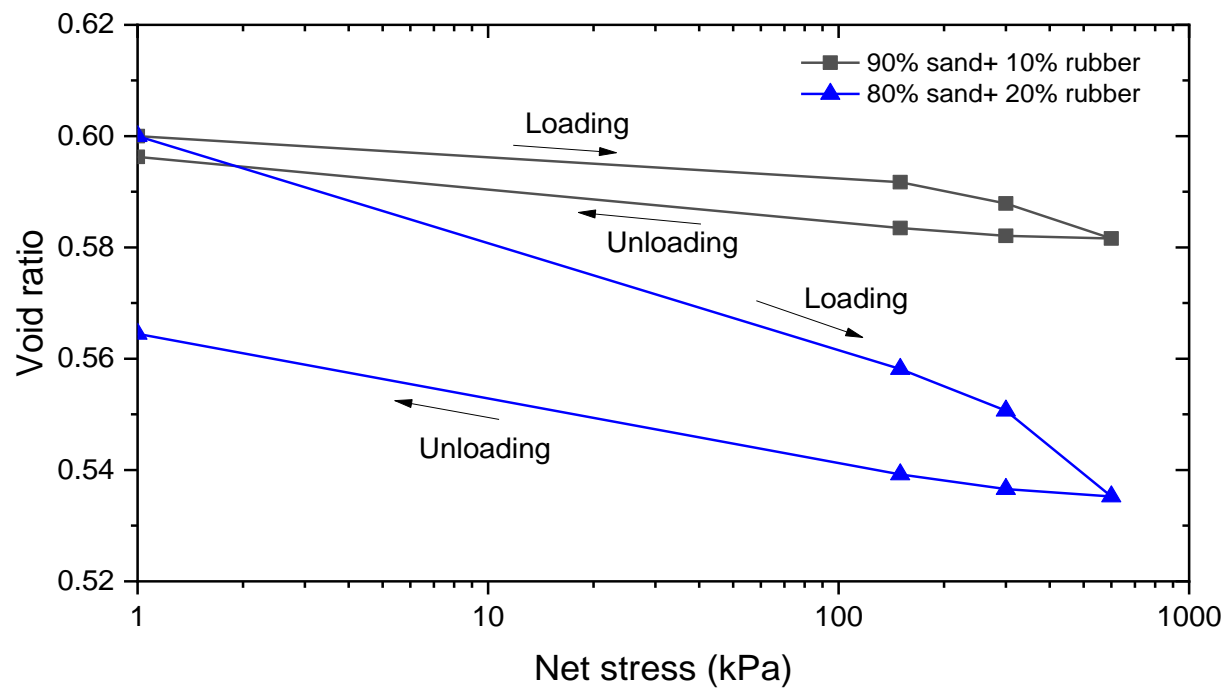


(a)

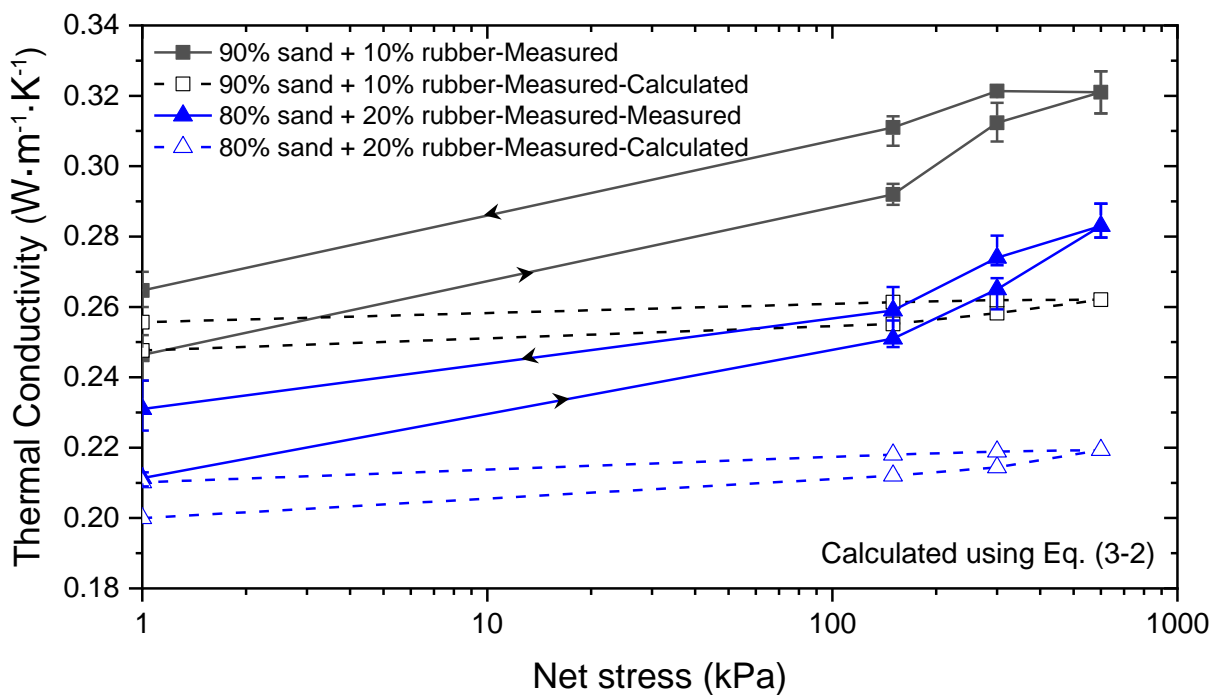


(b)

Figure 3.11. Test results of silt with initial  $S_r = 25\%$  and  $50\%$  (results of S6-S7 tests): (a) void ratio-stress relation; (b) thermal conductivity-stress relation.

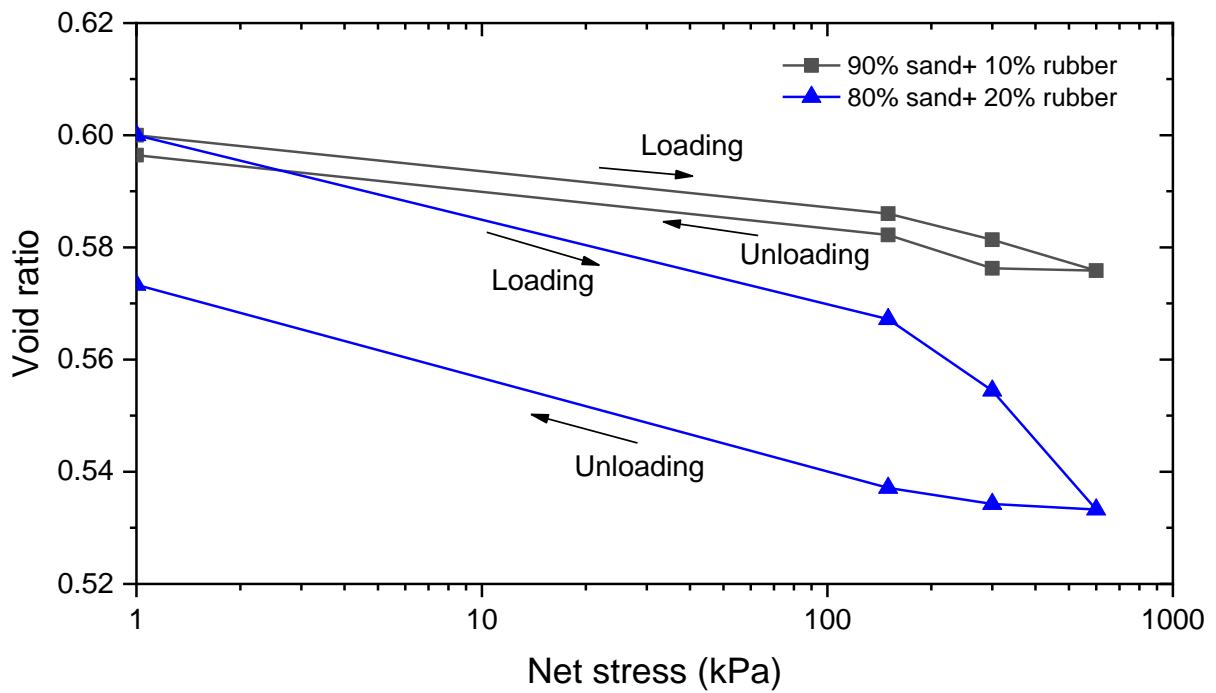


(a)

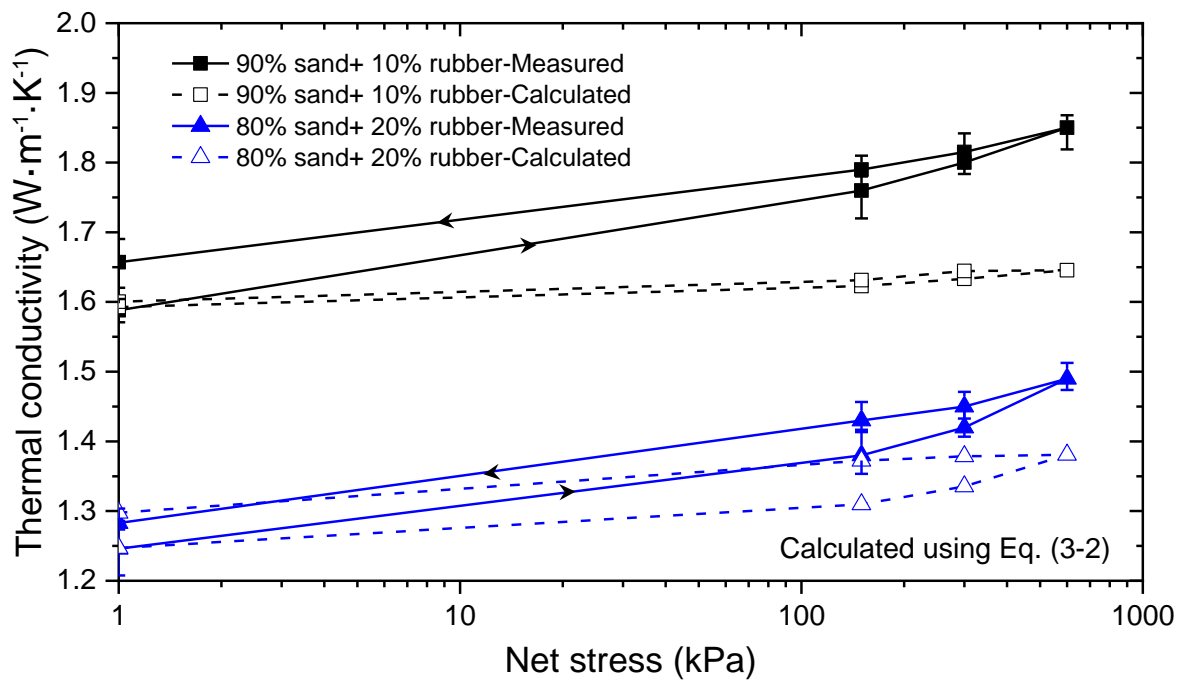


(b)

Figure 3.12. Test results of dry sand-rubber mixtures (results of S8-S9 tests): (a) void ratio-stress relation; (b) thermal conductivity-stress relation.

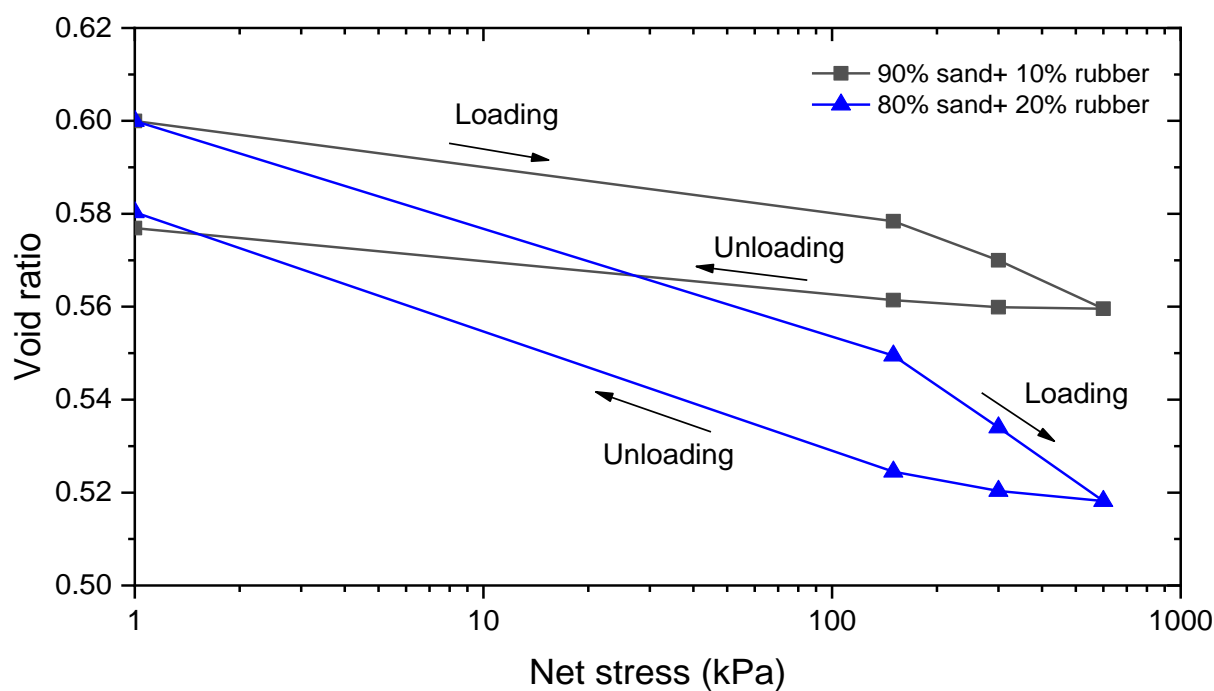


(a)

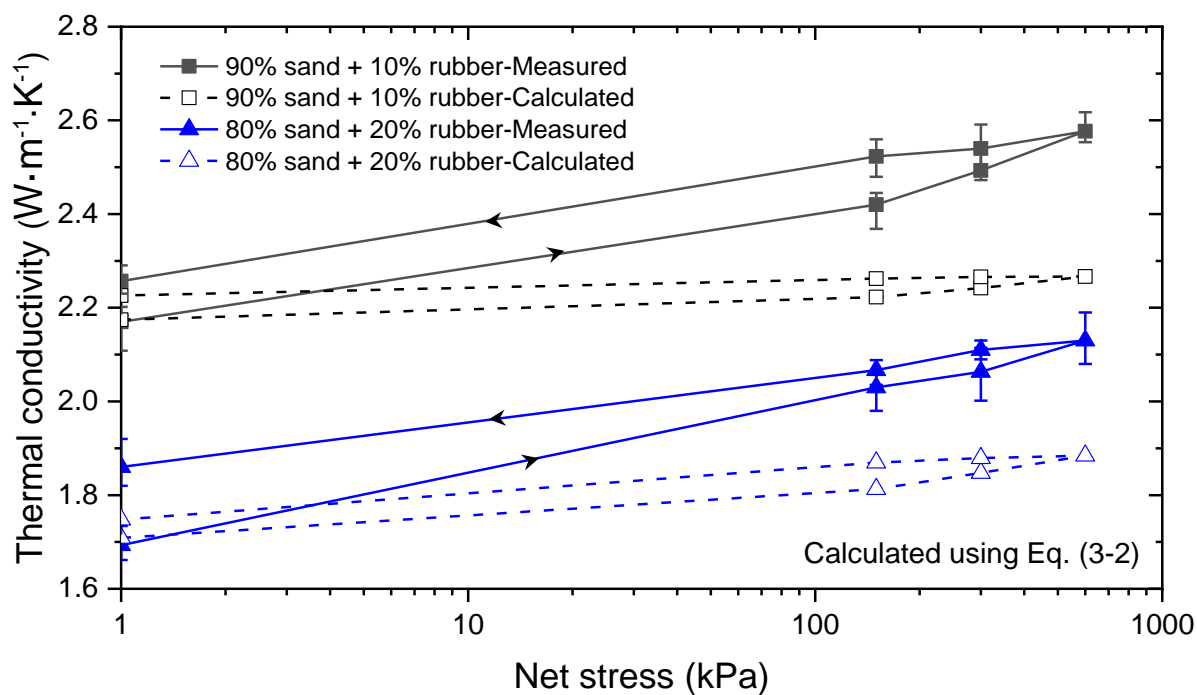


(b)

Figure 3.13. Test results of sand-rubber mixtures with initial  $S_r = 50\%$  (results of S10-S11 tests): (a) void ratio-stress relation; (b) thermal conductivity-stress relation.



(a)



(b)

Figure 3.14. Test results of saturated sand-rubber mixtures (results of S12-S13 tests): (a) void ratio-stress relation; (b) thermal conductivity-stress relation.

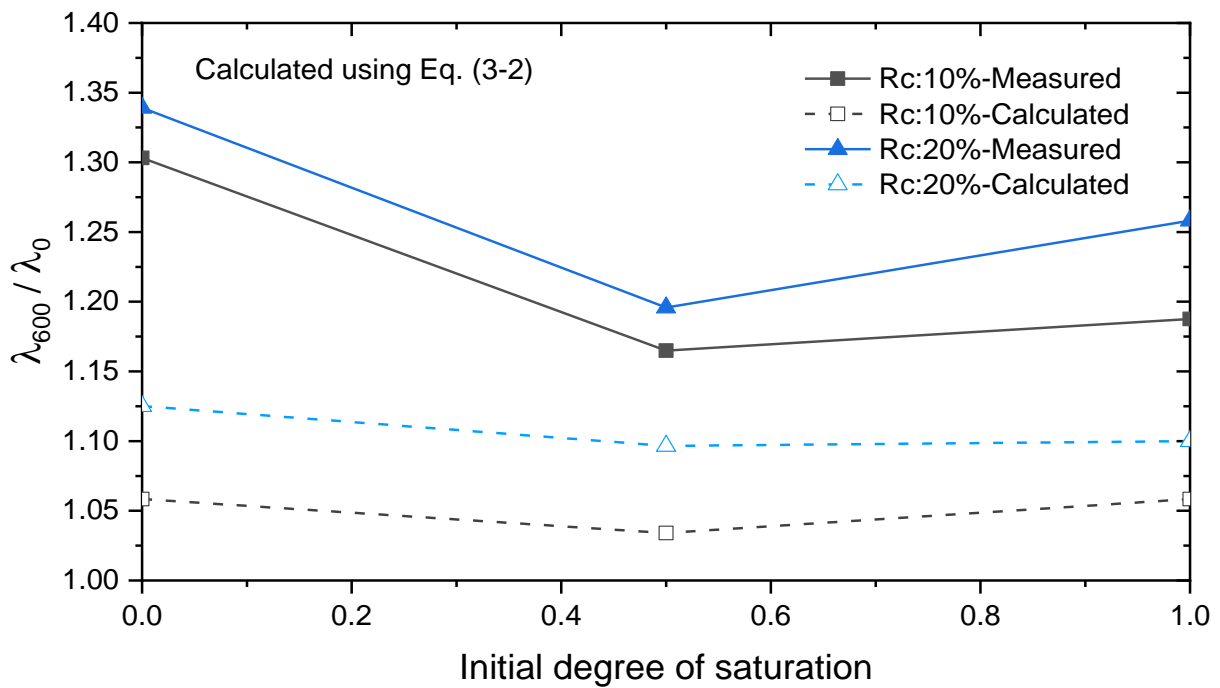


Figure 3.15. Influence of initial degree of saturation and rubber content on  $\lambda_{600}/\lambda_0$  ( $\lambda_{600}$  and  $\lambda_0$  are the thermal conductivities at net stresses of 600 and 0 kPa, respectively).

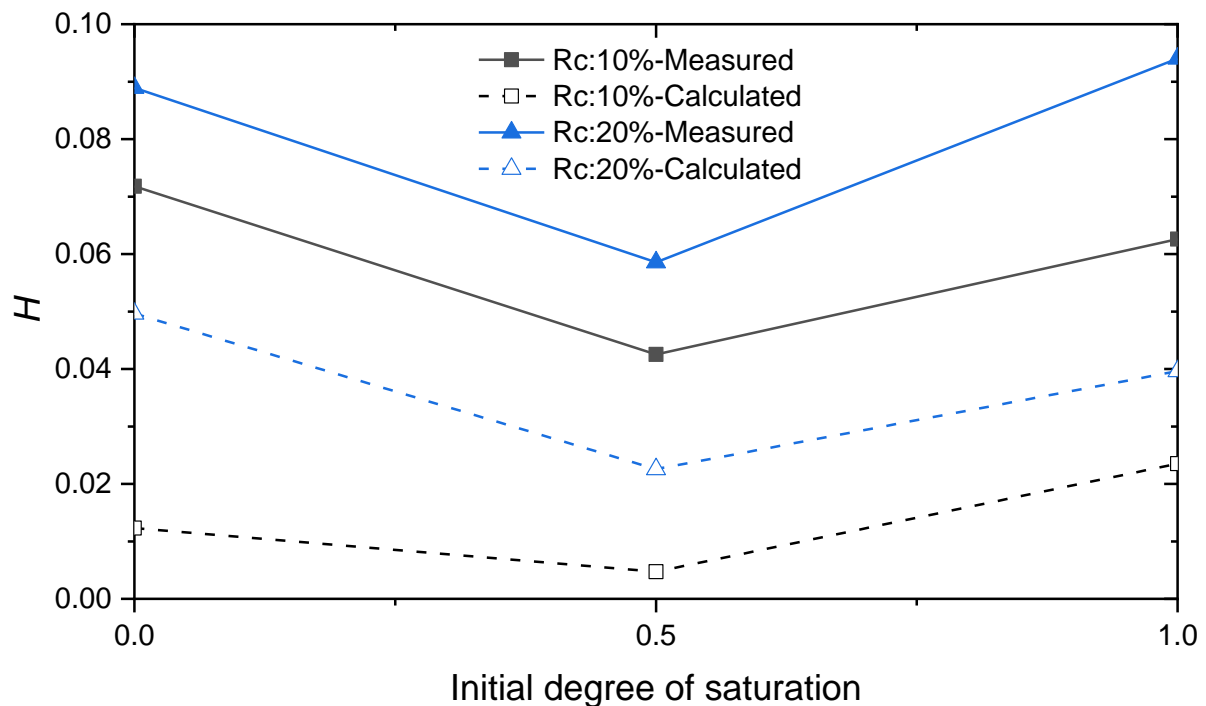


Figure 3.16. Increase in the thermal conductivity induced by a loading and unloading cycle ( $H = \frac{\lambda_0^* - \lambda_0}{(\lambda_0^* + \lambda_0)/2}$ , where  $\lambda_0$  is the initial thermal conductivity, and  $\lambda_0^*$  is the thermal conductivity after a loading-unloading cycle).

## **CHAPTER 4: A New Model for Soil Thermal Conductivity and Its Applications for Analyzing the Thermal Efficiency of Energy Pile**

According to the experimental results in Chapter 3, stress can affect the thermal conductivity of saturated and unsaturated soils. The existing models cannot capture the stress effects. To address this problem, a semi-empirical equation is newly proposed in this chapter to model the state-dependent thermal conductivity of saturated and unsaturated soils. Then, the new model is applied in finite element analysis to study the thermal efficiency of energy piles under different conditions.

### **4.1 A new model for the thermal conductivity of soil**

#### 4.1.1 Evaluation of existing models for considering stress effects

In the literature, some theoretical models have been proposed for the thermal conductivity of soil (e.g., equation (3.2)). They mainly focused on the influence of void ratio on thermal conductivity of soil. Only in recent years, several studies have been carried out to investigate stress effects on the thermal conductivity of porous materials (Yun and Santamarina, 2008; Cui and Zhou, 2022; Choo et al., 2013; Yao et al., 2021; Cui et al., 2022; Roshankhah et al., 2021; Duc Cao et al., 2021). Two semi-empirical equations were proposed for stress effects (Duc Cao et al., 2021; Roshankhah et al., 2021; Roshankhah and Santamarina, 2014). Both of them assume a logarithmic function between thermal conductivity and stress, and the equation of Roshankhah and Santamarina (2014) is analyzed here as one example:

$$\lambda = \lambda_1 \left[ 1 + \beta \log \left( \frac{\sigma}{1 \text{ kPa}} \right) \right] \quad (4-1)$$

where  $\lambda_1$  is the thermal conductivity at a reference effective stress of 1 kPa;  $\beta$  is a soil parameter. To evaluate the capability of this equation, it is used to calculate the thermal conductivity of Toyoura sand, CDG (silt) and kaolin clay during a loading-unloading cycle. The parameters (see Table 4.1) were calibrated using the results in Figures 3.5 and 3.14.

Figure 4.1 compares the measured and calculated thermal conductivities normalized by that at zero stress. The predictions by equation (3-2) are also included for comparison. The results of different soils consistently suggest that equation (3-2) underestimates the influence of stress on thermal conductivity, similar to the findings in Chapter 3. Equation (4-1) shows better performance, but it also has several limitations. Firstly, it does not reproduce the hysteresis loop of the  $\lambda - \ln \sigma$  relation, mainly because it does not incorporate the influence of irreversible soil deformation induced by mechanical loads. Secondly, it cannot capture the bi-linearity of the  $\lambda - \ln \sigma$  relation, which is closely related to yielding. Finally, for a given soil, this equation requires different values for  $\beta$  at different void ratios. Apart from these limitations, it should be noted that the stress effects on the thermal conductivity of unsaturated soil have not been investigated.

#### 4.1.2 A new semi-empirical equation for thermal conductivity of saturated soil

The existing equations are unable to well capture the coupled effects of void ratio and stress on the thermal conductivity, as demonstrated in the previous section. To address this problem, a new equation is proposed by modifying equation (3-2):

$$\lambda = a \exp\left(-b \frac{e}{1+e}\right) \left(1 + \frac{\sigma}{1 \text{ kPa}}\right)^c \quad (4-2)$$

where  $c$  is a model parameter for controlling the dependency of thermal conductivity on stress, which is related to the soil types. This equation is expected to capture the coupled influence of stress and void ratio on the thermal conductivity of saturated soils. When the net stress is zero, it is able to reduce to equation (3-2). Note that stress-induced change in void ratio can be considered through the second term on the right-hand side of equation (4-2). Other additional effects of stress, such as the variation of inter-particle contact, are lumped together and incorporated using the third term. The power function for the third term was selected based on the Hertzian contact theory (Hertz, 1881) about inter-particle contact in granular soils. This theory was developed to analyze the contact between two spheres under externally imposed loads. It suggests that the ratio  $A/F^{2/3}$  is constant, where  $A$  and  $F$  are the inter-particle contact area and applied load, respectively. Although the natural soils are much more complicated than the case of two spheres, the power function is still used to provide a close approximation. Any potential influence of other factors, such as the particle shape, particle size distribution, edge-to-face and face-to-face contacts in clay, could be indirectly considered through the parameter  $c$ .

Equation (4-2) was used to calculate the thermal conductivities of different soils, including sand, silt and clay. The measured and calculated results are also compared in Figure 4.1, including all the data during the loading-unloading cycle. They are closely matched with the experimental data. Particularly, equation (4-2) can well capture the bi-linearity and hysteresis of the  $\lambda - \ln \sigma$  relation, which cannot be simulated using existing models.

The model parameters and their values are summarized in Table 4.1. The value of  $c$  at the saturated condition is the highest for the clay and lowest for the sand. This is likely because when the soil is more compressible, the plastic strain is higher and hence the associated particle rearrangement would be more significant. This would alter the inter-particle contact more significantly (i.e., the second mechanism is more important). Consequently, the value of  $c$  is larger for a soil with a higher compressibility. However, this finding should be applied with caution and more experimental studies are required to fully verify it in the future.

At the same stress state, the thermal conductivity should be greatly affected by the yielding and preconsolidation pressure. As revealed by the data of silt and clay in Figure 4.1, the relationship between thermal conductivity and stress is bi-linear and the slope changes after yielding. Furthermore, the thermal conductivity along the unloading path is consistently higher than that along the loading path, because of a larger preconsolidation pressure along the unloading path. The observed influence of preconsolidation pressure can be explained by applying equation (4-2).

Note that the current stress, void ratio and preconsolidation pressure are not independent. The preconsolidation pressure can be calculated from the other two with an assumption of a unique normal compression line. By incorporating the void ratio and current stress in equation (4-2), which can be easily estimated in the field, the influence of preconsolidation pressure is considered in an indirect approach. This simplified approach can well capture the bi-linearity and hysteresis, as shown in Figure 4.1.

#### 4.1.3 Extension of the new equation from saturated to unsaturated soils

In equation (4-2), parameter  $b$  describes the sensitivity of thermal conductivity to void ratio. As illustrated by Chen (2008) and Zhang et al. (2017), the value of this parameter is affected by the degree of saturation. When the degree of saturation is larger, the value of  $b$  is smaller, suggesting that thermal conductivity is less sensitive to a change in the void ratio. Based on the results of tests through M1 to M4 in Table 3.3, the relationship between the degree of saturation and parameter  $b$  is determined and presented in Figure 4.2. An equation could be used to describe the  $S_r$ - $b$  curve, with a coefficient of determination  $R^2$  of 0.98:

$$b = \frac{A}{(1+B \cdot S_r)} \quad (4-3)$$

where  $A$  and  $B$  are empirical parameters accounting for the influence of soil type;  $S_r$  is the degree of saturation. For CDG, parameters  $A$  and  $B$  are 5.05 and 3.03, respectively. For sand-rubber mixture A (i.e., rubber content: 10%), parameters  $A$  and  $B$  are 7.47 and 2.16, respectively. For sand-rubber mixture B (i.e., rubber content: 20%), parameters  $A$  and  $B$  are 7.47 and 1.81, respectively.

As shown in Table 4.1, the value of parameter  $c$  can be maintained constant at different degrees of saturation for one type of soil, even though the soil compressibility is influenced by the degree of saturation (Zhou et al., 2012; Alonso et al., 1990). This is an advantage of the new model for soil thermal conductivity because the number of model parameters can be minimized.

Substituting equations (4-3) and (4-4) into equation (4-2), a new model is developed for the state-dependent thermal conductivity of unsaturated soils:

$$\lambda = a \cdot \exp \left[ -\frac{A}{(1+B \cdot S_r)} \cdot \frac{e}{1+e} \right] \cdot \left( 1 + \frac{\sigma'}{1 \text{ kPa}} \right)^c \quad (4-4)$$

When the degree of saturation is zero, it reduces to equation (4-2). Based on the model parameters in Table 4.1, equation (4-4) was used to calculate the thermal conductivities of unsaturated CDG and sand-rubber mixtures. The measured and calculated results are compared in Figures 4.3 and 4.4, showing a good match. Particularly, equation (4-4) can well capture the variations of thermal conductivity during the loading-unloading cycle at different degrees of saturation. Furthermore, the calculated thermal conductivities of all soils are compared with the measured results from tests S1 through S13 (see Figure 4.5). It is clear that the new model can well capture the coupled effects of stress, void ratio and degree of saturation.

## 4.2 A numerical model for analysing the thermal efficiency of energy piles

The new model of thermal conductivity is applied to analyze the thermal efficiency of energy piles in different ground conditions. Soils surrounding energy piles have different overburden pressures, void ratios and degrees of saturation. Thus, this part focuses on the coupled effects of stress, void ratio and saturation on the thermal efficiency of energy piles.

### 4.2.1 Governing equations for the water flow in soils and piles

For the mass balance of water in porous media (i.e., soils and piles), it is described using the following equation:

$$\frac{\partial}{\partial t}(S_r n \rho_w) + 3S_r n \alpha_w \rho_w \cdot \frac{\partial T}{\partial t} + \nabla \cdot (\rho_w \mathbf{u}) = 0 \quad (4-5)$$

where  $S_r$  is degree of saturation (SI unit: 1);  $n$  is soil porosity (SI unit: 1);  $\rho_w$  is water density at a reference temperature (i.e., 20°C in this study) (SI unit: kg·m<sup>-3</sup>);  $\alpha_w$  is the linear thermal expansion coefficient of water (SI unit: 1·K<sup>-1</sup>);  $T$  is the soil or pile temperature (SI unit: K);

$\mathbf{u}$  is the Darcy velocity (SI unit:  $\text{m}\cdot\text{s}^{-1}$ ). The first part on the left-hand side can be also expressed as the following equation (Bear, 1979; Bear, 1972):

$$\frac{\partial}{\partial t}(S_r n \rho_w) = \rho_w \left( \frac{C_m}{\rho_w g} + S_e S \right) \frac{\partial p^w}{\partial t} \quad (4-6)$$

where  $p^w$  is the water pressure (SI unit: Pa);  $C_m$  is the specific moisture capacity (SI unit: 1);  $S_e$  is the effective degree of saturation (SI unit: 1);  $S$  is the storage coefficient (SI unit:  $\text{Pa}^{-1}$ ).  $C_m$ ,  $S_e$  and  $S$  are related to the soil water retention curve (SWRC). Based on van Genuchten model (Van Genuchten, 1980) and linearized storage model in COMSOL, they can be obtained by using the following equations:

$$S_e = \frac{S_r - S_{res}}{S_{sat} - S_{res}} = \left[ 1 + (\alpha \psi)^{\frac{1}{1-m_1}} \right]^{m_1} \quad (4-7)$$

$$C_m = \alpha \frac{m_1}{1-m_1} (\theta_s - \theta_r) S_e^{\frac{1}{m_1}} \left( 1 - S_e^{\frac{1}{m_1}} \right)^{m_1} \quad (4-8)$$

$$S = S_r n c^w \quad (4-9)$$

where  $S_{res}$  and  $S_{sat}$  are the degree of saturation at residual and saturated states, respectively;  $\theta_r$  and  $\theta_s$  are the volumetric water contents corresponding to  $S_{res}$  and  $S_{sat}$ , respectively;  $\psi$  is the soil suction (SI unit: kPa);  $c^w$  is the water compressibility (SI unit:  $\text{Pa}^{-1}$ ).  $\alpha$  and  $m_1$  are model parameters.

With reference to the work (Gallipoli, 2012; Grant and Salehzadeh, 1996; Ghavam-Nasiri et al., 2019), the effects of temperature and void ratio on the SWRC can be considered by modifying the equation (4-7) as follows:

$$S_e = \frac{S_r - S_{res}}{S_{sat} - S_{res}} = \left\{ 1 + \left[ \alpha \psi \frac{\beta + T_0}{\beta + T} \cdot \left( \frac{e}{e_0} \right)^{m_2} \right]^{\frac{1}{1-m_1}} \right\}^{m_1} \quad (4-10)$$

where  $T_0$  is the reference temperature (i.e., 291.15 K in this study);  $\beta$  and  $m_2$  are the model parameter;  $e_0$  is the initial void ratio at zero vertical stress;  $e$  is the void ratio at different normal stresses, which can be obtained based on the normally consolidated line measured in Chapter 3.

According to Darcy's law, the water velocity is described as follows:

$$\mathbf{u} = -\frac{k_r K}{\mu} (\nabla p^w + \rho_w \mathbf{g} \cdot \nabla Z) \quad (4-11)$$

where  $K$  is the intrinsic permeability of the porous medium (SI unit:  $\text{m}^2$ );  $\mu$  is the dynamic viscosity of water (SI unit:  $\text{Pa}\cdot\text{s}$ );  $\mathbf{g}$  is the gravitational acceleration (SI unit:  $\text{m}\cdot\text{s}^{-2}$ ); and  $\nabla Z$  is a unit vector in the vertical direction.

The permeability of saturated and unsaturated soils can be modelled using the following equation (Van Genuchten, 1980):

$$k_r = S_e^l \left[ 1 - (1 - S_e^{\frac{1}{m_1}})^{m_1} \right]^2 \quad (4-12)$$

where  $k_r$  is the relative permeability;  $l$  is the model parameter.

The temperature effects on the water density and dynamic viscosity can be captured by the following equations (Thomas and King, 1994):

$$\mu = 0.6612 \cdot (T - 229)^{-1.562} \quad (4-13)$$

$$\rho_w = 838.5 + 1.4T - 0.003T^2 + 3.72e^{-7} \cdot T^3 \quad (4-14)$$

#### 4.2.2 Governing equations for the heat transfer in soils and piles

It is well recognized that the heat transfer surrounding an energy pile is through heat conduction and heat convection, while heat radiation can be neglected. To describe the

conductive-convective heat transfer process, the heat transfer in porous materials (i.e., soils and piles) is described using the following equation (Nield and Bejan, 2013):

$$(\rho c)_{eff} \frac{\partial T}{\partial t} + \rho_w c_w \mathbf{u} \cdot \nabla T - \lambda \nabla^2 T - \alpha_p T \left( \frac{\partial p^w}{\partial t} + \mathbf{u} \cdot \nabla p^w \right) \quad (4-15)$$

$$(\rho c)_{eff} = (1 - n)\rho_s c_s + S_r n \rho_w c_w \quad (4-16)$$

where  $c_s$  and  $c_w$  are the specific heat capacity of solid skeleton and water (SI unit: J·kg<sup>-1</sup>·K<sup>-1</sup>), respectively;  $\rho_s$  is the density of skeleton soils (SI unit: kg·m<sup>-3</sup>);  $(\rho c)_{eff}$  is the effective volumetric heat capacity of soils or piles (SI unit: J·m<sup>-3</sup>·K<sup>-1</sup>);  $\nabla^2$  is the Laplace operator. The third part on the right-hand side represents the pressure work induced by heating expansion or cooling contraction of water.  $\lambda$  is the effective thermal conductivity of soil mixtures or piles. In this study, the thermal conductivity of piles is considered as a constant value. The soil thermal conductivity is calculated by using the equation (4-4) (with a unit of W·m<sup>-1</sup>·K<sup>-1</sup>). For simplicity, the net normal stress applied on soils is calculated by using the equation:

$$\sigma_{net} = \gamma' z \quad (4-17)$$

where  $\gamma'$  is effective unit weight of soils (SI unit: kN·m<sup>-3</sup>);  $z$  is the soil depth (SI unit: m).

#### 4.2.3 Governing equations for the water flow and heat transfer inside pipes

For calculation of fluid convection inside the pipes, the conservation of momentum and continuity equations mass are used (Barnard et al., 1966), as follows:

$$\rho_f \frac{\partial \mathbf{u}}{\partial t} + \rho_f \mathbf{u} \cdot \nabla \mathbf{u} = -\nabla p - f_D \frac{\rho}{2d_h} \mathbf{u} |\mathbf{u}| \quad (4-18)$$

$$\frac{\partial}{\partial t} \rho_f + \nabla \cdot (\rho_f \mathbf{u}) = 0 \quad (4-19)$$

where  $\rho_f$  is the density of heat fluid (SI unit: kg·m<sup>-3</sup>);  $u$  is the cross-section averaged velocity (SI unit: m·s<sup>-1</sup>);  $p$  is the pressure (SI unit: Pa);  $d_h$  is the mean hydraulic diameter (SI unit: m).

The second term on the right-hand side in equation (4-18) represents the pressure drop due to viscous shear. Here,  $f_D$  (dimensionless) the Darcy friction factor is calculated by using Churchill equation (Churchill, 1997):

$$f_D = 8 \left[ \left( \frac{8}{Re} \right)^{12} + (C_A + C_B)^{-1.5} \right]^{1/12} \quad (4-20)$$

The calculations of  $C_A$  and  $C_B$  are as follows:

$$\begin{cases} C_A = \left[ -2.457 \ln \left( \left( \frac{7}{Re} \right)^{0.9} + 0.27 \left( \frac{e}{d} \right) \right) \right]^{16} \\ C_B = \left( \frac{37530}{Re} \right)^{16} \end{cases} \quad (4-21)$$

$$Re = \frac{\rho u d_h}{\mu} \quad (4-22)$$

where  $Re$  is the Reynolds number;  $\mu$  is the dynamic viscosity of heat fluid.

For the heat transfer inside the pipes, the following equations are used (Lurie, 2008):

$$\rho_f A C_f \frac{\partial T}{\partial t} + \rho_f A C_f u \cdot \nabla T = \nabla \cdot A \lambda_f \nabla T + f_D \frac{\rho A}{2d_h} |u|^3 + Q_{wall} \quad (4-23)$$

where  $A$  is the cross-section area of pipe flow (SI unit:  $m^2$ );  $C_f$  is the heat capacity of heat fluid at constant pressure (SI unit:  $J \cdot kg^{-1} \cdot K^{-1}$ );  $T$  is the fluid temperature (SI unit: K);  $\lambda_f$  is the thermal conductivity of heat fluid (SI unit:  $W \cdot m^{-1} \cdot K^{-1}$ ). The second term on the right-hand side is related to the friction heat dissipated due to viscous shear. And the third term  $Q_{wall}$  (SI unit:  $W \cdot m^{-1}$ ) represents external heat exchange through the pipe wall. The detailed calculation for  $Q_{wall}$  is below.

$$Q_{wall} = (hZ)_{eff} (T_{ext} - T) \quad (4-24)$$

where  $h$  is the heat transfer coefficient (SI unit:  $W \cdot m^{-2} \cdot K^{-1}$ );  $Z$  is the pipe wall perimeter (SI unit: m).  $T_{ext}$  is the external temperature outside of the pipe (SI unit: K), which is equal to the soil-pile interface temperature from the heat conduction in soil domains;  $T$  is the fluid

temperature (SI unit: K). By multiplying the  $h$  and  $Z$ ,  $(hZ)_{eff}$  is an effective value of the heat transfer coefficient.

Considering the internal film resistance and wall resistance, the effective heat transfer coefficient can be obtained by using the following equations:

$$(hZ)_{eff} = \frac{2\pi}{\frac{1}{r_0 h_{int}} + \sum_{n=1}^N \left( \frac{\ln\left(\frac{r_n}{r_{n-1}}\right)}{\lambda_n} \right)} \quad (4-25)$$

where  $r_n$  is the outer radius of wall  $n$  (SI unit: m);  $h_{int}$  is the internal film resistance (SI unit:  $\text{W} \cdot \text{m}^{-2} \cdot \text{K}^{-1}$ ), which can be calculated as follows:

$$h_{int} = Nu \cdot \frac{\lambda_f}{2r_0} \quad (4-26)$$

where  $Nu$  (i.e., Nusselt number) is the ratio of convective to conductive heat transfer across a boundary in a fluid.  $Nu$  is equal to 3.66 for Laminar flow inside a round pipe, while the  $Nu$  of Turbulent flow is obtained via the following equation (Gnielinski, 1976):

$$Nu = \frac{(f_D/8)(Re-1000)Pr}{1+12.7\left(\frac{f_D}{8}\right)^{1/2} (Pr^{2/3}-1)} \quad (4-27)$$

#### 4.2.4 Model implementation and verification

The above governing equations (i.e., water mass balance and energy conservation in soils and pipes) were derived from the component libraries of COMSOL Multiphysics (Comsol, 2015). It includes the packages of ‘‘Darcy’s law’’, ‘‘Heat transfer in porous media’’ and ‘‘Nonisothermal pipe flow’’. Based on these COMSOL packages, several modifications were made in this study: (i) the variation of water density and dynamic viscosity resulting from temperature changes (see equations (4-13) and (4-14)) is considered in the ‘‘Nonisothermal pipe flow’’ and ‘‘Darcy’s law’’ packages; (ii) the thermal strain (see equation (4-5)) and pressure work (see equation (4-15)) are incorporated in the ‘‘Heat transfer in porous media’’ model; (iii)

effects of temperature and void ratio on the soil water retention characteristics are considered (see equation (4-10)); (iv) soil thermal conductivity is calculated by using equation (4-4) rather than the formulations available in the package of “Heat transfer in porous media”.

To verify the newly developed numerical code, it is applied to simulate the field test of Abdelaziz (2013). According to the field condition, a numerical model is built in COMSOL, as shown in Figure 4.6. The ground consists of two different soil layers, including a silty sand layer with a thickness of 12.8 m and a shale layer with a depth of 22.68 m. The testing energy pile is made of concrete with a diameter of 25.4 cm and a length of 30.48 m. A single U-pipe was installed inside the pile, with a shank spacing (center-to-center) of 7.5 cm. The initial temperature of the ground was 14.7 °C. The inlet temperature as an input parameter was from the measured data in the field (see Figure 4.7). The relationship between the measured inlet temperature and time was applied to the boundary condition of the pipe. The heat-exchange fluid inside the U-pipe was water. The values of input parameters are summarized in Table 4.3. Figure 4.7 compares the computed and measured outlet temperatures. It can be seen that the temperature distribution computed using the newly developed code is well matched with the measured data.

### **4.3 Numerical parametric studies**

The newly developed code was used to analyze the thermal performance of energy piles. Figure 4.8 shows the three-dimensional numerical model. It consists of a cuboid ground, a cylindrical pile and a U-shape pipe inside the pile. The triangular elements are used to develop the model mesh. The ground domain is 20 m in width, while the distance between pile and

model bottom is also set to be 10 m. The dimensions of numerical model are large enough to ensure a constant temperature condition at the surrounding boundaries during the heat transfer process. The top boundary at the ground surface is adiabatic with no heat exchange between the ground and atmosphere. Initially, the temperatures of soil and pile within the whole domain are 18°C. For the pipe, it is 22 mm in diameter and 2 mm in thickness, falling in the typical range for pipe dimension (Ozudogru et al., 2015; Kaltreider et al., 2015; Zhao et al., 2016). The high-density polyvinyl chloride pipe is used in this simulation, with thermal conductivity of 0.42 W·m<sup>-1</sup>·K<sup>-1</sup>. The distance between the pipe and pile edge is a constant value of 10 cm. The water is chosen as the heat-exchange fluid inside the pipe. In addition, concrete piles are investigated here, since they are the dominant type in the practice of energy piles. The concrete parameters were determined based on the experimental results of Asadi et al. (2018). The thermal conductivity of different soils was calibrated from the results in Figure 4.1, and all other input parameters are summarized in Tables 4.4 and 4.5.

A comprehensive program of numerical simulations was finished in this study, as shown in Tables 4.6 and 4.7, considering different soil types, pile dimensions, pipe flow conditions (i.e., velocity and inflow temperature) and water table depths. The design of the numerical programme is explained as follows:

(1) Two parameters (i.e., diameter and aspect ratio) were used to describe pile dimension, where the aspect ratio is defined as the pile length over the pile diameter. According to the summary of previous researchers (McCartney, 2011; Sekine et al., 2007; Loveridge and Powrie, 2013), the diameter of concrete energy piles generally falls in the range of 0.6 to 1.5

m. The aspect ratio usually ranges from 10 to 50. Within these ranges, different diameters and aspect ratios were considered in the numerical simulations.

(2) Based on previous studies (Gao et al., 2008; Park et al., 2013; Kaltreider et al., 2015), three different pipe flow rates are chosen, including  $3 \times 10^{-2}$ ,  $6 \times 10^{-3}$  and  $6 \times 10^{-4} \text{ m}^3 \cdot \text{s}^{-1}$ .

(3) To study the coupled effects of ground moisture conditions, three different depths were chosen (i.e., 6, 12 and 18 m) for the water table.

(4) To study the effects of stress on pile thermal performance, two cases were compared in each working condition, with and without considering stress effects on soil thermal conductivity. The comparisons can reveal the effects of stress on the thermal efficiency of energy piles under various working conditions.

The following variables were computed and reported in the following section: soil and pile temperatures at different locations and times, as well as the heat exchange rate between the pile and ground.

## **4.4 Interpretations of numerical results**

### 4.4.1 Typical temperature distributions around energy piles

Figure 4.9 shows the typical contours of temperature in the horizontal plane at the mid-depth of an energy pile with a diameter of 0.6 m and an aspect ratio of 30. As expected, the soil and pile temperatures increased with time in both cases (i.e., with and without stress effects). On the other hand, to investigate temperature variation in the vertical direction, a vertical plane was chosen along the red line in Figure 4.9. The temperature contours in this vertical plane are shown in Figure 4.10. In addition, the temperature contours along pipe length are presented in

Figure 4.11. It should be noted that the results in these two figures serve as examples and the results in other conditions show a similar trend.

Based on the results in Figure 4.10, the vertical temperature profiles at different distances from the pile surface are determined and shown in Figure 4.12. The temperature distribution at the soil-pile interface and three other sections (1D, 2D and 4D away from the interface) are included, where D is the pile diameter. The two cases, with and without considering stress effects on soil thermal conductivity, show obviously different results. At the soil-pile interface, when stress effects on thermal conductivity are considered, the temperature is always smaller than that without considering stress effects. This is because when stress effects are considered, the thermal conductivity and hence the rate of heat flow are larger, leading to a smaller temperature at the soil-pile interface. In contrast, at sections 2D and 4D away from the interface, the temperature considering stress effects is larger than that without considering stress effects. This is because when the thermal conductivity is larger due to stress effects, more heat is transferred from the energy pile to the surrounding soils. Regarding the section 1D away from the interface, the temperature difference induced by stress effects shows different trends at different stages. Compared to the results without consideration of stress effects on thermal conductivity, the temperature with stress effects is smaller when the working time is relatively short (i.e., 3 and 15 days) but becomes larger when the working time is relatively long (i.e., 30 days).

Figure 4.13 shows the typical temperature distribution along the red line in Figure 4.9. The results at 3 days, 15 days and 30 days are shown. According to the contours, the influence

zone increases with the time for both cases (i.e., with and without stress effects). At each time, the two curves with and without considering stress effects have an intersection (e.g., located at about 0.5D away from the interface at 3 days). This phenomenon agrees well with the observation in Figure 4.12. The results imply that with consideration of stress effects, the near-field temperature is smaller, while the far-field temperature is larger. This would affect the heat exchange rate between energy piles and soils. A detailed discussion is given in the following section.

#### 4.4.2 Thermal efficiency of energy piles with different dimensions

The following variable is adopted to describe the thermal efficiency of energy piles (Caulk et al., 2016; Ozudogru et al., 2014):

$$Q = c_w \rho_w v_f \cdot \frac{T_{inlet} - T_{outlet}}{L_{pile}} \quad (4-28)$$

where  $T_{inlet}$  and  $T_{outlet}$  are the inlet and outlet temperatures of pipe flow, respectively;  $v_f$  is the flow rate inside the pipe (SI unit:  $\text{m}^3 \cdot \text{s}^{-1}$ ). According to this definition,  $Q$  represents the heat exchange rate between the ground and energy pile per unit pile length. Its values with and without considering stress effects on soil thermal conductivity are denoted by  $Q_{\text{stress}}$  and  $Q_0$ , respectively. The ratio  $Q_{\text{stress}}/Q_0$  is analysed later to reveal stress effects on the thermal efficiency of energy piles. The results for energy piles in the clay ground are reported here as one example.

Figure 4.14(a) shows the computed values of heat exchange rate for energy piles with various aspect ratios and a constant diameter of 0.6 m. With an increase in the aspect ratio, the heat exchange rate decreases obviously. This observation is mainly attributed to the reduction

of pipe fluid temperature with increasing pipe length, as shown in Figure 4.11. From Figure 4.11, it can be seen that the outlet temperature decreases with increasing pipe length at both 3 and 30 days. The decrement of pipe fluid temperature would reduce the temperature gradient between the pile and soil and then decrease their heat exchange rate. Furthermore, considering stress effects on soil thermal conductivity, the heat exchange rate is slightly larger.

To better analyze the stress effect on the heat exchange rate, the ratio  $Q_{\text{stress}}/Q_0$  is calculated and shown in Figure 4.14(b). The values of  $Q_{\text{stress}}/Q_0$  are consistently above 1, meaning that energy piles can harvest more energy when stress effects on soil thermal conductivity are considered. This result suggests that previous analyses in the literature underestimated the efficiency of energy piles, because of the ignorance of stress effects. The ratio  $Q_{\text{stress}}/Q_0$  increases with increasing pile aspect ratio. This is because the stress effect is more significant when the pile is longer. Furthermore, the ratio  $Q_{\text{stress}}/Q_0$  for each condition becomes larger with an increase in time, suggesting that stress effects are more significant in the long term. This is because the heat exchange rate is affected by the thermal conductivities of the pile and soil. The latter plays a more important role in the long term than in the short term.

It can be seen from Figure 4.15 that the significance of stress effects is almost independent of the pile diameter when the aspect ratio is constant. Compared to the pile aspect ratio, the pile diameter plays a much less important role in the value of  $Q$ . On the one hand, the difference induced by stress effects on soil thermal conductivity is minor. On the other hand, the value of  $Q_{\text{stress}}/Q_0$  decreases slightly with increasing pile diameter, as shown in Figure

4.15(b). This is because as pile diameter increases, the thermal conductivity of concrete (pile material) plays a more important role, whereas the importance of soil properties becomes lower.

#### 4.4.3 Thermal efficiency of energy piles at different flow conditions in pipes

The condition of heat-exchange fluid inside pipes is expected to greatly affect the thermal performance of energy piles. In this section, the influence of flow rate and inlet temperature is investigated based on the computed results.

Figure 4.16 shows the heat exchange rate between energy piles and soils, considering different flow rates. The pile diameter is maintained at 0.6 m. When the aspect ratio is 30 and 50, the heat exchange rate initially presents a sharp increase with increasing flow rate from  $6 \times 10^{-4} \text{ m}^3/\text{min}$  to  $6 \times 10^{-3} \text{ m}^3/\text{min}$ , but then slightly increases when the flow rate is larger than  $6 \times 10^{-3} \text{ m}^3/\text{min}$ . This is probably because when the flow rate increases from  $6 \times 10^{-4} \text{ m}^3/\text{min}$  to  $6 \times 10^{-3} \text{ m}^3/\text{min}$ , the Reynolds number increases from 572 to 5720 and hence the pipe flow changes from laminar flow to transitional and turbulent flow. Moreover, the increment of flow rate after  $6 \times 10^{-3} \text{ m}^3/\text{min}$  is not able to improve heat exchange rate significantly. This observation implies that there is no need to keep increasing the pipe flow, if the pipe flow is already turbulent flow, which is consistent with the previous investigations (Kaltreider et al., 2015; Cecinato and Loveridge, 2015). In addition, the increment of pile aspect ratio still reduces the heat exchange rate, similar to results in Figure 4.14. From Figure 4.16, it can be seen that the effect of pipe flow rate seems to be minor for the pile with an aspect ratio of 50. This implies that the variations of pipe fluid temperatures resulting from the increasing flow

rate play an insignificant role for longer piles since the pipe length is more important. This speculation is consistent with the results in Figure 4.11.

To better evaluate stress effects on the thermal efficiency of energy piles at various flow rates,  $Q_{\text{stress}}/Q_0$  is calculated and shown in Figure 4.17. When the flow rate increases from  $6 \times 10^{-4} \text{ m}^3/\text{min}$  to  $6 \times 10^{-3} \text{ m}^3/\text{min}$ , the stress effects become more significant. In contrast, the ratio reduces with the increment of pipe flow rate from  $6 \times 10^{-3} \text{ m}^3/\text{min}$  to  $3 \times 10^{-2} \text{ m}^3/\text{min}$ . This is probably attributed to the reduction of difference between the inlet and outlet temperatures (i.e.,  $T_{\text{inlet}} - T_{\text{outlet}}$ ). Taking the results after 30 days as an example, the relationship between temperature difference and flow rate is presented in Figure 4.18. The increasing pipe flow rate results in a decrement of temperature difference, which agrees well with the previous studies (Kaltreider et al., 2015). Based on the equation (4-28), the  $Q$  is not only dependent on the flow rate but also governed by the temperature difference. When the flow rate varies between  $6 \times 10^{-4} \text{ m}^3/\text{min}$  and  $6 \times 10^{-3} \text{ m}^3/\text{min}$ , the temperature difference is relatively larger and hence the influence of soil thermal conductivity on the heat exchange is more significant. As a result, it is observed that the stress effects increase soil thermal conductivity and hence  $Q_{\text{stress}}$ . However, with the flow rate increasing to  $3 \times 10^{-2} \text{ m}^3/\text{min}$ , the temperature difference becomes smaller and thus soil thermal conductivity plays a less important role in the heat transfer process. Then stress effects on  $Q$  become weaker. The ratio  $Q_{\text{stress}}/Q_0$  presents a slight decrement when the flow rate increases from  $6 \times 10^{-3} \text{ m}^3/\text{min}$  to  $3 \times 10^{-2} \text{ m}^3/\text{min}$ . This observation shows coupled effects of stress and flow rate on the  $Q$  at the first time, which has not been reported in the literature.

Furthermore, the ratio  $Q_{\text{stress}}/Q_0$  increases with increasing pile aspect ratio when the flow rate is larger than  $6 \times 10^{-4} \text{ m}^3/\text{min}$  but decreases with increasing pile aspect ratio when the flow rate is  $6 \times 10^{-4} \text{ m}^3/\text{min}$ . This observation is also related to the variations of temperature differences (i.e.,  $T_{\text{inlet}} - T_{\text{outlet}}$ ). As shown in Figure 4.18, when the flow rate is  $6 \times 10^{-4} \text{ m}^3/\text{min}$ , the temperature difference is two to three times of those under  $6 \times 10^{-3} \text{ m}^3/\text{min}$  and  $3 \times 10^{-2} \text{ m}^3/\text{min}$  flow conditions. It implies that the soil thermal conductivity plays a more important role in the heat transfer between soils and pile under slow flow rate condition. As a result, the stress effects on soil thermal conductivity and thermal efficiency of energy piles become more significant. As discussed above, the stress effects on soil thermal conductivity increase with soil depth (i.e., pile aspect ratio). Therefore, the ratio  $Q_{\text{stress}}/Q_0$  presents an incremental relationship with pile aspect ratio under the  $6 \times 10^{-4} \text{ m}^3/\text{min}$  condition. The results suggest that the effects of pile aspect ratio on the heat exchange rate may be governed by the flow type (e.g., Laminar flow and Turbulent flow). Further studies could be conducted to investigate this.

Figure 4.19(a) shows the heat exchange rate when the inlet temperature is  $38^\circ\text{C}$ . Compared to the results at  $28^\circ\text{C}$  (see Figure 4.13(a)), as expected, the heat exchange rate increases with increasing inlet temperature. Taking the pile with a diameter of 0.6 m and an aspect ratio of 50 as an example, when the inlet temperature increases from  $28^\circ\text{C}$  to  $38^\circ\text{C}$ , the heat exchange rate increases by around 95% after heating for three days. Furthermore, the significance of stress effects is almost independent of the fluid temperature, by comparing the

results in Figures 4.13(b) and 4.19(b). For instance, when the pile aspect ratio is 50, the  $Q_{\text{stress}}/Q_0$  is around 1.14 for both inlet temperatures.

#### 4.4.4 Stress effects on the thermal efficiency of energy piles in different soils

Figure 4.20 shows the comprehensive results of  $Q_{\text{stress}}/Q_0$ , with the influence of pile diameter, aspect ratio and soil type. Similar to the findings in Figures 4.13 and 4.15, the pile aspect ratio significantly affects the value of  $Q_{\text{stress}}/Q_0$ , but the influence of pile diameter is very minor.

When the aspect ratio is 50, the value of  $Q_{\text{stress}}/Q_0$  is about 1.18, 1.13 and 1.02 for the clay, silt and sand, respectively. The value of  $Q_{\text{stress}}/Q_0$  is the largest for clay, mainly because the effects of stress on soil thermal conductivity are the most significant for clay, as shown in Figure 4.1.

#### 4.4.5 Coupled effects of stress and unsaturation on pile thermal responses

To study the coupled effects of stress and degree of saturation on the thermal efficiency of energy piles, the heat exchange rates at different water table depths are computed and shown in Figure 4.21(a). The heat exchange rate increases with rising groundwater table, due to the increment of soil degree of saturation and thermal conductivity. To analyze the stress effects at different groundwater levels, the  $Q_{\text{stress}}/Q_0$  are summarized in Figure 4.21(b). The results present that stress effects are more significant with a deeper groundwater table. This observation is mainly attributed to the larger significance of stress effects on the thermal conductivity of unsaturated soils, as discussed in Chapter 3 (see Figure 3.15). Apart from the changes in void ratio and interparticle contact, the varying degree of saturation during a

loading-unloading cycle is believed to provide more contribution to soil thermal conductivity, since the stress effects on SWRC has been considered via equation (4-10). Therefore, the underestimation of heat exchange between piles and soils is probably more significant in unsaturated conditions.

## 4.5 Summary

In this chapter, a semi-empirical equation was newly proposed to model the coupled effects of stress, degree of saturation and void ratio on soil thermal conductivity. This new equation was applied in a finite element code, which was developed based on libraries in the COMSOL Multiphysics. Using this numerical code, comprehensive parametric studies were carried out to investigate the effects of various factors on the thermal performances of energy piles, including stress, pile diameter, pile aspect ratio, flow rate inside the pipe, inlet temperature and groundwater table. Based on the above studies, the following conclusions can be drawn:

(1) The existing equations for soil thermal conductivity in the literature are able to well capture void ratio effects but underestimate stress effects by at least 50%. The newly proposed semi-empirical equation has greatly improved the predictions, mainly because it explicitly considers stress effects on the void ratio and inter-particle contacts of soils.

(2) The heat exchange rate between energy pile and soil is higher when stress effects on the thermal conductivity of soils are considered. This suggests the previous methods may have underestimated the thermal efficiency of energy piles. The degree of underestimation is generally higher (i.e.,  $Q_{\text{stress}}/Q_0$  is larger) under the conditions of a larger pile aspect ratio,

higher soil compressibility and deeper groundwater table. The ratio of  $Q_{\text{stress}}/Q_0$  is not sensitive to the variation of pile diameter and inlet temperature. In addition, with an increase in water flow rate inside pipes,  $Q_{\text{stress}}/Q_0$  firstly increases and then shows a minor reduction.

Table 4.1. Model parameters of the soils used in the study.

Model parameters	Toyoura sand (Sr = 1)	Silt (CDG) (Sr =0.25)	Silt (CDG) (Sr =0.5)	Silt (CDG) (Sr =1)	Kaolin clay (Sr =1)
Parameter $a$	6.56	3.26	3.26	3.26	2.89
Parameter $b$	2.0	--	--	1.5	1.2
Parameter $c$	0.01	0.012	0.012	0.012	0.02
Parameter $\beta$	0.029 ( $e_0=0.76$ )	--	--	0.073 ( $e_0=0.63$ )	0.159
	0.019 ( $e_0=0.60$ )			0.054 ( $e_0=0.48$ )	( $e_0=1.93$ )
Parameter $A$	--	5.05	5.05	--	--
Parameter $B$	--	3.03	3.03	--	--

Note: Sr is the initial degree of saturation.

Table 4.2. Pipe and heat flow parameters used to simulate the field test (Abdelaziz, 2013).

Parameter	Value
Heat fluid (water)	
Density ( $\text{kg}\cdot\text{m}^{-3}$ )	1000
Flow velocity ( $\text{dm}\cdot\text{min}^{-1}$ )	5.68
Thermal conductivity ( $\text{W}\cdot\text{K}^{-1}\cdot\text{m}^{-1}$ )	0.6048
Dynamic viscosity ( $\text{Pa}\cdot\text{s}$ )	0.9772
Specific heat capacity ( $\text{J}\cdot\text{Kg}^{-1}\cdot\text{K}^{-1}$ )	4180
Pipes	
Thermal conductivity ( $\text{W}\cdot\text{K}^{-1}\cdot\text{m}^{-1}$ )	0.4
Specific heat capacity ( $\text{J}\cdot\text{Kg}^{-1}\cdot\text{K}^{-1}$ )	2300
Density ( $\text{kg}\cdot\text{m}^{-3}$ )	940
Inner diameter (mm)	21.844
Wall thickness (mm)	2.413
Shank spacing (mm)	75

Table 4.3. Pile and ground parameters used to simulate the field test (Abdelaziz, 2013).

Parameter	Value
Heat exchanger (borehole)	
Density ( $\text{kg}\cdot\text{m}^{-3}$ )	1600
Diameter (cm)	25.4
Thermal conductivity ( $\text{W}\cdot\text{K}^{-1}\cdot\text{m}^{-1}$ )	1.28
Length (m)	30.48
Specific heat capacity ( $\text{J}\cdot\text{Kg}^{-1}\cdot\text{K}^{-1}$ )	880
Soil layer 1 (silty clayey sand)	
Thermal conductivity ( $\text{W}\cdot\text{K}^{-1}\cdot\text{m}^{-1}$ )	1.0
Specific heat capacity ( $\text{J}\cdot\text{Kg}^{-1}\cdot\text{K}^{-1}$ )	1500
Density ( $\text{kg}\cdot\text{m}^{-3}$ )	1900
Layer thickness (m)	12.80
Soil layer 2 (shale)	
Thermal conductivity ( $\text{W}\cdot\text{K}^{-1}\cdot\text{m}^{-1}$ )	2.9
Specific heat capacity ( $\text{J}\cdot\text{Kg}^{-1}\cdot\text{K}^{-1}$ )	1200
Density ( $\text{kg}\cdot\text{m}^{-3}$ )	2400
Layer thickness (m)	22.68

Table 4.4. Values of input parameters for numerical parametric studies.

Parameter	Value
Pipe and heat fluid	
Thermal conductivity of pipe ( $W \cdot K^{-1} \cdot m^{-1}$ )	0.4
Pipe diameter (m)	0.022
Pipe wall thickness (mm)	2
Inlet temperature in the pipe ( $^{\circ}C$ )	28; 18
Flow rate ( $m^3 \cdot min^{-1}$ )	$3 \cdot 10^{-2}$ ; $6 \cdot 10^{-3}$ ; $6 \cdot 10^{-4}$
Thermal conductivity of heat fluid ( $W \cdot K^{-1} \cdot m^{-1}$ )	0.5
Specific heat capacity of heat fluid ( $J \cdot kg^{-1} \cdot K^{-1}$ )	4200
Concrete	
Thermal conductivity of concrete ( $W \cdot K^{-1} \cdot m^{-1}$ )	1.5
Density of concrete ( $kg \cdot m^{-3}$ )	2400
Specific heat capacity of concrete ( $J \cdot kg^{-1} \cdot K^{-1}$ )	880
Initial temperature of concrete and soil ( $^{\circ}C$ )	18

Table 4.5. Soil parameters for numerical parametric studies.

Parameter	Value
Compressibility index from the results in Chapter 3	
Totoyoura sand	0.04
CDG	0.15
Kaolin clay	0.33
Parameters for SWRC of CDG	
$m_1$ (Hossain and Yin, 2010)	0.42
$\alpha$ (SI unit: Pa <sup>-1</sup> ) (Hossain and Yin, 2010)	0.3
$l$	0.5
$\theta_s$	0.324
$\theta_r$ (Hossain and Yin, 2010)	0.195
$K$ (SI unit: m <sup>-2</sup> )	$1 \cdot 10^{-13}$
$c^w$ (SI unit: Pa <sup>-1</sup> ) (Kell, 1970)	$4 \cdot 10^{-10}$
$\beta$ (Grant and Salehzadeh, 1996)	-400
$m_2$ (Ghavam-Nasiri et al., 2019)	1.1

Table 4.6. Numerical program for parametric studies at saturated condition (90 cases in total).

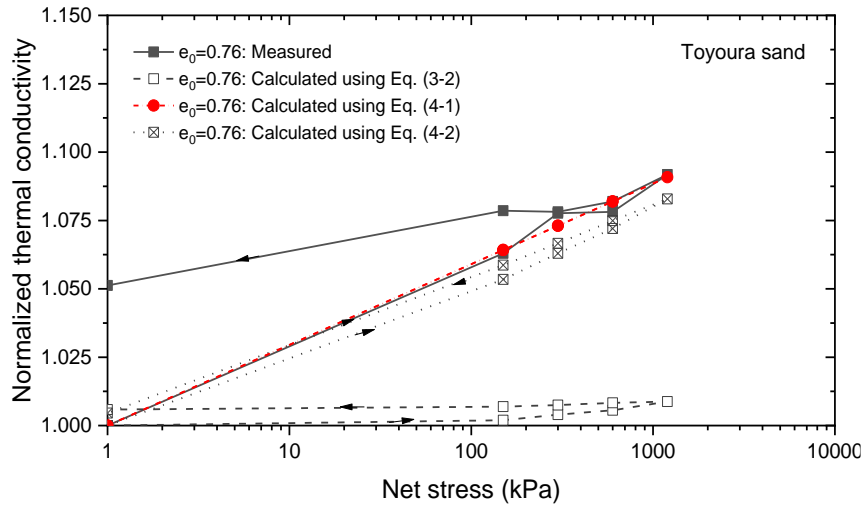
Series ID	Soil type*	Considering stress effects	Flow rate ( $\text{m}^3 \cdot \text{min}^{-1}$ )	Inlet fluid temperature ( $^{\circ}\text{C}$ )	Pile diameter (m)	Pile aspect ratio
Sa-N	Sand	No				
Sa-Y	Sand	Yes				
Si-N	Silt (CDG)	No	$6 \cdot 10^{-3}$	28	0.6, 0.9,	10, 30, 50
Si-Y	Silt (CDG)	Yes			1.2, 1.5	
Cl-N	Kaolin clay	No				
Cl-Y	Kaolin clay	Yes				
Cl-F1-N	Kaolin clay	No	$6 \cdot 10^{-4}$	28	0.6	10, 30, 50
Cl-F1-Y	Kaolin clay	Yes				
Cl-F2-N	Kaolin clay	No	$3 \cdot 10^{-2}$			
Cl-F2-Y	Kaolin clay	Yes				
Cl-T1-N	Kaolin clay	No	$6 \cdot 10^{-3}$	38	0.6	10, 30, 50
Cl-T2-Y	Kaolin clay	Yes				

Note: \*the initial void ratio of the sand, silt and clay prior to the application of stress are 0.76, 0.63 and 1.93, respectively.

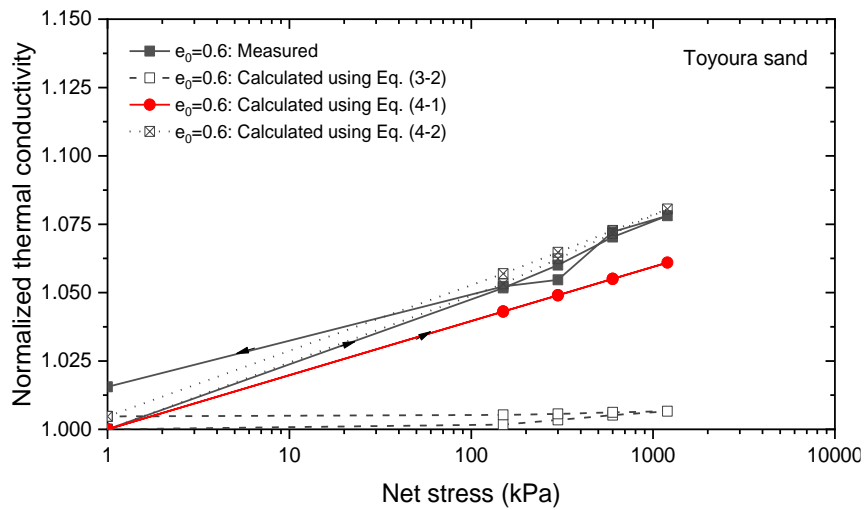
Table 4.7. Numerical program for parametric studies at unsaturated condition. (6 cases in total)

Series ID	Soil type*	Considering stress effects	Depth of water table (m)
Si -W1-N	Silt (CDG)	No	6
Si -W1-Y	Silt (CDG)	Yes	
Si -W2-N	Silt (CDG)	No	12
Si -W2-Y	Silt (CDG)	Yes	
Si -W3-N	Silt (CDG)	No	18
Si -W3-Y	Silt (CDG)	Yes	

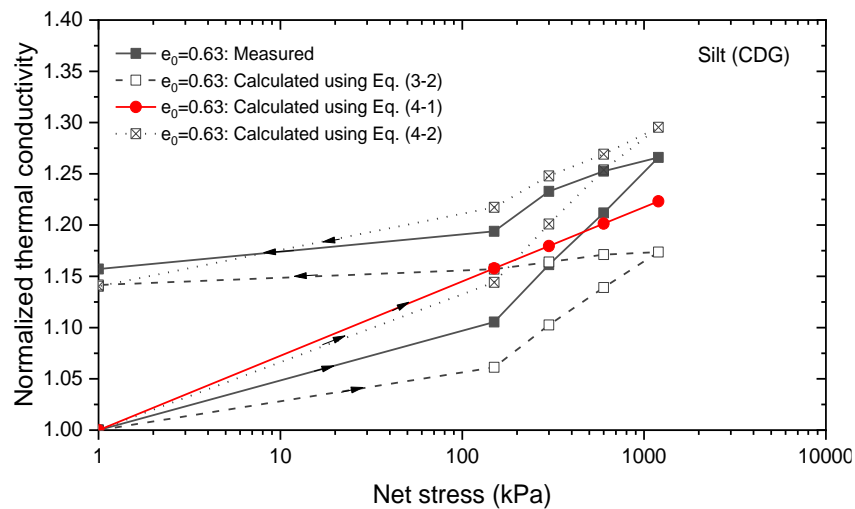
Note: \*the initial void ratio of silt is 0.63; pile diameter and aspect ratio are 0.6 m and 30 respectively; inlet fluid temperature is 28°C; pipe flow rate is  $6 \cdot 10^{-3} \text{ m}^3 \cdot \text{min}^{-1}$ .



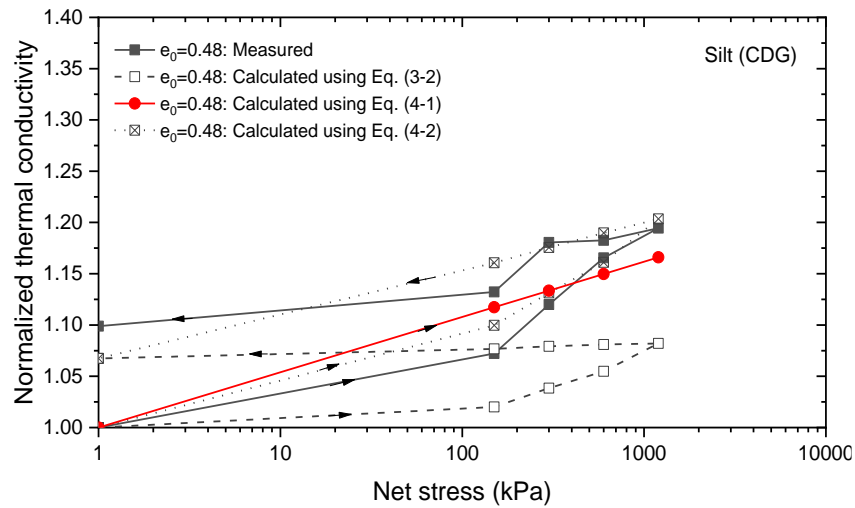
(a)



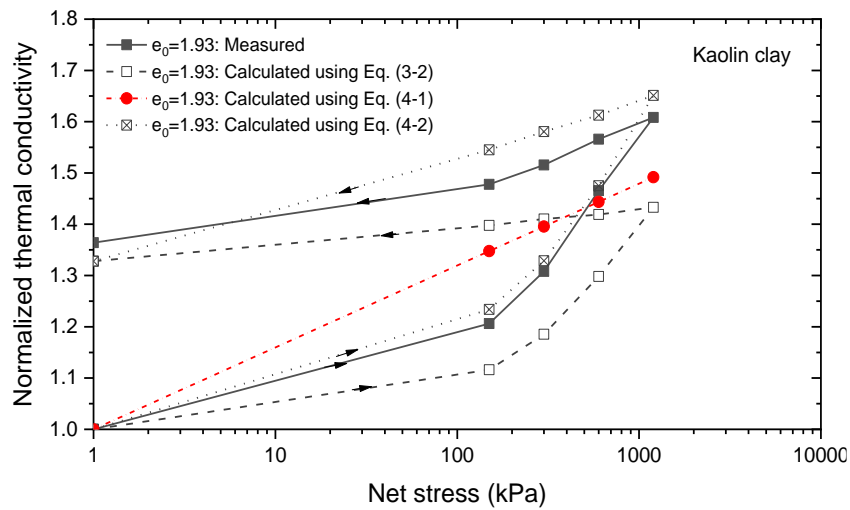
(b)



(c)



(d)



(e)

Figure 4.1. Comparisons between measured and calculated thermal conductivities of saturated soils: (a) Toyoura sand with initial void ratio of 0.76; (b) Toyoura sand with initial void ratio of 0.6; (c) CDG with initial void ratio of 0.63; (d) CDG with initial void ratio of 0.48; (e) Kaolin clay with initial void ratio of 1.93.

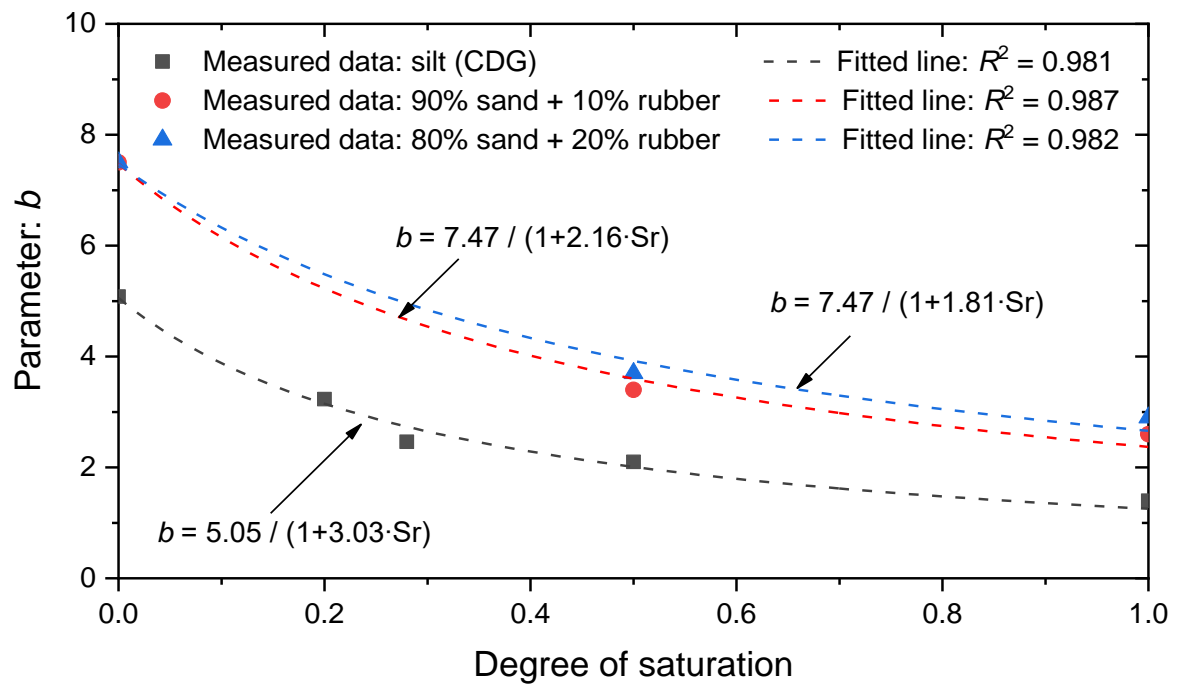


Figure 4.2. The relationship between parameter  $b$  and degree of saturation.

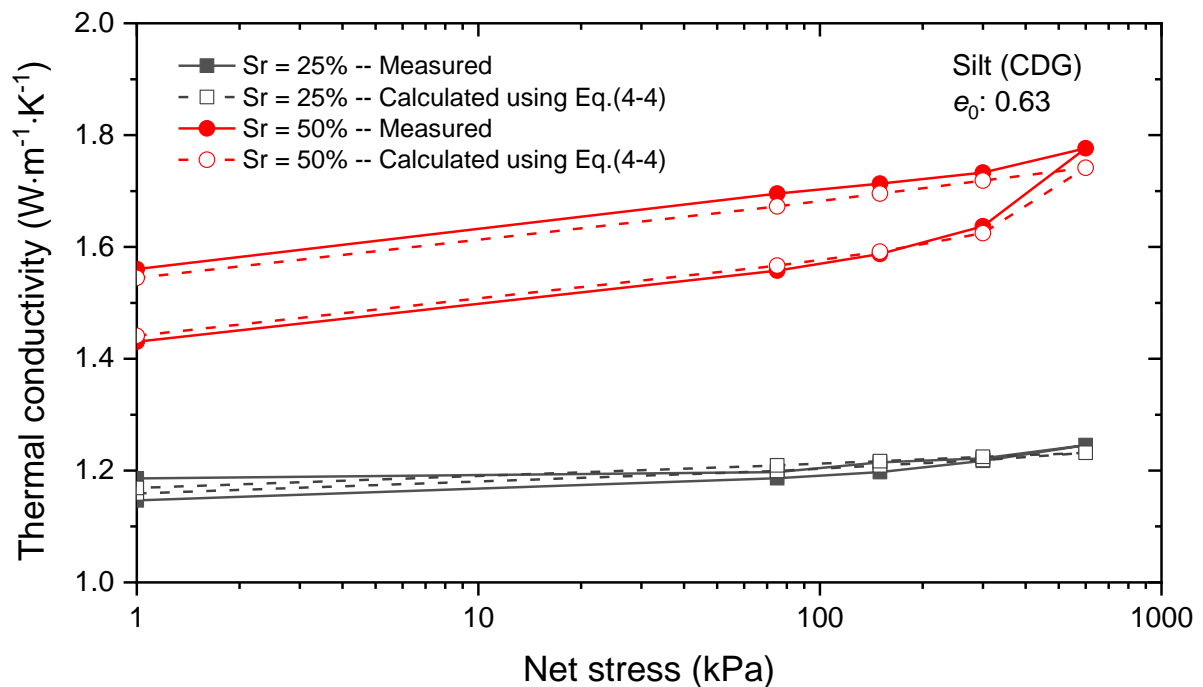


Figure 4.3. Comparisons between measured and calculated thermal conductivities of unsaturated CDG with initial void ratio of 0.63.

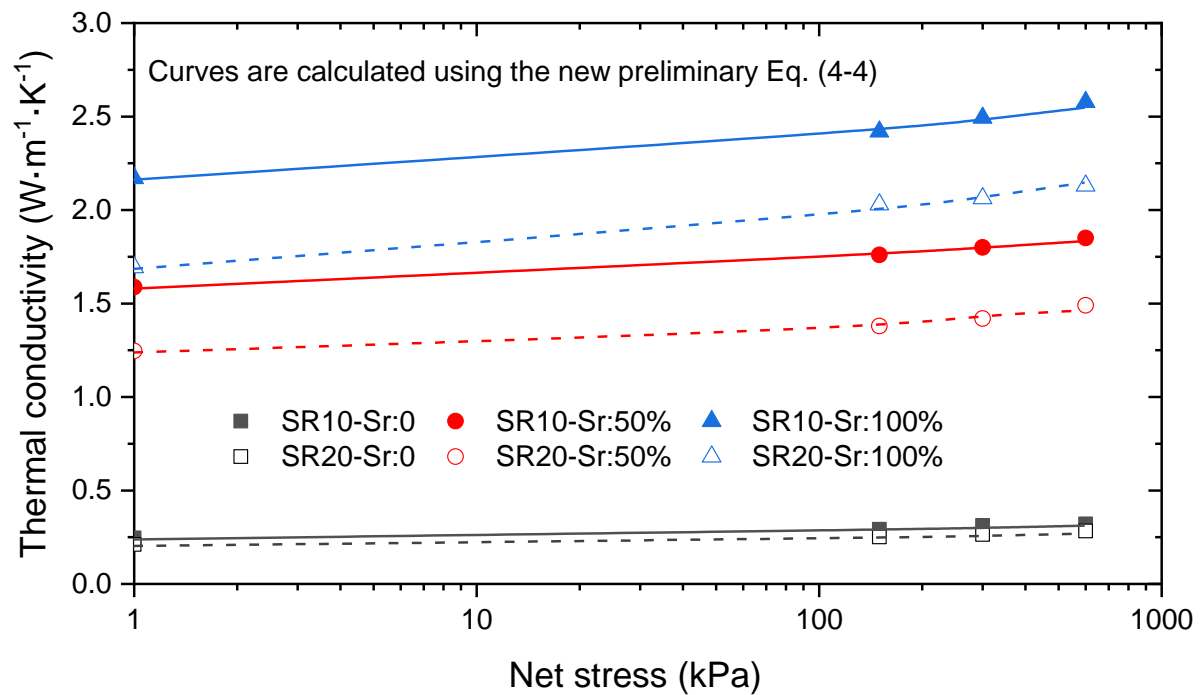


Figure 4.4. Comparisons between measured and calculated relations between thermal conductivity and net stress for saturated and unsaturated sand-rubber mixtures.

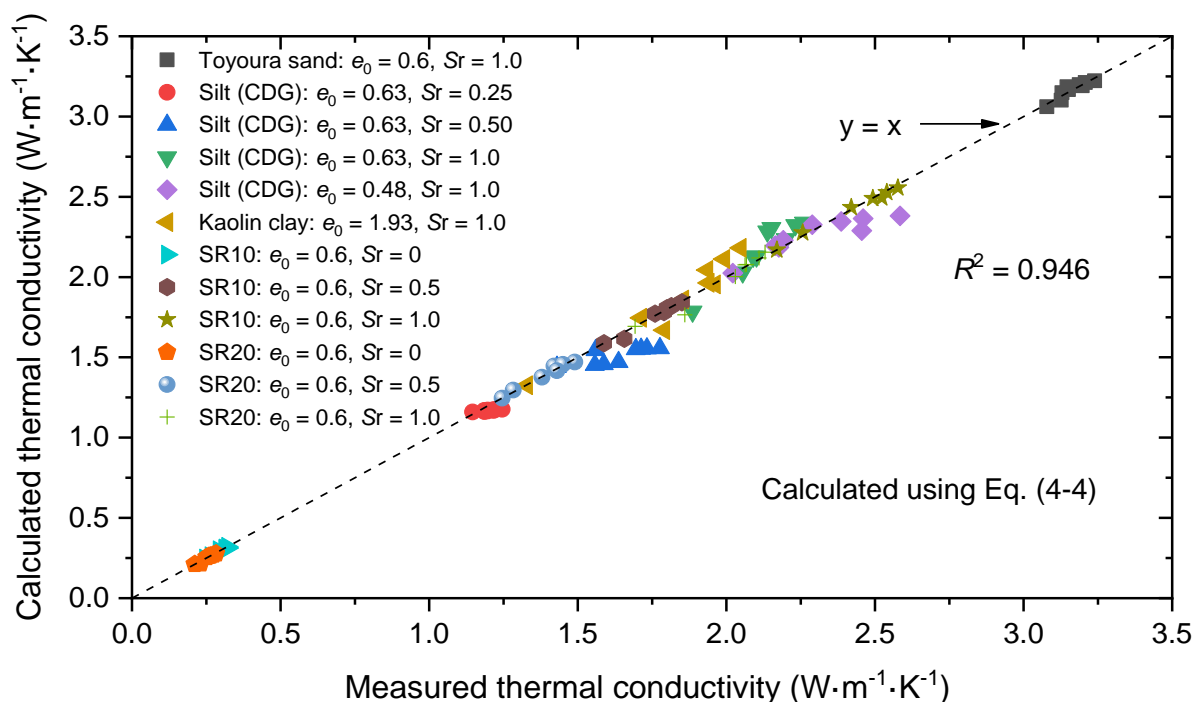


Figure 4.5. Comparison between measured and calculated thermal conductivities with considering coupled effects of stress, void ratio and degree of saturation.

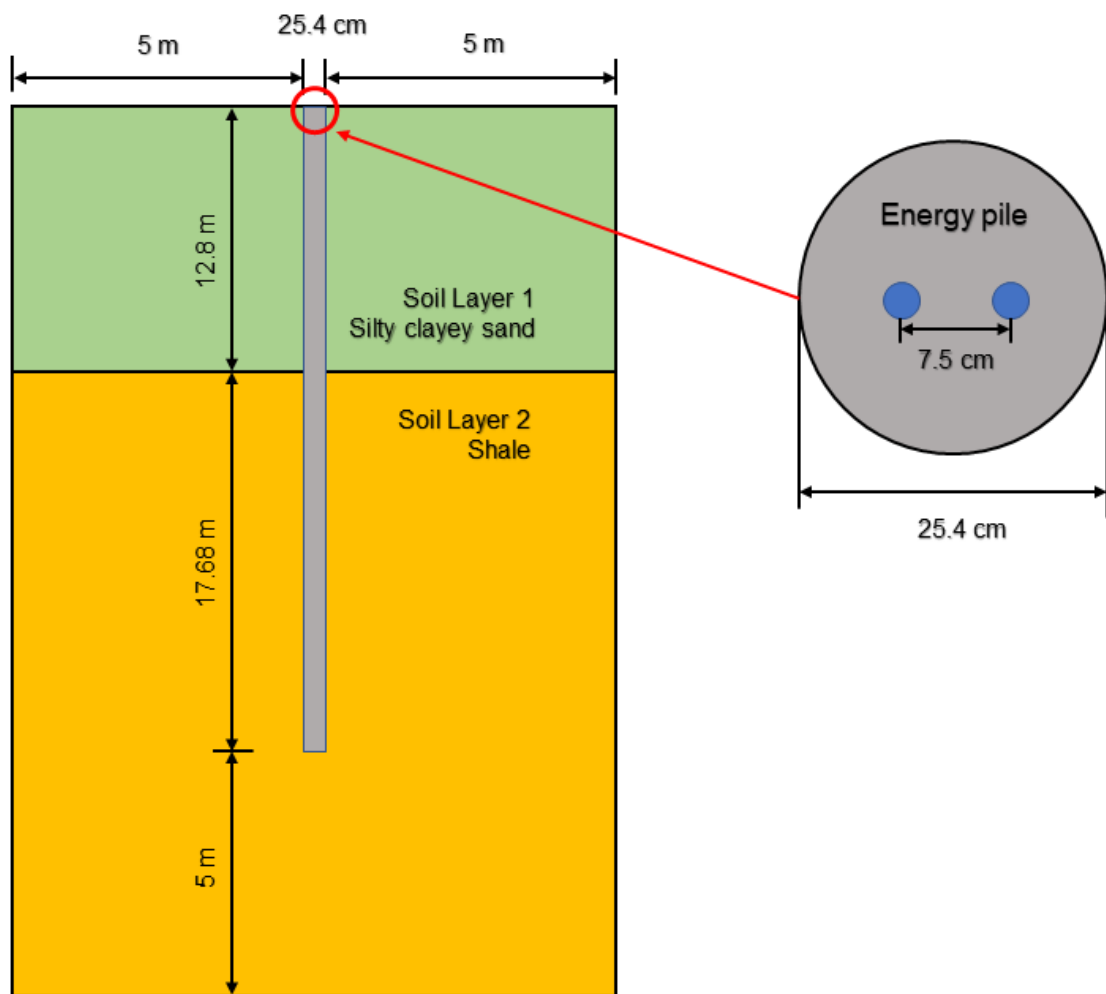


Figure 4.6. Model setup based on the Virginia Tech field test site (after Ozudogru et al. (2015)).

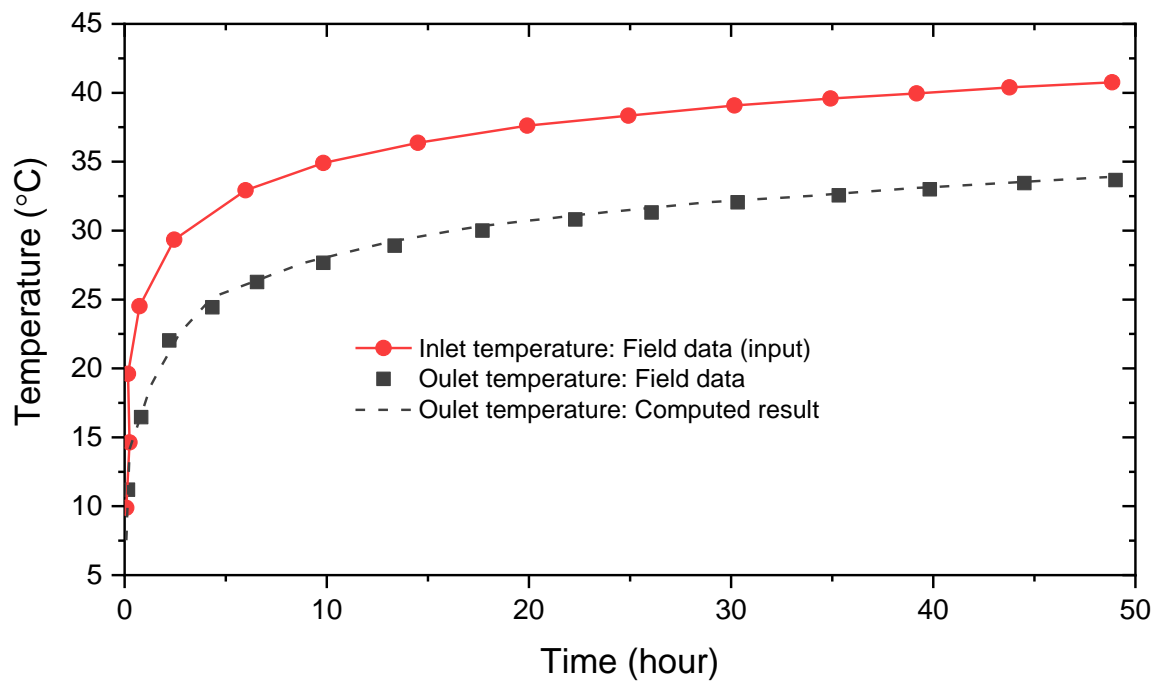


Figure 4.7. Comparison between computed and measured results.

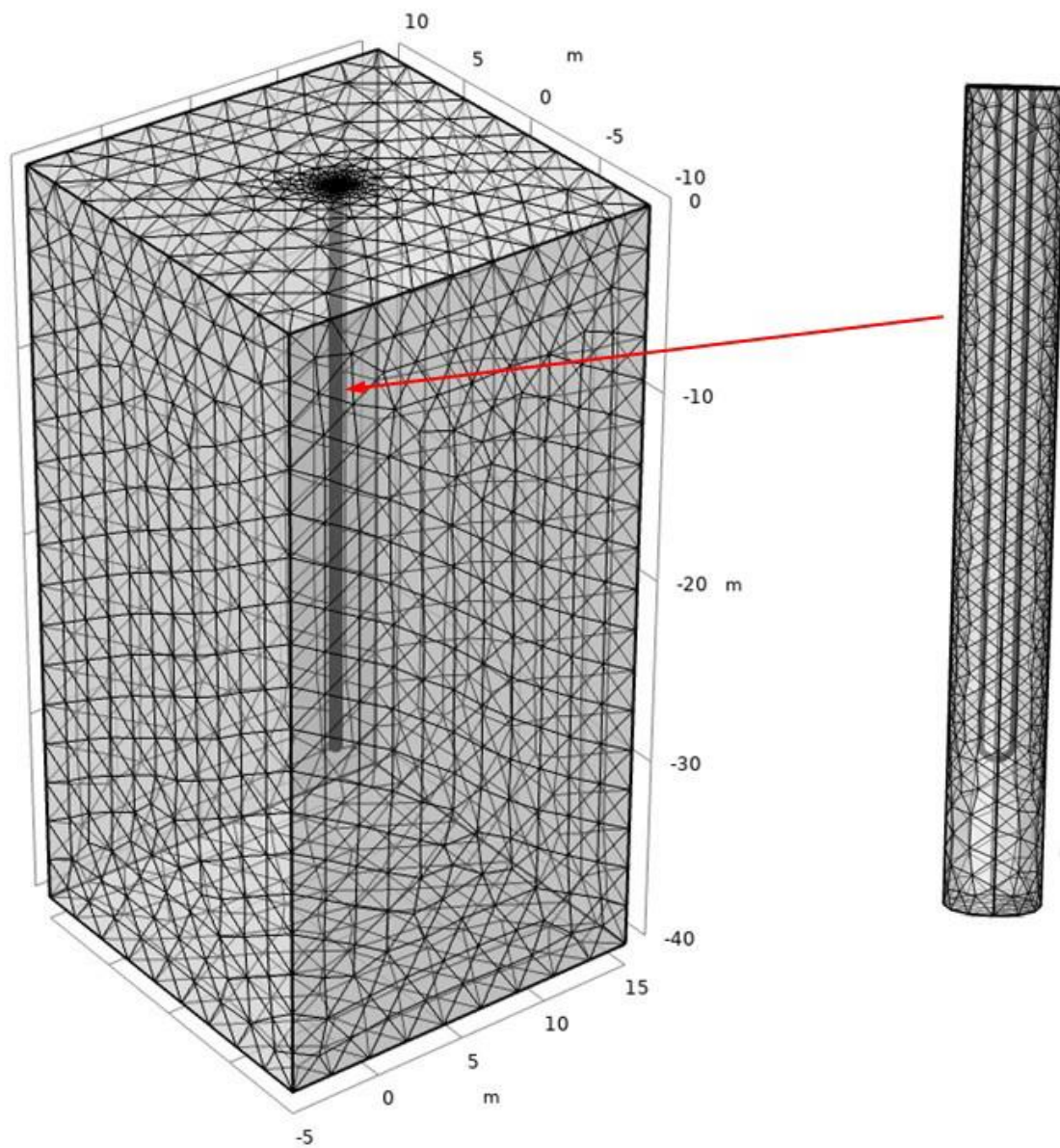


Figure 4.8. Finite element mesh of the numerical model for parametric studies.

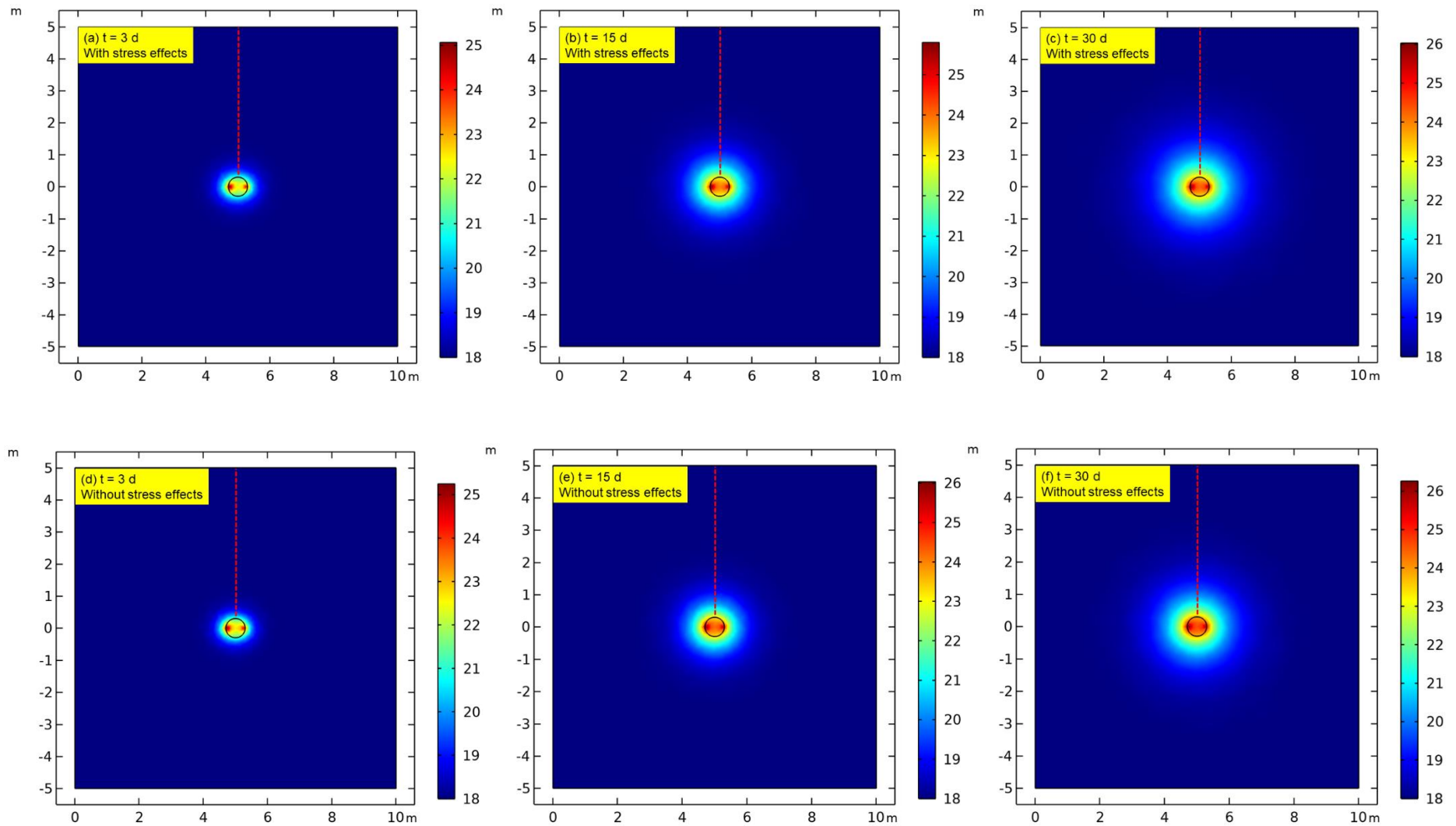


Figure 4.9. Temperature distribution in the horizontal direction at the mid-height of pile (unit: °C).

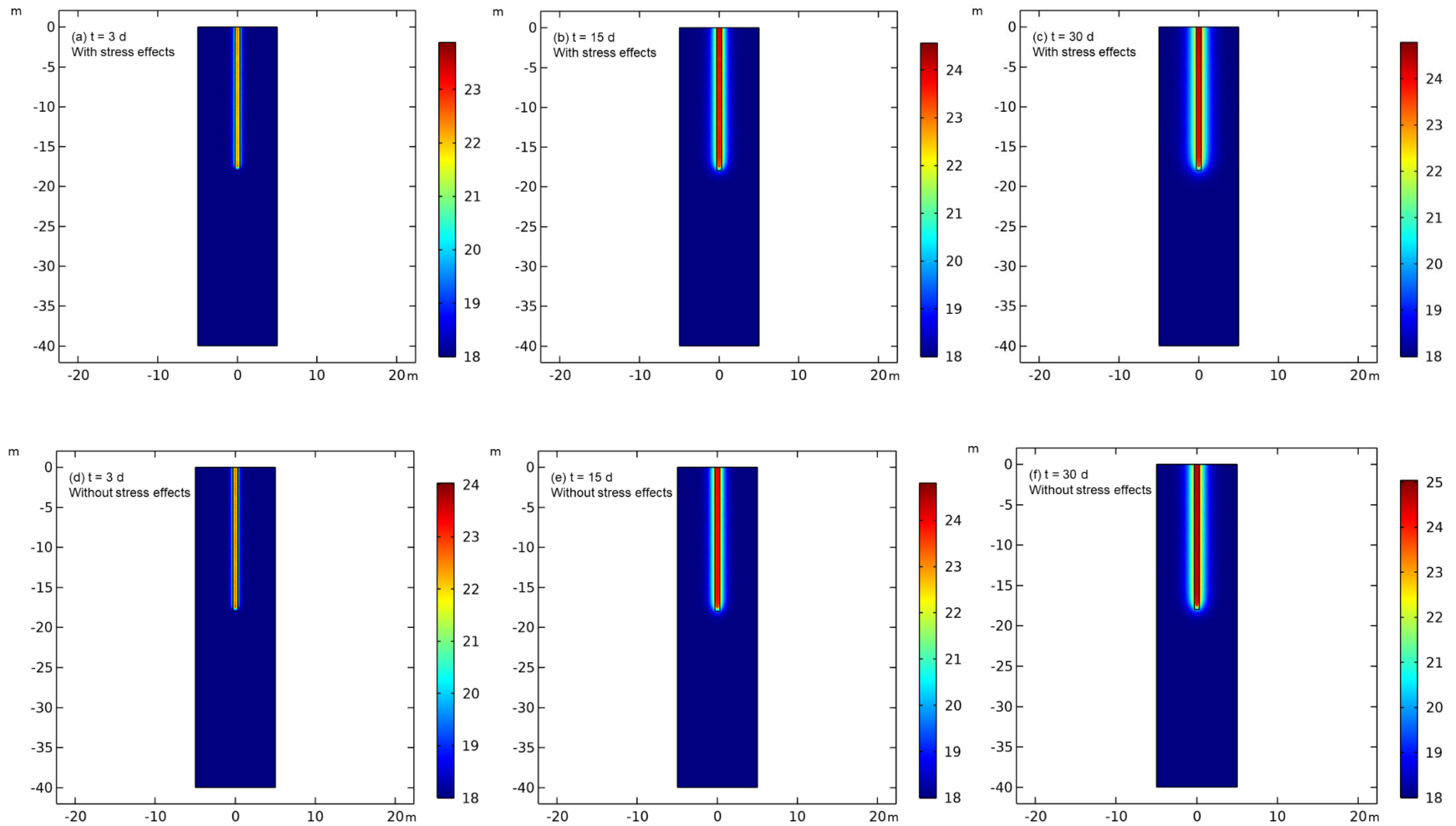


Figure 4.10. Contour of temperature during heating (pile diameter: 0.9 m; pile aspect ratio: 30; soil: kaolin clay; unit: °C).

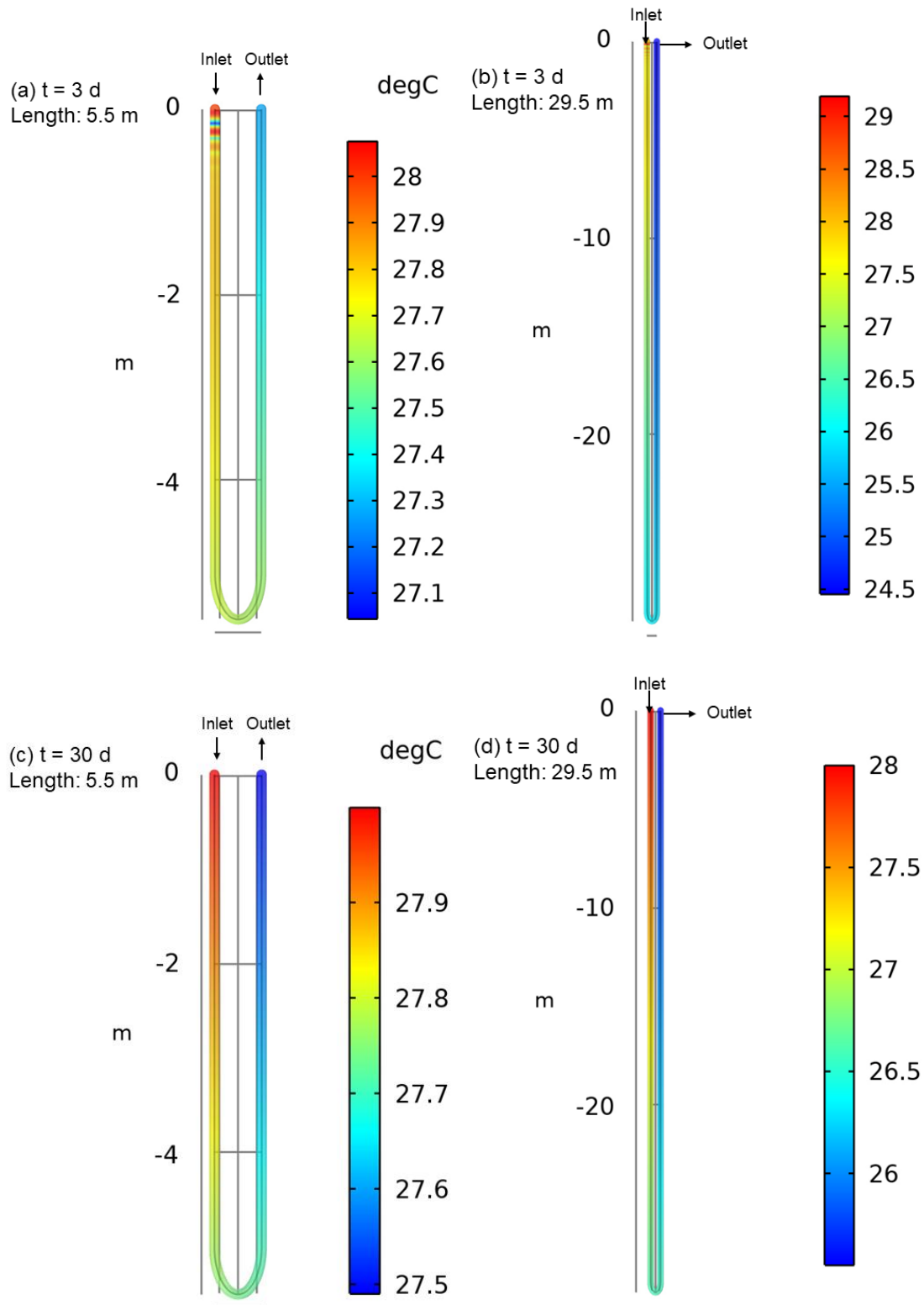
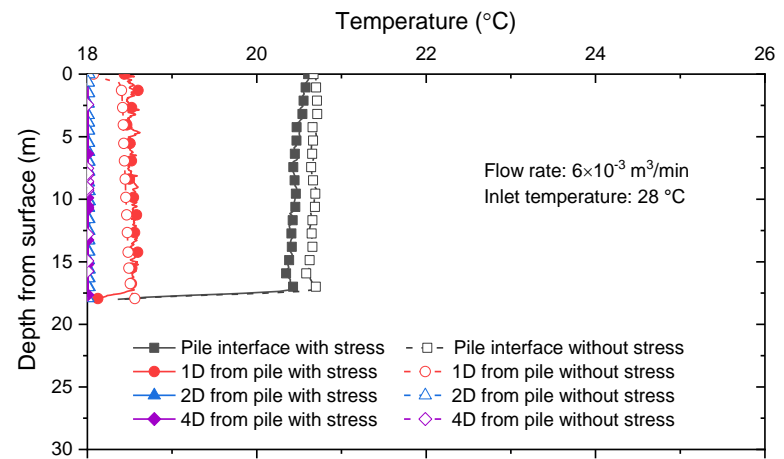
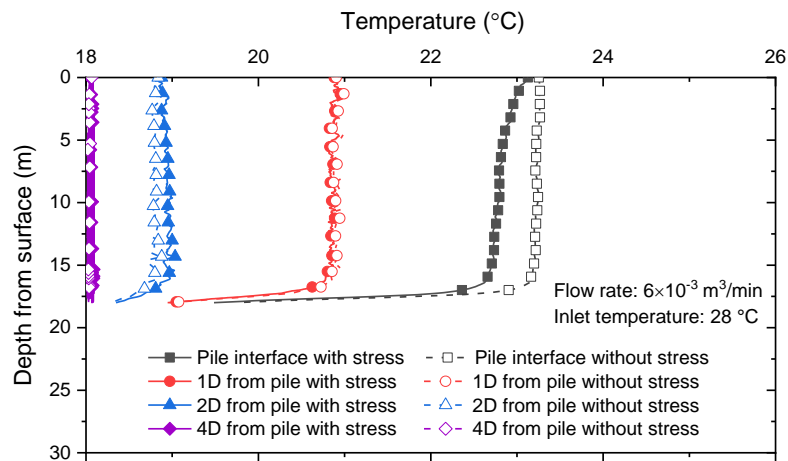


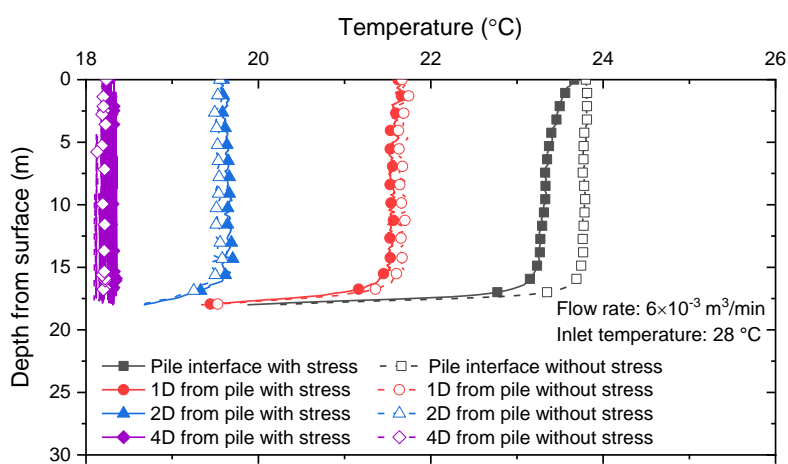
Figure 4.11. Typical contour of temperature inside pipe (pile diameter: 0.6 m; soil: kaolin clay): (a) (c) pile aspect: 10; (b) (d) pile aspect: 50.



(a)



(b)



(c)

Figure 4.12. Temperature distribution at different distances from the pile surface (pile diameter: 0.6 m; pile aspect ratio: 30; soil: kaolin clay): (a) 3 days; (b) 15 days; (c) 30 days.

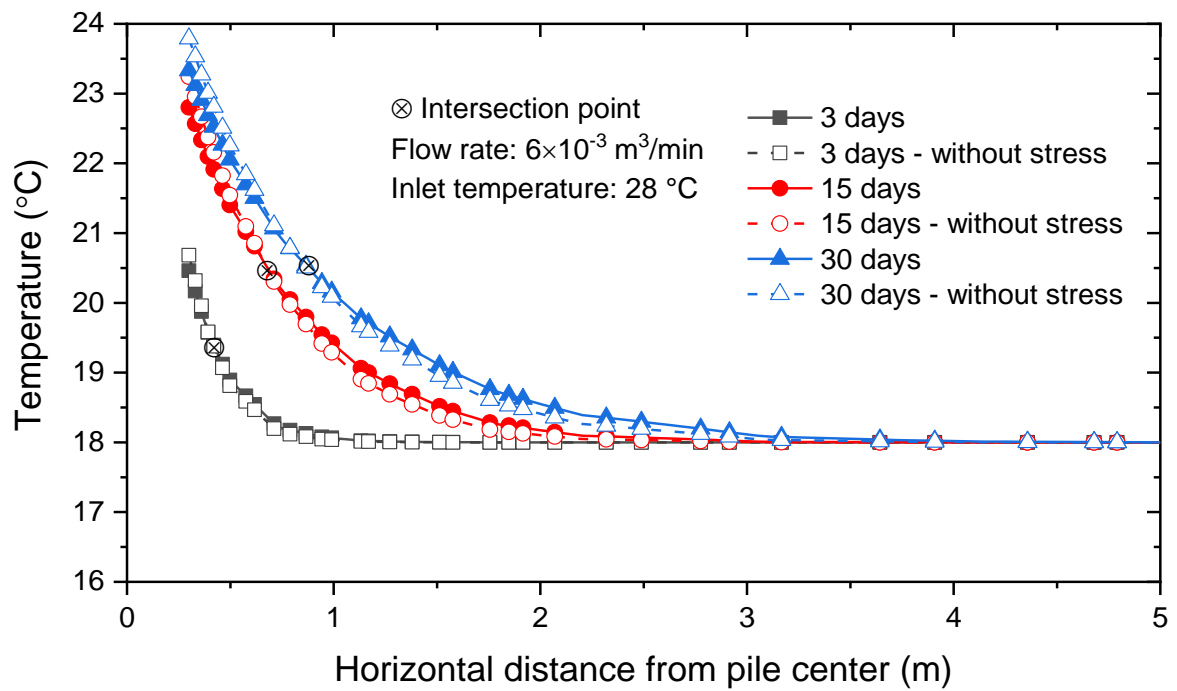
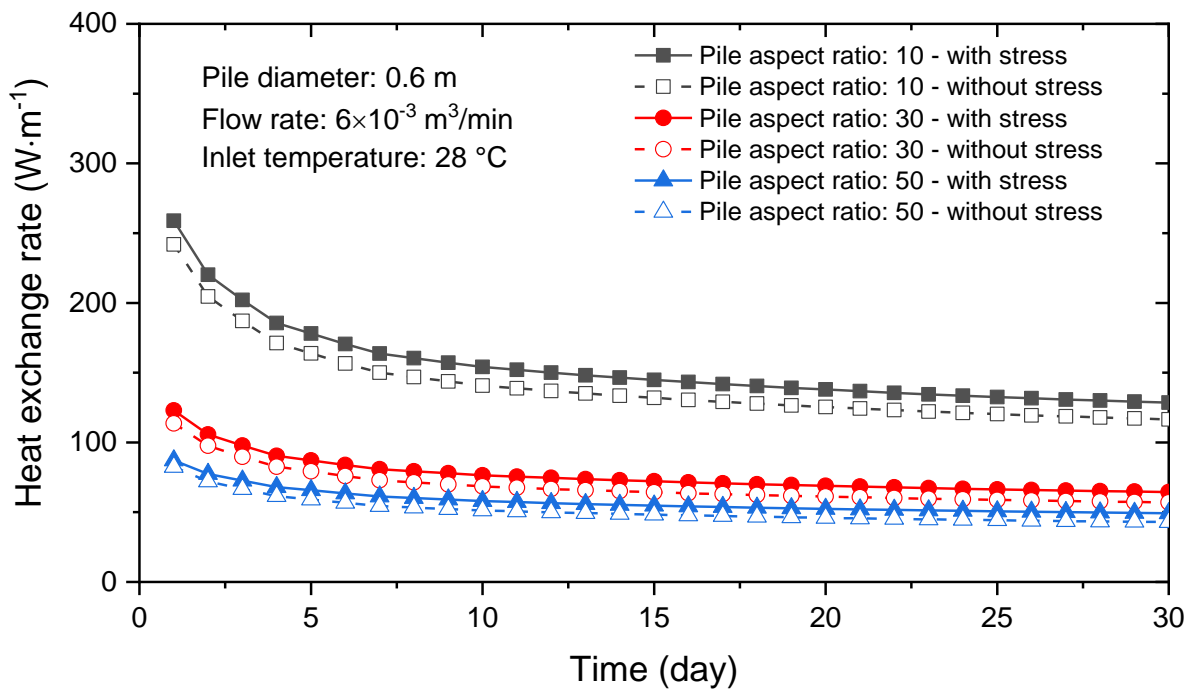
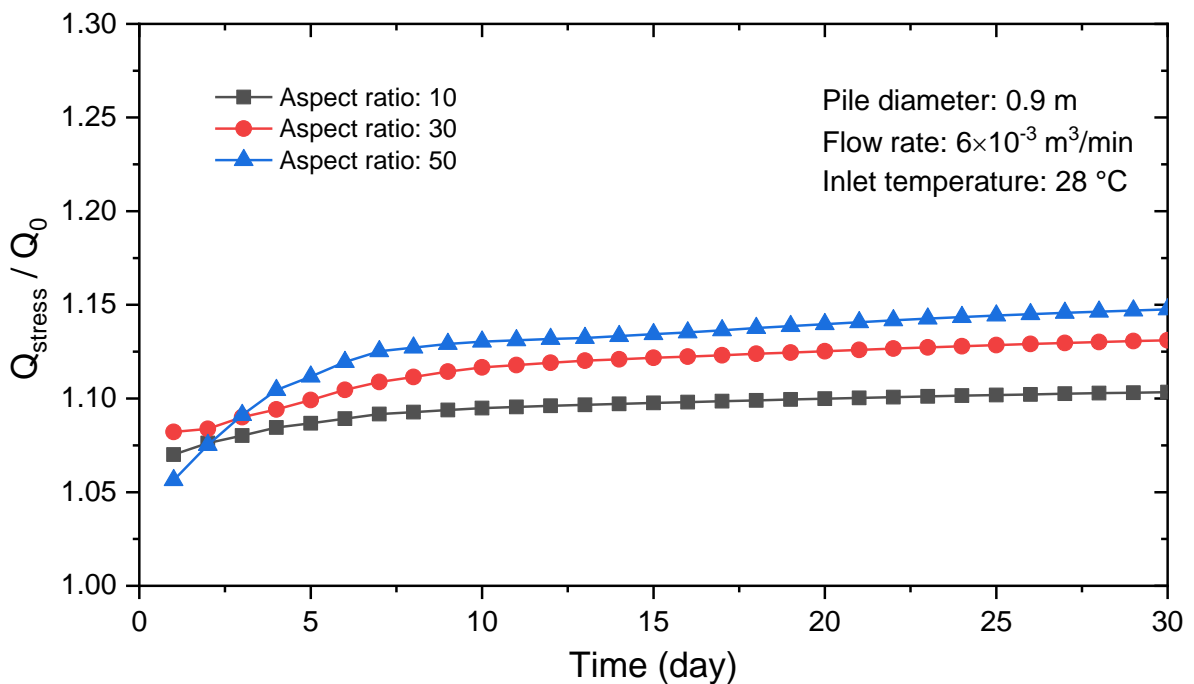


Figure 4.13. Typical temperature distribution in the horizontal direction at the mid-height of pile (pile diameter: 0.6 m; pile aspect ratio: 30; soil: kaolin clay).

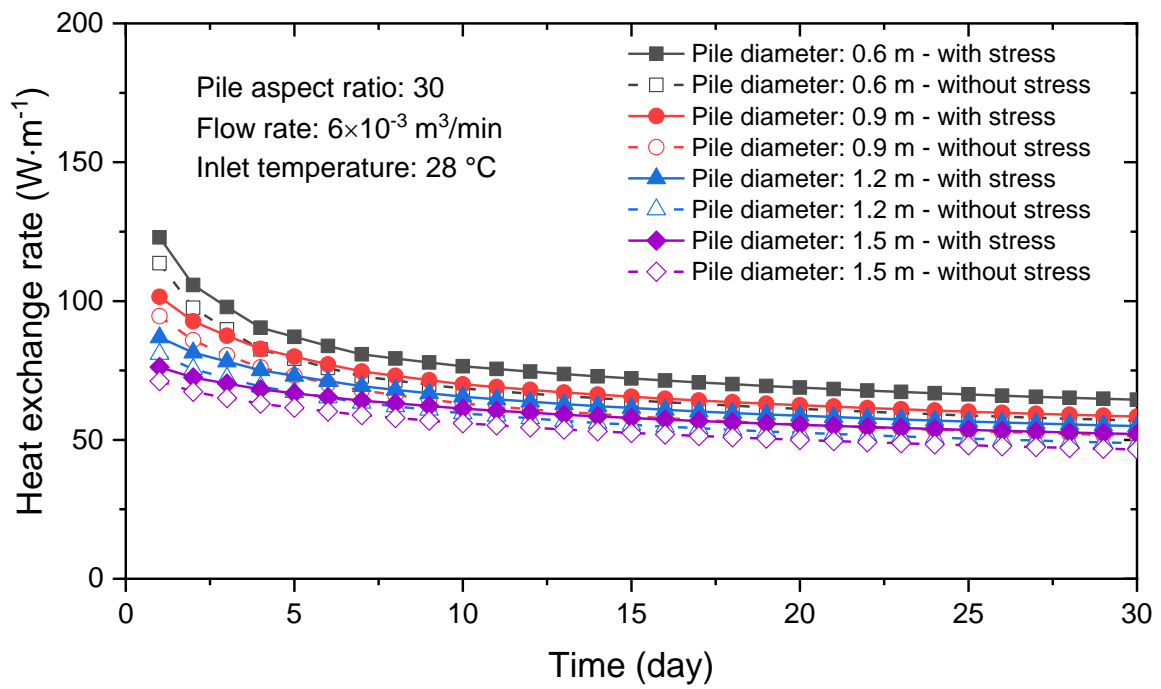


(a)

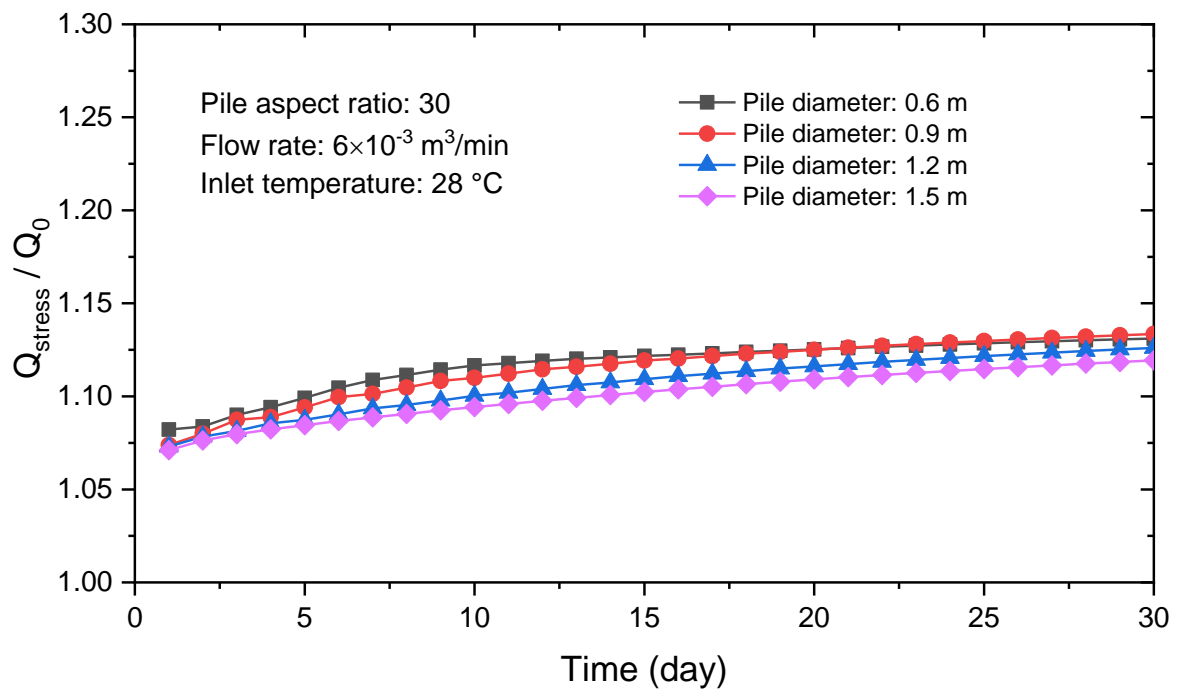


(b)

Figure 4.14. Coupled effects of stress and aspect ratio on heat exchange rate at a typical condition (pile diameter: 0.6 m; soil: kaolin clay): (a) heat exchange rates with and without stress effects; (b) heat exchange rate with stress effects  $Q_{stress}$  over that without stress effects  $Q_0$ .

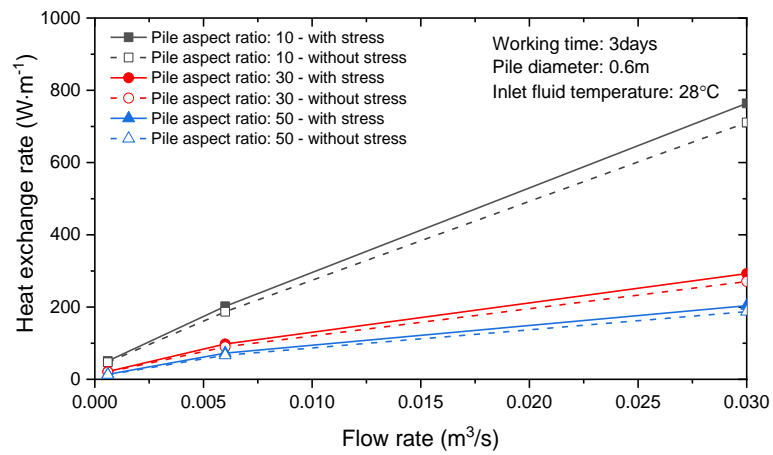


(a)

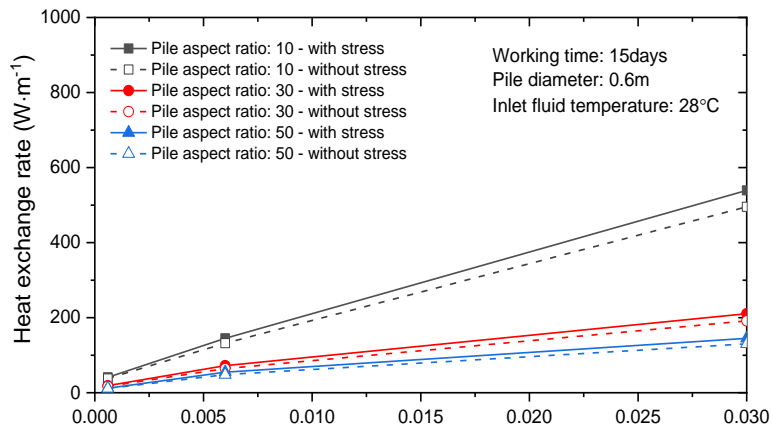


(b)

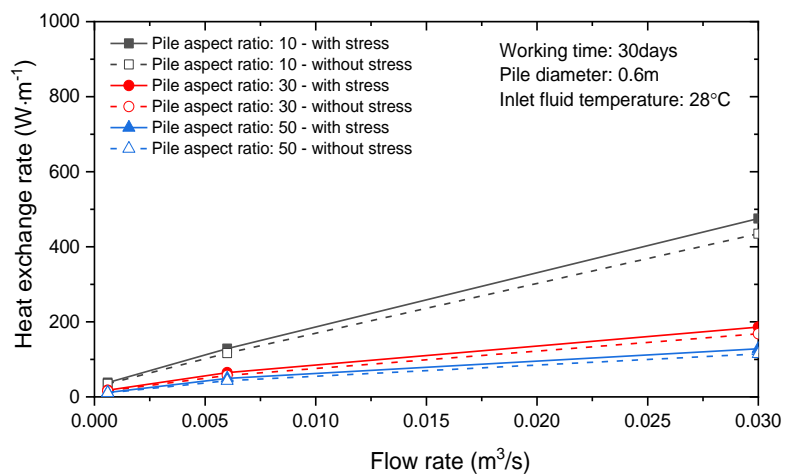
Figure 4.15. Coupled effects of stress and pile diameter on the heat exchange rate at a typical condition (pile aspect ratio: 30; soil: kaolin clay): (a) heat exchange rates with and without stress effects; (b) the ratio  $Q_{stress}/Q_0$ .



(a)



(b)



(c)

Figure 4.16. Heat exchange rate at different flow rate conditions: (a) 3 days; (b) 15 days; (c) 30 days.

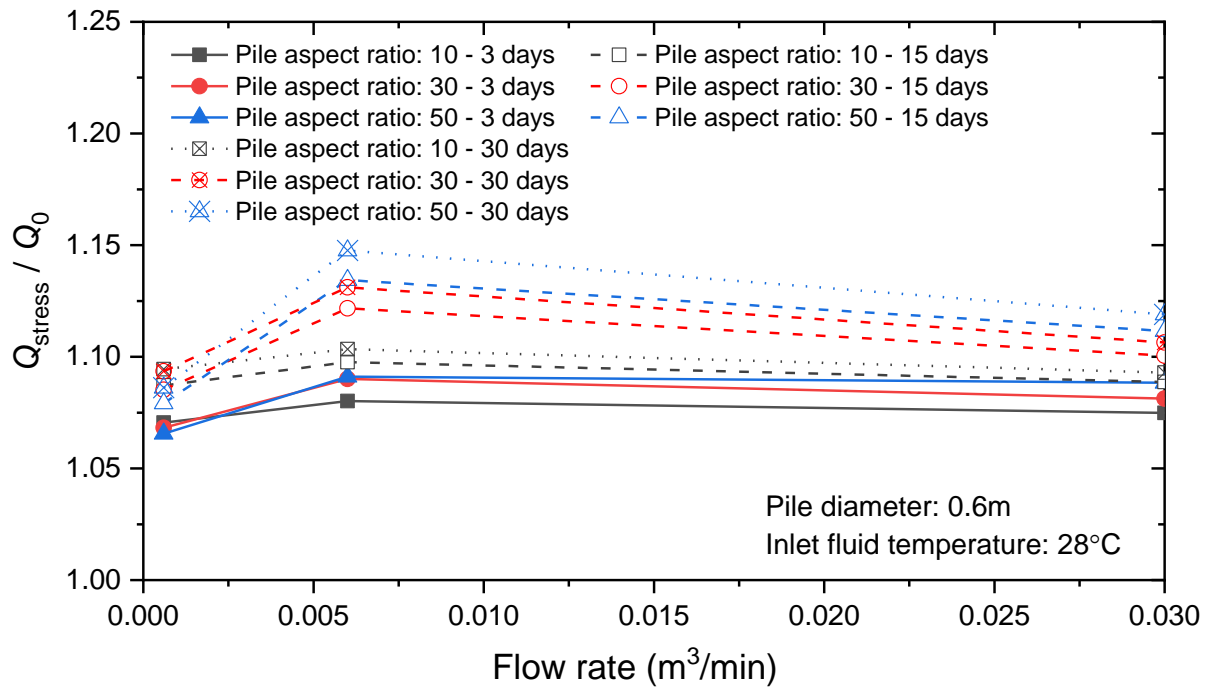


Figure 4.17. Coupled effects of stress and pile aspect ratio on the heat exchange rate at different flow rate conditions.

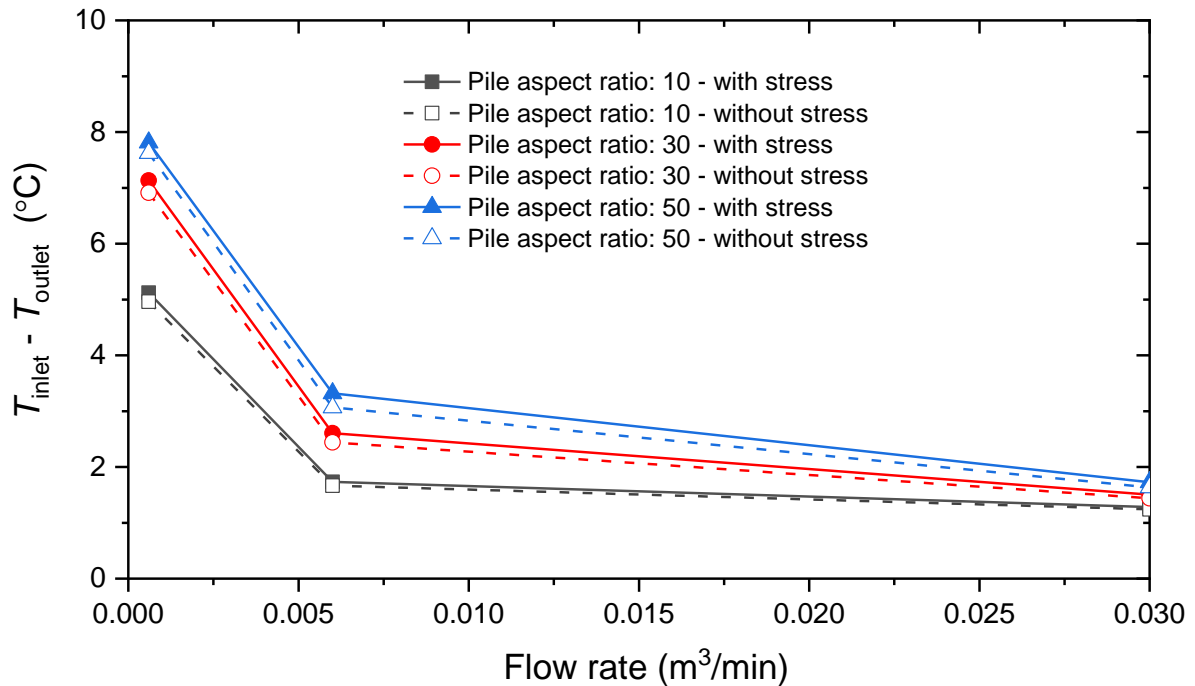
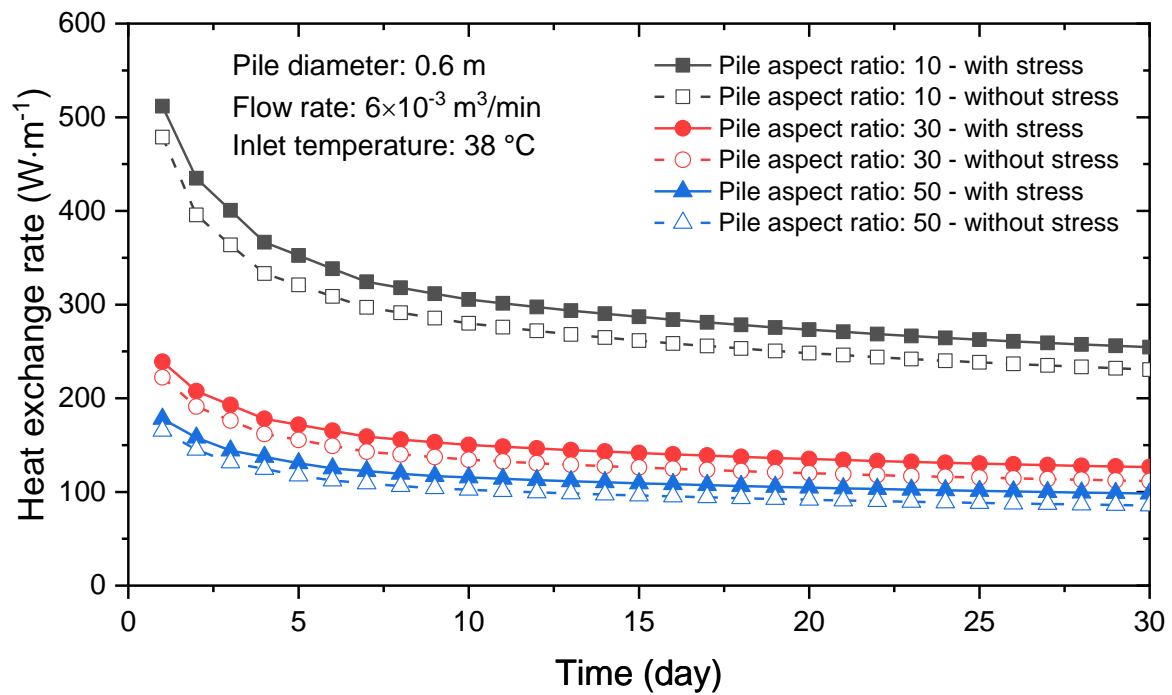
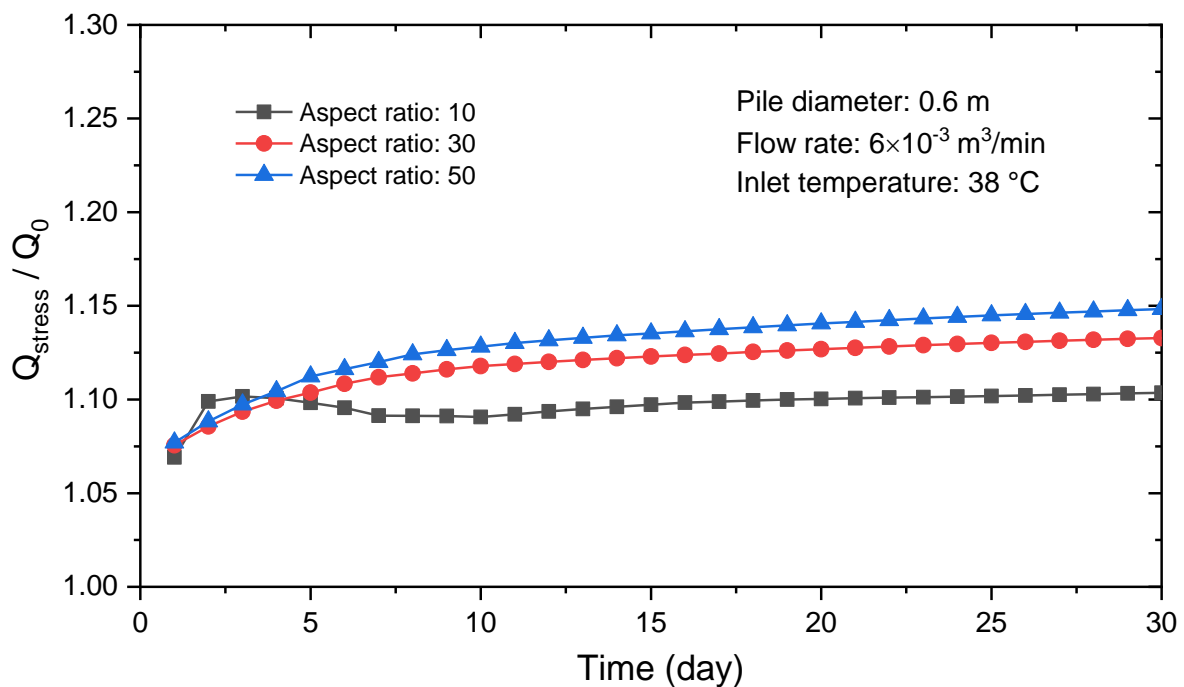


Figure 4.18. Effects of flow rate on the difference between inlet and outlet temperatures.



(a)



(b)

Figure 4.19. Effects of stress on the heat exchange rate with inlet fluid temperatures of 38°C: (a) heat exchange rates with and without stress effects; (b) the ratio  $Q_{stress}/Q_0$ .

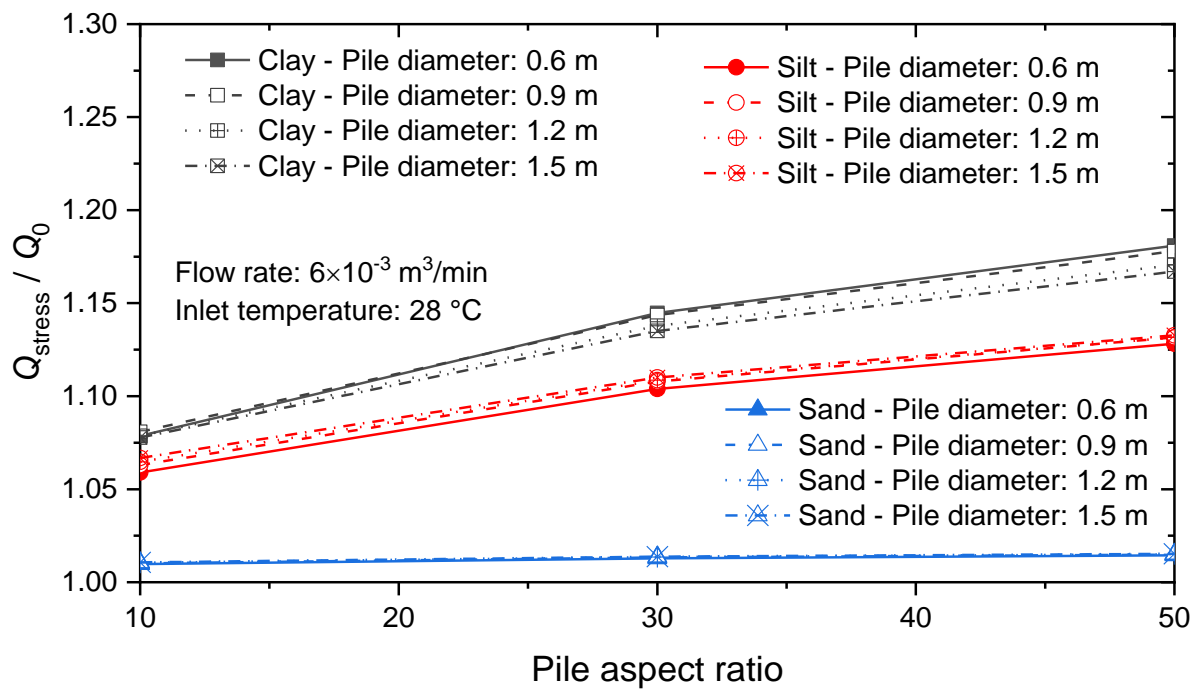
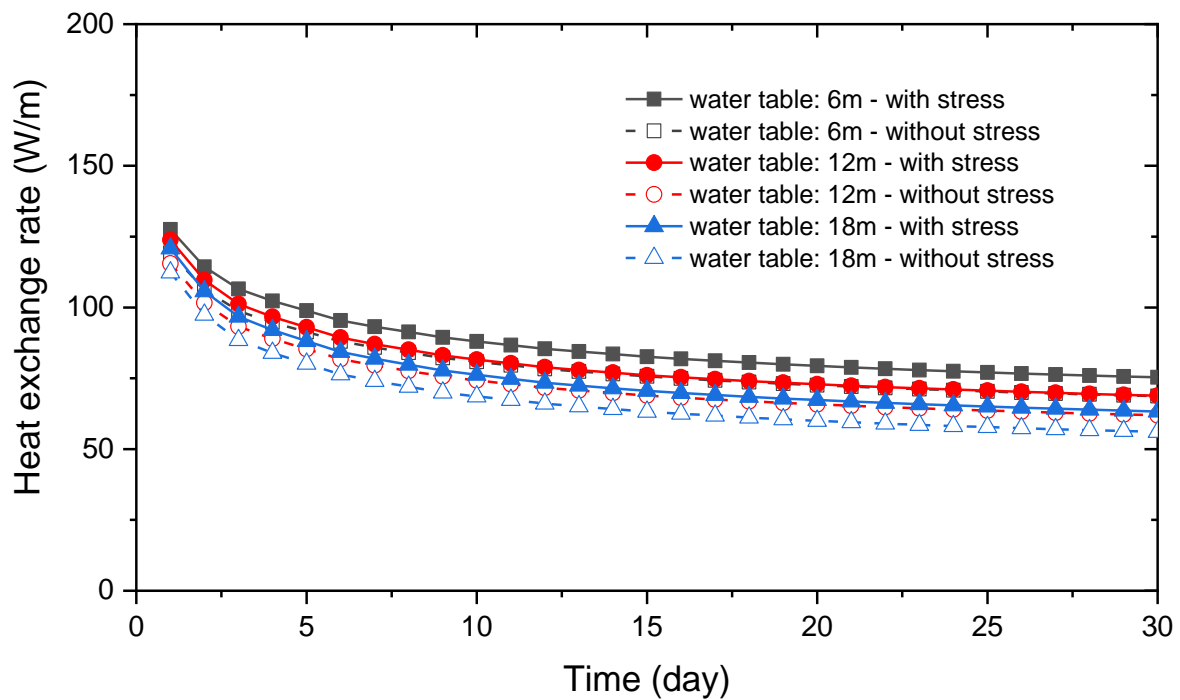
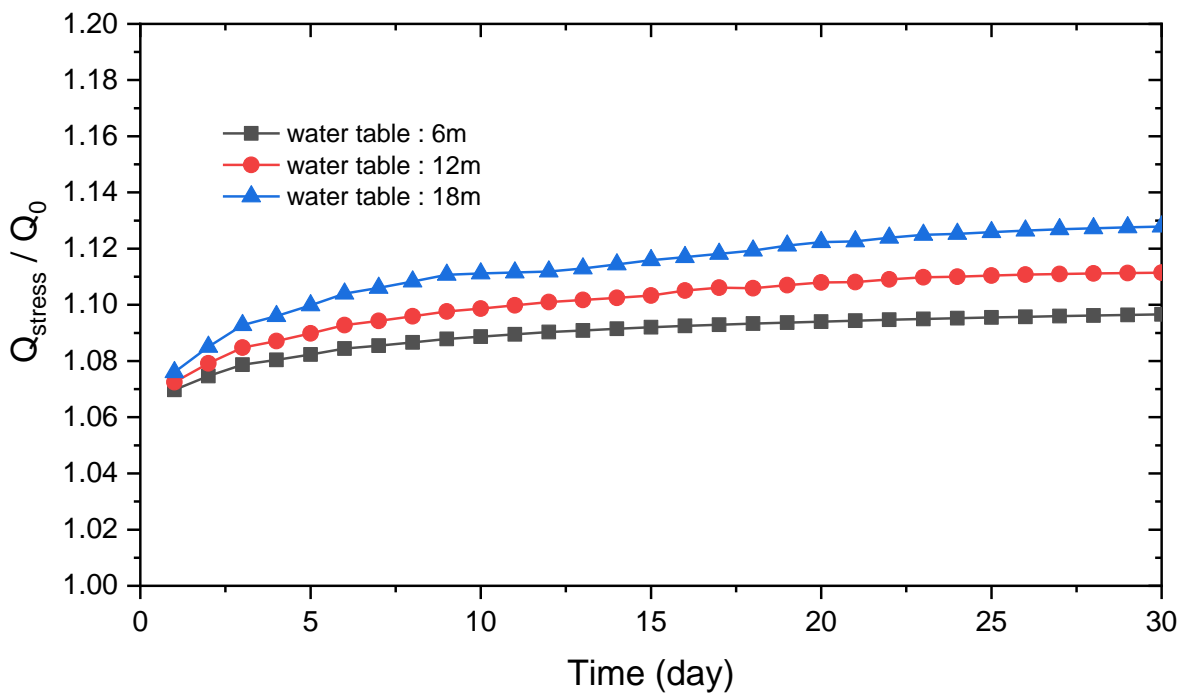


Figure 4.20. Stress effects on the heat exchange rate for piles in different soils considering typical pile diameters and aspect ratios.



(a)



(b)

Figure 4.21. Effects of water table locations on the heat exchange rate: (a) heat exchange rates with and without stress effects; (b) the ratio  $Q_{stress}/Q_0$ .

## **CHAPTER 5: Coupled Effects of Temperature and Suction on the Shear Behaviour of Interfaces**

In this chapter, a new temperature- and suction-controlled direct shear apparatus was described, which permits not only displacement control but also force control loading modes. It was used to study the thermo-mechanical behaviour of a CDG-structure interface under saturated and unsaturated conditions through two different types of tests. The first one is constant-temperature direct shearing using the displacement control loading mode, while the other one is constant-stress heating-cooling with the force control loading mode. Comprehensive tests were conducted at various temperatures (8, 20 and 42 °C), net normal stresses (25, 50, 100, 150 and 225 kPa) and suctions (0, 50 and 200 kPa). As far as the author is aware, this study is the first to investigate the coupled effects of temperature, stress and suction on the shear behaviour of unsaturated soil-structure interfaces. The unique data are useful for developing constitutive models for unsaturated soil-structure interfaces and analyzing the thermo-mechanical behaviour of energy piles. The test methods and results are discussed in detail in the following sections.

### **5.1 A new suction- and temperature-controlled apparatus for testing soil-structure interfaces**

Figures 5.1 and 5.2 shows the schematic diagram and photo of a new temperature- and suction-controlled direct shear apparatus for testing soil-structure interfaces, respectively. The upper part of the shear box accommodates a soil specimen with a surface area of 60 mm × 60 mm and a height of 20 mm, while its lower part contains a counterface with a surface area of

100 mm × 100 mm and a height of 20 mm. The dimension of the counterface is larger than that of the soil specimen so that their contact area can be kept constant during the shearing process. The normalized roughness  $R_n$  is widely used to quantify interface roughness, and one of its definitions was given by Uesugi and Kishida (1986):

$$R_n = \frac{R_{max}}{D_{50}} \quad (5-1)$$

where  $R_{max}$  is the maximum vertical distance between the highest and lowest peak on the surface along a profile equaling to the mean soil grain size ( $D_{50}$ ). In the current study, a stainless-steel plate manufactured by the Industry Centre of The Hong Kong Polytechnic University was used, with a  $R_{max}$  of 80 μm and a normalized roughness  $R_n$  of 1, because the tested soil has a  $D_{50}$  of 0.08 mm. Based on previous research (Yoshimi and Kishida, 1981), the value of  $R_{max}$  is within the typical range of pile surface roughness. Hence, the steel plate has reasonable roughness for simulating pile surfaces.

To control interface temperature, a refrigerated/heated circulating bath from *PolyScience* is used. The water bath is connected to channels in the lower shear box and then heated/cooled water is circulated. The interface can be heated/cooled through heat exchange with circulating water. Two trial tests were carried out to check the performance of the temperature-control system, with a temperature of 45 and 5 °C in the water bath, respectively. Two thermocouples were inserted inside the soil specimen. One was placed in the center and the other one was put in the boundary. As shown in Figure 5.3, the temperatures measured by the two thermocouples are almost identical at the equilibrium state. The maximum difference is less than 0.2 °C, demonstrating homogeneous temperature distribution in the specimen.

Additionally, the temperatures in the soil and water bath are different by about 3 °C because of heat loss.

Matric suction of the soil specimen, which is defined as the difference between pore air and water pressures, is controlled via the axis-translation technique (Hilf, 1956). Pore air pressure is imposed through the air pressure in the chamber, and pore water pressure is controlled through a ceramic disk with an air-entry value of 3 bars.

During a test, the vertical load is controlled by dead weight, while the shear load is provided by a motor. A load cell from *Applied Measurement* (capacities: 0-2.45 kN; accuracy: 0.001 kN) is connected to the upper shear box through a loading ram to measure the shear load. Two linear variable differential transformers (LVDTs) manufactured by *VJ Tech* are used to measure both horizontal and vertical displacements. Horizontal and vertical LVDTs have a stroke length of 50 (accuracy: 0.01 mm) and 5 mm (accuracy: 0.001 mm), respectively. All sensors are connected to the *Clisp Studio* software through the datalogger *MiniSCANNER 2* provided by *VJ Tech*.

Sensors were rigorously calibrated in this study. Particularly, the measurement of soil deformation during heating/cooling was affected by apparent deformation as a result of the thermal response of different equipment components. The apparent deformation was calibrated by conducting heating-cooling tests on a stainless-steel specimen with a linear thermal expansion coefficient of  $10.4 \times 10^{-6} \text{ } ^\circ\text{C}^{-1}$ . Calibration tests were also conducted to check the friction between the lower and upper shear boxes and that between the loading rod and chamber at different temperatures and air pressures in the chamber. The total friction is presented in

Figure 5.4, in which the shear stress is the measured shear force due to device friction divided by the interface area during a test with soil. When relative displacement is larger than 1 mm, shear stress is always small ( $0.75 \pm 0.5$  kPa) under different temperature and air pressure conditions.

## 5.2 Test soil and specimen preparation

CDG was tested in this work, whose particle size distribution is given in Figure 3.3 and the water retention curve (WRC) is shown in Figure 5.5. Consisting of 53% sand, 34% silt and 13% clay, the soil has a liquid limit of 31% and a plastic limit of 21% (Hossain and Yin, 2010). The maximum dry density and optimum water content are  $1.84 \text{ g/cm}^3$  and 13.4%, respectively. More detailed properties of the CDG are given in Table 5.1.

To prepare compacted specimens, the CDG was oven-dried at  $105 \text{ }^\circ\text{C}$  and then broken up with a rubber pestle. After that, the soil particles were passed through a 2 mm sieve, followed by a mix of the collected soil and distilled water to reach the optimum water content (i.e., 13.4%). The soil-water mixture was sieved through the 2 mm sieve again, and any remaining lumps were crushed with the rubber pestle. Next, the mixture was kept in a plastic bag for 24 hours to achieve uniform water distribution (Zhang et al., 2015). Following that, the prepared soil was statically compacted in the upper shear box by using a static compaction machine that can record the compaction pressure and control the compaction rate (i.e., 1 mm/min) during the process. The target dry density is  $1.748 \text{ g/cm}^3$  (corresponding to 95% degree of compaction) and the recorded compaction stress is 875 kPa. The initial void ratio and water content after specimen preparation are  $0.48 \pm 0.01$  and  $13.4 \pm 0.2\%$ , respectively. Notably, water loss

occurred during specimen preparation, and hence the final water content slightly deviated from the target value (less than 0.2%). After static compaction, all specimens were set up in the test chamber and immersed in the water. Then, the whole chamber was exposed to a vacuum of 10 kPa for 24 hours. It was found that this method could remove air bubbles inside the soil specimen and hence saturate it efficiently.

### **5.3 Test program and procedures**

#### **5.3.1 Constant-temperature direct shear tests**

For the constant-temperature direct shear tests using the displacement control loading mode, three series of temperature- and suction-controlled direct shear tests were conducted. Tests in series S1 were performed under fully saturated conditions at three different temperatures (8, 20 and 42 °C). Series S2 and S3 were designed for unsaturated interfaces at various suctions (50 and 200 kPa) and temperatures (20 and 42 °C). The temperature range was selected based on the working conditions of energy piles (Association, 2012). At each temperature and suction condition, three different net normal stresses (50, 100 and 150 kPa) were applied. Details of the test program are illustrated in Tables 5.2 and 5.3.

Figure 5.6(a) shows thermo-hydro-mechanical paths of soil-structure interfaces for the constant-temperature shear tests. Saturated tests in Tables 5.2 contain three stages: (i) applying the target normal stress to the specimen (A–B in the figure) and waiting for 24 hours for consolidation; (ii) applying thermal loadings to the specimen (B–C and B–D) and waiting for 12 hours to allow for the dissipation of thermally induced excess pore water; (iii) shearing the specimen at constant normal stress and temperature at a drained condition.

Unsaturated tests in Tables 5.3 have the following thermo-hydro-mechanical path: (i) imposing the predefined net normal stress (A–B) and waiting for 24 hours; (ii) applying the given air and water pressures to achieve the target suction equalization at room temperature (B–E and B–G); (iii) applying thermal loadings (E–F and G–H); (iv) shearing the specimen. In the second and third stages, suction equalization was considered to be reached when the variation of gravimetric water content was less than 0.05% per day (Sivakumar, 1993). The duration for achieving suction equilibrium was about two to three days in the second stage and two days in the third stage.

In addition, Gan and Fredlund (1994) studied the shear behaviour of unsaturated CDG and found that a shearing rate of 0.005 mm/min could ensure a drained condition. A slightly smaller shearing rate (0.004 mm/min) was consistently used in the above three series of tests to consider the potential influence of temperature on the water permeability of soil specimens.

### 5.3.2 Constant-stress heating and cooling tests

Seven series of constant-stress heating-cooling tests were conducted to study the effect of heating and cooling on the relative movement between soil and counterpart under constant shear stress, as summarized in Table 5.4. Tests in series S0N50 through S0N150 were performed at the fully saturated condition. Different stress conditions were considered, including three net normal stresses (50, 100 and 150 kPa) and two levels of shear stress ( $\tau/\tau_s=0.5$  or  $0.75$ ), where  $\tau$  is the applied shear stress and  $\tau_s$  is the shear strength obtained from constant-temperature shear tests at the same test conditions. Series S50n50, S50N100 and S200N100 were designed for unsaturated interfaces at two different suctions (i.e., 50 and 200

kPa) and two different net normal stresses (i.e., 50 and 100 kPa). At each test condition of suction, net normal stress and shear stress, the specimen is subjected to one thermal cycle as follows:  $25^{\circ}\text{C} \rightarrow 35^{\circ}\text{C} \rightarrow 45^{\circ}\text{C} \rightarrow 35^{\circ}\text{C} \rightarrow 25^{\circ}\text{C} \rightarrow 15^{\circ}\text{C} \rightarrow 5^{\circ}\text{C} \rightarrow 15^{\circ}\text{C} \rightarrow 25^{\circ}\text{C}$ .

Figure 5.6(b) presents the thermo-hydro-mechanical paths for the constant-stress heating and cooling tests. For the tests in series S0N50 through S0N150, three stages are included: (1) applying the target normal stress to the specimen for 24 hours (i.e., path A–B); (2) shearing the specimen to the desired shear stress at constant temperature (i.e., path B–C) for 12 hours; (3) controlling the temperature at the constant stress condition, including heating (path C–E and D–C) and cooling (path E–D). Each temperature stage was maintained for 12 hours for the temperature equilibrium.

For the unsaturated tests in S50n50, S50N100 and S200N100, their thermo-hydro-mechanical paths are very similar to that described above. The only difference is after consolidation (Step 1) but before shearing (Step 3), it is necessary to increase the suction to the predefined value (i.e., paths B<sub>1</sub>–B<sub>2</sub> and B<sub>1</sub>–B<sub>3</sub>). The suction was controlled using the axis-translation technique. The duration for achieving suction equilibrium is around three days. Another difference between saturated and unsaturated tests is that in the latter one, the heating/cooling process may alter soil suction. Therefore, each temperature stage was maintained for two days to ensure both thermal and suction equalization.

#### **5.4 Repeatability of the test results**

To assess the reproducibility of the test results, some tests were conducted twice, as shown in Tables 5.2 and 5.3. It can be seen from Figure 5.7(a) that the shear stress-horizontal

displacement relations at the same test condition almost coincide with each other. The shearing-induced vertical displacement shown in Figure 5.7(b) indicates that the deformations under the same conditions of temperature, normal stress and suction are also identical. These findings confirm the good reproductivity of the test results.

## **5.5 Interpretations of constant-temperature shear test results**

### **5.5.1 Thermally induced soil deformation before shearing**

Figure 5.8(a) displays the thermally induced volume change behaviour of saturated and unsaturated CDG specimens before shearing. In Figure 5.8(a), for all saturated specimens, contractive deformation was observed during cooling from room temperature to 8 °C because of elastic deformation. During heating from room temperature to 42 °C, the specimens under net normal stress of 25 and 50 kPa were observed to have a slight expansion of 0.06% and 0.03%, respectively, while others contracted by about 0.15%. Heating-induced deformation is closely related to soil specimens' over-consolidation ratio (OCR). The preconsolidation pressure of the specimens used in this study is around 75 kPa after static compaction and saturation, determined using the method of Casagrande (1936). This preconsolidation pressure is much less than the compaction pressure of 875 kPa, mainly because the preconsolidation pressure reduces greatly upon saturation (Alonso et al., 1990). The specimens under 25 and 50 kPa were overconsolidated ( $OCR = 3$  and  $1.5$ , respectively), while others were normally consolidated ( $OCR = 1$ ). According to previous studies (Demars and Charles, 1982; Plum and Esrig, 1969; Cekerevac and Laloui, 2004), the specimens at normally and over-consolidated

conditions generally show plastic contraction and elastic expansion during heating, respectively.

In Figure 5.8(b), all unsaturated specimens showed more expansive/less contractive deformations with increasing suction during the heating process, consistent with previous studies suggesting that heating-induced soil deformation changes from contraction to expansion with the increase of suction (Uchaipichat and Khalili, 2009; Alsherif and McCartney, 2015; Romero et al., 2003; Tang et al., 2008b). This can be explained by suction hardening, namely the increase of OCR with an increase in suction. In addition, the CDG specimens presented contractions at the net normal stresses of 100 and 150 kPa but expansion at a net normal stress of 50 kPa, due to the reduced OCR with increasing net normal stress. This observation also coincides with the previous studies (Salager et al., 2008; Uchaipichat and Khalili, 2009).

### 5.5.2 Temperature effects on the shear behaviour of saturated interfaces

Figure 5.10(a) shows the relationships between horizontal displacement and shear stress of the saturated interface at a net normal stress of 50 kPa and three different temperatures (8, 20 and 42 °C). At each temperature, shear stress reached a maximum value at an approximately 2 mm horizontal displacement and then remained constant. Shear strength decreased by 12.7% when the temperature increased from 8 to 42 °C. Similar results were observed at net normal stresses of 100 and 150 kPa, as shown in Figures 5.9(a), 5.11(a), 5.12(a), 5.13(a) and 5.14(a).

Figure 5.10(b) shows the shearing-induced volume change at a net normal stress of 50 kPa. It is clear that temperature rise reduced the contraction. The accumulated contractions were approximately 0.065, 0.04 and 0.02 mm at 8, 20 and 42 °C, respectively. At the other net normal stresses, similar results were obtained, as presented in Figures 5.9 (b), 5.11(b), 5.12(b), 5.13(b) and 5.14(b). At all test conditions, the soil contracted during shearing, which is consistent with the strain-hardening behaviour shown in Figures 5.9-14. The reduction of contraction with increasing temperature was also supported by experimental data about a variety of clay-structure interfaces by previous researchers (Di Donna et al., 2016; Maghsoodi et al., 2020) who attributed it to thermal strain before shearing. It seems that the postulation is inapplicable to the CDG-structure interface tested in this study because its thermal deformation is consistently less than 0.15% (see Figure 5.8), much smaller than that of clay-structure interfaces (Li et al., 2019).

The above thermal effects on shear strength and contraction/dilatancy are at least partially related to the thermal expansion coefficients of the soil and counterface. The linear thermal expansion coefficients of the steel and CDG are about  $1 \times 10^{-5}$  and  $4 \times 10^{-5}$  per degree, respectively (Plevova et al., 2015). Thus, the normalized roughness of the test interface decreases upon heating. The reduction of roughness would reduce the thickness of the shear band, the shearing-induced volume change and the shear strength of interfaces, as revealed by extensive experimental data in the literature (Wang et al., 2020; Chen et al., 2015; Tsubakihara et al., 1993).

In addition, thermal effects on contraction/dilatancy were possibly related to the strength property of interfaces. At a given net normal stress, shearing-induced contraction is larger at a lower temperature. Given a shear displacement, the void ratio in the shear zone of unheated specimens is smaller than that of heated specimens, leading to more significant inter-particle friction and larger shear strength.

### 5.5.3 Temperature effects on the friction angle of saturated interfaces

The results in Figures 5.9-5.14 showed little difference between the peak and critical state strengths. This could be related to the OCR of soil and the roughness of the counterface used in this study. Similarly, shear-hardening behaviour was widely observed for relatively smooth soil-structure interfaces in previous studies (e.g., Hamid and Miller, 2009). Hence, the critical state shear strengths are further analysed here.

From the results in Figures 5.9-5.14, the critical state shear strengths at various net normal stresses and temperatures are determined and shown in Figure 5.15. The failure envelope at each temperature was fitted using a straight line in reference to the Mohr-Coulomb failure criterion with an assumption of zero adhesion, considering the use of saturated and compacted CDG. The obtained friction angles with respect to net stress (i.e.,  $\delta'$ ) are 27.3°, 26.1° and 25.1° at temperatures of 8, 20 and 42 °C, respectively. The slight reduction of friction angle upon heating is likely attributed to the decrease in interface roughness and the increase of the void ratio in the shear zone, as discussed above. Moreover, the interface friction angle is smaller than that of the pure CDG, which generally fell in the range of 38 and 42 degrees

(Zhang et al., 2008). It implies that the failure was attributed to not only the shearing inside the soil but also the sliding at the interface (Lupini et al., 1981; Takada, 1993; Littleton, 1976).

To further analyze thermal effects on  $\delta'$  of saturated soil-structure interfaces, the results from this study and previous ones are summarized in Figure 5.16. The variation of  $\delta'$  with temperature does not follow a consistent trend. For example,  $\delta'$  of the illite clay-structure interfaces decreases with increasing temperature (Di Donna et al., 2016), whereas that of the kaolin clay-structure interface (Maghsoodi et al., 2020; Yavari et al., 2016a) seems to be independent of temperature. The increase of  $\delta'$  with heating was only reported based on the tests on a red clay-structure interface (Li et al., 2019). This comparison implies that thermal effects on  $\delta'$  are dependent on soil type.

Figure 5.16 suggests that the variation of  $\delta'$  is consistently less than  $3^\circ$  for all interfaces in the typical temperature range (about 4 to 40 °C) of energy piles. In the design of energy piles,  $\delta'$  could be measured at room temperature only (about 20 °C) and used for simplicity, as long as an appropriate factor of safety is used to ensure pile performance.

#### 5.5.4 Coupled effects of temperature and suction on the shear strength of unsaturated interfaces

Figures 5.17(a)-5.19(a) show the shear stress-horizontal displacement relations of the unsaturated interface. Three net normal stresses (50, 100 and 150 kPa), two temperatures (20 and 42 °C) and three suction (0, 50 and 200 kPa) were taken into consideration. The corresponding relationships between vertical and horizontal displacements are summarized in Figures 5.17(b)-5.19(b). The water content during the shearing process was monitored but unreported here since its variations were almost negligible (less than 0.3%) in all tests.

At all stress and temperature conditions, the shear strength of interfaces increased with an increase in suction, which is mainly because the increment in suction can enhance the average skeleton stress of soil and apparent adhesion between soil and structure (Wheeler et al., 2003a). When suction increased from 50 to 200 kPa at a net normal stress of 50 kPa, shear strength increased by 27.5% and 14.4% at 20 and 42 °C, respectively (see Figure 5.17(a)). When net normal stress was 100 kPa, suction effects on shear strength were almost the same at 20 and 42 °C (see Figure 5.18(a)). Given the same suction increment at a net normal stress of 150 kPa, the increase in shear strength at 42 °C (i.e., 60.7%) was much larger than that at 20 °C (i.e., 40.3%) (see Figure 5.19(a)). The data suggest that the incremental rate of shear strength with suction is dependent on both temperature and net normal stress, most probably because they affect the equilibrium degree of saturation and thus the capillary force at a given suction. Detailed discussion is given later. Consequently, the variation of shear strength with heating presented different trends. At lower net normal stress like 50 kPa, heating reduced shear strength and the reduction was more significant at a higher suction. In contrast, at higher net normal stress like 150 kPa, heating decreased interface shear strength at zero suction, but increased interface shear strength at a suction of 200 kPa.

Temperature effects on the shear behaviour show distinct behaviour at different suction conditions, as shown in Figures 5.17(b)-5.19(b). At zero suction, heating appeared to have a minor influence on the shear-displacement behaviour at each net normal stress. The small reduction of critical state shear strength was due to the decrease in  $\delta'$  (see Figure 5.16). At a suction of 50 kPa, the heating also induced a slight reduction of shear strength. When the

suction increased to 200 kPa, the temperature elevation reduced the shear strength at a net normal stress of 50 kPa but increased the shear strength at higher net normal stresses (100 and 150 kPa). The different trends may be because heating can alter interface behaviour via different mechanisms. Firstly, heating causes a reduction in the surface tension of the water, which affects the shape of the capillary menisci for a given suction. According to the Young-Laplace equation, a decrease in surface tension would necessitate a decrease in the capillary radius to maintain the same suction. This would suggest that water would have to recede deeper into the soil pores, resulting in a lower degree of saturation and lower strength. Secondly, heating could change the void ratio and pore size distribution, affecting the equilibrium degree of saturation for a given suction. This affects the solid-water interfacial area and the shear strength. A higher solid-water interfacial area for a given suction will result in higher strength (Vanapalli et al., 1996). It would be expected that the degree of saturation would increase for the same suction as the void ratio decreases, which would also contribute to an increase in shear strength upon heating. In the current study, when the soil was heated under net normal stress of 50 kPa, soil response upon heating was essentially elastic, and the change in pore size distribution was minor. The first mechanism plays a dominant role, and the shear strength reduction was due to the decrease in water surface tension and the degree of saturation (see Table 5.3). At a higher net normal stress like 150 kPa, soil response upon heating was elastoplastic, and particle rearrangements resulted in thermal contraction and more small-size pores. The reduction of pore size can increase the equilibrium degree of saturation at a given suction. As suggested by the data in Table 5.3, the degrees of saturation at various temperatures

were almost the same, implying that the change in pore size distribution compensated for the influence of surface tension on the degree of saturation. The heated specimen was likely to have more small-size pores and, therefore, a greater number of menisci water lenses at a given suction, which could improve interparticle contact (Wheeler et al., 2003b) and increase the shear strength.

To further investigate the coupled effects of temperature, suction and net normal stress on the shear strength of unsaturated interface, the failure envelopes in the plane of shear strength versus suction are determined and presented in Figure 5.20. Equation (5-2) was applied to analyse the results:

$$\tau = c' + [(\sigma_n - u_a) + (u_a - u_w) \cdot (S_r)^\kappa] \cdot \tan \delta' \quad (5-2)$$

where  $u_a - u_w$  is the matric suction;  $\sigma_n - u_a$  is the net normal stress;  $c'$  is the true adhesion;  $\delta'$  is the friction angle of soil and interface;  $S_r$  is the degree of saturation;  $\kappa$  is a model parameter. Note that this equation uses Bishop's stress  $(\sigma_n - u_a) + \chi \cdot (u_a - u_w)$  with  $\chi = (S_r)^\kappa$ . A similar form was used by some previous researchers (Vanapalli et al., 1996; Alonso et al., 2010; Han and Vanapalli, 2016) to model the shear strength of pure unsaturated soils. Parameter  $\kappa$  is a model parameter for controlling the dependency of shear strength on the degree of saturation. The value of  $\kappa$  is assumed to be 1 in many studies, and some researchers (Alonso et al., 2010; Hossain and Yin, 2010; Vanapalli et al., 1996) found that  $\kappa > 1$  can give a better fitting of experimental data for many soils. Alonso et al. (2010) analysed several soils and found that the  $\kappa$  values were in the range of 1.0 to 6.4. In the current study, it is also found that  $\kappa = 1$  results in a significant overestimation of the shear strength of unsaturated interface.

The results in Figure 5.20 were fitted with equation (5-2) by using the measured degree of saturation in Table 5.3 and the true adhesion and friction angle in Figure 5.15. It can be seen that the calculated non-linear failure envelopes agree well with the measured data. The parameter  $\kappa$  was determined to be 4.7. For pure CDG, it was reported that the parameter  $\kappa$  is 2.2 (Hossain and Yin, 2010), which is smaller than the  $\kappa$  value of the CDG-structure interface. This is probably because there are fewer water menisci between soil particles and the counterpart compared to water meniscus within pure soil per unit area. What's more, thermal effects on the value of  $\kappa$  for the CDG-structure interface are insignificant, and the interface shear strength at different temperatures could be predicted accurately by using a constant  $\kappa$ .

The above finding of coupling effects of temperature, suction and net normal stress on interface shear strength should be carefully considered in analysing energy piles located in the unsaturated ground. The interface strength may decrease during both heating and cooling, depending on the stress and suction conditions (see Figure 5.20). The reduction of interface shear strength likely affects the mobilisation of shaft resistance and induces irreversible settlement. This mechanism could partially explain the successive pile settlement during heating-cooling cycles in the physical model tests of Stewart and McCartney (2014), as reported in the Introduction section.

### 5.5.5 Suction and temperature effects on dilatancy

Based on the data from Figures 5.17(b)-5.19(b), the dilatancy  $d = -\delta y/\delta x$  during shearing was calculated, where  $\delta y$  and  $\delta x$  refer to the displacement increments in vertical and horizontal directions, respectively. A positive value of  $d$  means dilation, whereas a negative

value means contraction. The peak values of dilatancy during the shearing process at each stress, suction and temperature condition are determined and shown in Figure 5.21. As expected, dilative behaviour was more significant under lower net normal stresses. More importantly, the interface became more dilative at all stress and temperature conditions with the increase of suction. Taking the interface at a net normal stress of 100 kPa and a temperature of 42 °C as an example, the value of  $d$  changed from -0.2 to 0.1 when suction increased from 0 to 200 kPa. This is in line with previous investigations showing that suction could enhance the dilatancy of unsaturated interfaces (Borana et al., 2018; Hamid and Miller, 2009).

In addition, temperature elevation generally induced an increment of dilatancy at each condition of suction and stress despite small variations, which is probably attributed to the thermal expansion of soil particles and pore water at high temperatures. Concerning energy piles, an increase in dilatancy could enhance normal stress from the soil to the pile and the bearing capacity of the pile.

## 5.6 Interpretations of constant-stress heating and cooling test results

### 5.6.1 Tangent and normal displacements during heating and cooling

Figure 5.22 shows the results of constant-stress heating and cooling tests on fully saturated interfaces, obtained from tests in series S0N50, S0N100 and S0N150 (see Table 5.4). To assess the tangent displacement at the soil-structure interface, a new variable (i.e., normalized tangent displacement) is proposed and used here. It is the ratio of thermally induced tangent displacement  $d_h$  to ten times the median soil particle size  $D_{50}$ . The choice of  $10D_{50}$  is because the thickness of the shear zone at the soil-structure interface is generally in the range

of  $7\sim 14 D_{50}$  (Hoteit, 1990; Pra-ai and Boulon, 2017). Thus, the normalized horizontal displacement (i.e.,  $d_h/(10 * D_{50})$ ) can be used to approximate the shear strain of soil inside the shear zone. Regarding the sign convention of  $d_h$ , the tangent displacement induced by an increase in the shear stress is positive. If the thermally induced displacement has the same direction as the shearing-induced one, the value of  $d_h/(10 * D_{50})$  is positive and it is described as “forward displacement” in the following sections. Similarly, if the thermally induced displacement has an opposite direction to the shearing-induced one, the value of  $d_h/(10 * D_{50})$  is negative and the displacement is described as “backward displacement”. In addition, it is assumed that the normal displacement is uniform for simplicity. Volumetric strain, defined as the normal displacement over soil specimen height, is presented. A positive value means contraction and a negative value means expansion.

According to the results in Figures 5.22(a-c), there is a general trend that the value of  $d_h/(10 * D_{50})$  slightly decreases during heating but significantly increases during cooling. For example, when the net normal stress is 50 kPa and the shear stress ratio is 0.75, the change of  $d_h/(10 * D_{50})$  along the cooling path is around 0.15, while it is only 0.03 during the heating process. The heating-induced backward movement is likely induced by the expansion of soil particles. The cooling-induced forward movement is likely related to the re-arrangement of soil particles near the soil-structure interface. According to the investigation of Vargas and McCarthy (2007) using discrete element modelling, cooling can reduce the contact force between particles because of the shrinkage of particles. As a result, some force chains become unstable, leading to forward movement at the soil-structure interface. This interpretation is

supported by the results in Figures 5.22(d-f). The specimens show obvious contraction during the cooling process. Based on the study of Chen et al. (2006) on the interaction between grain particles and a container, this phenomenon is more significant when the grains and counterface are made of different materials with different thermal expansion coefficients. The soil and steel used in this study have very different thermal expansion coefficients, so the thermally induced displacement is expected to be obvious.

Figure 5.23 shows the results of constant-stress heating and cooling tests on unsaturated interfaces. Unsaturated interfaces show similar behaviour at a qualitative level as saturated interfaces. Heating induces a backward displacement and cooling induces a forward displacement at the soil-pile interface.

#### 5.6.2 Effects of stress and suction on the irreversible tangent displacement

Figures 5.22 and 5.23 reveal that the tangent displacement at the soil-structure interface is more critical during the cooling process. The value of tangent displacement is clearly affected by several factors, such as the net/effective normal stress, suction and stress ratio. To further analyze the influence of these factors, the irreversible tangent displacements induced by one thermal cycle are determined and discussed here.

Figure 5.24(a) also clearly shows that  $d_h/(10 * D_{50})$  induced by one thermal cycle is consistently smaller when the net normal stress is higher. Taking the saturated interface at  $\tau/\tau_s=0.75$  as an example,  $d_h/(10 * D_{50})$  is about 0.12, 0.1 and 0.05 under normal stresses of 50, 100 and 150 kPa, respectively. This is probably because the increment of net normal pressure on the soil-structure interface restricts thermal deformation, which is similar to the

observation of Vargas and McCarthy (2007) from the discrete element modelling. The results in Figure 5.24(b) indicate that the irreversible tangent displacement is not sensitive to a change in suction. Hence, suction effects are not analyzed in detail.

Figure 5.25 summarizes the relationships between  $d_h/(10 * d_{50})$  and  $\tau/\tau_s$  at various normal stresses and suctions. The results consistently show a bilinear relationship and the increase rate of  $d_h/(10 * d_{50})$  with  $\tau/\tau_s$  is larger when the stress ratio is higher. This suggests the existence of a yielding point, above which the irreversible displacement occurs, even though the limited data cannot be used to determine the exact yielding point. Moreover, the observation suggests that to minimize the thermally induced settlement of energy pile, it seems efficient to keep the value of  $\tau/\tau_s$  less than 0.5.

## 5.7 Summary

In this chapter, a new direct shear apparatus was developed for testing soil-structure interfaces. Different from existing apparatuses in the literature, the apparatus allows for the control of not only temperature but also matric suction, which was used to study the thermo-mechanical behaviour of the unsaturated CDG-structure interface through three series of tests. Meanwhile, this direct shear device can achieve two kinds of loading modes: displacement-control and shear force-control loading modes. With reference to energy piles, three net normal stresses (25, 50, 100, 150 and 225 kPa), suctions (0, 50 and 200 kPa) and temperatures (8, 20 and 42 °C) were considered in the test program. The unique data are useful for developing constitutive models for unsaturated soil-structure interfaces and analyzing the performance of energy piles. Based on the results, some conclusions are drawn below:

(1) The friction angle  $\delta'$  of the tested CDG-structure interface slightly decreases with increasing temperature since temperature elevation results in an increment of void ratio in the shear zone. Furthermore, the shear strength of the unsaturated interface increases nonlinearly with increasing suction, and the incremental rate is dependent on temperature and stress. At net normal stress of 50 kPa, heating the interface reduces this rate. This is because heating could reduce the surface tension coefficient and the degree of saturation at a given suction. In contrast, this rate increases at a net normal stress of 150 kPa with the same temperature increment. This is probably because the heated specimen has more small-size pores due to thermal strain and more menisci water lenses, whose influence outweighs the effects of surface tension.

(2) The shear strength of saturated CDG-structure interfaces decreases with increasing temperature, which is attributed to the reduction of effective friction angle induced by the temperature elevation. For the unsaturated CDG-structure interface, the variation of its shear strength with heating shows different trends. At lower net normal stress like 50 kPa, heating reduces shear strength, and the reduction is more significant at a higher suction. In contrast, at higher net normal stress like 150 kPa, heating decreases interface shear strength at zero suction, but increases interface shear strength at a suction of 200 kPa. The difference is mainly because  $\delta^b$  is affected by temperature and net normal stress in a coupled way, as explained above.

(3) For the shear-induced deformation of interfaces, the results indicate that a higher suction resulted in more dilative deformation. For example, saturated and unsaturated interfaces at a net normal stress of 50 kPa exhibit contractive and dilative behaviour,

respectively. Furthermore, temperature elevation would reduce shearing-induced contraction, which is at least partially attributed to the reduction of interface roughness with heating.

(4) Under constant net normal stress and shear stress conditions, the relative movement at the soil-pile interface reduces slightly during heating but increases significantly during cooling. The cooling-induced forward movement is most likely due to the thermally induced contraction of soil particles and hence the collapse of force chains. Furthermore, the thermally-induced relative movement is dependent on the net normal stress and shear stress but not sensitive to suction. The relative movement is larger under lower net normal stress and higher shear stress conditions, under which the role of temperature variation is relatively more important. Furthermore, the relationship between relative movement and stress ratio (i.e., the ratio of shear stress to effective normal stress) is bilinear with a critical stress ratio of 0.5. To minimize the settlement of energy piles, it may be necessary to keep the stress ratio at soil-pile interfaces between this critical value.

Table 5.1. Basic properties of the soil used in the chapter.

Properties	Value
Unified soil classification system (ASTM D2487, 2017)	ML
Specific gravity	2.59
Clay content (<0.002 mm) (%)	13
Silt content (0.002-0.063 mm) (%)	34
Sand content (0.063-2.0 mm) (%)	55
Liquid limit (%)	31
Plastic limit (%)	21
Plasticity index (%)	10
Maximum dry density (kg/m <sup>3</sup> )	1840
Optimum moisture content (%)	13.4
Friction angle with respect to net stress $\phi'$ (°) (Zhang et al., 2008)	38-42

Table 5.2. Summary of the constant-temperature direct shear tests at zero suction (24 tests in total).

Series ID	Test ID	Matric suction (kPa)	Net stress (kPa)	Temperature (°C)	Void ratio before shearing
S1	N25S0T8	0	25	8	0.46
	N25S0T20	0	25	20	0.46
	N25S0T42	0	25	42	0.46
	N50S0T8	0	50	8	0.44
	N50S0T20	0	50	20	0.45
	N50S0T42*	0	50	42	0.45
	N100S0T8	0	100	8	0.42
	N100S0T20	0	100	20	0.42
	N100S0T42	0	100	42	0.42
	N150S0T8*	0	150	8	0.41
	N150S0T20	0	150	20	0.41
	N150S0T42	0	150	42	0.41
	N225S0T8	0	225	8	0.40
	N225S0T20	0	225	20	0.40
	N225S0T42	0	225	42	0.40
	N300S0T8	0	300	8	0.39
	N300S0T20	0	300	20	0.39
	N300S0T42	0	300	42	0.39

Note: \* the tests were carried out twice to evaluate the repeatability of experimental results. The initial void ratio and water content after specimen preparation are  $0.48 \pm 0.01$  and  $13.4 \pm 0.2\%$ , respectively.

Table 5.3. Summary of the constant-temperature direct shear tests at different suctions (12 tests in total).

Series ID	Test ID	Matric suction (kPa)	Net stress (kPa)	Temperature (°C)	Soil state before shearing		
					Void ratio	Gravimetric water content (%)	Degree of saturation (%)
S2	N50S50T20	50	50	20	0.44	13.7	76.8
	N50S50T42	50	50	42	0.44	13.2	71.3
	N100S50T20*	50	100	20	0.42	13.8	79.4
	N100S50T42	50	100	42	0.42	12.9	76.4
	N150S50T20	50	150	20	0.41	13.9	81.2
	N150S50T42	50	150	42	0.41	13.8	80.6
S3	N50S200T20	200	50	20	0.43	11.1	68.3
	N50S200T42	200	50	42	0.43	10.8	62.8
	N100S200T20	200	100	20	0.41	10.9	68.8
	N100S200T42*	200	100	42	0.41	10.9	67.2
	N150S200T20	200	150	20	0.40	11.2	71.4
	N150S200T42	200	150	42	0.38	11.2	76.9

Note: \* the tests were carried out twice to evaluate the repeatability of experimental results. The initial void ratio and water content after specimen preparation are  $0.48 \pm 0.01$  and  $13.4 \pm 0.2\%$ , respectively.

Table 5.4. Summary of constant-stress heating and cooling tests. (12 tests in total).

Test ID	Suction (kPa)	Net normal stress (kPa)	Applied shear stress $\tau$ (kPa)	Shear strength $\tau_s$ (kPa)	Stress ratio ( $\tau/\tau_s$ )
S0N50	0	50	14.2	28.3	0.5
			21.2	28.3	0.75
S0N100	0	100	29.2	58.3	0.5
			43.7	58.3	0.75
S0N150	0	150	35.3	70.6	0.5
			53	70.6	0.75
S50N50	50	50	16.4	32.7	0.5
			24.5	32.7	0.75
S50N100	50	100	31	61.9	0.5
			46.4	61.9	0.75
S200N100	200	100	34.2	68.3	0.5
			51.2	68.3	0.75

Note: In each test, the specimen is subjected to one thermal cycle: 25°C → 35°C → 45°C → 35°C → 25°C → 15°C → 5°C → 15°C → 25°C.

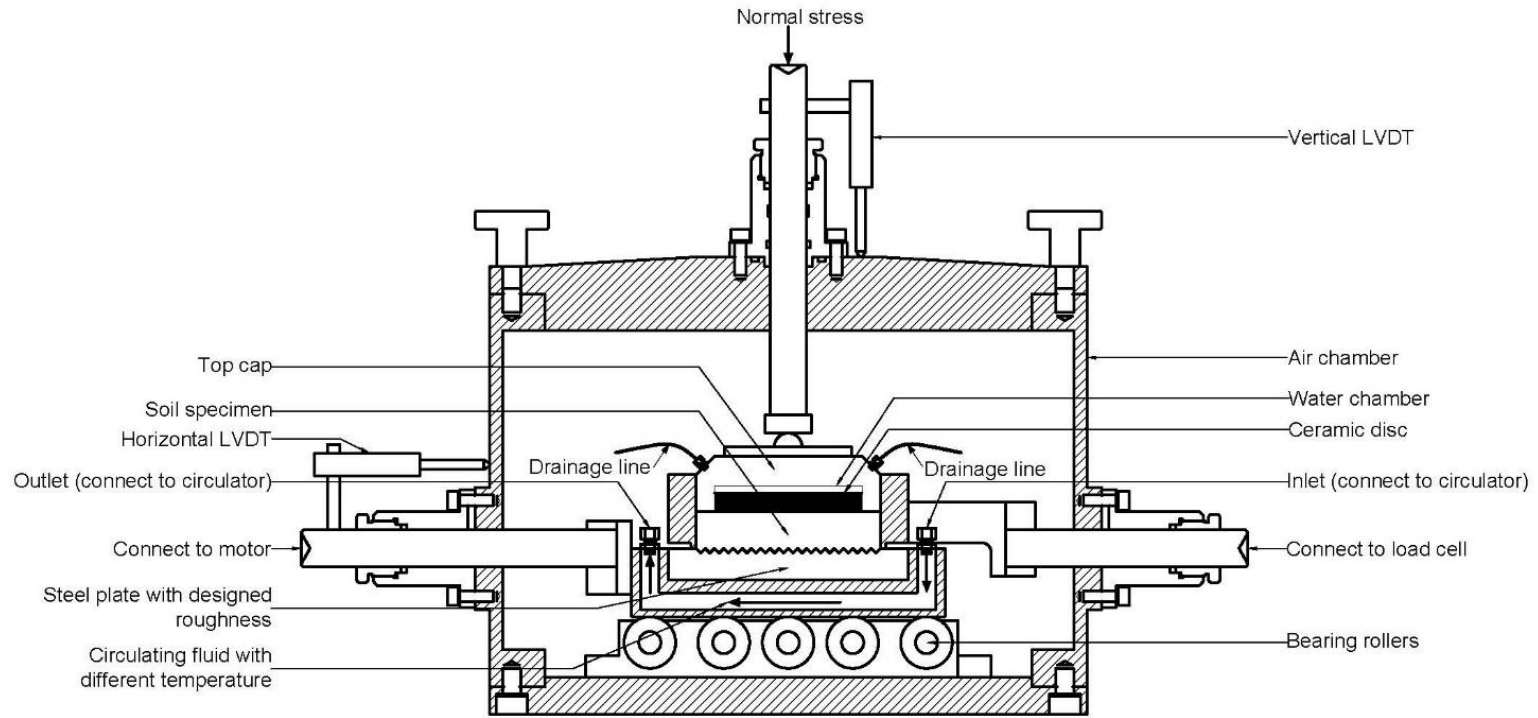


Figure 5.1. Schematic diagram of the new suction- and temperature-controlled direct shear apparatus.

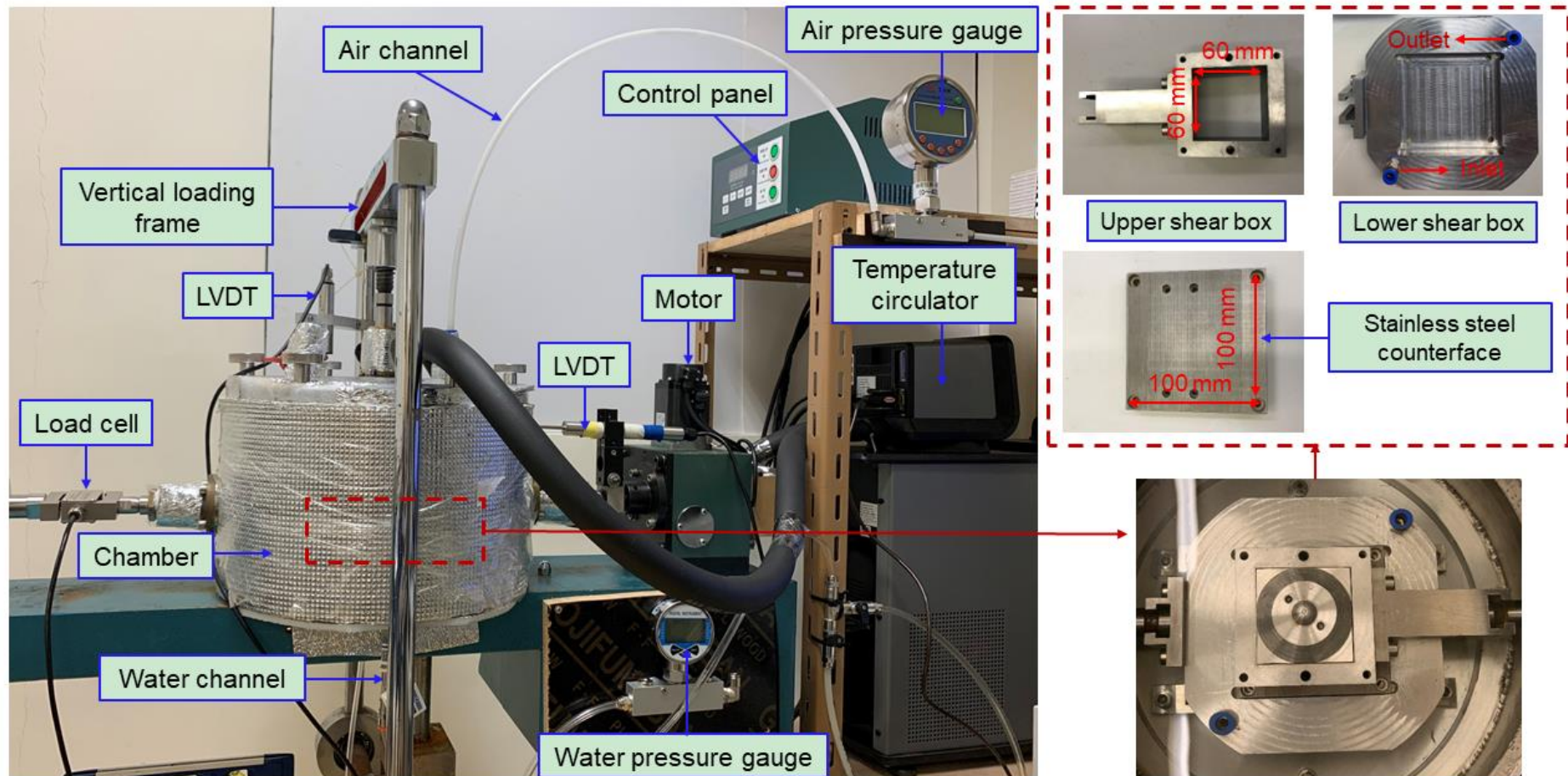


Figure 5.2. A photo of direct shear apparatus.

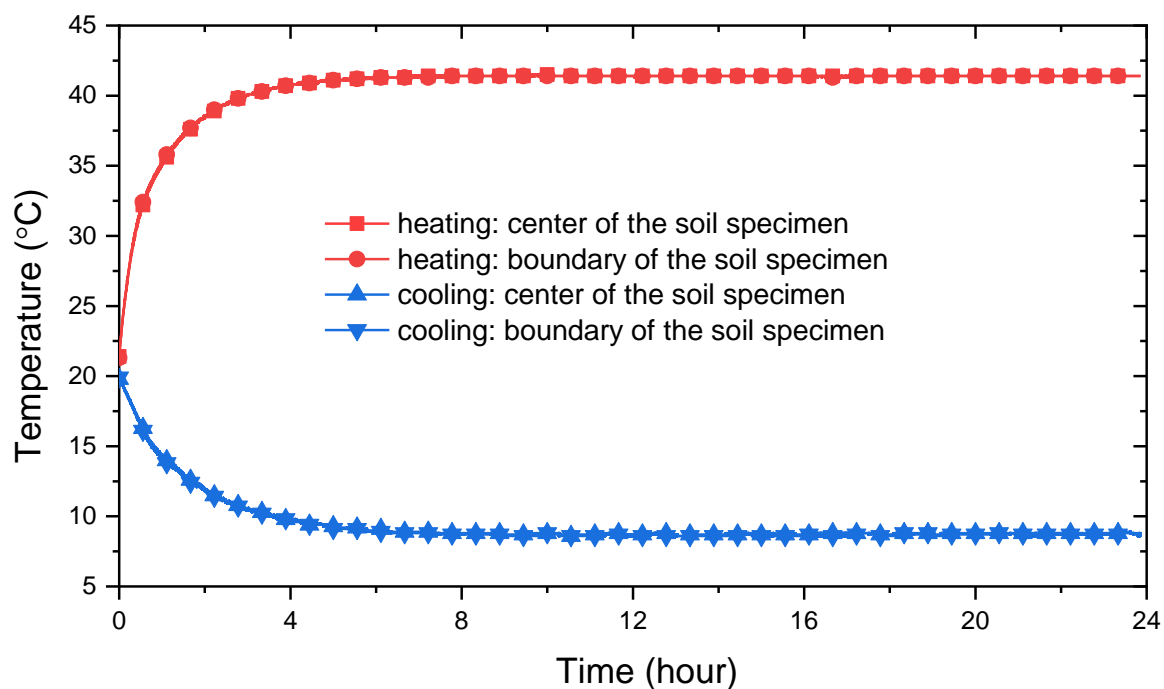


Figure 5.3. Typical temperature-time relation monitored at different locations of soil specimen subjected to heating/cooling.

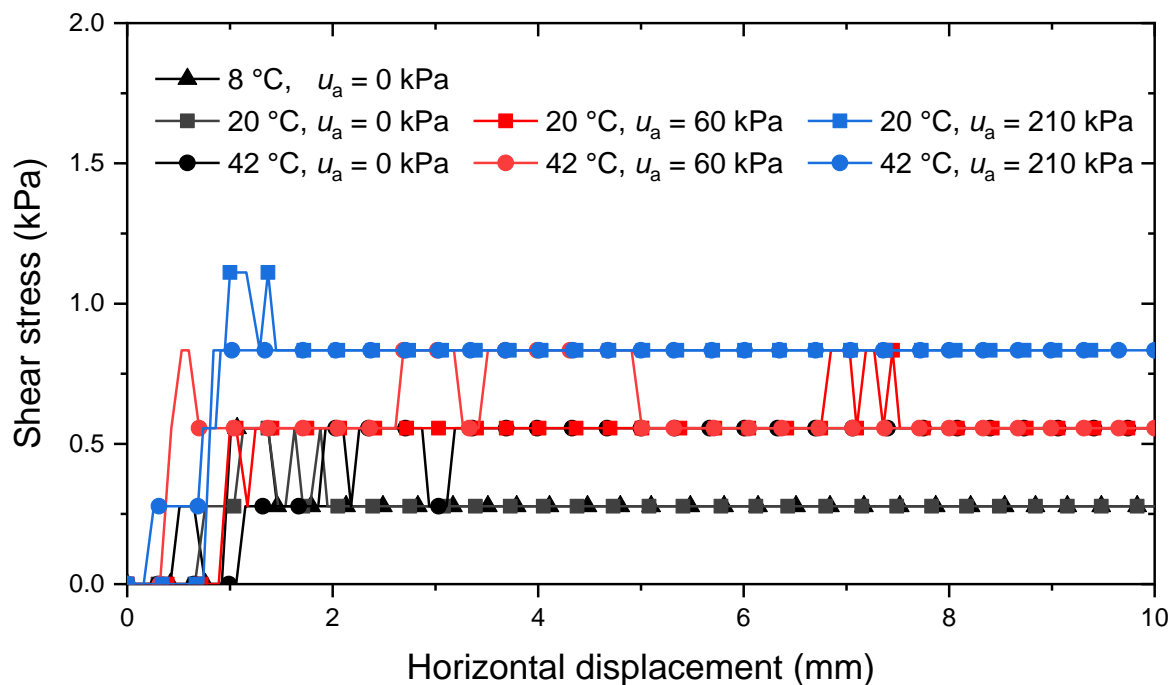


Figure 5.4. Calibration of the total frictional force, including the friction between lower and upper shear boxes and the friction between loading rod and chamber, at different temperatures and air pressures in the chamber.

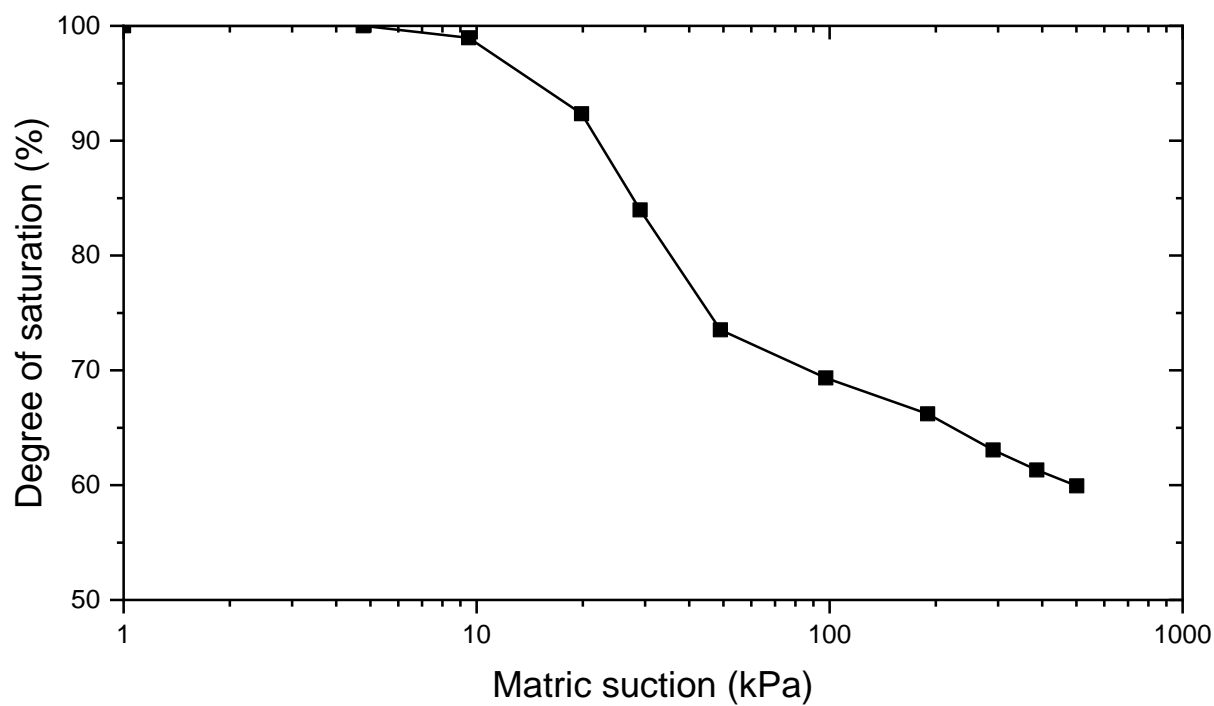


Figure 5.5. CDG water retention curve (data from Hossain and Yin (2010)).

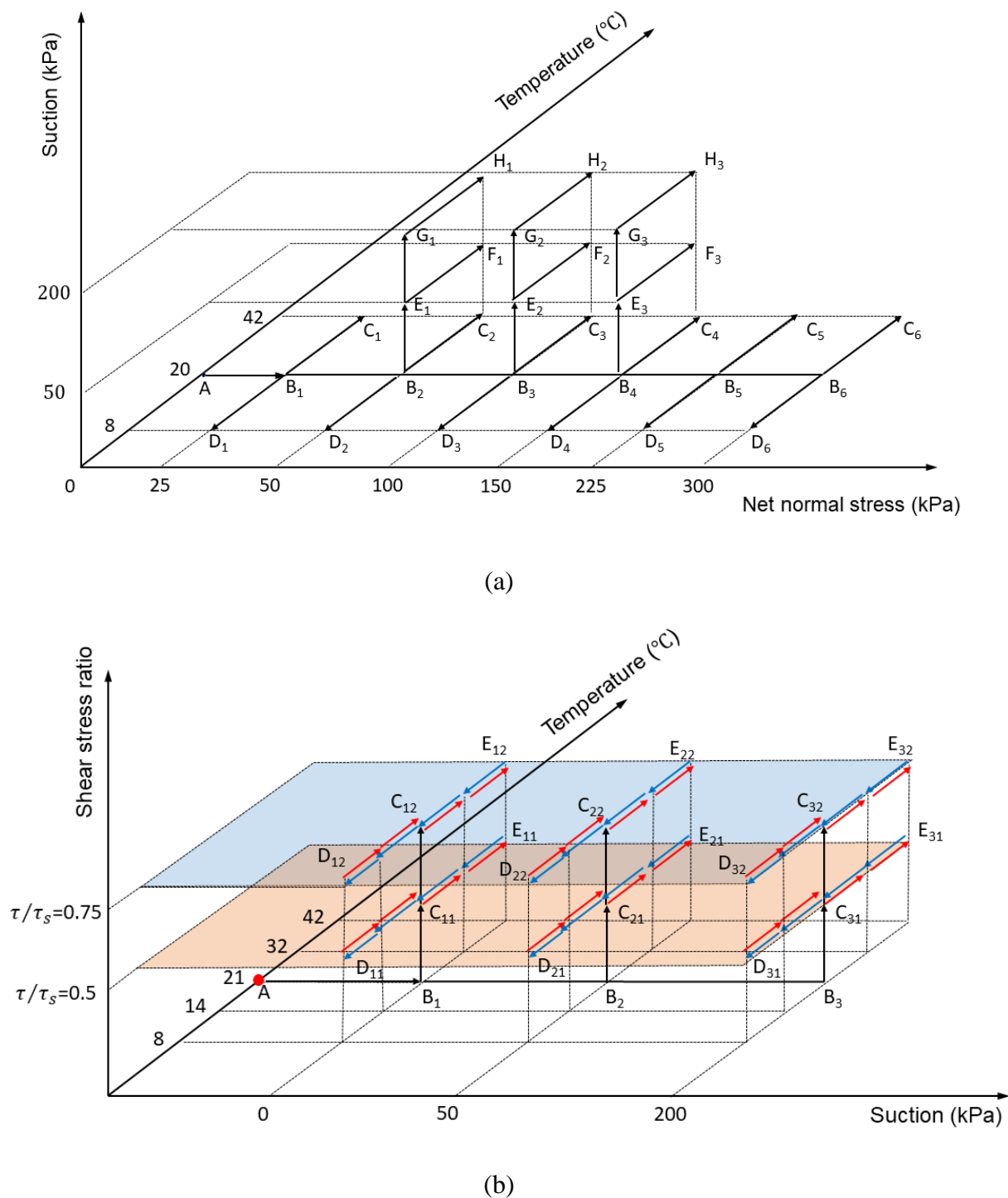
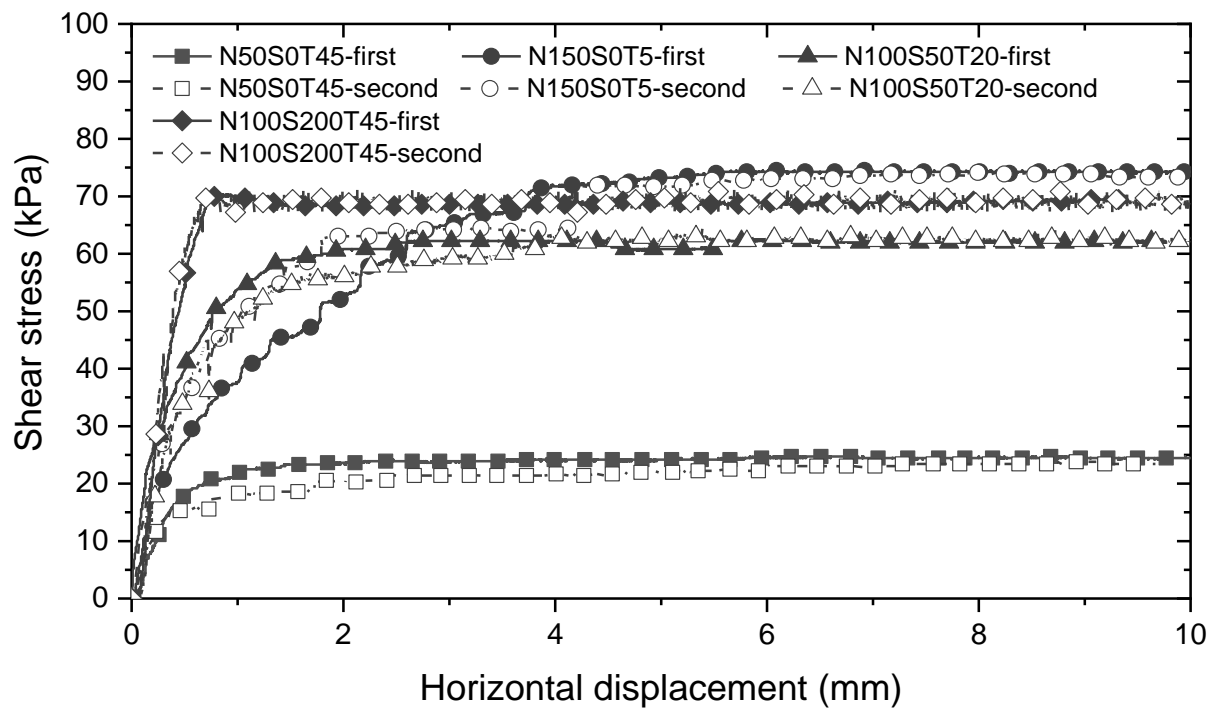
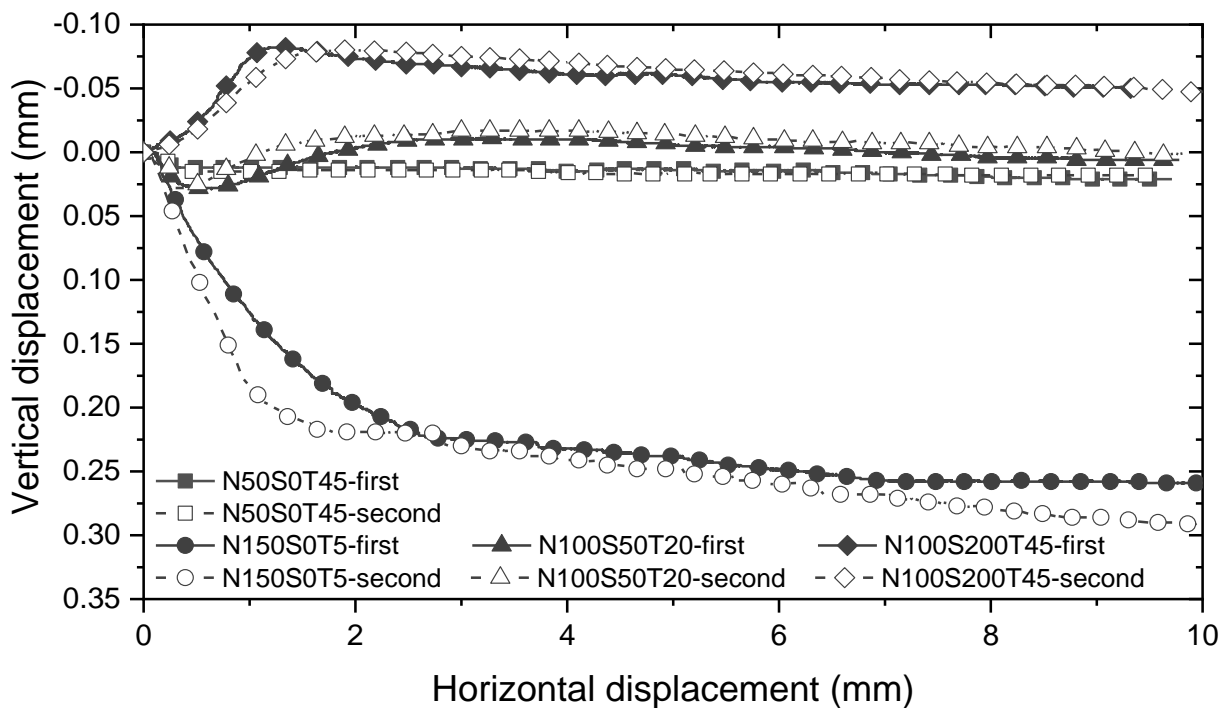


Figure 5.6. Thermo-hydro-mechanical path of the direct shear tests: (a) constant-temperature shearing tests; (b) constant-stress heating and cooling tests. (Point A represents the initial state after soil saturation).

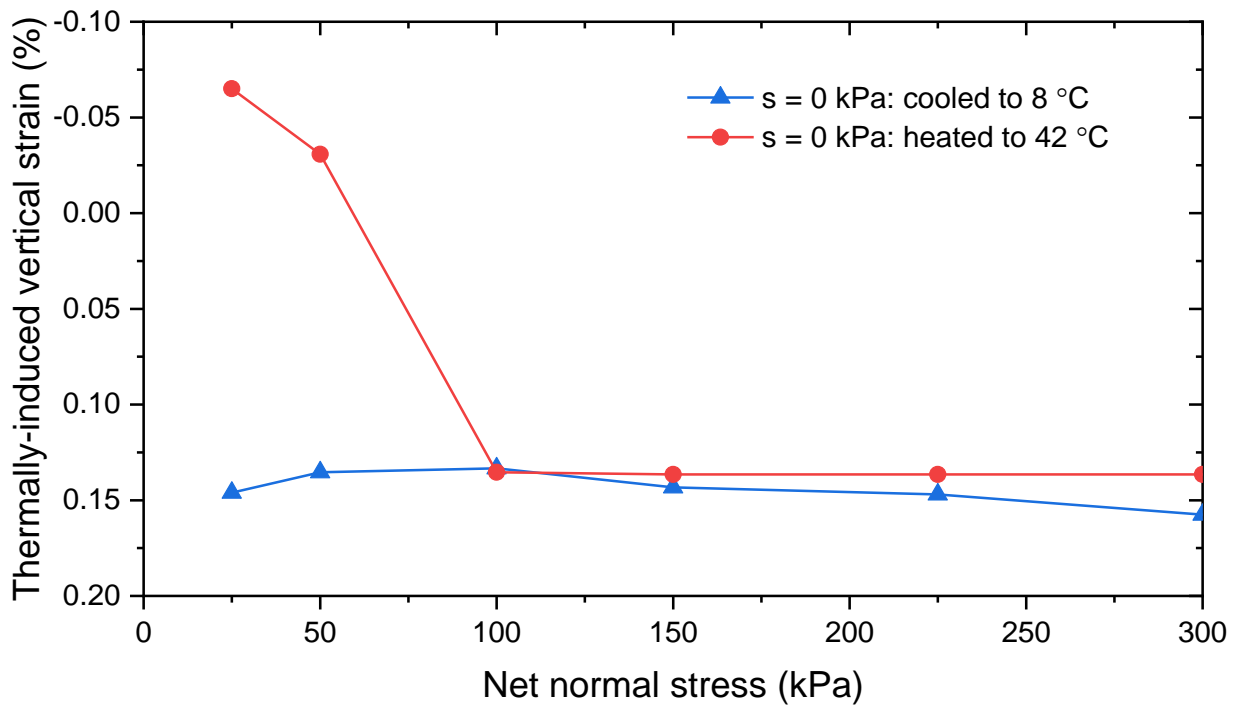


(a)

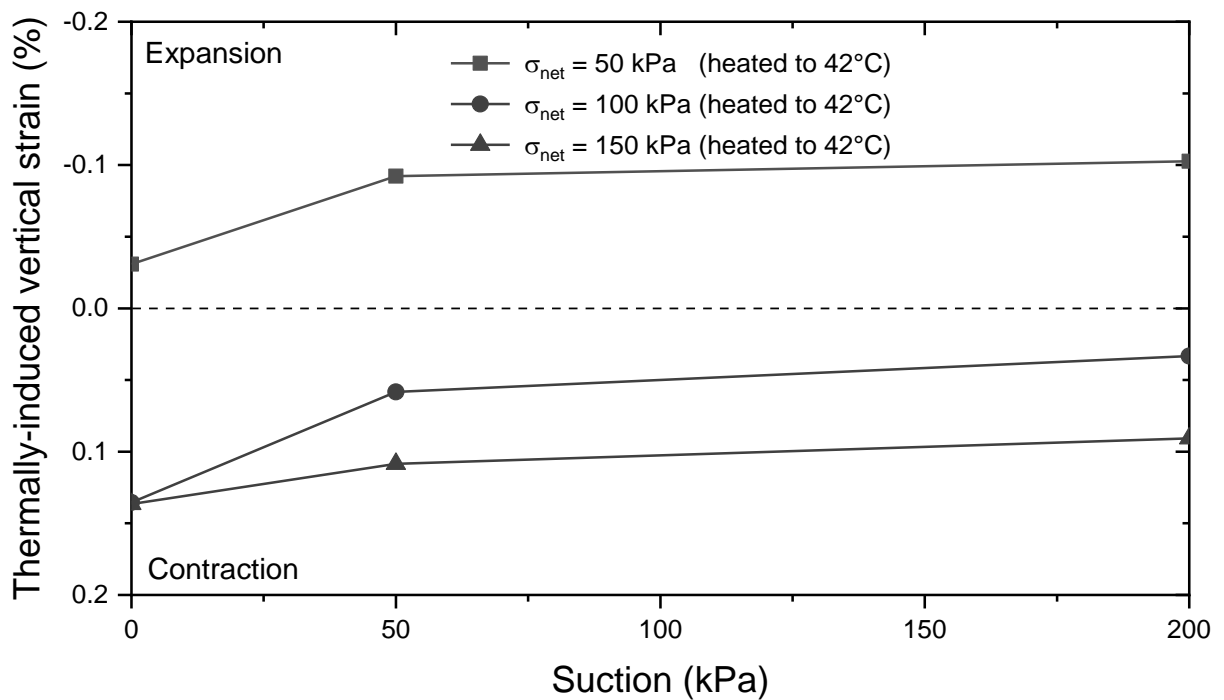


(b)

Figure 5.7. Repeatability of test results: (a) stress-horizontal displacement relation; (b) shearing induced vertical deformation (positive value means contraction).

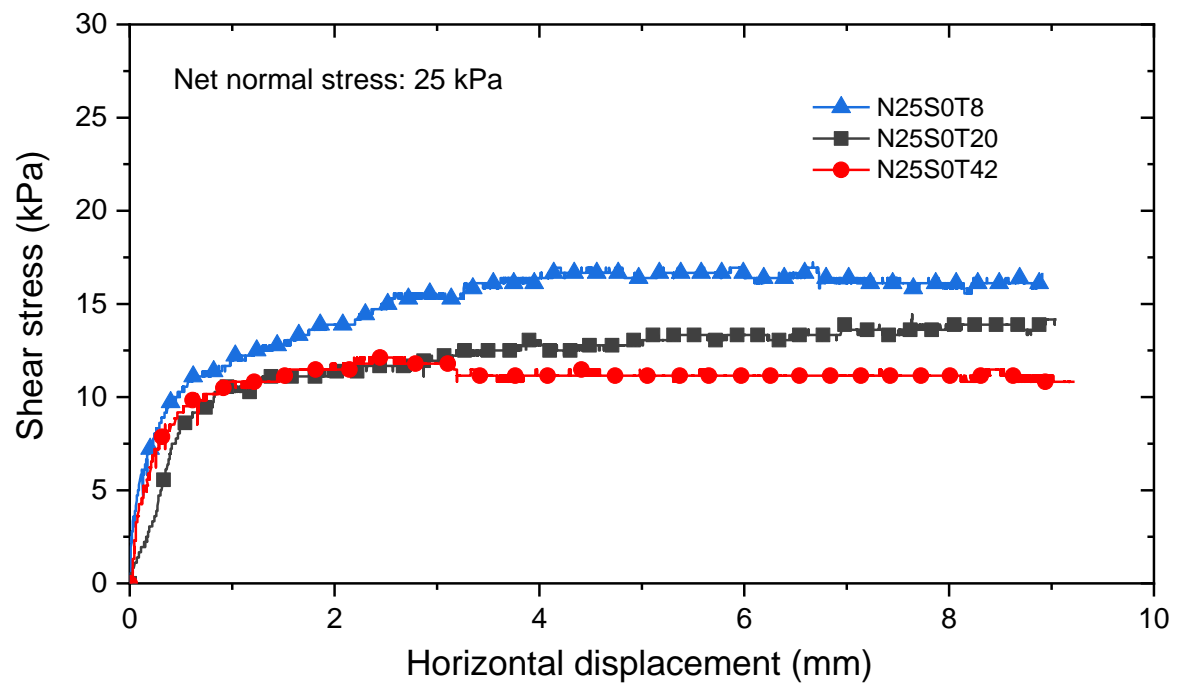


(a)

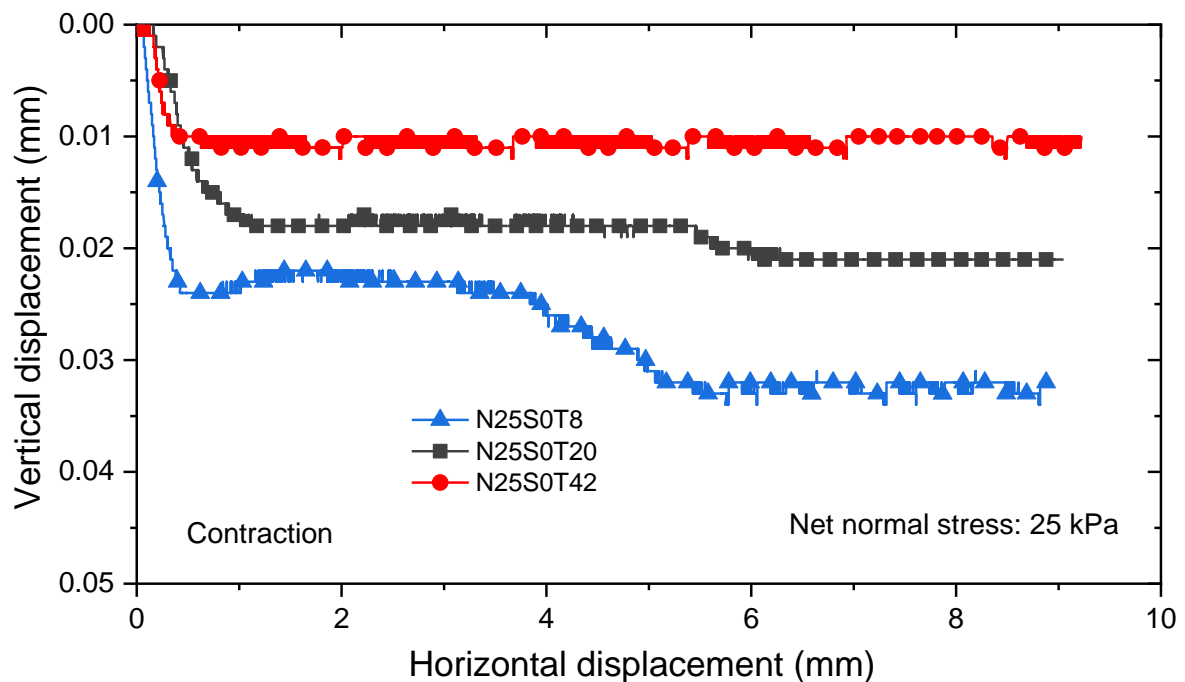


(b)

Figure 5.8. Thermal strain at various stresses and suctions (positive value means contraction): (a) zero suction; (b) various suctions.

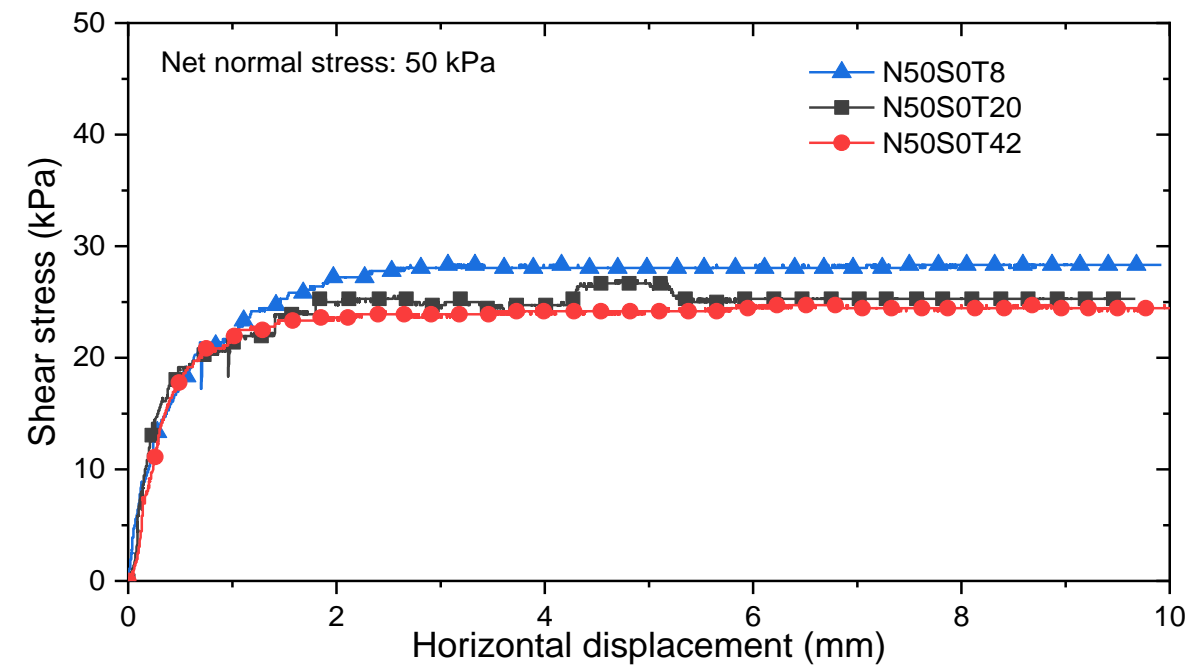


(a)

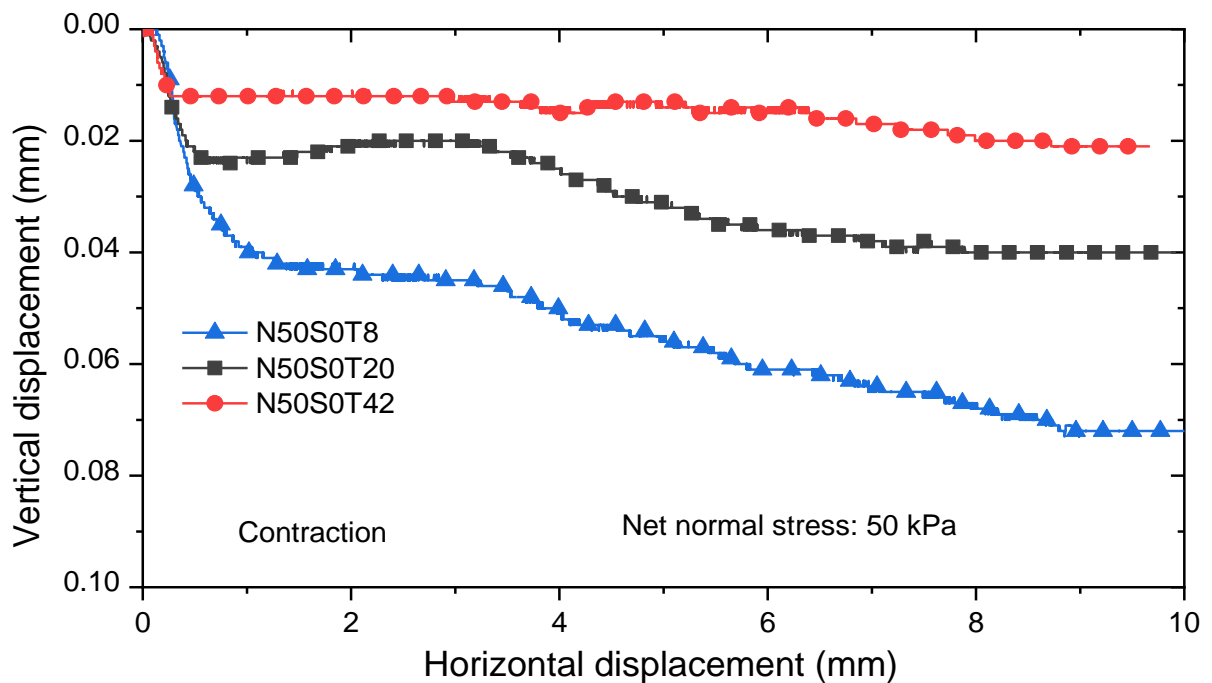


(b)

Figure 5.9. Shear behaviour of saturated CDG-structure interface at various temperatures and a net normal stress of 25 kPa: (a) stress-horizontal displacement relation; (b) shearing induced vertical deformation.

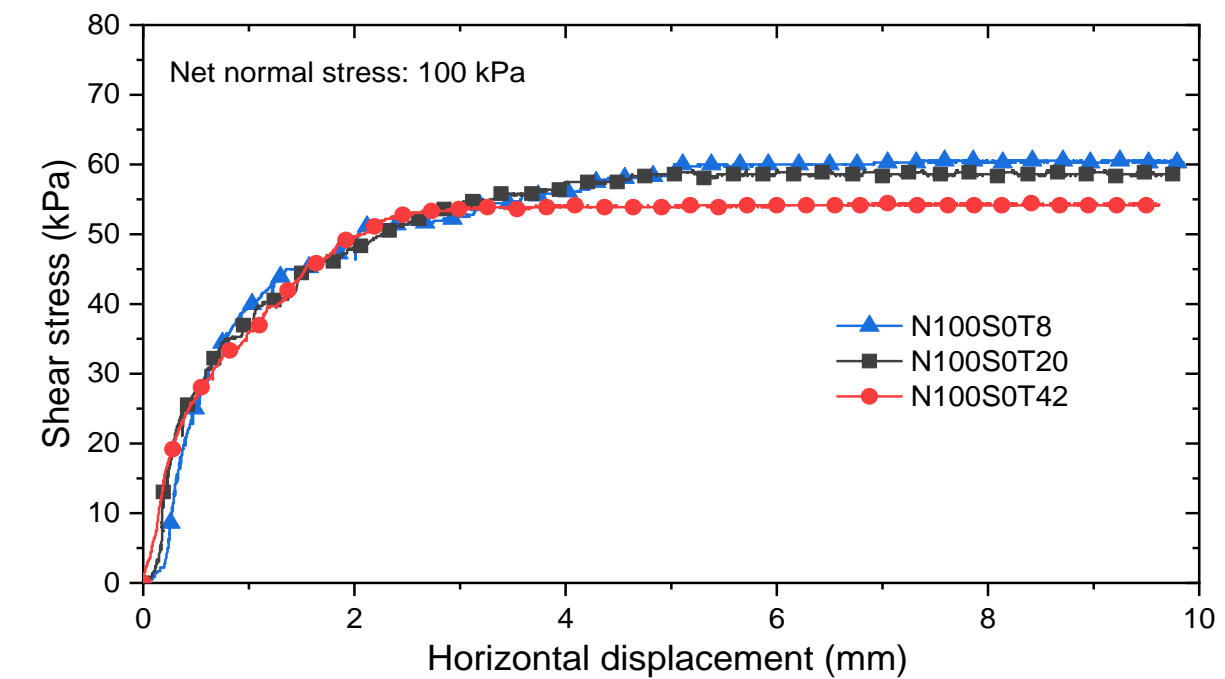


(a)

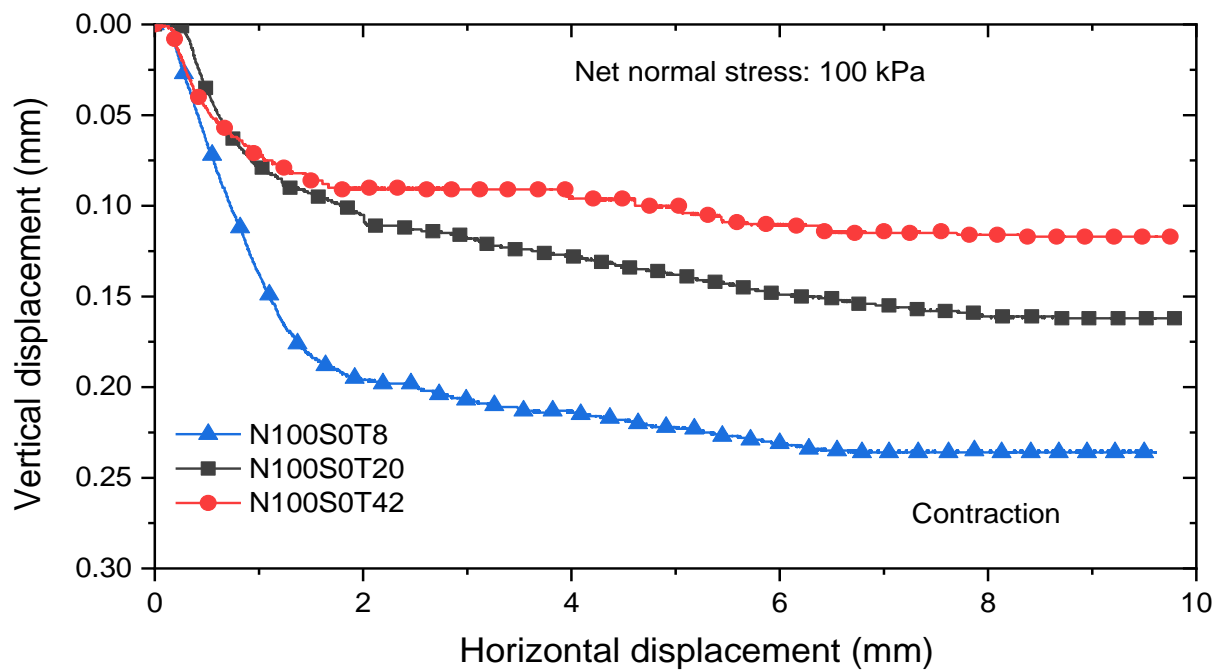


(b)

Figure 5.10. Shear behaviour of saturated CDG-structure interface at various temperatures and a net normal stress of 50 kPa: (a) stress-horizontal displacement relation; (b) shearing induced vertical deformation.

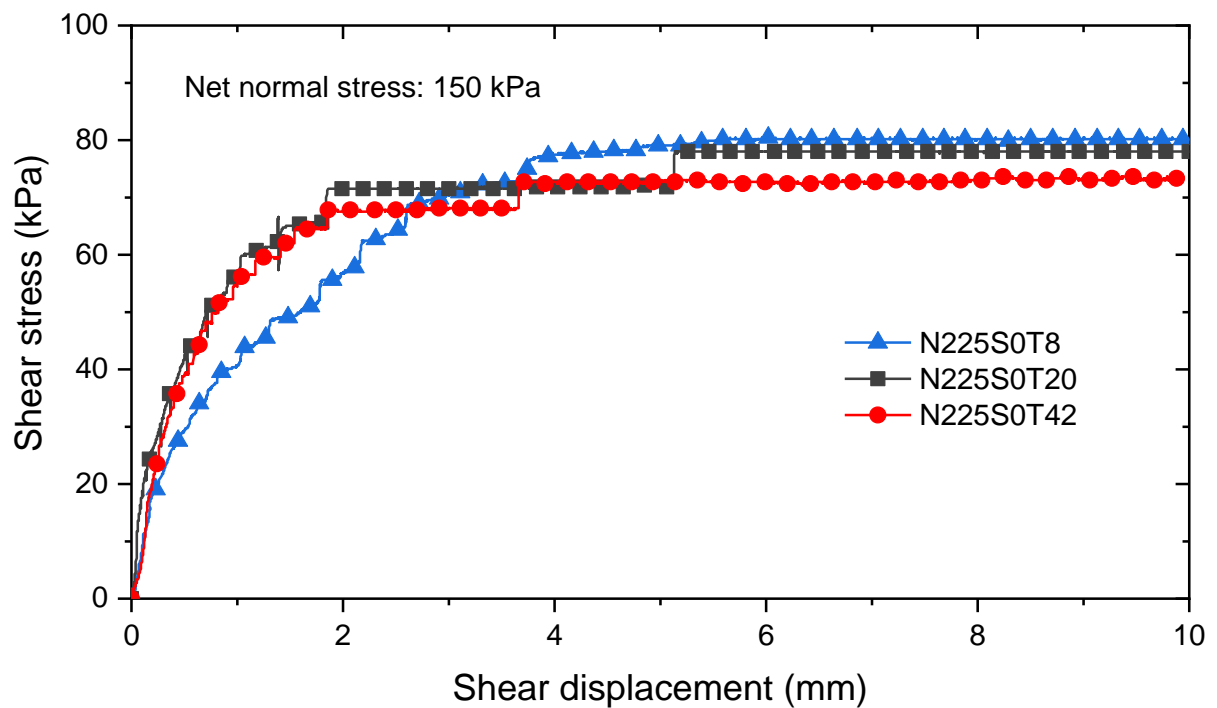


(a)

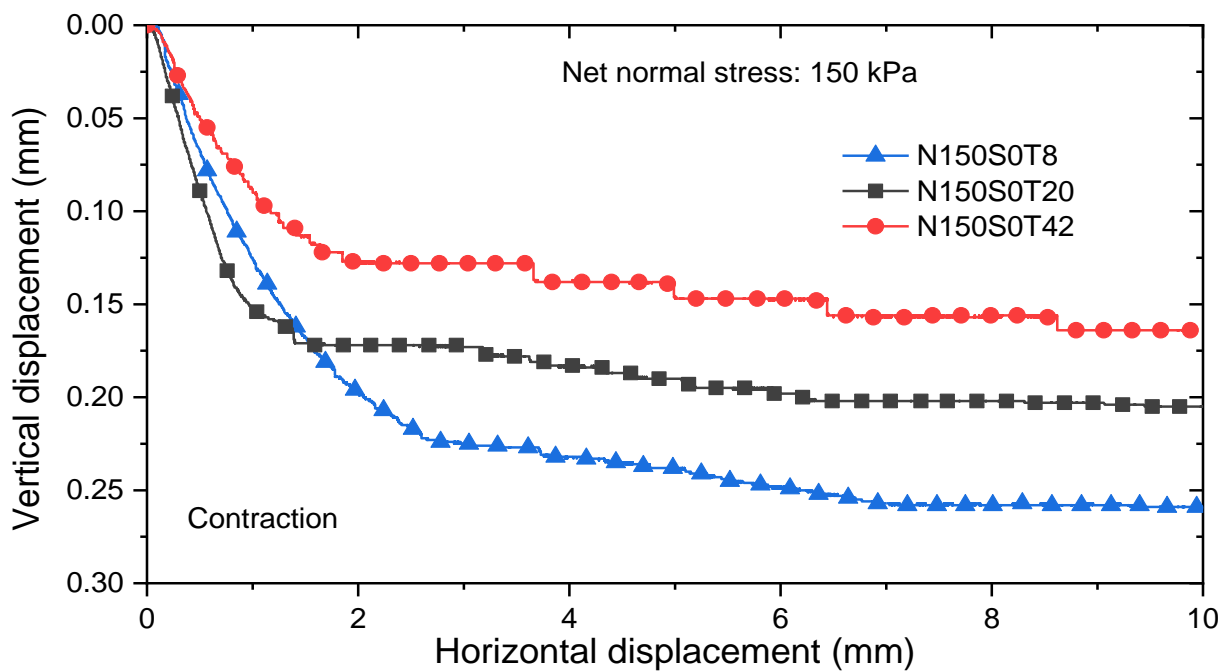


(b)

Figure 5.11. Shear behaviour of saturated CDG-structure interface at various temperatures and a net normal stress of 100 kPa: (a) stress-horizontal displacement relation; (b) shearing induced vertical deformation.

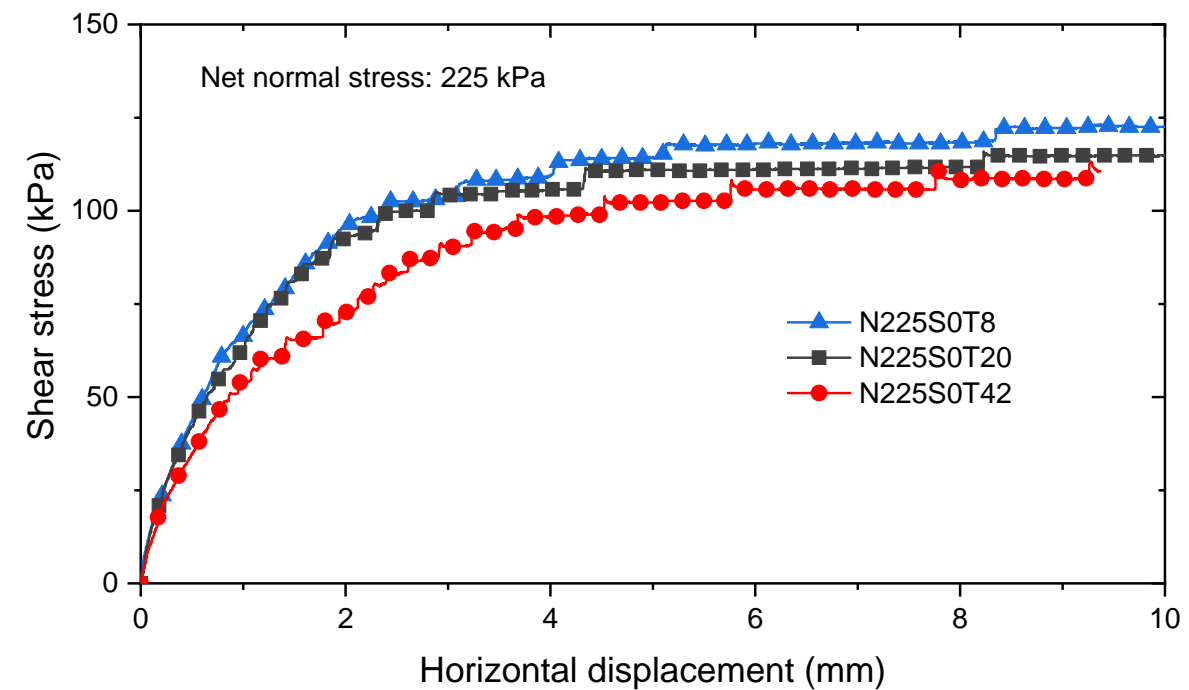


(a)

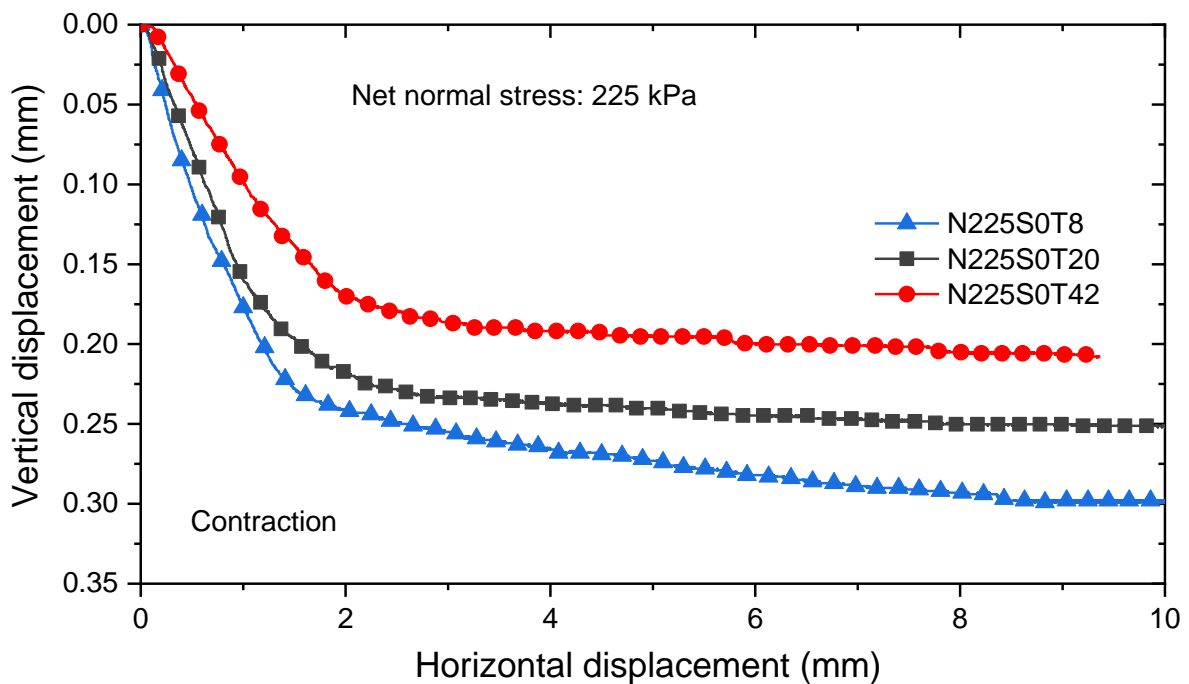


(b)

Figure 5.12. Shear behaviour of saturated CDG-structure interface at various temperatures and a net normal stress of 150 kPa: (a) stress-horizontal displacement relation; (b) shearing induced vertical deformation.

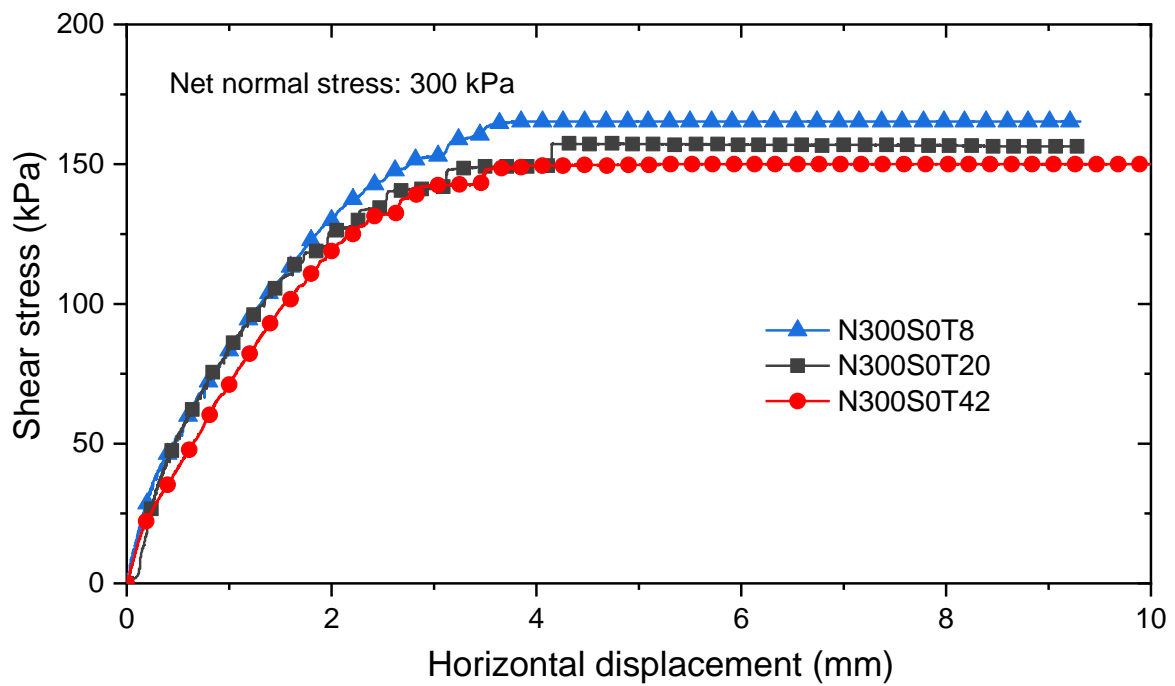


(a)

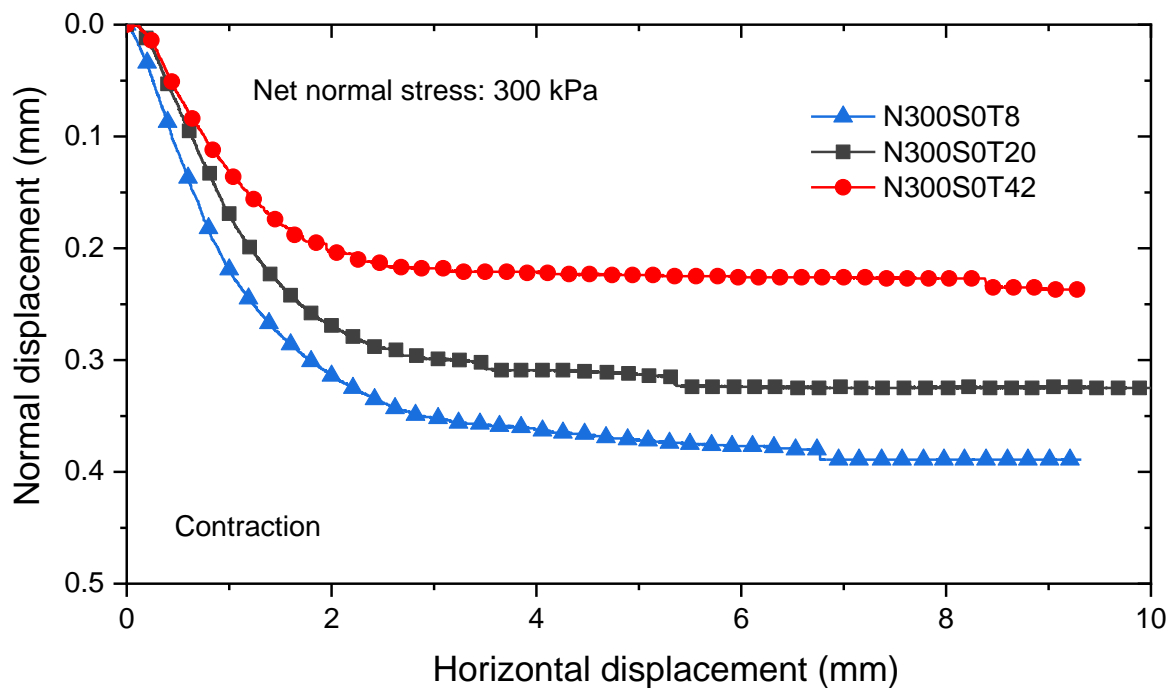


(b)

Figure 5.13. Shear behaviour of saturated CDG-structure interface at various temperatures and a net normal stress of 225 kPa: (a) stress-horizontal displacement relation; (b) shearing induced vertical deformation.



(a)



(b)

Figure 5.14. Shear behaviour of saturated CDG-structure interface at various temperatures and a net normal stress of 300 kPa: (a) stress-horizontal displacement relation; (b) shearing induced vertical deformation.

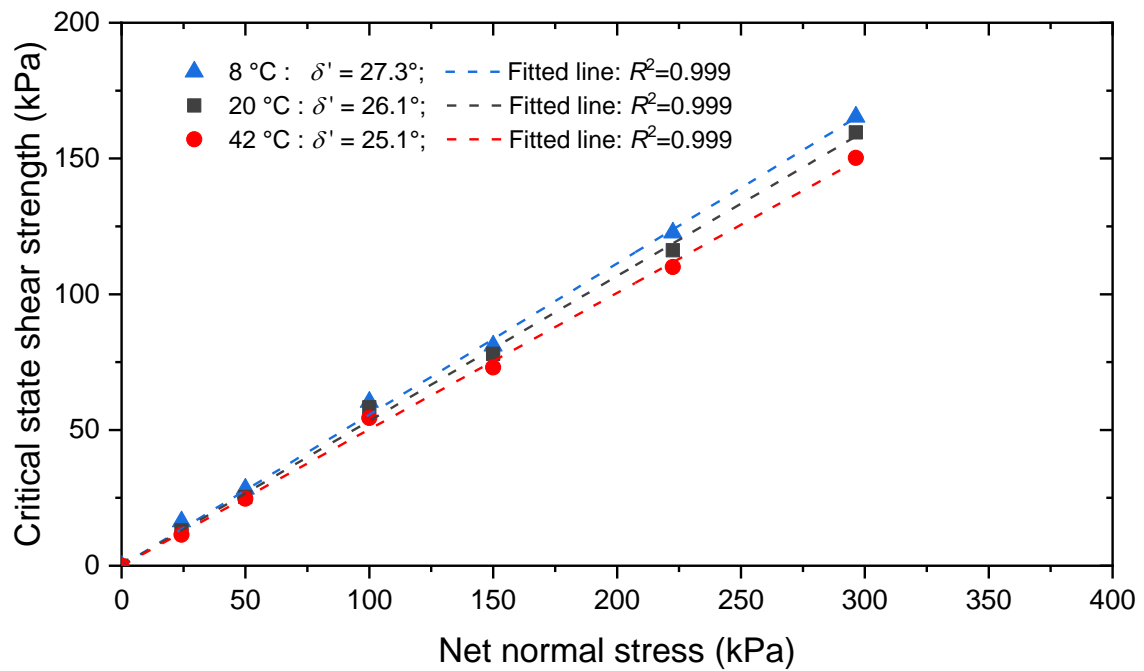


Figure 5.15. Critical state shear strength of saturated CDG-structure interface at different temperatures.

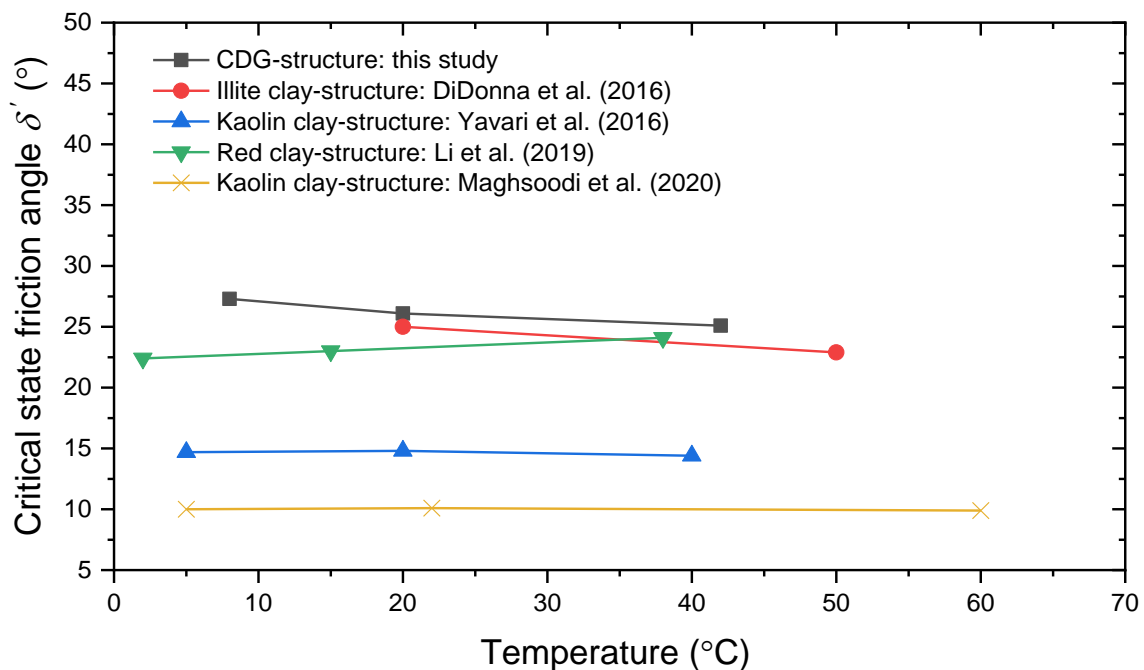
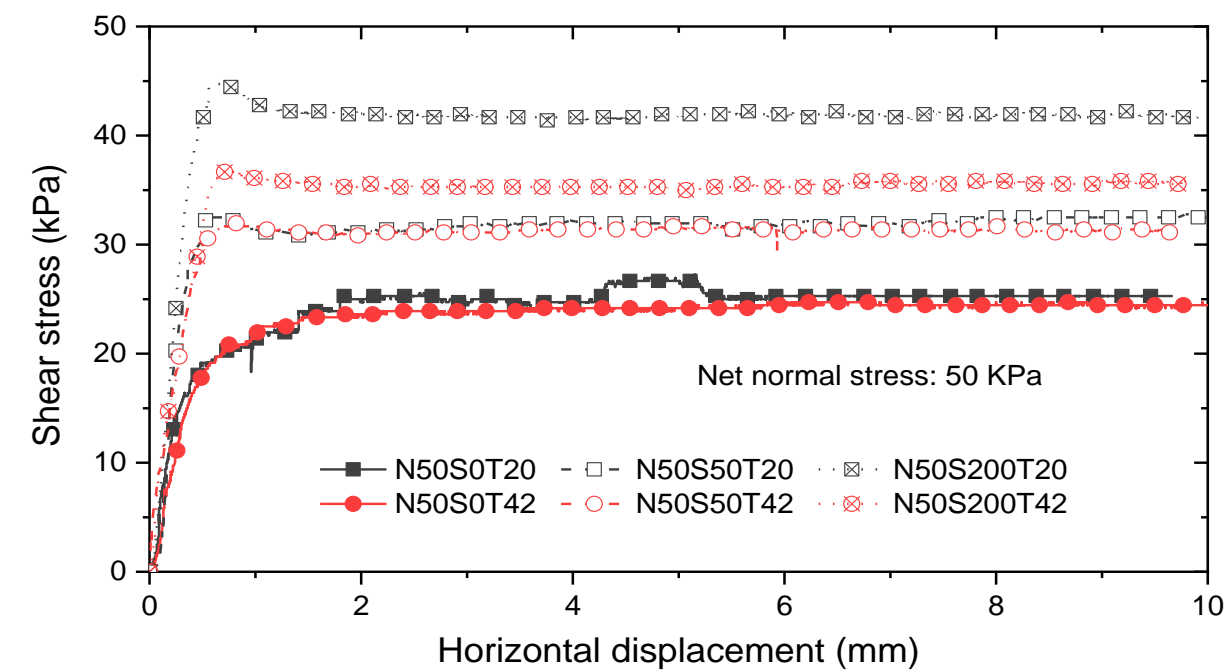
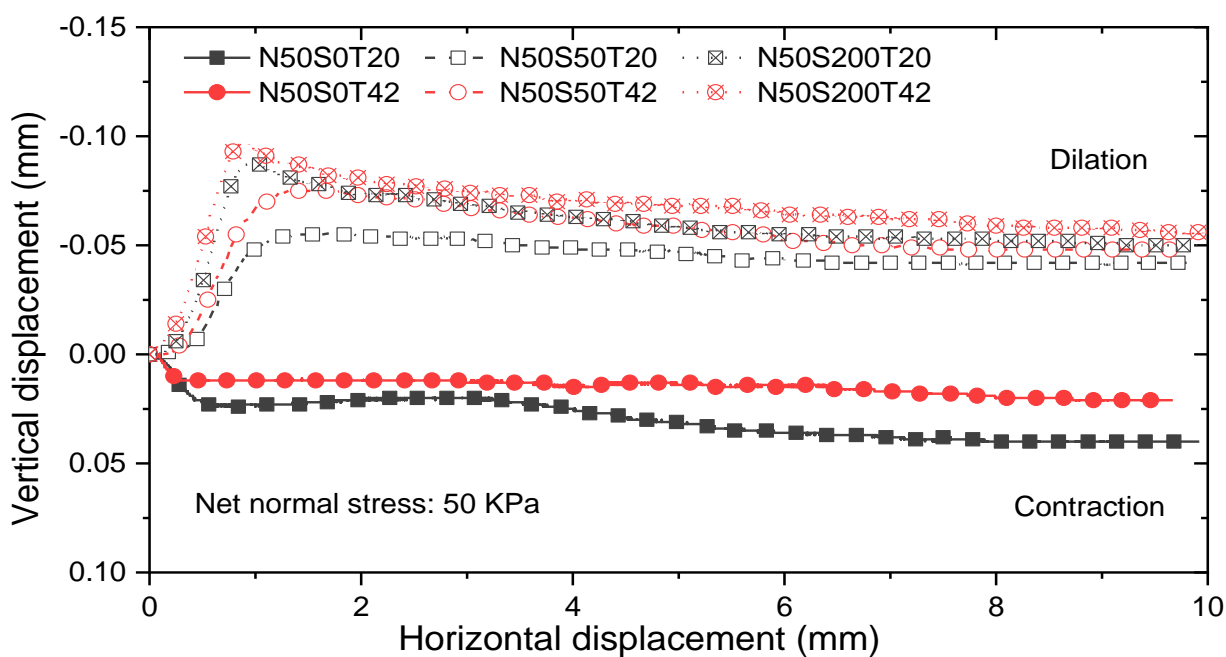


Figure 5.16. Temperature effects on the critical state friction angle of different soil-structure interfaces.

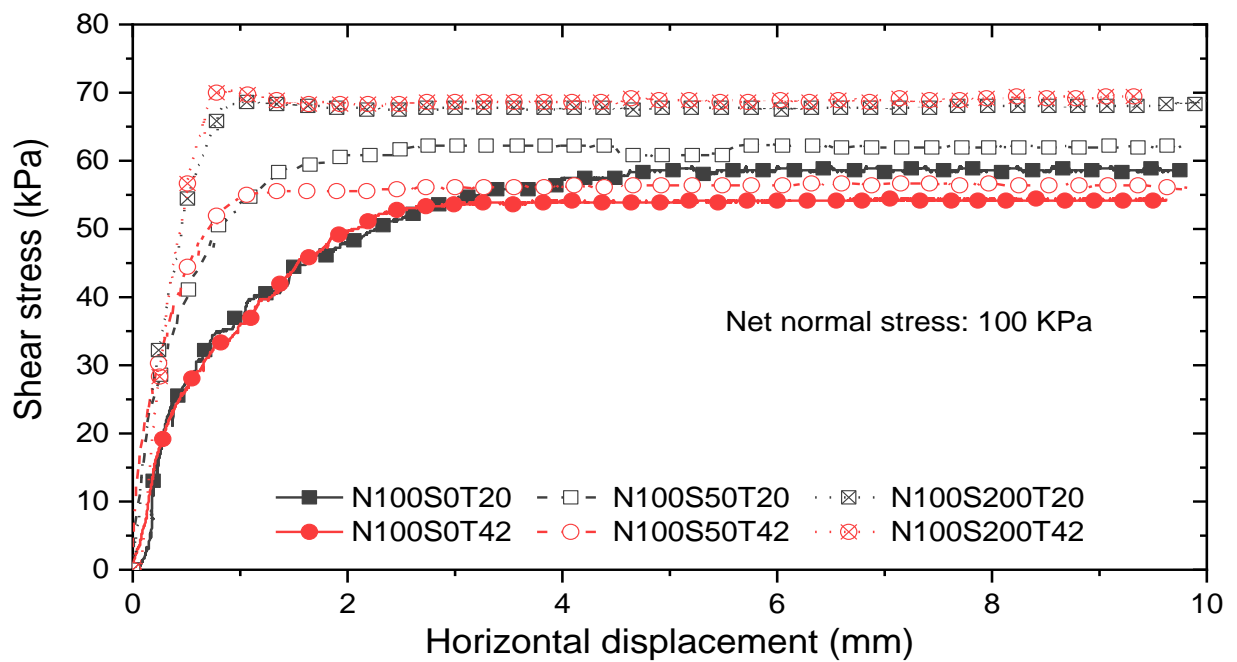


(a)

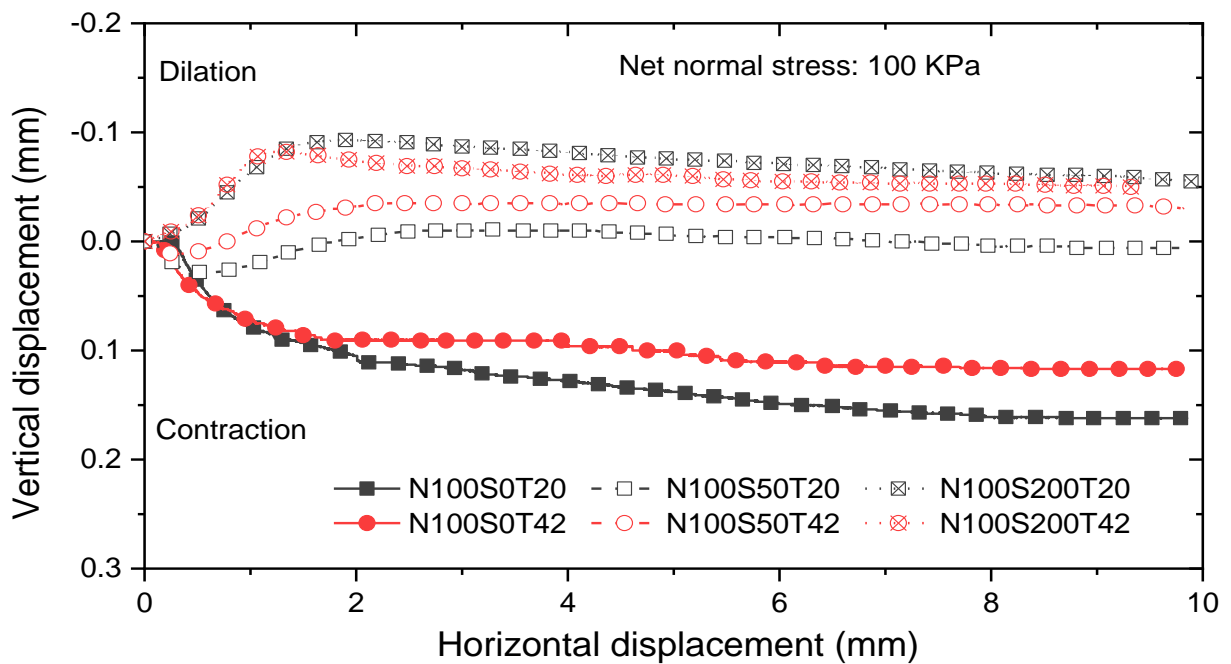


(b)

Figure 5.17. Shear behaviour of unsaturated CDG-structure interface at various temperatures and a net normal stress of 50 kPa: (a) stress-horizontal displacement relation; (b) shearing induced vertical deformation.

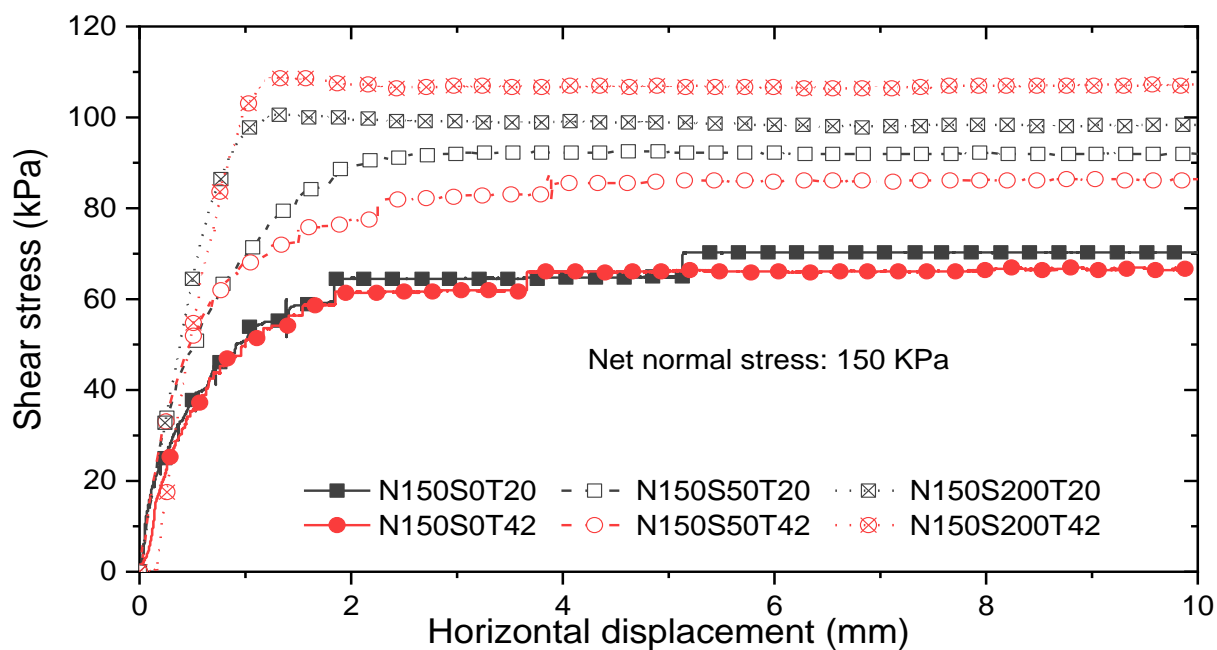


(a)

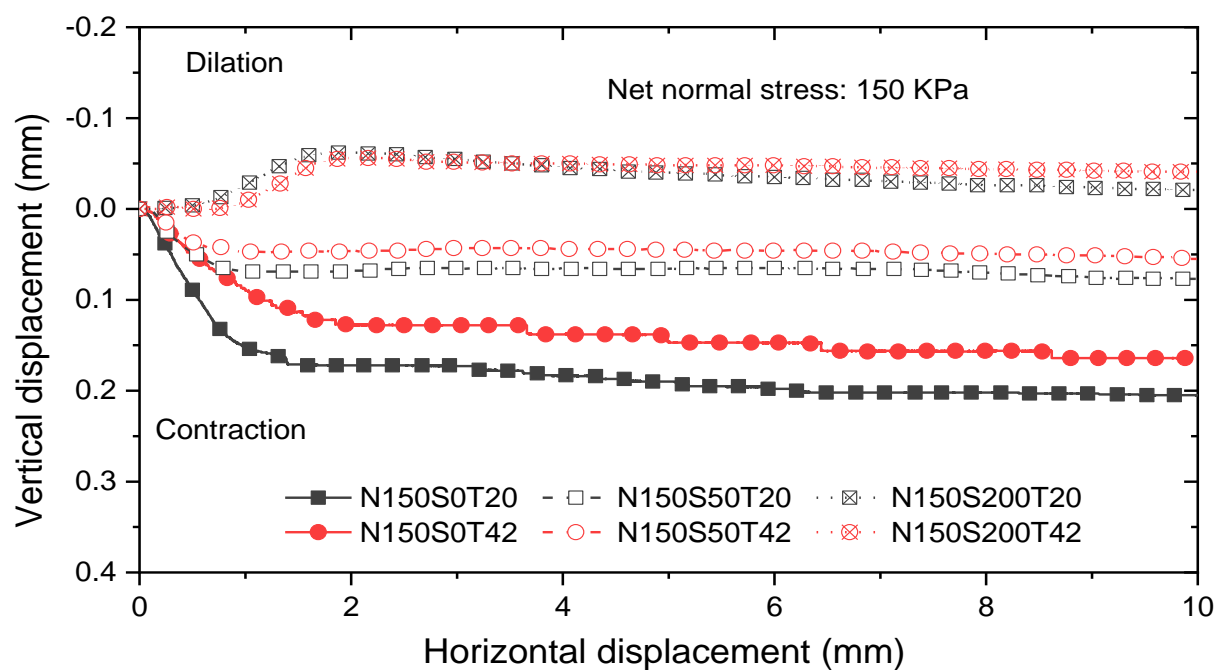


(b)

Figure 5.18. Shear behaviour of unsaturated CDG-structure interface at various temperatures and a net normal stress of 100 kPa: (a) stress-horizontal displacement relation; (b) shearing induced vertical deformation.



(a)



(b)

Figure 5.19. Shear behaviour of unsaturated CDG-structure interface at various temperatures and a net normal stress of 150 kPa: (a) stress-horizontal displacement relation; (b) shearing induced vertical deformation.

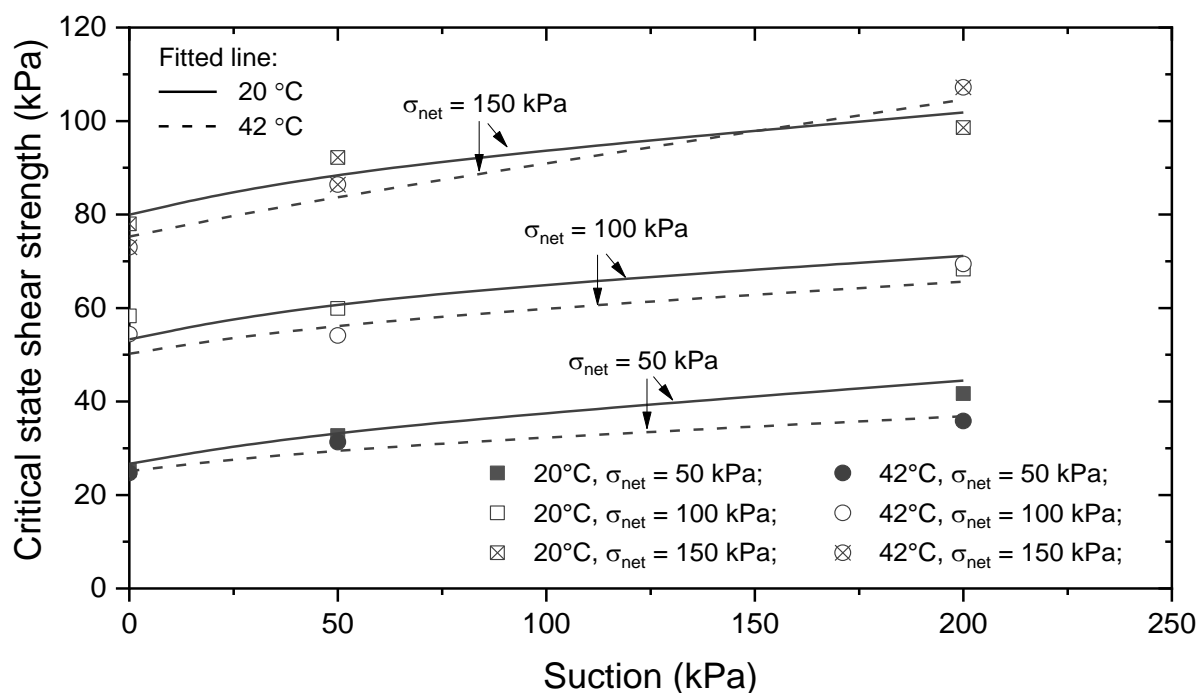


Figure 5.20. Critical state shear strength of unsaturated CDG-structure interface in the plane of: shear strength versus suction.

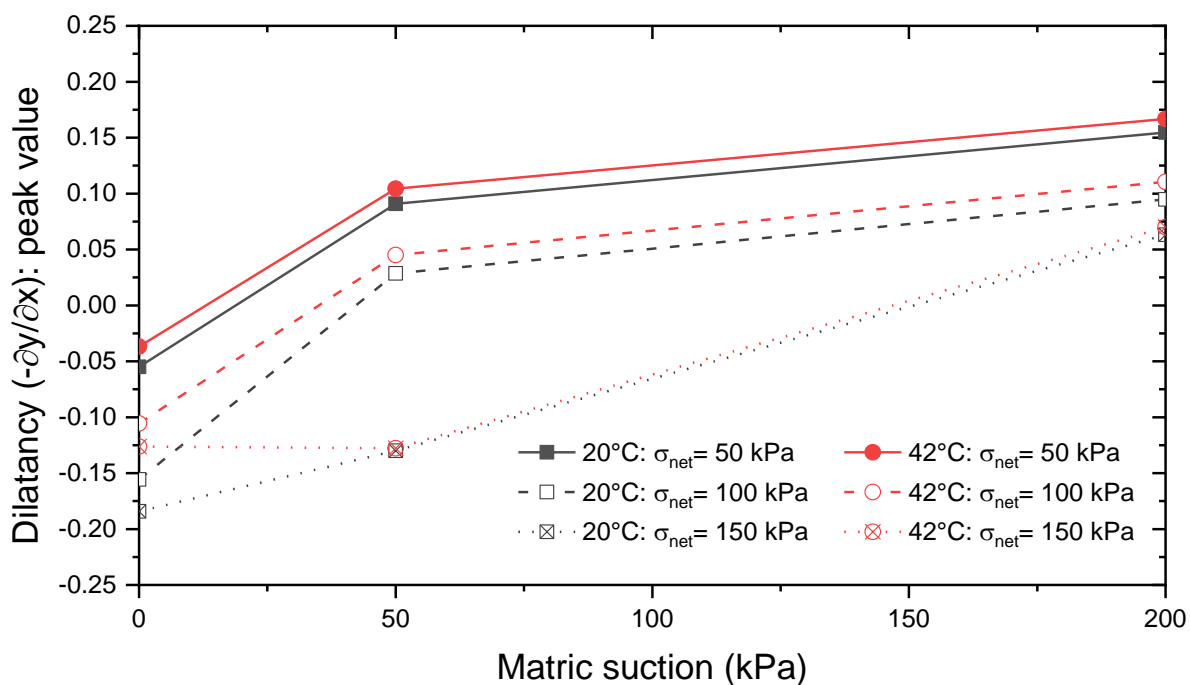


Figure 5.21. Dilatancy of CDG-structure interface at different suctions, temperatures and net normal stresses

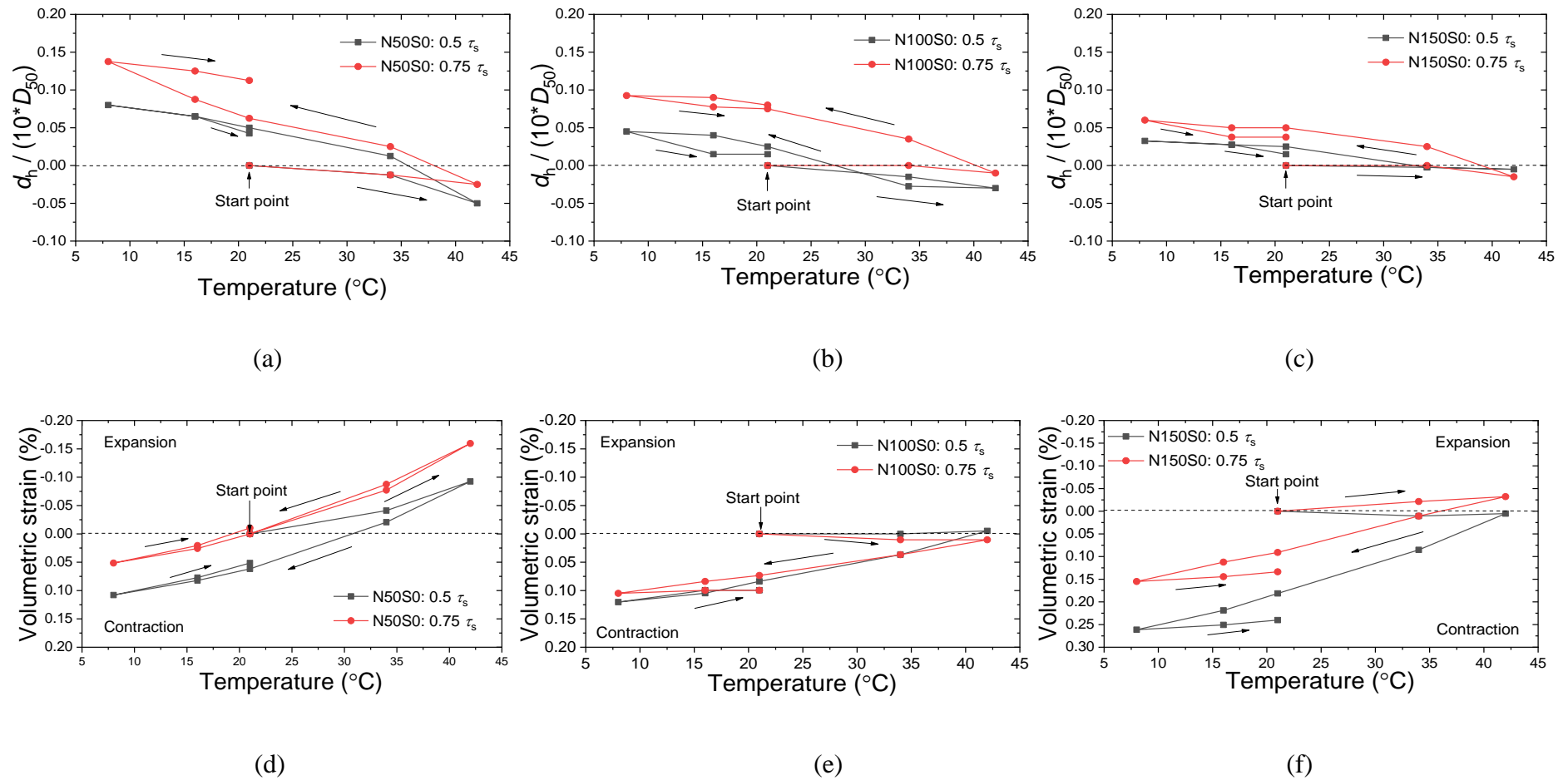


Figure 5.22. Shear behaviour of saturated CDG-structure interface during heating and cooling: (a), (b), (c) normalized tangent displacement; (d), (e), (f) volumetric strain.

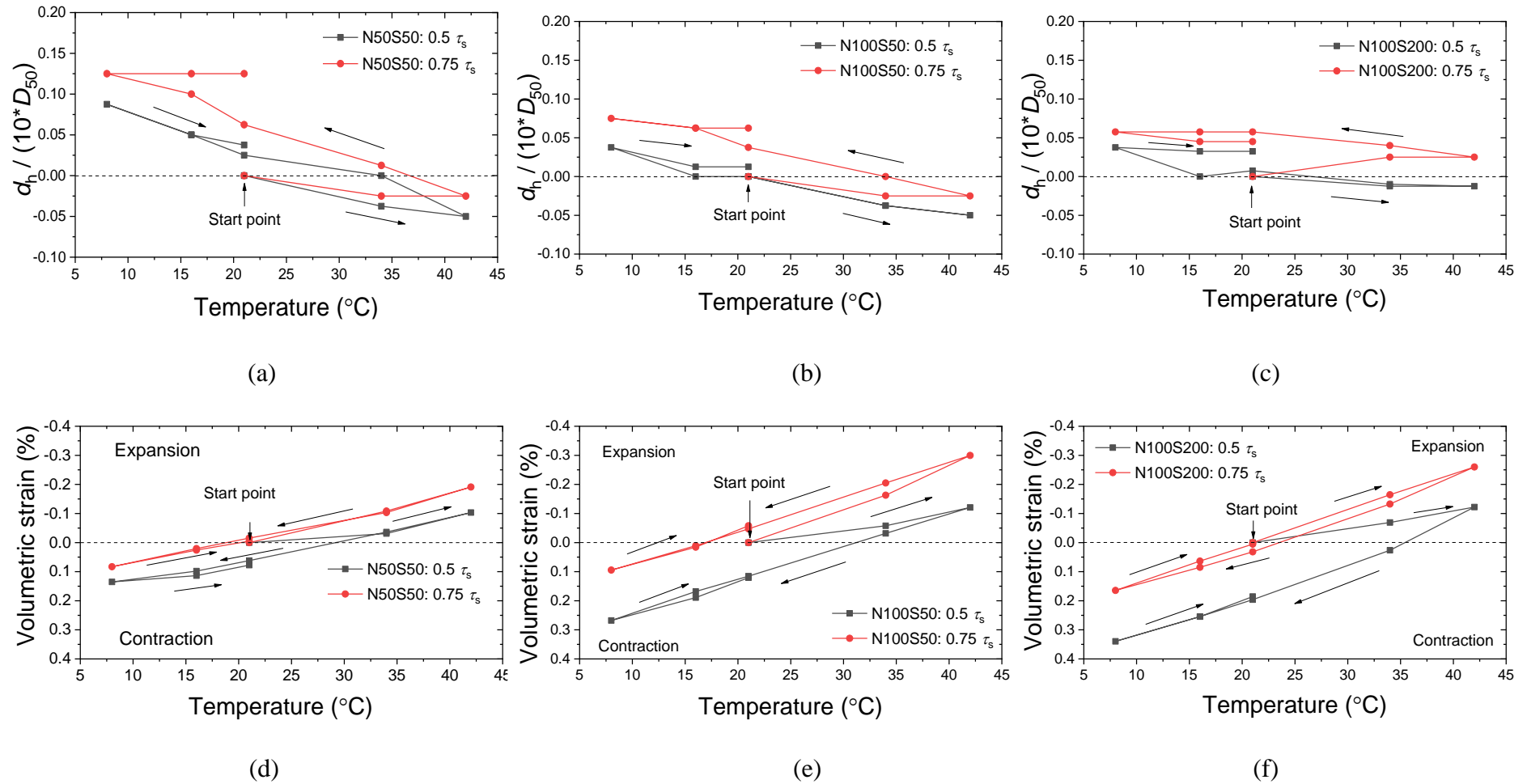
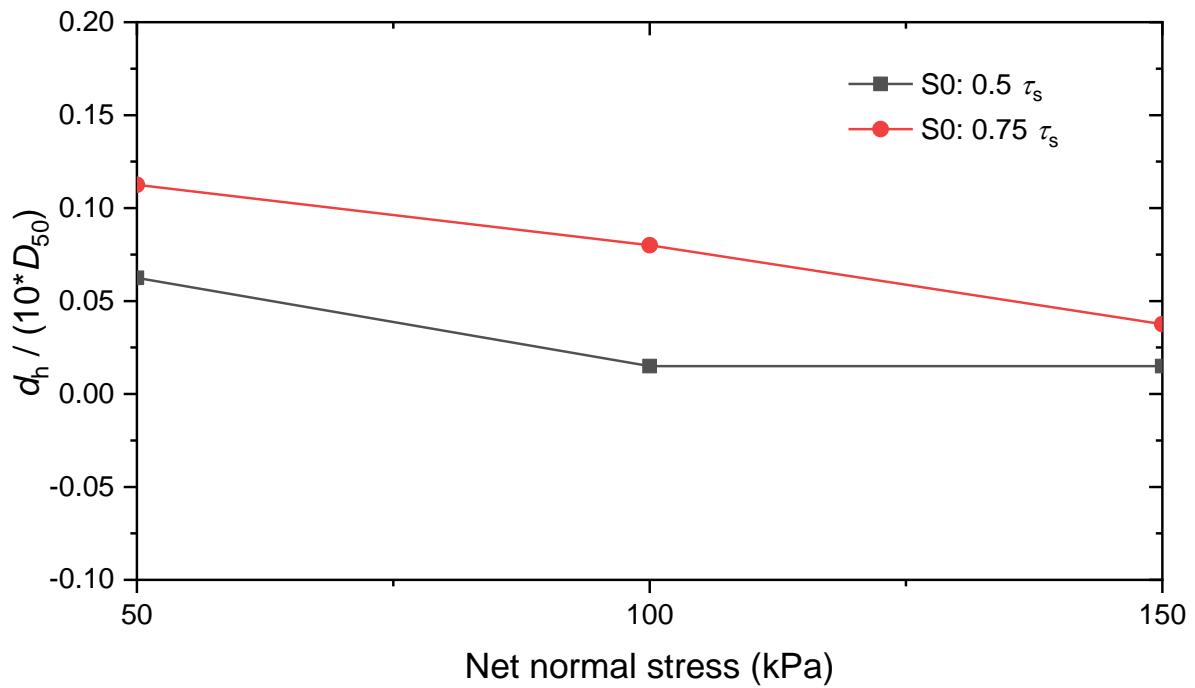
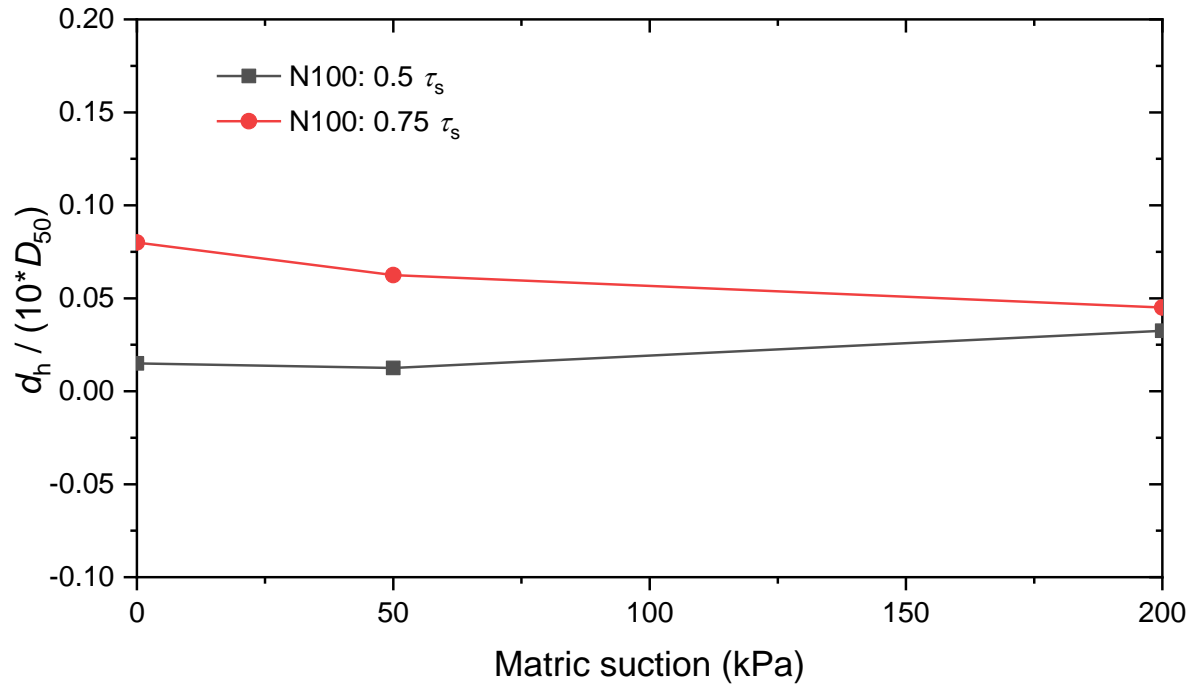


Figure 5.23. Shear behaviour of unsaturated CDG-structure interface during heating and cooling: (a), (b), (c) normalized tangent displacement; (d), (e), (f) volumetric strain.



(a)



(b)

Figure 5.24. Irreversible tangent displacement induced by one thermal cycle: (a) effects of net normal stress; (b) effects of suction.

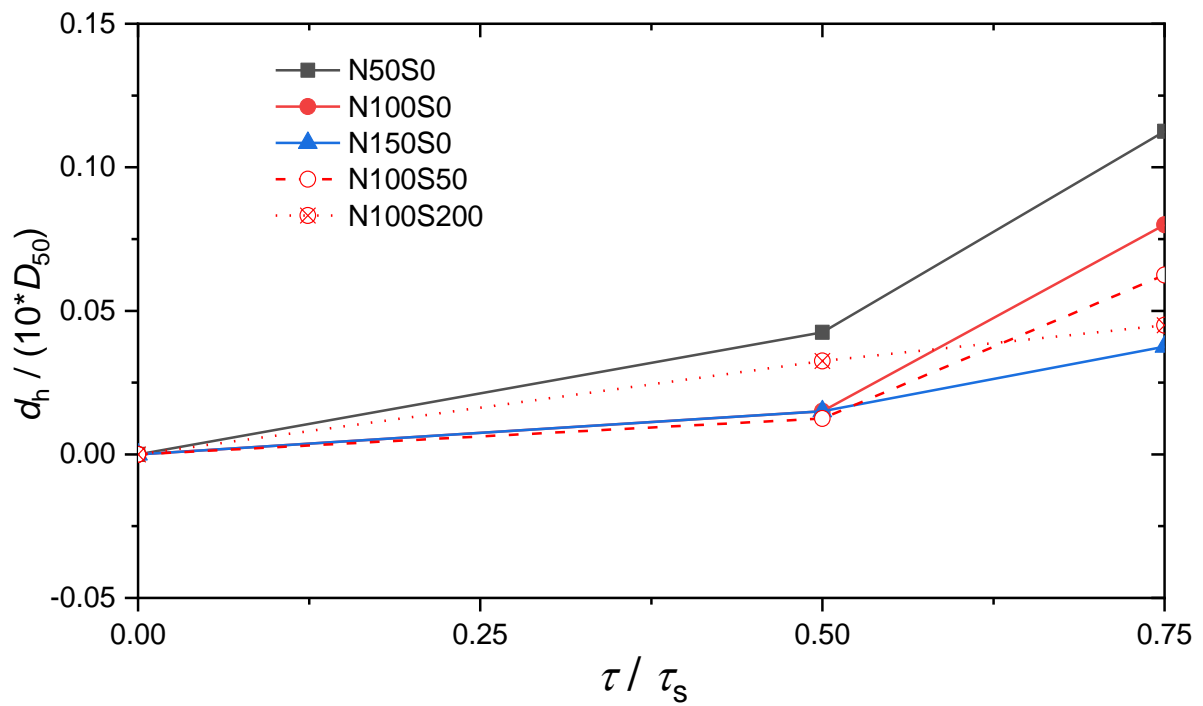


Figure 5.25. Influence of shear stress on the irreversible tangent displacement induced by one thermal cycle.

## CHAPTER 6: A Thermo-Mechanical Model For Saturated and Unsaturated Soil-structure Interfaces

In this chapter, a critical state-based constitutive model is newly developed to predict the thermo-mechanical behaviour of saturated and unsaturated interfaces. The development of mathematical formulations and calibration of model parameters are presented in detail. The model verification is conducted by using the data in the literature and Chapter 5. A good consistency between the measured data and computed results is obtained.

### 6.1 Mathematical formulations

#### 6.1.1. Constitutive stress variables

To simulate the thermo-mechanical behaviour of saturated and unsaturated soil-structure interfaces, the current model adopts temperature and the following two stress state variables:

$$\begin{Bmatrix} \sigma_n^* \\ \tau \end{Bmatrix} = \begin{Bmatrix} \sigma_{net} + (S_r)^\kappa \cdot (u_a - u_w) \\ \tau \end{Bmatrix} \quad (6-1)$$

where  $\sigma_n^*$  is the effective normal stress at the interface, a positive value of which means compression;  $\tau$  is the shear stress at the interface;  $\sigma_{net}$  is the net normal stress at the interface defined as the difference between total normal stress and pore air pressure;  $S_r$  is the degree of saturation of soil;  $\kappa$  is a model parameter;  $u_a$  and  $u_w$  are the pore air and water pressures of soil, respectively. The difference between pore air and water pressures ( $u_a - u_w$ ) is defined as matric suction and it is referred to as suction in the following paragraphs for simplicity.

The definition for  $\sigma_n^*$  in equation (6-1) is based on Bishop's stress with  $\chi = (S_r)^\kappa$ , which is a scaling parameter (Bishop, 1959). This expression for  $\chi$  has the same effects as

achieved by Alonso et al. (2013), who used the effective degree of saturation  $S_r^e$  for the definition of scaling parameter (i.e.  $\chi = S_r^e$ ) but then proposed that  $S_r^e$  could be approximated by a power function of  $S_r$ . It should be noted that some theoretical studies based on thermodynamic analysis suggest that the value of  $\kappa$  should be equal to 1 for unsaturated soil. For the modelling of unsaturated interface, it is found in this study that  $\kappa = 1$  would result in significant errors. This is likely because the shear-induced drainage occurred inside the shear band at the interface and hence the degree of saturation at the interface is not equal to that of the soil specimen. To elaborate this problem, the critical state shear strength is used as one example, as it is one of the most important components in many models. It is desired that the critical state lines (CSLs) at various suctions converge to a unique line in the  $\sigma_n^* - \tau$  plane, which can be described by equation (6-2):

$$\tau = \sigma_n^* M \quad (6-2)$$

where  $M$  is the critical state stress ratio that is usually assumed independent of suction.

This equation is applied to calculate the critical state shear strength of an unsaturated soil-cement interface tested by Hossain and Yin (2012) in a suction range of 0 to 300 kPa. The value of  $M$  is calibrated based on test results at zero suction and then used to calculate the shear strength in unsaturated conditions. Three cases with different scaling parameters are considered:  $\chi = S_r$ ,  $\chi = S_r^e$  and  $\chi = (S_r)^\kappa$ . Figure 6.1 compares the calculated and measured results of critical state shear strength. In the case of  $\chi = S_r$ , suction effects on the critical state shear strength are greatly overestimated. At some stress and suction conditions, the calculated value is more than 1.5 times the measured one. For the case of  $\chi = S_r^e$ , the residual degree of

saturation is calibrated to be 60% based on the test data of Hossain and Yin (2010). The underestimation of the shear strength is up to 50%, which is still very significant. In addition, it is often difficult to determine the residual degree of saturation for fine-grained soils (Vanapalli et al., 1996). Finally, the model prediction with  $\chi = (S_r)^k$  is also determined and shown in Figure 6.1. The value of  $a$  is determined to be 4 using the least squares method. The measured and calculated results are well matched. As compared to the two cases above, the modelling of critical state shear strength has been significantly improved. This is one of the major differences between the current model and previous models for unsaturated interfaces.

When soil becomes fully saturated (*i.e.*  $S_r = 1$ ),  $\sigma_n^*$  reduces to the effective stress formulation (Terzaghi, 1943). Therefore, equation (6-1) can be used for both saturated and unsaturated interfaces with a single set of parameters and it allows for a smooth transition between unsaturated and saturated conditions.

In addition, it is well recognized that it remains challenging to model unsaturated soil behaviour, particularly the volume change behaviour under various hydro-mechanical loads, by using  $\sigma_n^*$  only. This is because suction can affect soil behaviour via different mechanisms, such as changing the average skeleton stress and increasing the inter-particle normal stress by water meniscus (Wheeler et al., 2003a; Ng et al., 2020; Gens Solé, 2009). Hence,  $S_r$  in addition to  $\sigma_n^*$  is used in the development of constitutive model.

### 6.1.2. Critical state shear strength

As illustrated above, the CSLs of saturated and unsaturated interfaces in the  $\sigma_n^* - \tau$  plane can be modelled by a unified equation with  $\chi = (S_r)^k$ . Note that similar findings were

reported for the critical state shear strengths of pure soils, where the value of  $\kappa$  could be maintained at 1 to obtain good predictions (Nuth and Laloui, 2008; Lashkari and Torkanlou, 2016; Lloret-Cabot et al., 2013). Furthermore, the data in Chapter 5 suggests that the value of  $a$  is independent of temperature, and equal to a constant value of 4.7.

Test data suggests that the friction angle of a soil-structure interface is slightly affected by temperature. The relationship between friction angle and temperature can be approximated by a straight line in the typical temperature range of energy geostructures (i.e., 4 to 40°C), as shown in Figure 5.11.

Based on these two findings, the CSLs at various suctions and temperatures are modelled using equations (6-2) to (6-3):

$$M = M_0 - r_M(T - T_0) \quad (6-3)$$

where  $M_0$  is the critical state stress ratio at the reference temperature;  $r_M$  is a parameter describing the sensitivity of critical state stress ratio to temperature. Figure 5.11 reveals that the critical state stress ratio either increases or decreases with an increase in temperature, depending on the specific type of soil-structure interface. Thus, the value of  $r_M$  could be either positive or negative.

### 6.1.3. Critical state void ratio and state parameter

Similar to the behaviour of pure soils (Zhou and Ng, 2016), it is observed that the critical state void ratio in the shear zone of a soil-structure interface is also affected by temperature and degree of saturation.

Under the saturated condition, the CSLs in the  $e - \ln\sigma_n^*$  plane at various temperatures can be assumed to be parallel, according to the experimental results in Chapter 5. They are therefore described using the following two equations:

$$e_{cs} = \Gamma(T) - \omega_0 \ln\left(\frac{\sigma_n^*}{p_{atm}}\right) \quad (6-4)$$

$$\Gamma(T) = \Gamma_0 - r_T(T - T_0) \quad (6-5)$$

where  $e_{cs}$  is the critical state void ratio under the saturated condition at a given  $\sigma_n^*$  value;  $\Gamma(T)$  and  $\omega$  are the intercept and slope of the CSL, respectively;  $p_{atm}$  is the atmospheric pressure (i.e., 103 kPa);  $\Gamma_0$  is the  $\Gamma$  value at the reference temperature;  $r_T$  is a parameter describing the sensitivity of critical state void ratio to temperature.

As soil desaturates, the critical state void ratio at a given  $\sigma_n^*$  generally becomes larger. This is because meniscus water lenses under unsaturated conditions can stabilize the soil skeleton, as illustrated by Wheeler et al. (2003a) in detail. The unsaturated CSLs is linked to the saturated one through the following equation (Gallipoli et al., 2003):

$$\frac{e_c}{e_{cs}} = (S_r)^{-\eta} \quad (6-6)$$

where  $e_c$  is the critical void ratio under unsaturated condition conditions at  $\sigma_n^*$ ;  $\eta$  is a model parameter to describe the influence of moisture condition on the critical state void ratio. Based on the experimental results in Chapter 5, it is observed that  $c$  is related to temperature. To model the coupling effects of temperature and suction on CSLs, the following equation is proposed:

$$\eta(T) = \eta_0 \cdot \left(\frac{T+273}{T_0+273}\right)^d \quad (6-7)$$

where  $\eta_0$  is the  $\eta$  value at the reference temperature. Based on equations (6-4) to (6-7), it is derived that:

$$e_c = \Gamma(T, S_r) - \omega(T, S_r) \cdot \ln\left(\frac{\sigma_n^*}{p_{atm}}\right) \quad (6-8)$$

$$\begin{cases} \Gamma(T, S_r) = [\Gamma_0 - r_\Gamma(T - T_0)] \cdot (S_r)^{\eta_0 \cdot \left(\frac{T+273}{T_0+273}\right)^d} \\ \omega(T, S_r) = \omega_0 \cdot (S_r)^{\eta_0 \cdot \left(\frac{T+273}{T_0+273}\right)^d} \end{cases} \quad (6-9)$$

where  $\Gamma(T, S_r)$  and  $\omega(T, S_r)$  are the intercept and slope of CSLs, respectively. Both of them are dependent on temperature and degree of saturation. When soil is wetted to the saturated condition, the values of  $\Gamma(T, S_r)$  and  $\omega(T, S_r)$  are equal to those in the saturated condition (i.e.,  $\Gamma_0 - r_\Gamma(T - T_0)$  and  $\omega_0$ ). Therefore, equations (6-8) and (6-9) are applicable for both saturated and unsaturated conditions.

Based on CSLs, Figure 6.2 shows the definition of a state parameter ( $\psi$ ) proposed by Been and Jefferies (1985):

$$\psi = e - e_c \quad (6-10)$$

where  $e$  and  $e_c$  are the current and critical state void ratios, respectively, with the same values of  $\sigma_n^*$  and  $S_r$ . For the value of  $\psi$ , a positive value means the wet sides of the CSL, while a negative value is representative of the dry side.

#### 6.1.4. Elasto-plasticity

The current interface model is developed based on the bounding surface plasticity framework of Dafalias (1986). Compared to the classical elastoplastic framework, it shows some advantages such as the smooth transition between elastic and elastoplastic behaviour. The increments of normal and shear strains at the interface are defined as follows:

$$\begin{cases} d\varepsilon_n = \frac{du_n}{t} \\ d\varepsilon_t = \frac{du_t}{t} \end{cases} \quad (6-11)$$

where  $u_n$  and  $u_t$  are the normal and shear displacements at the interface, respectively. A positive value of  $u_n$  means contraction, while the shear displacement at the interface (i.e.,  $u_t$ ) is equal to the relative displacement between soil and structure.  $t$  is the thickness of the shear band at the interface;  $d\varepsilon_n$  and  $d\varepsilon_t$  are the total increment of normal and shear strains, respectively. At each loading/unloading process, the total incremental strains consist of elastic and plastic components:

$$\begin{cases} d\varepsilon_n = d\varepsilon_n^e + d\varepsilon_n^p \\ d\varepsilon_t = d\varepsilon_t^e + d\varepsilon_t^p \end{cases} \quad (6-12)$$

where  $d\varepsilon_n^e$  and  $d\varepsilon_t^e$  are the elastic increments of normal and shear strains, respectively;  $d\varepsilon_n^p$  and  $d\varepsilon_t^p$  are the plastic increments of normal and shear strains, respectively. For each strain variable, its elastic and plastic components are determined using a decoupled approach as follows:

$$\begin{cases} d\varepsilon_n^e = \frac{d\sigma_n^*}{D_n} - \frac{\alpha_c dT}{1+e} \\ d\varepsilon_t^e = \frac{d\tau}{D_t} \end{cases} \quad (6-13)$$

$$\begin{cases} d\varepsilon_n^p = \Lambda_t d_t \\ d\varepsilon_t^p = \Lambda_t \end{cases} \quad (6-14)$$

where  $D_n$  is the elastic normal modulus;  $D_t$  is the elastic tangent modulus;  $\Lambda_t$  is the loading index associated with shearing, determined by using the condition of consistency and the hardening law;  $d_t$  is the dilatancy defined as the ratio of plastic normal strain to plastic shear strain during the shearing process, and it is obtained from the flow rule.

For simplicity, equation (6-14) has three assumptions: (i) the behaviour of an interface subjected to constant stress ratio compression is elastic; (ii) the plastic normal and shear strains upon drying/wetting are indirectly considered by the shearing mechanism; (iii) the plastic

normal and shear strains upon heating-cooling are not considered, considering that there is no relevant experimental data in the literature and the limited data in Chapter 5 (i.e., the results of constant-stress heating-cooling tests) may not be sufficient for drawing a general conclusion. These three assumptions can minimize the number of soil parameters, while the proposed model is still able to well capture the key features of interface behaviour, as shown later.

### 6.1.5 Bounding and yield surfaces

To model the elastoplastic interface behaviour and determine the plastic strain components in equation (6-13), the current model adopts the approach of Wang et al. (1990). Two bounding surfaces are defined in the  $\sigma_n^* - \tau$  plane, including a memory bounding surface and a failure bounding surface, as shown in Figure 6.3. The memory bounding surface is described by equation (6-15) and its location is governed by the maximum stress ratio ( $M_m$ ) of the interface in the stress history:

$$F_t = \tau - M_m \sigma_n^* \quad (6-15)$$

The so-called failure bounding surface is mathematically defined as:

$$\bar{F}_t = \tau - M_b \sigma_n^* \quad (6-16)$$

$$M_b = M \exp(-n_b \psi) \quad (6-17)$$

where  $M_b$  is the attainable peak stress ratio (failure stress ratio) (Dafalias and Manzari, 2004) at the current state parameter and net normal stress;  $n_b$  is a positive model parameter.

In addition, a yield surface is defined in the  $\sigma_n^* - \tau$  plane using the following equation (Gajo and Muir Wood, 1999; Dafalias and Manzari, 2004):

$$f_t = \left| \frac{\tau}{\sigma_n^*} - \alpha \right| - m \quad (6-18)$$

where  $\alpha$  is a stress ratio depending on the stress history;  $m$  is a soil parameter. Equation (6-18) defines a “wedge”, which is the elastic threshold of an interface subjected to shearing. The use of this elastic wedge could eliminate the problems of numerical oscillation.

#### 6.1.6. Condition of consistency

Among the two bounding surfaces, the condition of consistency is applied on the memory bounding surface. It suggests that

$$\frac{\partial F_t}{\partial \sigma_n^*} d\sigma_n^* + \frac{\partial F_t}{\partial \tau} d\tau + \frac{\partial F_t}{\partial T} dT + \frac{\partial F_t}{\partial M_m} \frac{\partial M_m}{\partial \varepsilon_n^p} d_t \Lambda_t = 0 \quad (6-19)$$

It should be noted that the memory bounding surface is assumed to be independent of temperature, so the term  $\frac{\partial F_t}{\partial T} dT$  is equal to zero. Similar to some state-dependent models for saturated and unsaturated soils (Zhou et al., 2015; Chiu and Ng, 2003; Li and Dafalias, 2000), a plastic modulus ( $K_t^p$ ) is defined as follows:

$$K_t^p = -\frac{\partial F_t}{\partial M_m} \frac{\partial M_m}{\partial \varepsilon_n^p} d_t \quad (6-20)$$

By substituting equation (6-20) into (6-19), it is obtained that:

$$\Lambda_t = \frac{1}{K_t^p} \left( \frac{\partial F_t}{\partial \sigma_n^*} d\sigma_n^* + \frac{\partial F_t}{\partial \tau} d\tau \right) = \frac{1}{K_t^p} (d\tau - M_m d\sigma_n^*) \quad (6-21)$$

According to equations (6-12), (6-14) and (6-21), the relationship between stress and strain of the interface can be predicted when  $D_n$ ,  $D_t$ ,  $d_t$  and  $K_t^p$  are available. These four variables are determined using the same method as Zhou et al. (2020), in which a more detailed discussion is available. Some key equations are summarized in the appendix.

It should be highlighted that the model of Zhou et al. (2020) was proposed for isothermal interface behaviour with an assumption of  $\chi = S_r$ . The current model has two major differences from this model. Firstly, the current model improves the modelling of critical state shear strength by using  $\chi = (S_r)^\kappa$ . Secondly, the CSLs in the  $\sigma_n^* - \tau$  and  $e - \ln \sigma_n^*$  planes are

affected by temperature in the current model. Consequently, the coupled effects of temperature and degree of saturation on the interface behaviour can be considered.

## 6.2 Calibration of model parameters

The proposed model has 15 parameters and they are summarized in Table 6.1. Ten of them ( $t$ ,  $M_0$ ,  $\omega_0$ ,  $\Gamma_0$ ,  $D_{i0}$ ,  $R$ ,  $n_b$ ,  $h$ ,  $n_d$  and  $d_0$ ) are required for the saturated/dry interfaces at the isothermal condition. Among these ten parameters,  $t$  is the interface thickness and a constant value (5 mm in the following simulations) can be used. Its value does not affect the model prediction much as long as the same value is also used in the calibration of model parameters (Liu et al., 2006).

Two parameters ( $\kappa$  and  $\eta_0$ ) are used to incorporate unsaturation effects. Two parameters ( $r_M$  and  $r_\Gamma$ ) are required to simulate the thermal effects under the saturated condition. The additional parameter ( $d$ ) are used for considering the coupling effects between temperature and degree of saturation.

All of these parameters can be calibrated based on suction-, temperature- and stress-controlled interface tests. The calibration of all parameters for the isothermal condition is similar to that illustrated by Zhou et al. (2020). The other three parameters ( $r_M$ ,  $r_\Gamma$  and  $d$ ) can be calibrated based on test data at different temperatures. Key procedures for calibrating these four parameters are explained in the following paragraphs:

(i) Parameters  $r_M$  and  $r_\Gamma$  are determined by fitting the measured CSLs at the saturated condition but at various temperatures. It is obtained that:

$$r_M = \frac{M_0 - M}{T - T_0} \quad (6-22)$$

$$r_{\Gamma} = \frac{\Gamma_0 - \Gamma(T)}{T - T_0} \quad (6-23)$$

(ii) The parameters  $a(T)$  and  $c(T)$  at a given temperature can be determined using the measured CSLs of an unsaturated interface at various degrees of saturation but a reference temperature. Equations (6-1), (6-2) and (6-6) suggest that

$$\kappa = \log_{S_r} \left( \frac{\frac{\tau}{M_0} - \sigma_{net}}{u_a - u_w} \right) \quad (6-24)$$

$$\eta_0 = -\log_{S_r} \left( \frac{e_c}{e_{cs}} \right) \quad (6-25)$$

The results at the reference temperature can be used to determine the value of  $a_0$  and  $c_0$ . The results at other temperatures are adopted to calibrate the parameter  $d$ :

$$d = \log_{\left(\frac{T+273}{T_0+273}\right)} \left[ \frac{\eta(T)}{\eta_0} \right] \quad (6-26)$$

To calibrate the above new model parameters, the test results in Chapter 5 are used. Firstly, the results of saturated interfaces are selected to calibrate the two parameters  $r_M$  and  $r_{\Gamma}$ . The critical shear strengths of saturated interfaces at various temperatures are plotted in Figure 6.4(a). Based on these data, the critical state stress ratios  $M$  at different temperatures are determined. Then, the new parameter  $r_M$  can be calculated through equation (6-22). The critical void ratios at different temperatures are presented in Figure 6.4(b). The compression indexes  $\Gamma$  are obtained by fitting the slopes of CSLs. Following the equation (6-23), the  $r_{\Gamma}$  is calibrated.

To capture the coupled effects of suction and temperature on interface behaviour, another four parameters  $\kappa$ ,  $\eta_0$  and  $d$  are used in the current model. The calibration processes of these three parameters are described in the following parts. Firstly, the critical shear strengths at various suctions are plotted in Figure 6.5(a). By using the known values of  $M_0$  at the reference temperature from Figure 6.4 and the measured degree of saturation in the test, the

parameter  $\kappa$  can be calculated through equation (6-24). According to the critical state ratios at different suctions shown in Figure 6.5(b), the  $\eta_0$  value can be calculated via the equation (6-25). By using the same method, the values of  $\eta(T)$  can be also obtained. Following the equations (6-26), the parameter  $d$  is obtained. In addition, for the volumetric deformation at unsaturated conditions, it is observed from Figure 6.5(b) that the measured and computed results are consistent, even though there are some minor differences.

### 6.3 Model validation

The proposed model is applied to simulate direct shear tests on interfaces at various stresses, suctions and temperatures. For each type of interface, the model parameters are calibrated using the above method and summarized in Table 6.1. First of all, the model is verified under two relatively conditions: unsaturated conditions at the reference temperature, and non-isothermal conditions at the saturated condition. Then, the model is applied to simulate the behaviour of unsaturated interfaces at different temperatures.

#### 6.3.1. Shear behaviour of unsaturated interfaces at the isothermal condition

Hossain and Yin (2012) conducted a series of suction- and stress-controlled direct shear tests to investigate the shear behaviour of an unsaturated soil-cement interface. The axis-translation technique was used to control soil suction (Hilf, 1956). In their study, five different soil suctions (0, 50, 100, 200 and 300 kPa) were considered. A constant net normal stress of 100 kPa was applied in all unsaturated tests, while the saturated tests were conducted under four different net normal stresses (50, 100, 200 and 300 kPa).

The measured results at 100 kPa net normal stress and three different suctions (i.e., 0, 50 and 100 kPa) are shown in Figure 6.6. The experimental results show that with suction increasing from 0 to 100 kPa, the peak shear strength increases by 90%, while the increment of shear strength is only around 30% at the critical state. The difference in the shear strength increments resulting from suction effects is mainly attributed to the different dilatancy shown in Figure 6.6(b). A higher suction would result in larger dilatancy and more significant strain-softening, which were also observed in many other previous studies (Hamid and Miller, 2009; Zhan and Ng, 2006; Borana et al., 2018).

The comparisons between computed and measured results indicate that the newly proposed model can well predict the behaviour of the unsaturated interface at the isothermal temperature. It can be seen that the computed peak shear strength significantly increases with increasing suction. This is mainly because the increment of suction would result in an upward movement of the CSL in the  $e - \ln\sigma_n^*$  plane, shown in equation (6-6). As a result, the state parameter reduces and hence the interface becomes more dilative (see equations (A-3) and (A-4)), leading to a larger peak shear strength (see equation (6-17)). When the shear displacement is large enough, the interface almost reaches the critical state, at which the shear strength is governed by equations (6-1) and (6-2). The model is able to well capture suction effects on the interface behaviour at the critical state. Even though suction increases as the interface desaturates, the value of  $\sigma_n^*$  does not change too much, because the value of  $(S_r)^k$  decreases. Hence, the critical state shear strength remains almost constant with an increase in suction.

Figures 6.6(c) and (d) also present the computed results by the model of Zhou et al. (2020). Compared to the computed results through this existing model, it can be seen that the softening behaviour can be better captured by the new model. Furthermore, the prediction of shear strength at the critical state is also improved by using the new model. When the suction increases from 0 to 100 kPa, the measured critical state strength increases by about 30%. The computed increments by the new model and the model of Zhou et al. (2020) are about 35% and 70%, respectively. This means that the suction effects at the critical state are overestimated in the previous model (Zhou et al., 2020). At the isothermal condition, the major difference between these two models comes from the stress state variable. Zhou et al. (2020) assumed that  $\chi = S_r^e$ , while  $\chi$  is considered as  $(S_r)^k$ .

Figure 6.7 shows the measured and computed shear behaviour of saturated interfaces at different net normal stresses of 50, 100 and 300 kPa. With effective normal stress increasing, the interface presents larger shear strength and higher contraction. The influence of effective normal stress is well matched by the new model, as shown in Figures 6.7(a) and (b). The experimental results were also simulated by the model of Zhou et al. (2020), shown in Figures 6.7(c) and (d). It is also able to give an accurate prediction of the interface behaviour at the saturated and isothermal conditions.

### 6.3.2. Shear behaviour of saturated interfaces at different temperatures

Di Donna et al. (2016) developed a temperature-control direct shear device to investigate temperature effects on the shear behaviour of a saturated illite clay-concrete interface. Figure 6.8 present the measured results at three different effective normal stress (50,

100 and 150 kPa) and two different temperatures (20 and 50°C). It can be seen that at a given effective normal stress, the temperature elevation increases the shear strength and decreases the contraction during the shearing process. Taking the specimen at 50 kPa as an example, when the temperature increases from 20°C to 50°C, the shear strength increases by around 30%, while the contraction reduces by about 20%. The experimental results are simulated by the new model, and the computed results are also presented in Figure 6.8. It can be seen that the computed results are well matched with the experimental data. This is because temperature effects on the critical state stress ratio and void ratio are properly modelled by equations (6-3) to (6-5) through the parameters  $r_M$  and  $r_\Gamma$ .

Different from the observations of Di Donna et al. (2016), the experimental results in Chapter 5 demonstrate that the temperature elevation decreases the shear strength and increases the contraction, as shown in Figures 6.9 to 6.11. This is probably related to the soil type and counterface material, as discussed in Chapter 5. The new model is also used to simulate these experimental results. Three different effective normal stresses (50, 100 and 150 kPa) and three different temperatures (8, 20 and 42°C) are considered. The proposed model is still able to give a reasonably good prediction, even though the temperature effects on interface behaviour are opposite to those in Figure 6.8. This is because the parameters  $r_M$  and  $r_\Gamma$  in equations (6-3) and (6-5) vary with the materials of soil and counterface. It also implies that the new model is applicable to simulate the behaviour of a wide range of interfaces under non-isothermal conditions.

### 6.3.3. Shear behaviour of unsaturated interfaces at different temperatures

As far as the author is aware, there is no experimental data about the coupled effects of temperature, stress and suction on the shear behaviour of unsaturated soil-structure interfaces in the literature. The test results in Chapter 5 are unique and it is used to evaluate the model performance at various suctions and temperatures.

Figures 6.12 to 6.17 presents the experimental results at three different net normal stresses (50, 100 and 150 kPa), three different suctions (0, 50 and 200 kPa) and two different temperatures (20 and 42 °C). The increment of shear strength resulting from suction effects is influenced by the temperature, showing the coupling effects of suction and temperature. For example, when the suction increases from 0 to 200 kPa at the net normal stress of 50 kPa, the interface shear strength increases by around 28% and 14% at 20 and 42 °C, respectively. Detailed interpretations have been given in Chapter 5. Furthermore, there is a consistent trend regarding the behaviour of shear-induced volume change. Both suction and temperature increments result in a more dilative behaviour.

The experimental results are simulated by the new model, and the computed results are also shown in Figures 6.12 - 6.17 for comparison. The computed results are able to show the same trend as the measured data, even though there are some minor differences between the calculated and measured results for some specific cases. The coupled effects of suction, temperature and stress on the shear behaviour of unsaturated interfaces are well captured. This is mainly because  $\eta(T)$  in equation (6-7) considers temperature effects. Hence, the effective normal stress and the critical state void ratio are dependent on both temperature and degree of

saturation. These modifications enable the new model to give an accurate prediction of the shear behaviour of unsaturated interfaces at various temperatures.

## 6.4 Summary

Based on the bounding surface plasticity framework and a reference model (Zhou et al., 2020) for the isothermal behaviour of saturated and unsaturated interfaces, a new thermo-mechanical model was developed to simulate the shear behaviour of saturated and unsaturated interfaces at various temperatures. The mathematical formulations and parameter calibration are described in detail. For the model validation, the shear behaviour of interfaces at various stress, suction and temperature conditions are used via three steps:

Firstly, the model was used to simulate the suction- and stress-control direct shear tests at the isothermal condition. Suction effects on the shear strengths at the peak and critical states are well captured in the new model. Moreover, the suction-dependent dilatancy and strain-softening can be also accurately predicted.

Then, the new model was applied to simulate temperature- and stress-controlled direct shear tests on saturated interfaces. Depending on the soil type and counterface material, the interface shear strength can either increase or decrease with increasing temperature. A good consistency between the computed and measured results is obtained. This implies that the new model is applicable to a wide range of interface types.

Finally, the experimental results in Chapter 5 were used to verify the new model at unsaturated and non-isothermal conditions. The computed results are well matched with the

measured data. The coupled effects of suction, temperature and net normal stress can be well captured by this new model.

Table 6.1. Summary of parameters for the current model and their values for the various soil-structure interfaces.

Soil parameters		Soil-cement interface (Hossain and Yin, 2012)	Soil-steel interface (Di Donna et al., 2016)	Soil-steel interface (Chapter 5)
Interface thickness	$t$ (mm)	5	5	5
Stress state variable	$\kappa$	4	NIL*	4.7
Critical state line	$M_0$	0.92	0.53	0.505
	$r_M$	NIL*	-0.004	0.0015
	$\Gamma_0$	0.51	1.08	0.4
	$r_\Gamma$	NIL*	-0.0007	-0.002
	$\omega_0$	0.04	0.113	0.078
	$\eta_0$	NIL*	NIL*	0.3
	$d$	NIL*	NIL*	2
Elastic modulus	$D_{t0}$ (kPa)	200	1000	500
	R	1	1	1
Plastic modulus	h	1	3	0.15
	$n_b$	2	0.5	5
Flow rule	$d_0$	0.4	1	0.15
	$n_d$	1	1.5	5

Note: \* These parameters are not necessary for simulating saturated and isothermal interfaces.

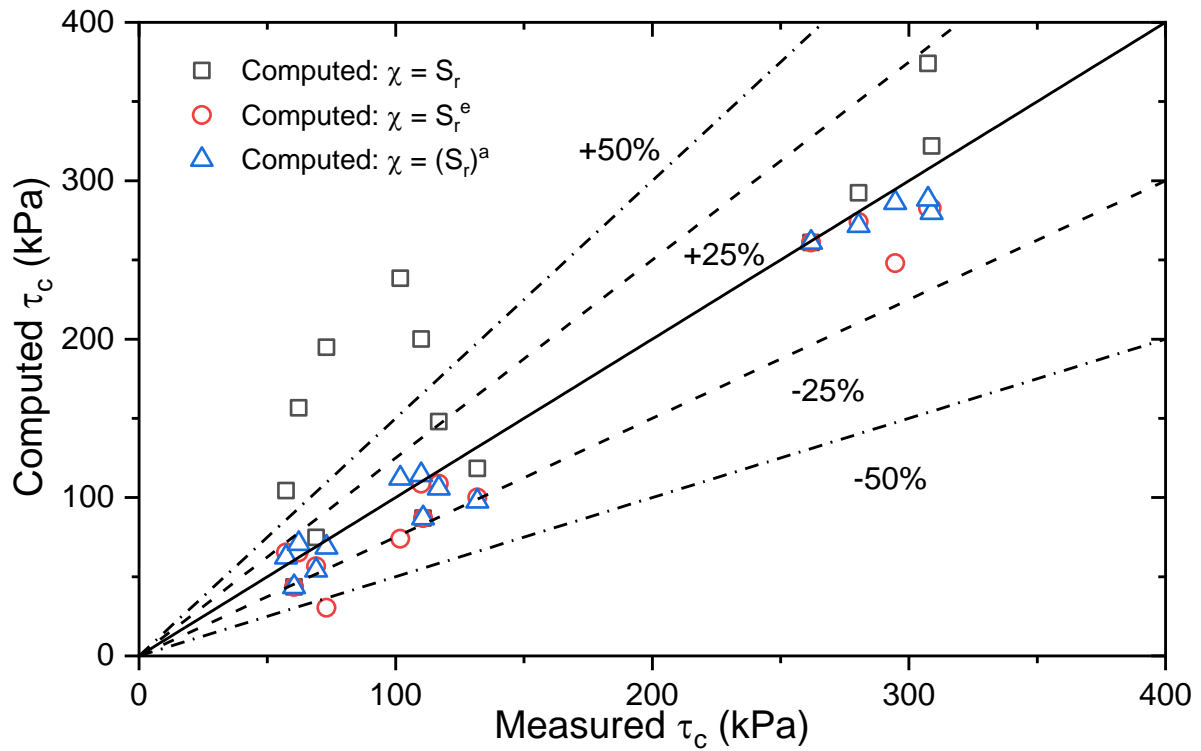


Figure 6.1. Comparisons between the measured (Hossain and Yin, 2012) and computed critical state shear strengths  $\tau_c$  using different formulations for normal skeleton stress.

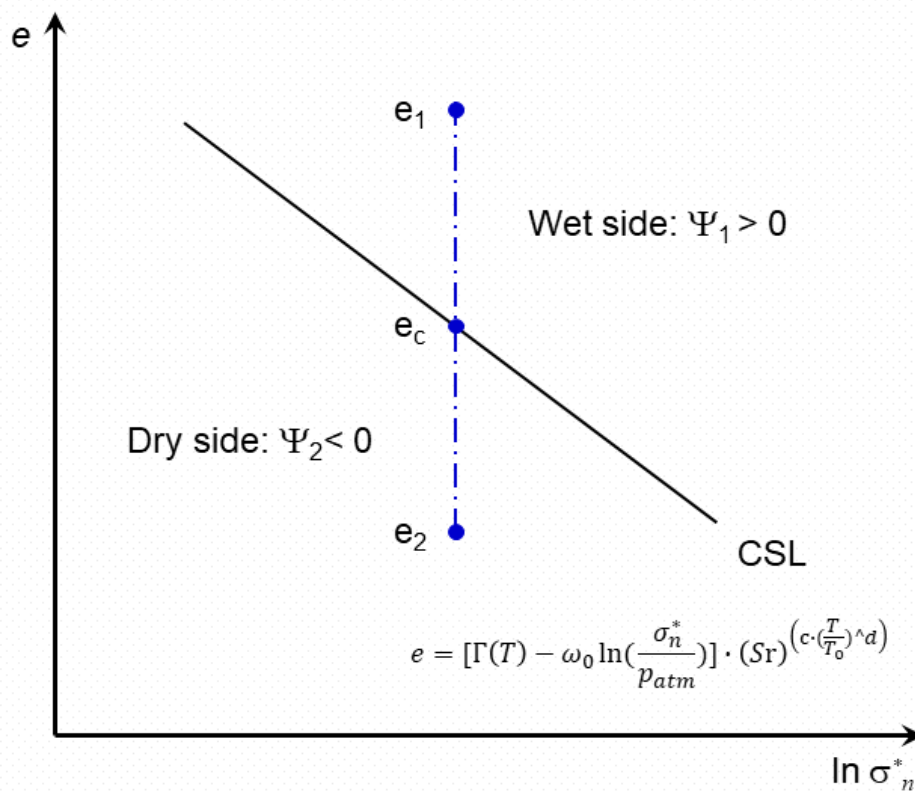


Figure 6.2. Definition of the state parameter ( $\psi$ ) in equation (6-11).

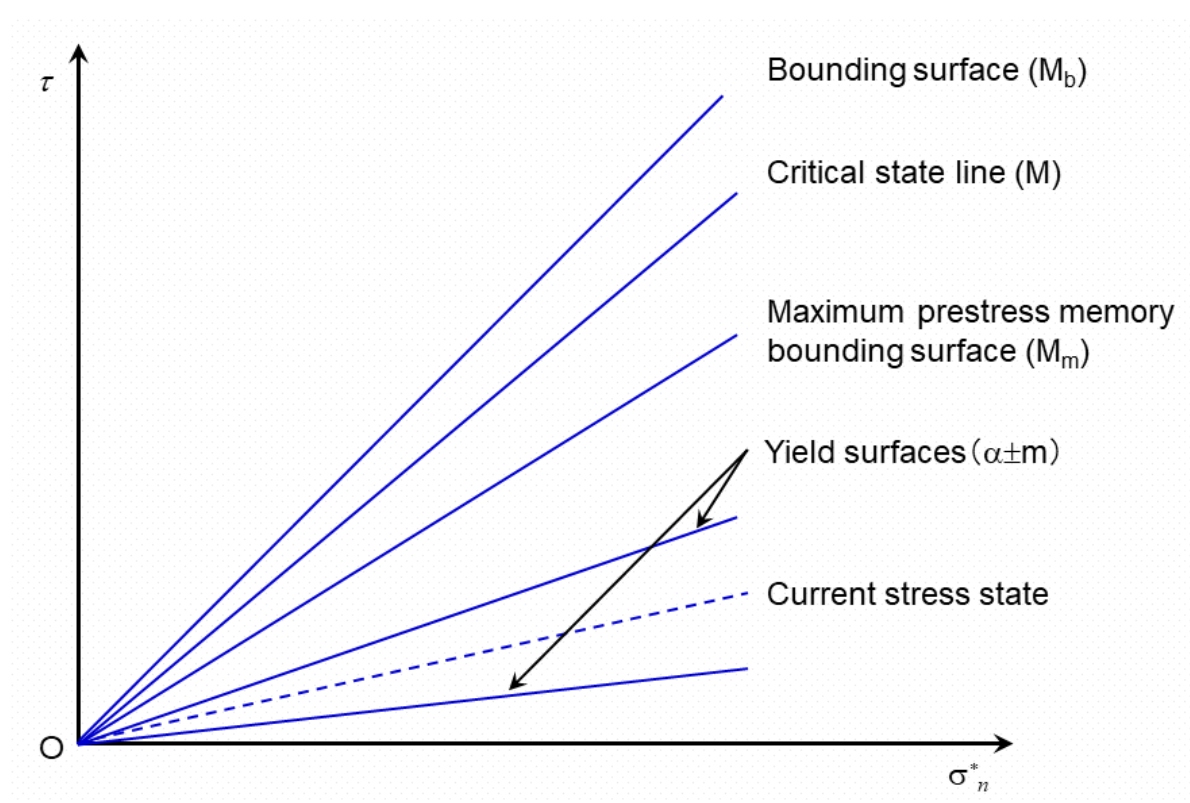
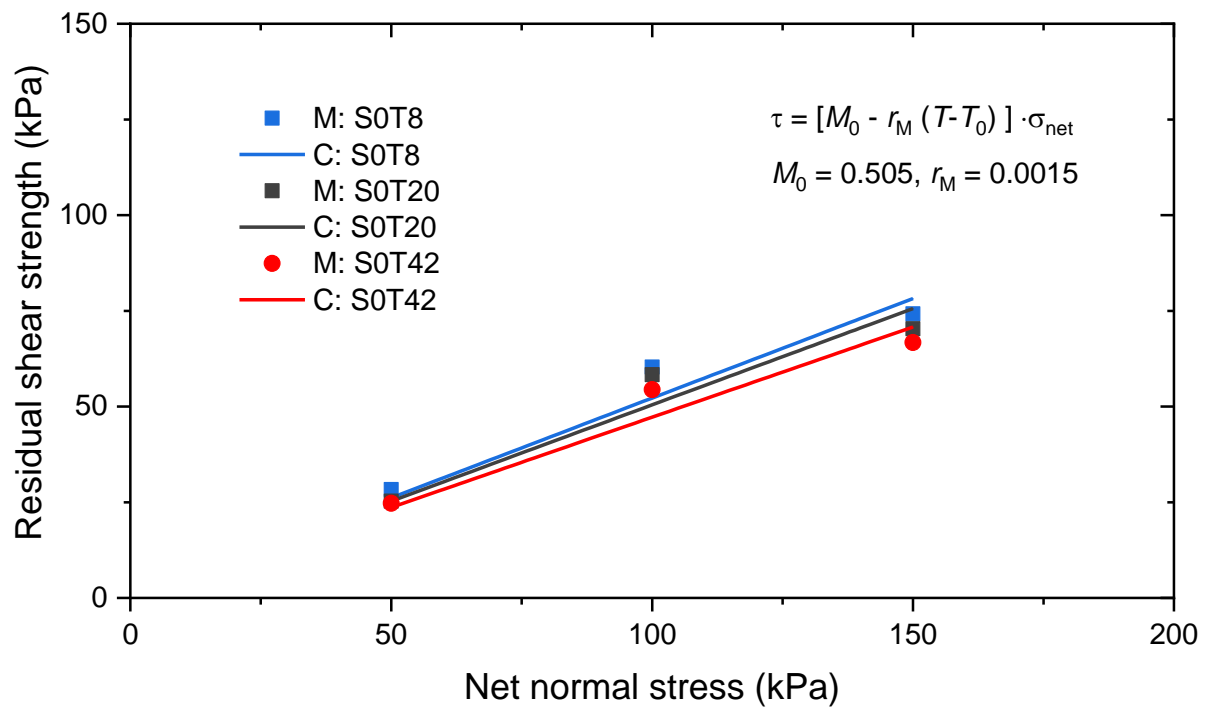
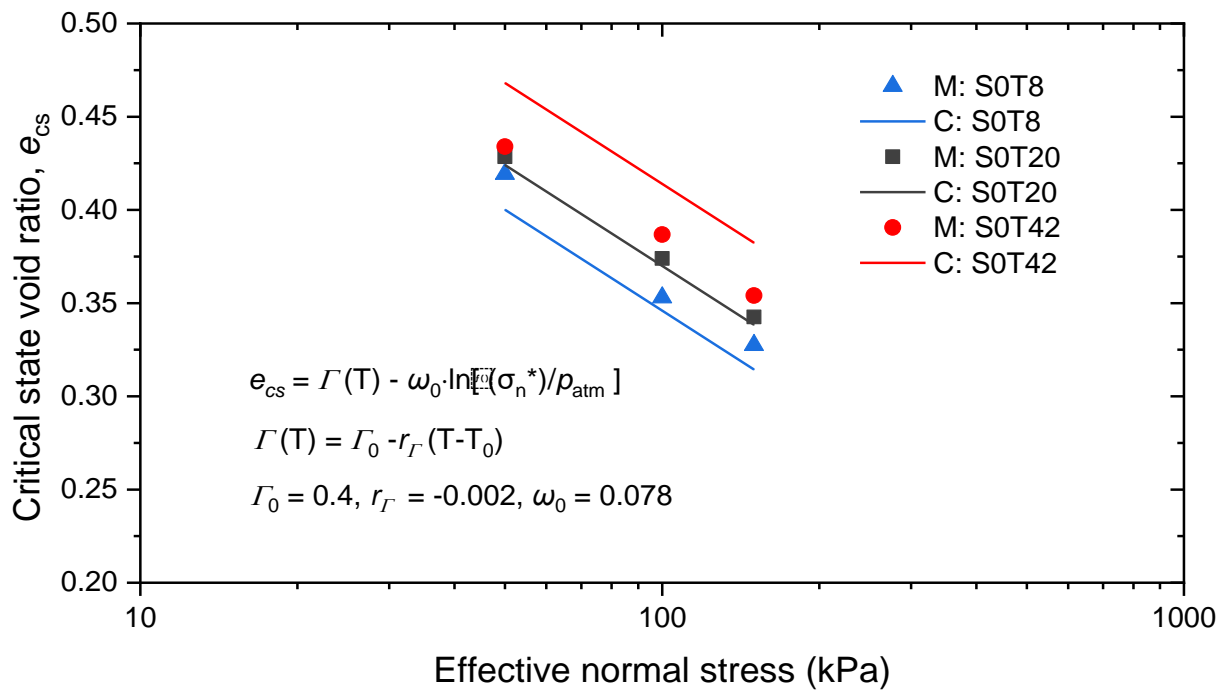


Figure 6.3. Schematic diagram of two bounding surfaces and one yield surface.

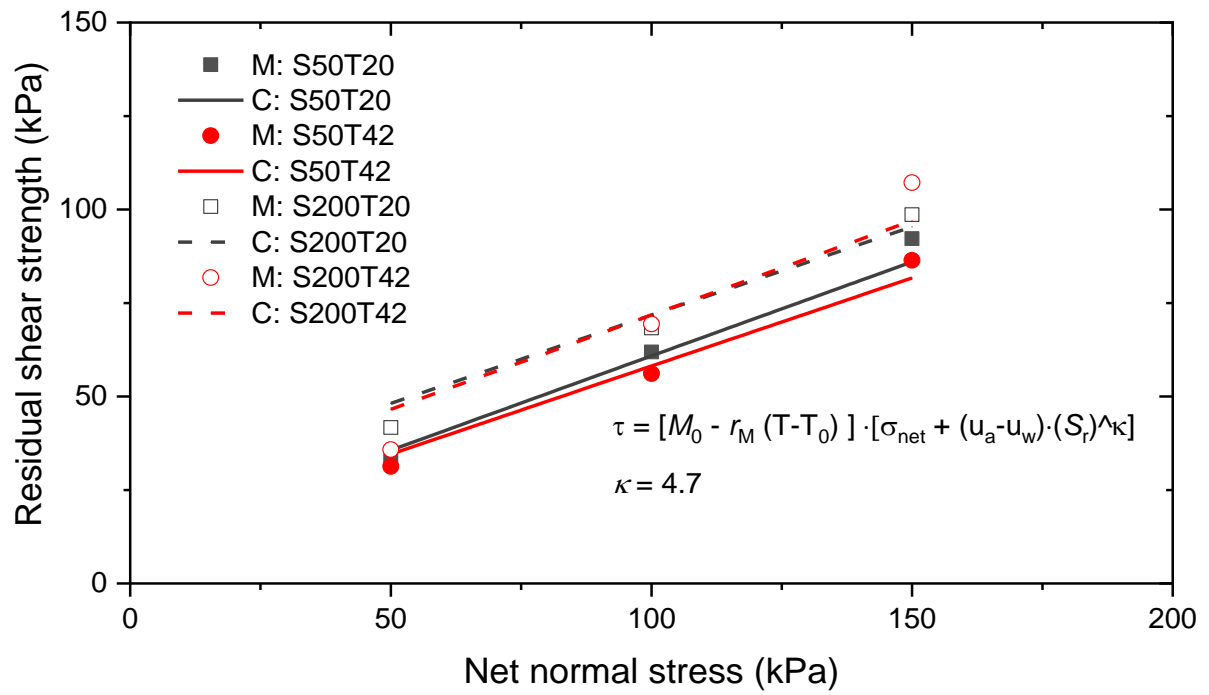


(a)

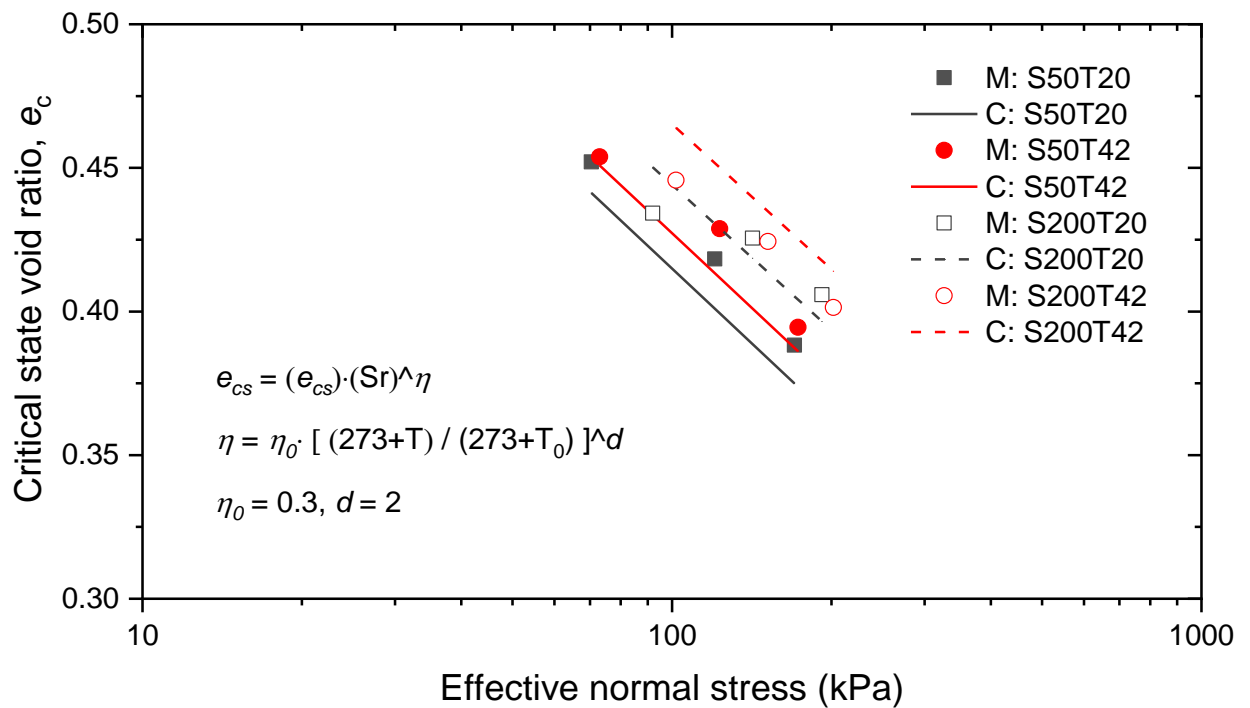


(b)

Figure 6.4. Calibration of the parameters:  $r_M$  and  $r_\Gamma$ .



(a)



(b)

Figure 6.5. Calibration of the parameters:  $a_0$ ,  $c_0$ ,  $b$  and  $d$ .

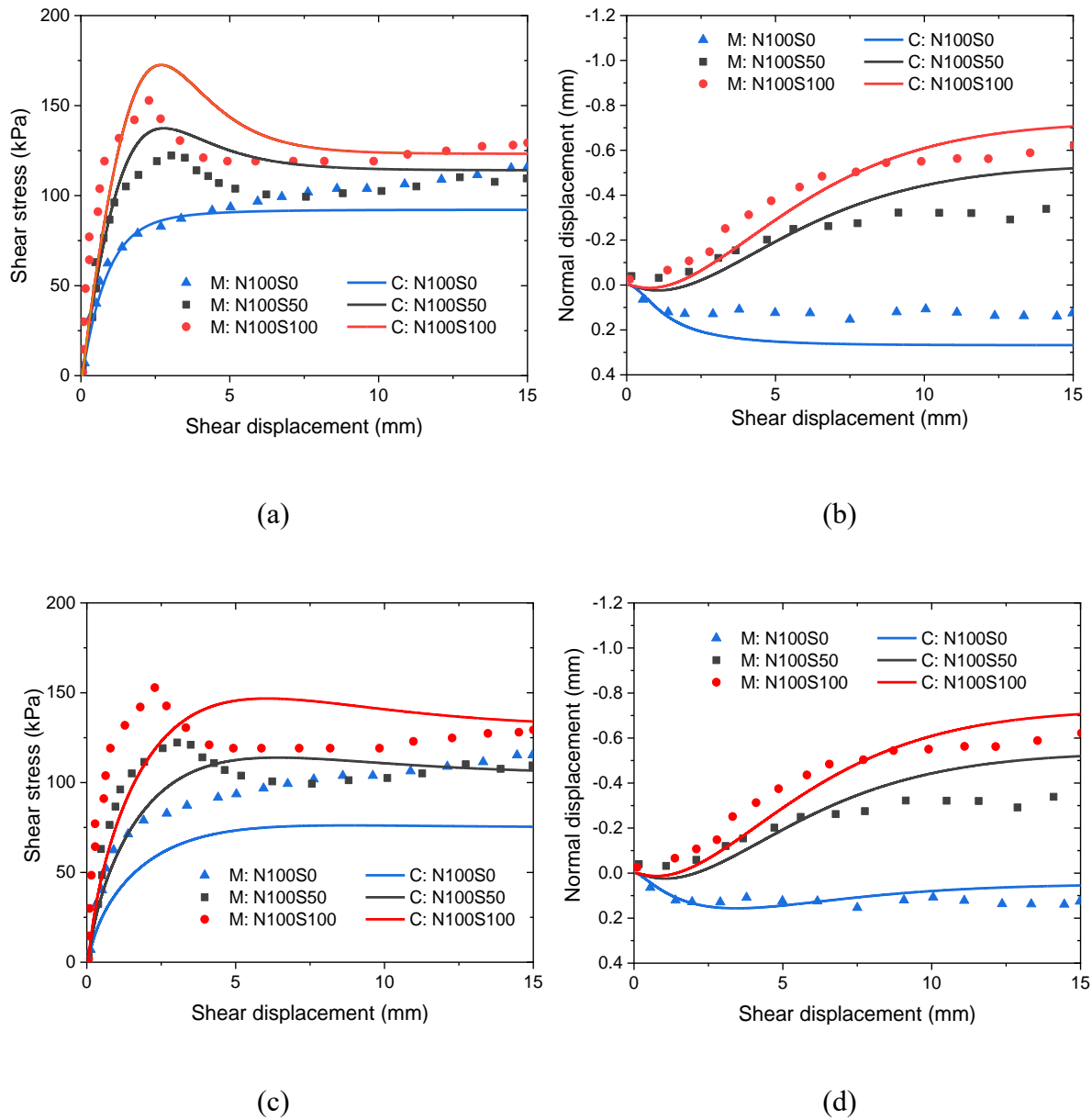


Figure 6.6. Comparisons between measured (Hossain and Yin, 2012) and computed shear behaviour of a soil-cement interface at a net normal stress of 100 kPa and suctions of 0, 50 and 100 kPa: (a) and (b) for the current model; (c) and (d) for the model of (Zhou et al., 2020).

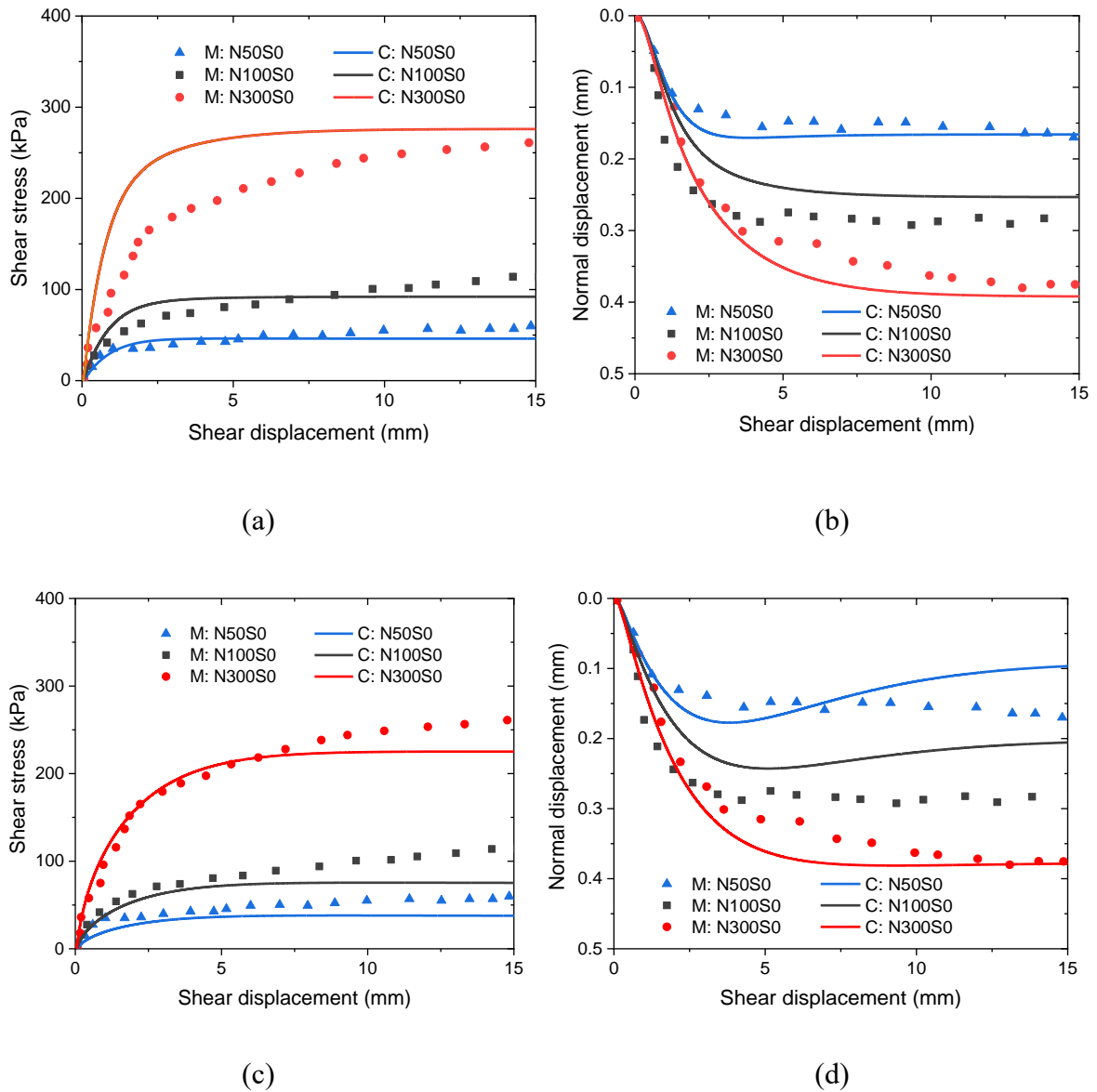


Figure 6.7. Comparisons between measured (Hossain and Yin, 2012) and computed shear behaviour of a soil-cement interface at zero suction and effective normal stresses of 50, 100 and 300 kPa: (a) and (b) for the current model; (c) and (d) for the model of (Zhou et al., 2020).

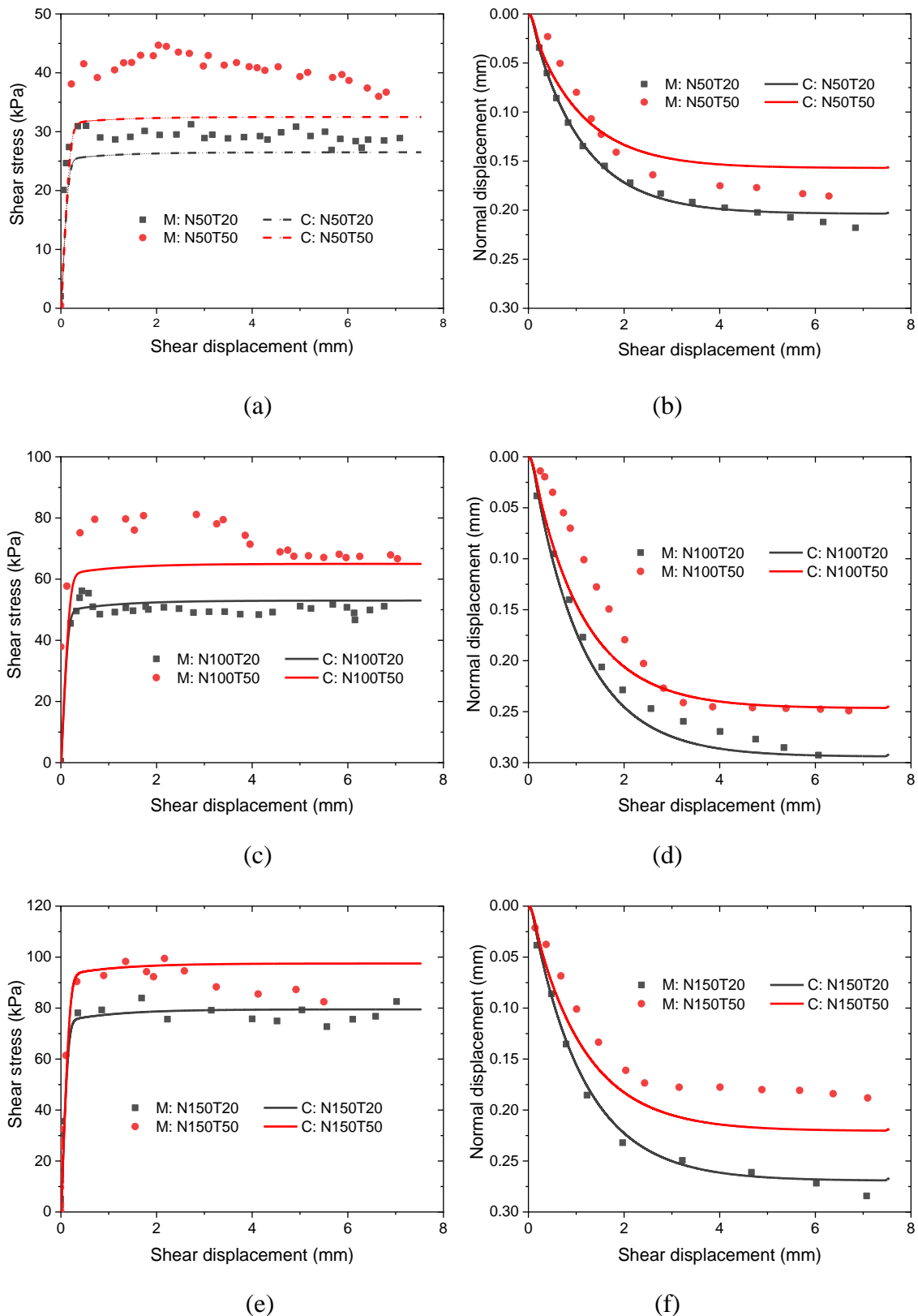
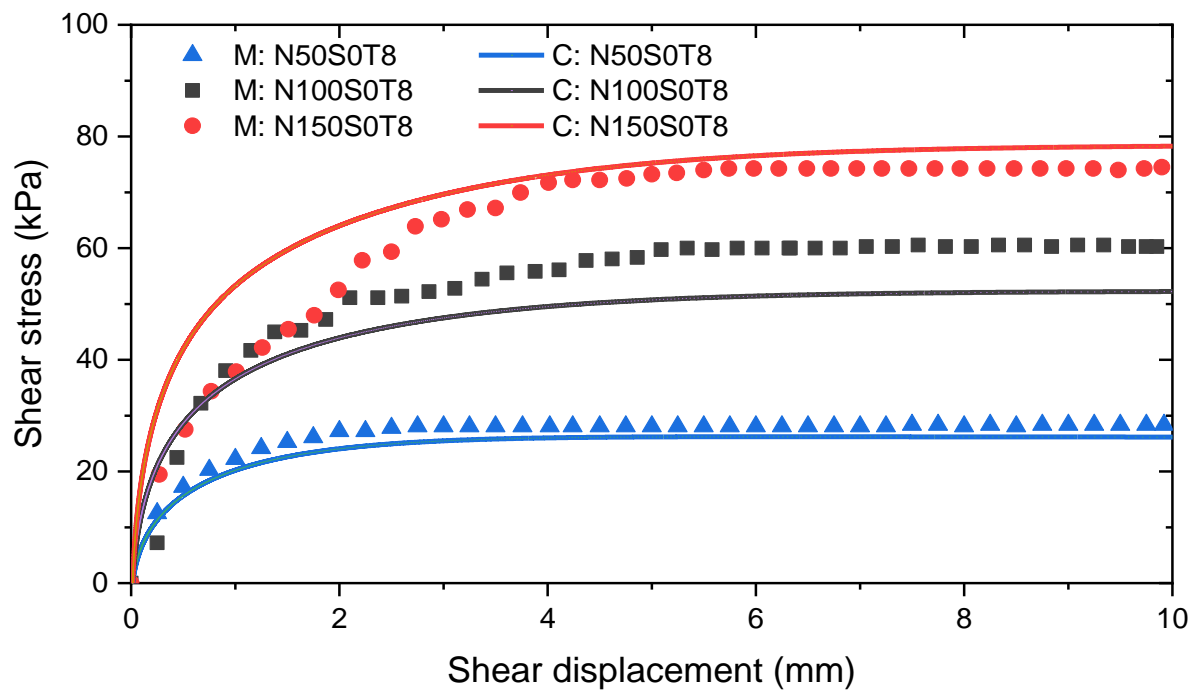
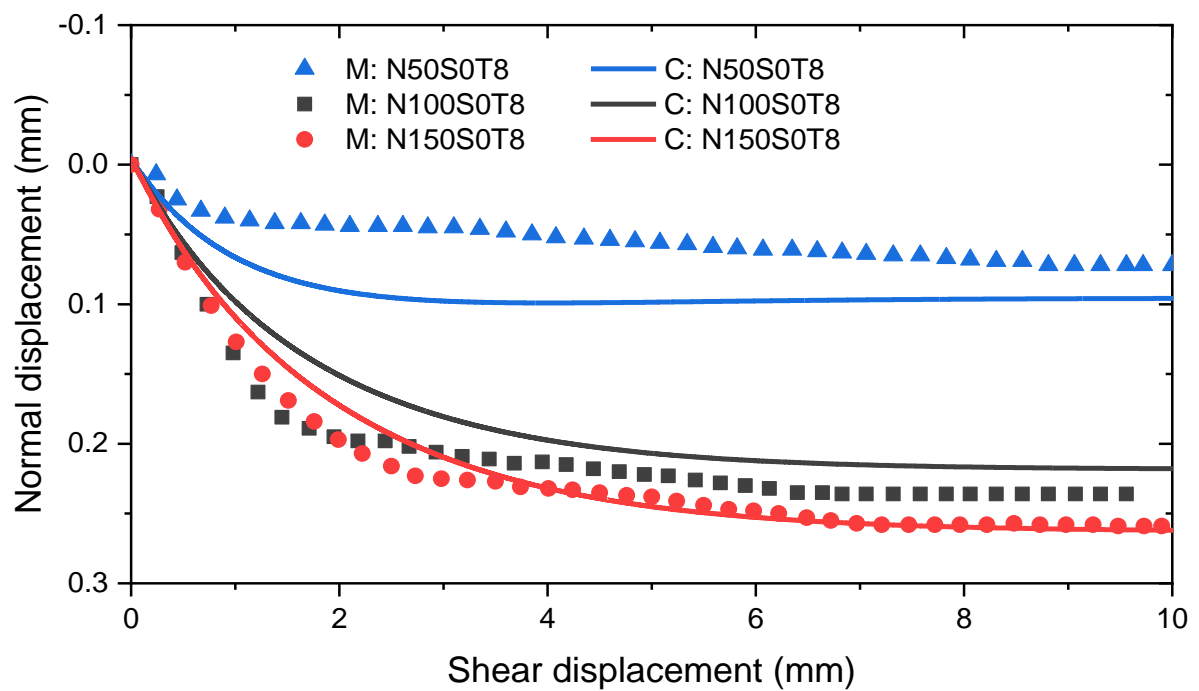


Figure 6.8. Comparisons between measured (M) (Di Donna et al., 2016) and computed (C) shear behaviour of saturated soil-concrete interfaces at various normal stresses and temperatures (the numbers after letters N and T denote the normal stress (unit: kPa) and temperature (unit: °C), respectively)

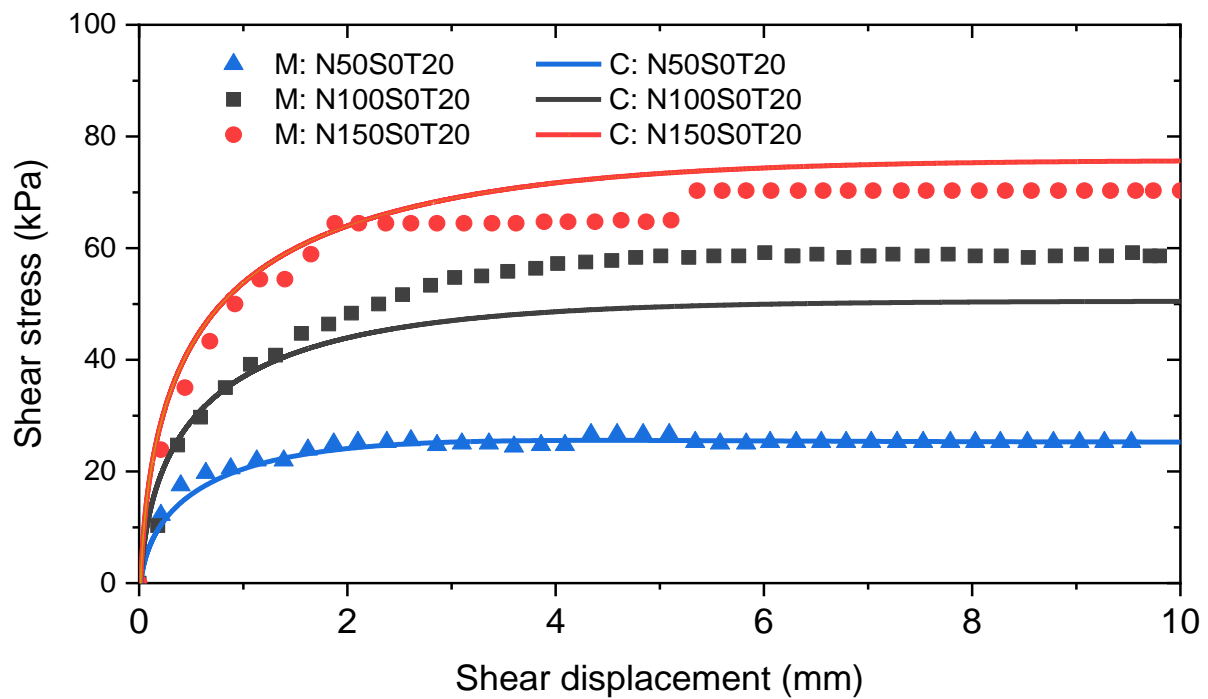


(a)

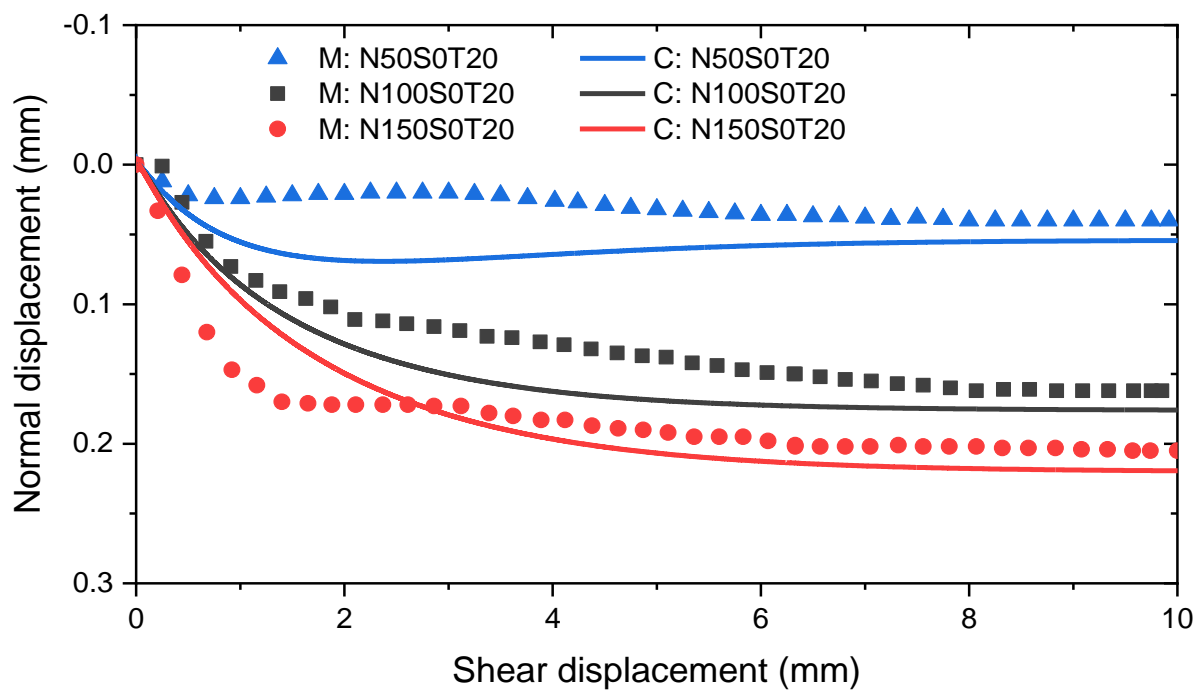


(b)

Figure 6.9. Comparisons between measured (M) (Chapter 5) and computed (C) shear behaviour of saturated soil-steel interfaces at 8°C: (a) stress-horizontal displacement relation; (b) shearing induced vertical displacement (the number after S denotes suction (unit: kPa)).

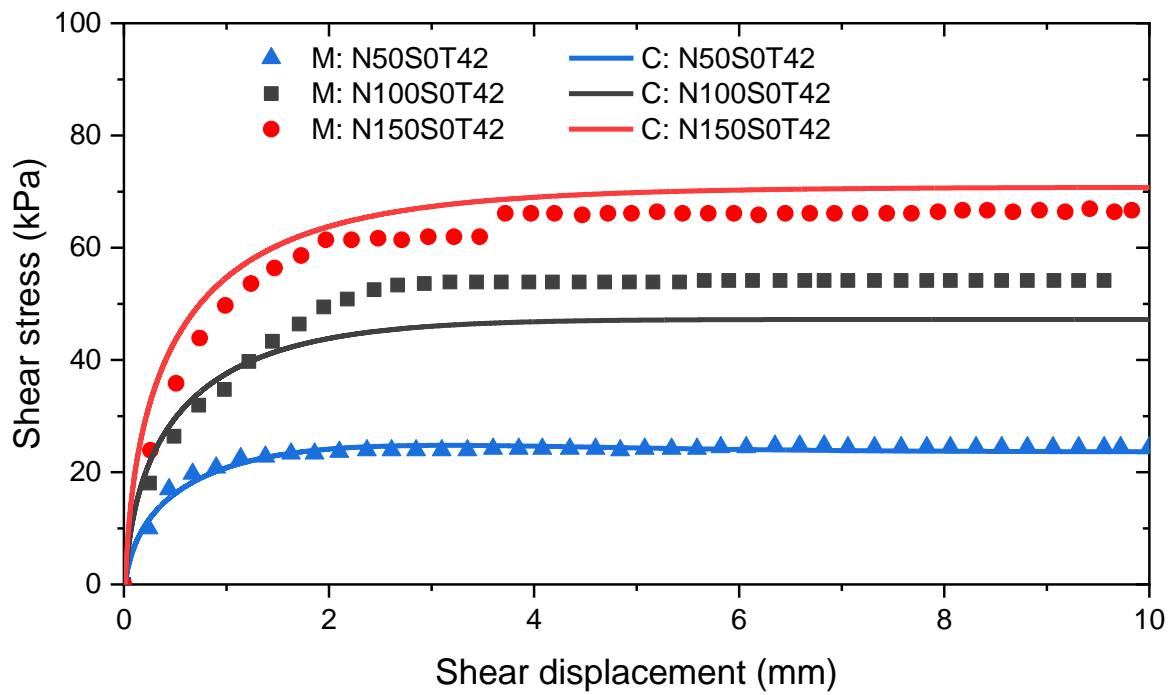


(a)

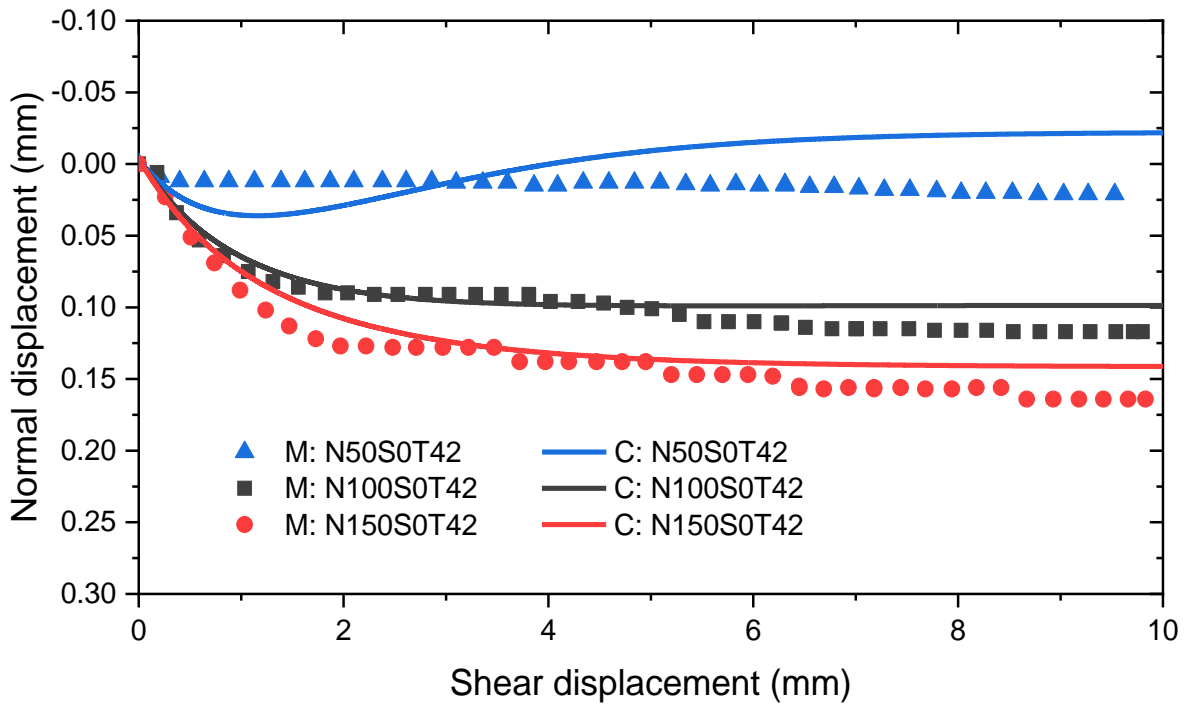


(b)

Figure 6.10. Comparisons between measured (M) (Chapter 5) and computed (C) shear behaviour of saturated soil-steel interfaces at 20°C: (a) stress-horizontal displacement relation; (b) shearing induced vertical displacement.

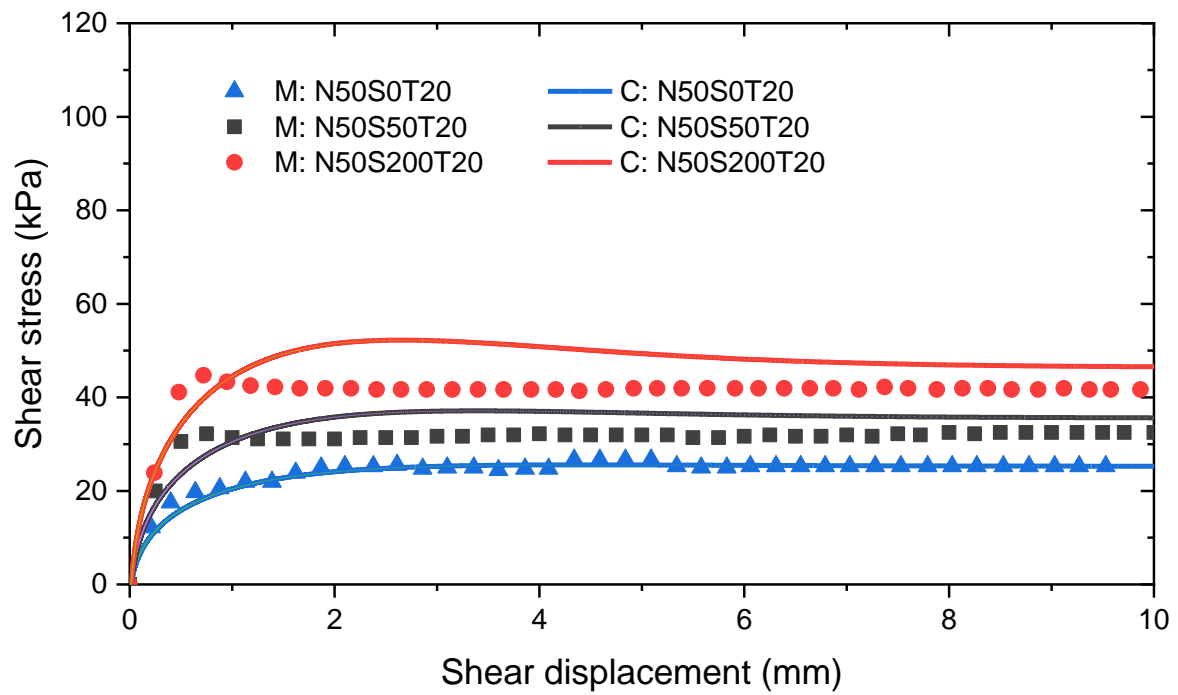


(a)

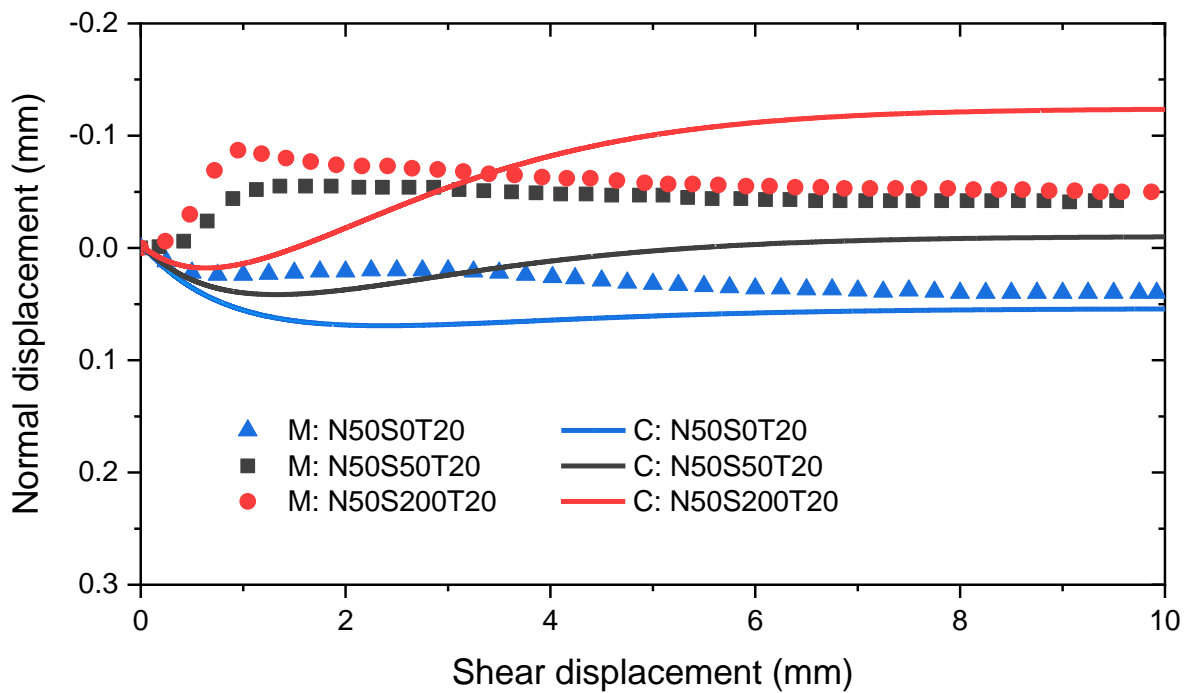


(b)

Figure 6.11. Comparisons between measured (M) (Chapter 5) and computed (C) shear behaviour of saturated soil-steel interfaces at 42°C: (a) stress-horizontal displacement relation; (b) shearing induced vertical displacement.

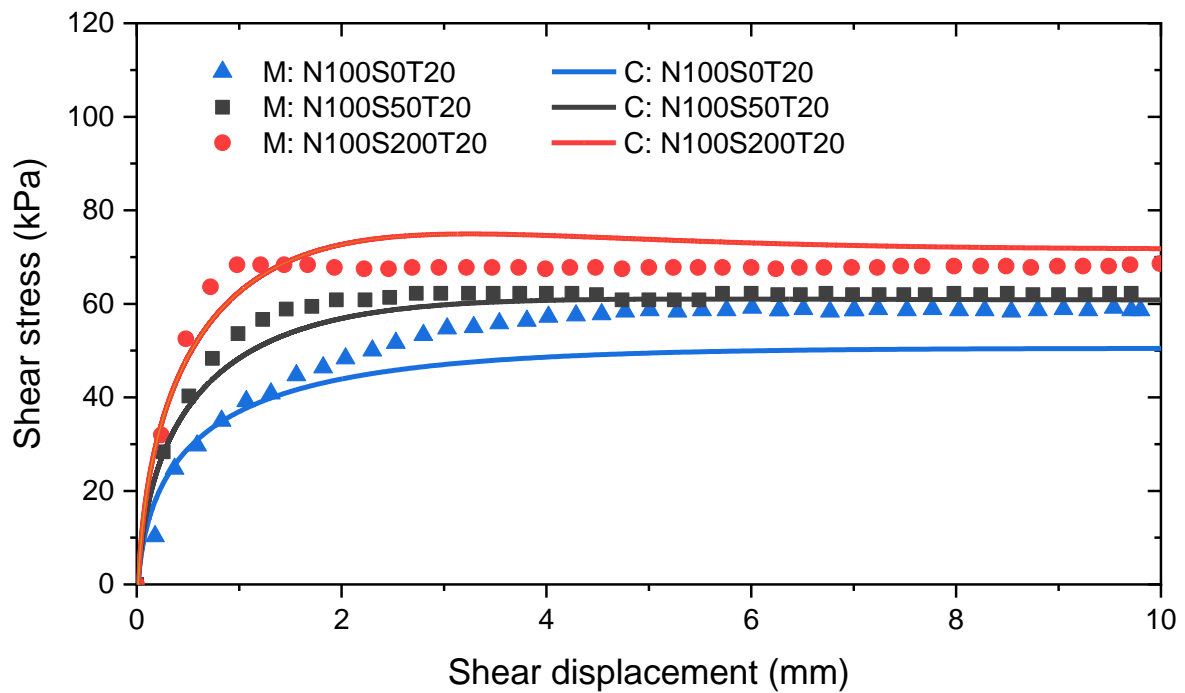


(a)

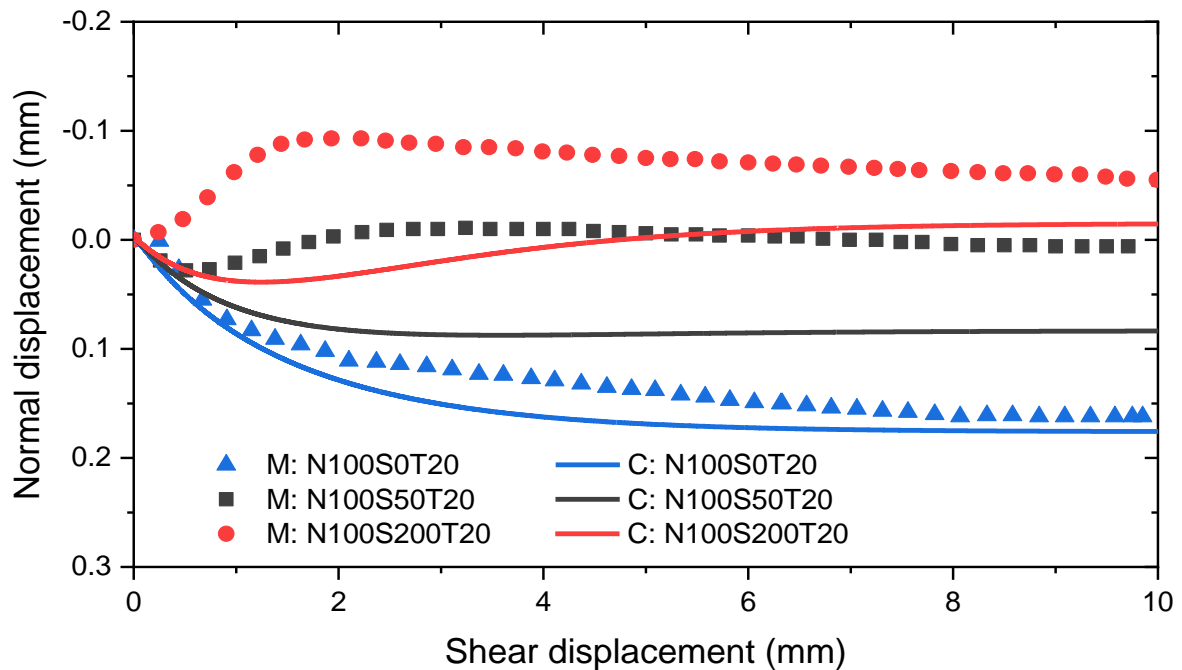


(b)

Figure 6.12. Comparisons between measured (M) (Chapter 5) and computed (C) shear behaviour of unsaturated soil-steel interfaces at 50 kPa net stress and 20°C: (a) stress-horizontal displacement relation; (b) shearing induced vertical displacement.

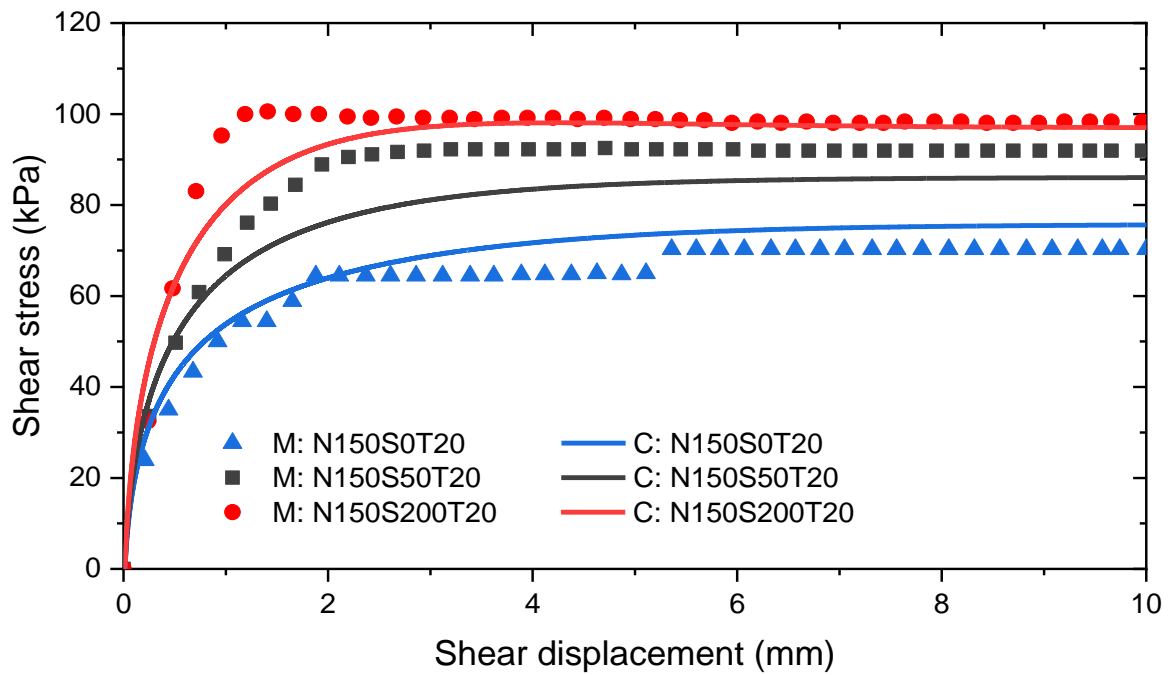


(a)

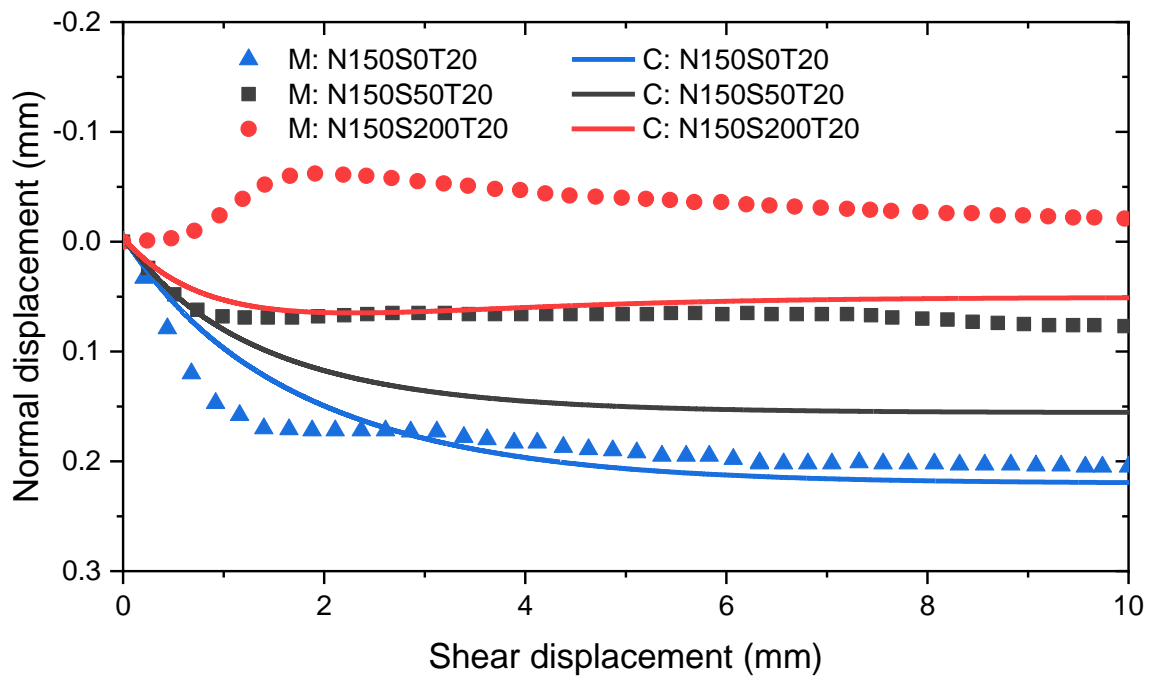


(b)

Figure 6.13. Comparisons between measured (M) (Chapter 5) and computed (C) shear behaviour of unsaturated soil-steel interfaces at 100 kPa net stress and 20°C: (a) stress-horizontal displacement relation; (b) shearing induced vertical displacement.

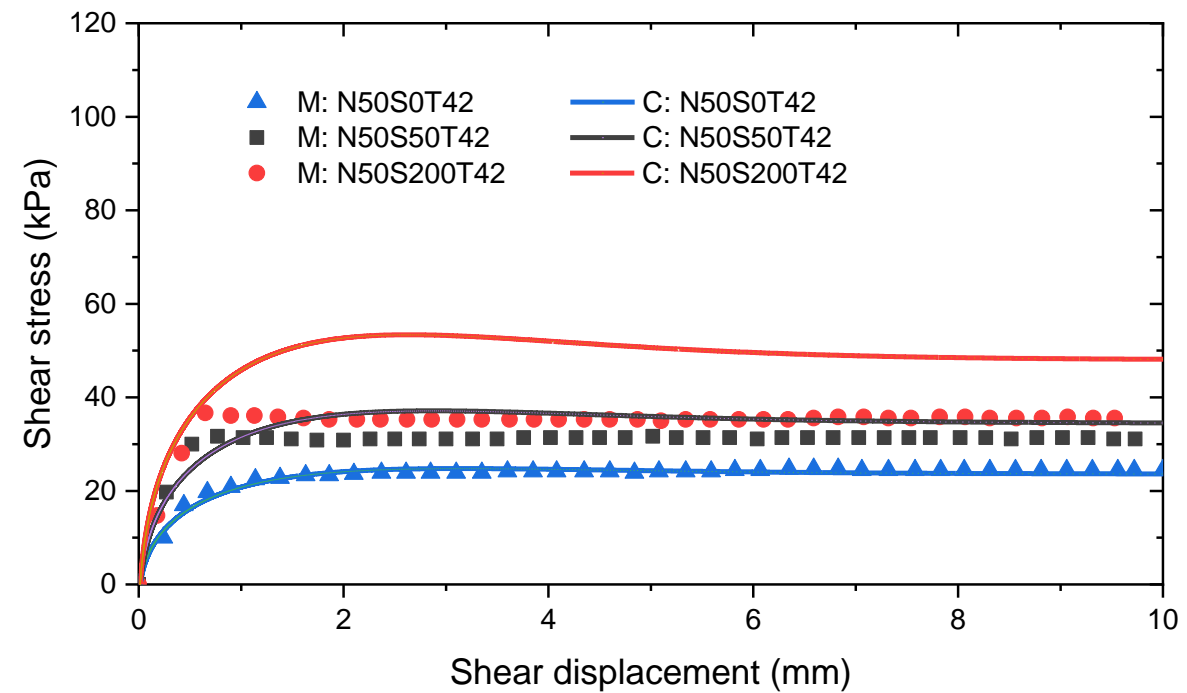


(a)

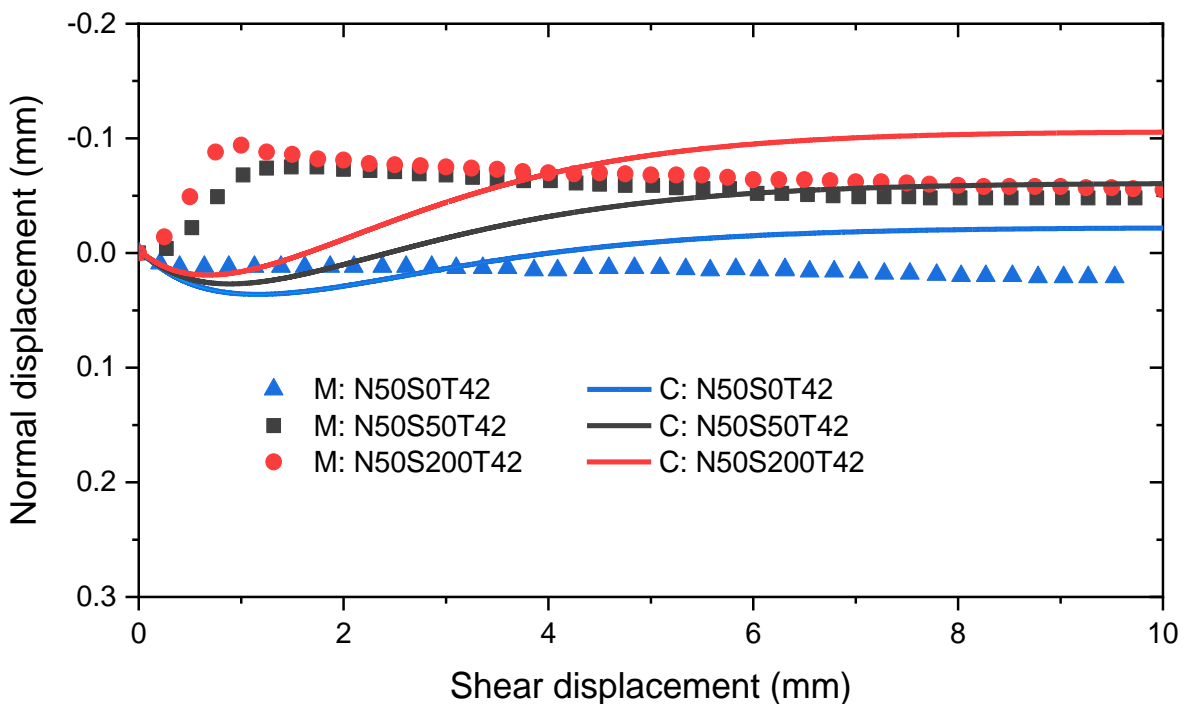


(b)

Figure 6.14. Comparisons between measured (M) (Chapter 5) and computed (C) shear behaviour of unsaturated soil-steel interfaces at 150 kPa net stress and 20°C: (a) stress-horizontal displacement relation; (b) shearing induced vertical displacement.

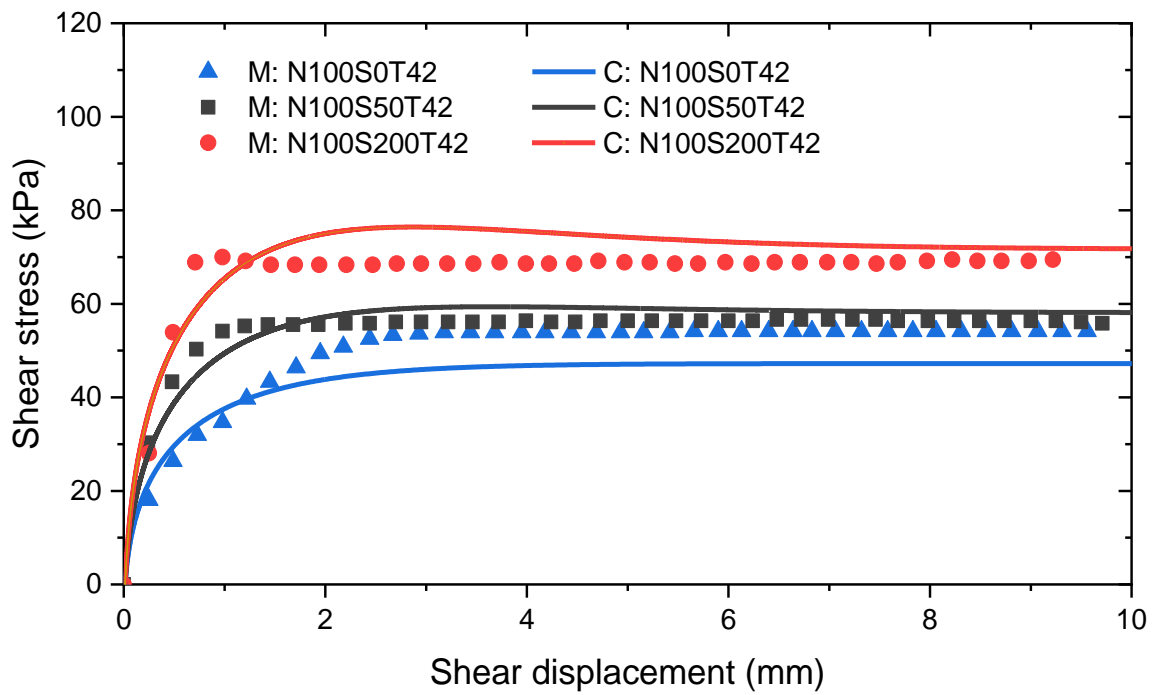


(a)

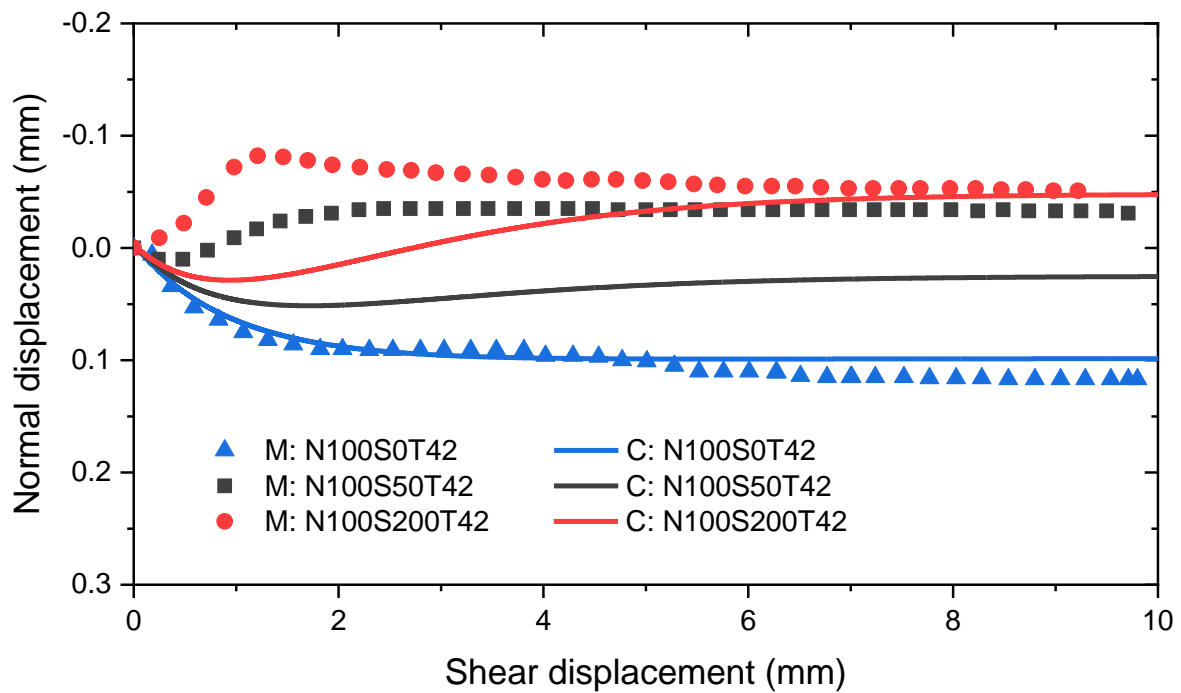


(b)

Figure 6.15. Comparisons between measured (M) (Chapter 5) and computed (C) shear behaviour of unsaturated soil-steel interfaces at 50 kPa net stress and 42°C: (a) stress-horizontal displacement relation; (b) shearing induced vertical displacement.

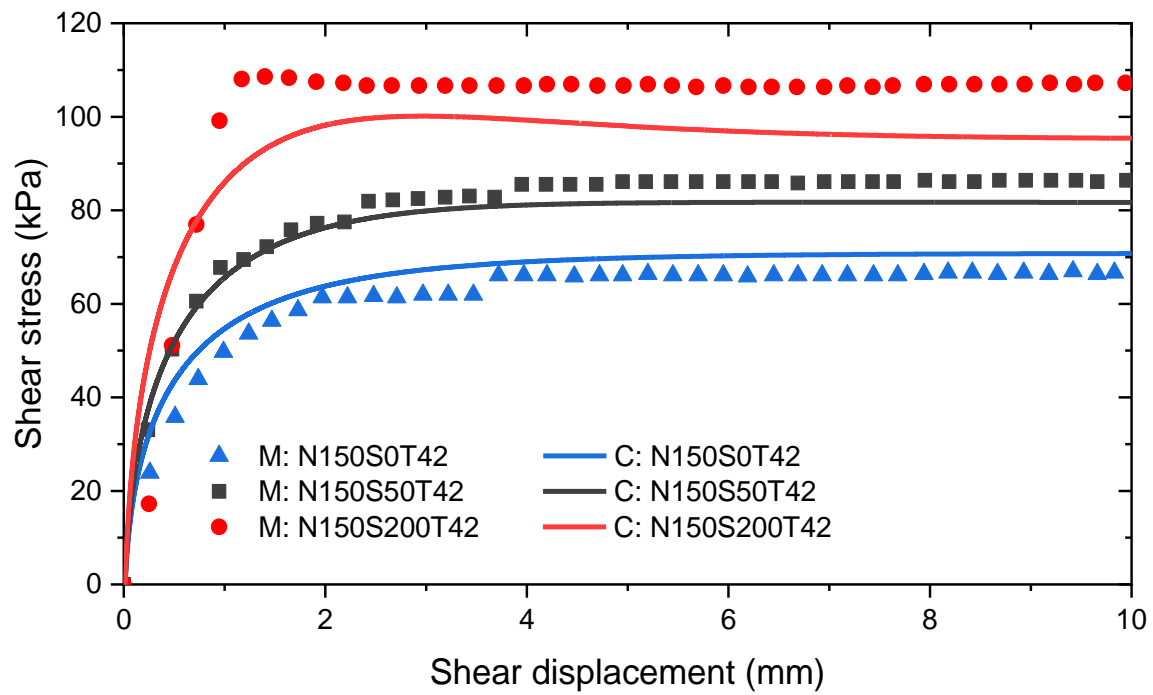


(a)

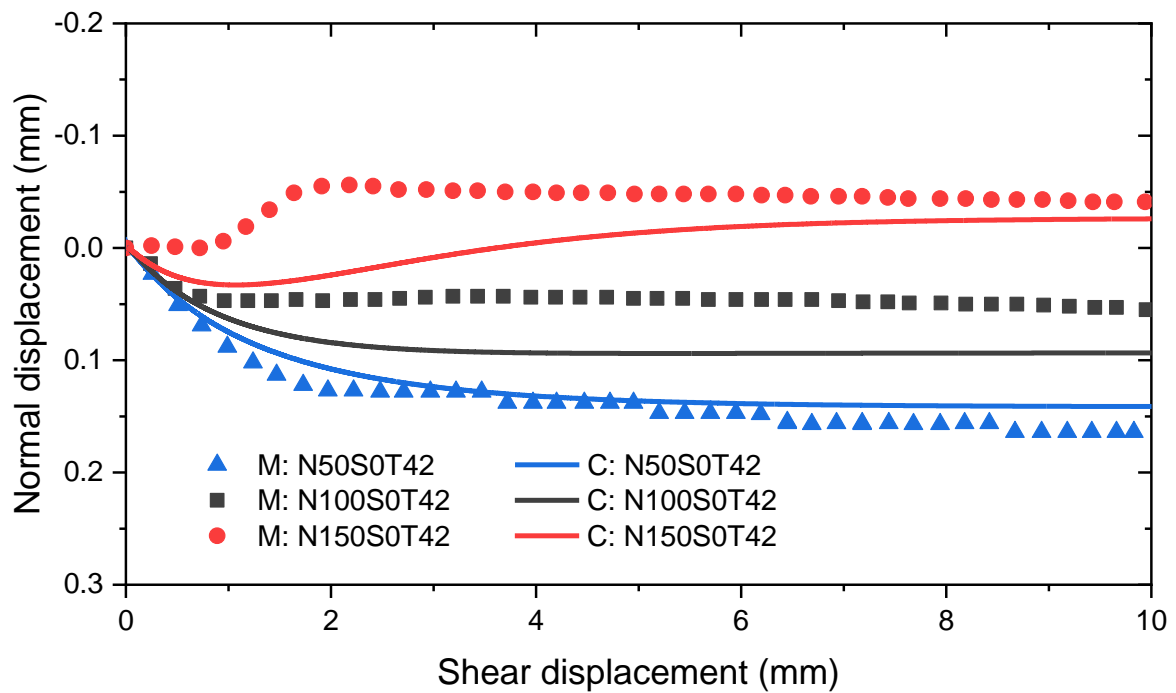


(b)

Figure 6.16. Comparisons between measured (M) (Chapter 5) and computed (C) shear behaviour of unsaturated soil-steel interfaces at 100 kPa net stress and 42°C: (a) stress-horizontal displacement relation; (b) shearing induced vertical displacement.



(a)



(b)

Figure 6.17. Comparisons between measured (M) (Chapter 5) and computed (C) shear behaviour of unsaturated soil-steel interfaces at 150 kPa net stress and 42°C: (a) stress-horizontal displacement relation; (b) shearing induced vertical displacement.

## **CHAPTER 7: Physical Modelling of Energy Piles in Saturated and Unsaturated Silts**

In this study, a series of small-scale physical model tests on energy piles were carried out. The principal objective is to investigate the pile bearing capacity and thermally induced settlement of energy piles. Particular attention was paid to the influence of soil suction and pile roughness on pile performance, which was not well revealed by previous studies. In this chapter, the test methods and results are discussed in detail.

### **7.1 Experimental program**

Two types of tests were conducted to study the ultimate and serviceability limit states of energy piles, including the constant-temperature pile load tests and constant-load heating and cooling tests. Three series of constant-temperature pile load tests were designed for investigating effects of suction, roughness and temperature on the bearing capacity of energy piles, as summarized in Table 7.1. Tests in series MS0 were performed at 21°C and in the fully saturated condition. Series MS90 was designed for 21°C and unsaturated conditions with an initial suction of 90 kPa. In both saturated and unsaturated conditions, model piles with two different degrees of roughness were tested. The pile with a relatively higher roughness is referred to as a “rough pile” in the following sections. Similarly, the other pile is described as a “smooth pile” for simplicity. The last series of MS90-T was conducted at 10°C and in unsaturated conditions. The results from MS90 and MS90-T are compared to investigate temperature effects on the bearing capacity of energy piles, which is denoted as  $Q_{ult}$ .

For the constant-load heating and cooling tests, three series were finished (see Table 7.2). Series TMS0 was carried out using a rough pile in the saturated condition, while series TMS90 was conducted using both rough and smooth piles in unsaturated conditions. Results from these two series can be used to analyze the influence of suction and roughness on pile performance. In each test, three different working loads ( $0.3Q_{ult}$ ,  $0.5Q_{ult}$  and  $0.7Q_{ult}$ ) were controlled during the cyclic heating and cooling. These three working loads were selected with reference to several guidelines of pile design (Department, 2017; Council, 2014; Day, 2010). The factor of safety for a pile foundation generally falls in the range of 2 to 3. Hence,  $0.3Q_{ult}$  and  $0.5Q_{ult}$  are used to represent allowable working loads, and  $0.7Q_{ult}$  is used to simulate the case of overloading. These three values are probably able to represent a wide range of loading situations. Under each vertical load, five thermal cycles were applied in the temperature range of 10°C to 40°C. This temperature range was selected based on the typical working conditions of energy piles (Association, 2012). Finally, for the test in series TMS90-C, a rough pile was loaded to  $0.5Q_{ult}$  in unsaturated conditions and then subjected to 15 thermal cycles. The results from TMS90 and TMS90-C can be compared for investigating the effects of thermo-mechanical history on pile settlement.

## 7.2 Model energy piles

Hollow circular tubes are used to model energy piles with various degrees of roughness. Their photos are shown in Figure 7.1. The total and embedded lengths of the model pile are 750 mm and 550 mm, respectively. The outer diameter, inner diameter and thickness are 22 mm, 16 mm and 3 mm. The outer diameter is larger than 200 times the soil median particle

size  $D_{50}$  (0.08 mm in this study), following the suggestion of previous researchers (Fioravante, 2002) for minimizing scale effects.

To enable the thermo-activation of model piles, a U-shaped copper tube is installed inside the piles and connected to a refrigerated/heated water bath. During the testing, temperature-controlled water is circulated between the water bath and the U-shaped copper tube to heat/cool the model pile. The hollow pile is filled with water to enhance heat exchange between the U-shaped tube and pile, because water has a much higher thermal conductivity than air, as shown in Chapter 3. To check the uniformity of temperature along the depth, several thermocouples were inserted into the pile to monitor the water temperature distribution. The temperature only showed very minor variations. Along the whole pile, the temperature difference was less than 0.3°C. It is thus assumed that the input temperature inside the model pile is homogenous, which is also consistent with the observations from field monitoring (Wang et al., 2015a; Murphy et al., 2015; Amatya et al., 2012).

The model piles were prefabricated using aluminium. Its thermal expansion coefficient is  $22.2 \times 10^{-6} \text{ K}^{-1}$ , around three times that of concrete ( $8.6 \times 10^{-6} \text{ K}^{-1}$ ) (Bourne-Webb et al., 2009). Consequently, the relative strain of model piles is larger than that of real piles in the field. The relative movement between pile and soil is also likely overestimated. Thus, the results of physical model tests should be valuable for revealing the mechanism of soil-pile interaction and for the verification of numerical models. They should be treated and applied with caution at a quantitative level.

As discussed in Chapter 5, the normalized roughness ( $R_n$ ) is widely used to quantify the roughness of soil-pile interfaces. One of its definitions was given by Uesugi and Kishida (1986) as follows:

$$R_n = \frac{R_{max}}{D_{50}} \quad (7-1)$$

where  $R_{max}$  is the maximum vertical distance between the highest peak and lowest trough on the surface along a profile equaling to  $D_{50}$ . To control the roughness of pile surfaces, they were treated by the Industry Centre of The Hong Kong Polytechnic University. The resultant  $R_{max}$  values are about 80  $\mu\text{m}$  and 4  $\mu\text{m}$  for the rough and smooth piles, respectively. Since the test soil has a  $D_{50}$  value of 80  $\mu\text{m}$  in this study, the corresponding  $R_n$  values are 1 and 0.05. These two values are within the typical range of  $R_n$  (Yoshimi and Kishida, 1981).

### 7.3 Model setup and instrumentation

Figure 7.2 shows a schematic diagram of the typical model setup. Each physical model can be used to test three model piles. This can minimize the time of sample preparation, which takes about three weeks. The model size is 1000 mm in length, 600 mm in width and 800 mm in height. The horizontal distance between the centers of two adjacent piles is 250 mm. It is around 11 times the pile diameter and should be sufficient to avoid pile interaction (Gui et al., 1998). The pile toe is 250 mm away from the tank bottom, and it is larger than 10 times the pile diameter to eliminate boundary effects (Le Kouby et al., 2004). In addition, insulation materials were used to cover different surfaces of the tank.

The vertical load was imposed by dead weight on the pile cap. Linear variable differential transformers (LVDTs) manufactured by *VJ Tech* were used to monitor pile

settlement. These LVDTs have a stroke length of 10 mm and an accuracy of 0.001 mm. They are connected to the *Clisp* Studio software through the datalogger *MPX3000* from *VJ Tech*. In addition, a temperature-controlled water bath by *PolyScience* was used to control pile temperature. The general layout of the whole system is shown in Figure 7.3.

The optical fiber sensing technology was applied to monitor the model pile, with the use of two types of fibers. One measures the thermal strain only, named T-fiber. The other one, denoted by TM-fiber, measures the total strain included by both thermal and mechanical loads. The difference between these two fibers allows for the calculation of axial strain distribution of the model pile. The T-fiber and TM-fiber are installed on the inner surface at opposite sides, as shown in Figure 7.4. Distributed fiber optic sensing (DFOS) was used to collect the measured axial strain from fibers. The accuracy of DFOS can be up to  $1 \mu\epsilon$ .

Before the physical model tests, the strain measurement with this technology was evaluated using the setup in Figure 7.4. A reaction frame and a closed-loop hydraulic servo-valve system were used to apply mechanical load on the model pile. A load cell from *VJ Tech* (capacities: 0-5 kN; accuracy: 0.001 kN) was used to measure the vertical load. The temperature was controlled by a refrigerated/heated circulating bath. Two kinds of calibration tests were conducted, including mechanical loading at the constant-temperature condition and thermal loading at zero mechanical load. In the former case, the mechanical strain is calculated from the vertical load and Young's modulus of the model pile. The theoretical strain value is compared with the fiber measurement in Figure 7.5(a). It is clear that at various temperatures, the strains monitored by the fiber are very close to the theoretical values. The temperature

variations have a negligible influence on the sensitivity of fiber to mechanical loading. The results of the heating and cooling tests are shown in Figure 7.5(b). The calculated strain is equal to the product of temperature change and the thermal expansion coefficient of aluminium. The results also show that the fiber can well capture the thermal strain. Based on these findings, it is reasonable to conclude that the optical fiber sensing technology is suitable for measurement of thermo-mechanical axial strains of energy piles in this study.

Apart from the monitoring of model piles, the state of surrounding soils was also measured. Six thermocouples were installed around each pile, at three different depths (100, 300 and 500 mm) from the ground surface and at two different horizontal distances (2D and 4D, where D is the pile diameter) away from the pile surface. Similarly, four tensiometers were used to determine the distribution of soil suction around each pile (see Figure 7.2). The installation of these sensors is presented in Figure 7.6.

### **7.4 Test soil and model preparation**

Same to the thermal conductivity tests in Chapter 3 and the soil-pile interface tests in Chapter 5, CDG was used for the physical model tests. All soil models were prepared using the method of moist tamping. First of all, CDG was oven-dried at 105°C and then broken up using a grinder. After that, soil particles were passed through a 2-mm sieve, followed by mixing the dry soil and distilled water to reach the optimum water content (i.e., 14.3%). The soil-water mixture was sieved using the 2-mm sieve again, and any remaining lumps were crushed with the grinder. Finally, the soil-water mixture was kept in a sealed container for 24 hours to achieve uniform water distribution (Zhang et al., 2015).

The prepared soil-water mixture was compacted using a hammer by layers. The target dry density was  $1.56 \text{ g/cm}^3$ , corresponding to 85% degree of compaction. Each layer of compacted soil was 50 mm. A small thickness for each layer can ensure a good homogeneity of soil (Yavari et al., 2016b; Stewart and McCartney, 2014). After compacting the first five layers, the model pile was fixed at the designed position through a steel frame. There was no movement for the model pile during the compaction of remaining soils, so the installation method of model piles is non-displacement.

The tests in unsaturated conditions were carried out under the as-compacted condition. The initial suction of soil falls in the range of 87 to 93 kPa. The average value (i.e., 90 kPa) is used in the data analysis later. For the tests under the saturated condition, the soil model was saturated before testing. Water with a pressure of 10 kPa, which was maintained by a pressure controller from *VJ Tech*, was supplied from the tank bottom. This process lasted for one week and it is able to ensure that the average degree of saturation, estimated from the amount of water inflow, is above 97%.

## **7.5 Test procedures**

The pile load tests in series MS0 and MS90 (see Table 7.1) were carried out to study effects of suction and roughness on the pile bearing capacity at room temperature. The mechanical load was increased stepwise in an approach similar to that in Yavari et al. (2016b), with an increment of 10% of the estimated pile bearing capacity  $Q_{ult}$ . Each level of load was maintained for one hour. When the pile head settlement exceeded 10% of the pile diameter, the loading path was terminated, followed by an unloading process. Similarly, the decremental rate

is 10% of the estimated  $Q_{ult}$  per hour. The test procedures in series MS90-T are identical to those in MS0 and MS90. The only difference is that prior to the mechanical loading-unloading, the pile in MS90-T was cooled down to 10°C.

For the constant-load heating and cooling tests in series TMS0 and TMS90 (see Table 7.2), the thermo-mechanical path is shown in Figure 7.7(a). As explained in the section of the test program, three vertical loads ( $0.3Q_{ult}$ ,  $0.5Q_{ult}$  and  $0.7Q_{ult}$ ) were applied to each pile. The  $Q_{ult}$  values were determined from the above pile load tests. At each level of working load, five heating and cooling cycles were applied. Consequently, the tests in series TMS0 and TMS90 have the following thermo-mechanical path:

- (i) imposing a vertical load of  $0.3Q_{ult}$  and waiting for one hour;
- (ii) changing the temperature of the model pile stepwise ( $21^{\circ}\text{C} \rightarrow 40^{\circ}\text{C} \rightarrow 21^{\circ}\text{C} \rightarrow 10^{\circ}\text{C} \rightarrow 21^{\circ}\text{C}$ ) and maintaining the temperature constant for two hours at each temperature stage;
- (iii) waiting for 16 hours to ensure the temperature recovery of the system;
- (iv) repeating the procedures in steps (ii) and (iii) for simulating four more thermal cycles;
- (v) increasing the vertical load to  $0.5Q_{ult}$  and repeating the procedures in steps (ii) to (iv);
- (vi) increasing the vertical load to  $0.7Q_{ult}$  and repeating the procedures in steps (ii) to (iv).

For the series TMS90-C, the thermo-mechanical path is shown in Figure 7.7(b). Only one vertical load (i.e.,  $0.5Q_{ult}$ ) was applied and the model pile was subjected to 15 thermal cycles. The test procedures are similar to those described in steps (i) to (iv).

## 7.6 Interpretations of the results of constant-temperature pile load tests

### 7.6.1 Load-settlement relationship and bearing capacity

Figure 7.8 shows the load-settlement relation of energy piles tested at different conditions. Based on the acceptance criterion of EN1997-1 (2004), the bearing capacity is the vertical load when the pile head settlement is equal to 10% of the pile diameter. This criterion is used to determine the bearing capacity in this study.

The bearing capacity in unsaturated conditions is consistently larger than that in the saturated condition, for both smooth and rough piles. This observation agrees well with the results of Al-Khazaali and Vanapalli (2019). The influence of suction on the bearing capacity could arise from different mechanisms, such as (i) the increase of apparent cohesion with increasing suction; (ii) the increase of dilation angle with an increase in suction. Both of them are supported by extensive testing of unsaturated soils and soil-pile interfaces, reported in the literature (Hamid and Miller, 2009; Borana et al., 2018) as well as in Chapter 5.

Furthermore, the results in this figure show that when suction increases from 0 to 90 kPa, the increment of bearing capacity is around 210% and 390% for the smooth and rough piles, respectively. Compared to the smooth piles, the influence of suction seems much more obvious for the rough piles. The coupling effects of suction and roughness on the bearing capacity could be explained based on the results of direct shear tests on unsaturated soil-pile

interfaces. It was reported that the soil-pile interfaces become more dilative as suction increases (see Figure 5.14). Given the same change in suction, the increment of dilation angle is larger when the interface roughness is higher (Borana et al., 2016). As a result, suction effects on the interface shear strength and pile bearing capacity would be more significant when the roughness is higher.

At a given suction, the bearing capacity of rough piles is higher than that of smooth piles because the increase of roughness is able to induce a thicker shear band and increase the friction angle of soil-pile interfaces (Uesugi and Kishida, 1986; DeJong et al., 2001; Tehrani et al., 2016; Tovar-Valencia et al., 2018; Chen et al., 2015). Due to the coupling effects of suction and roughness, as explained above, the influence of roughness on the bearing capacity is more obvious in unsaturated conditions than in saturated conditions. The increment of bearing capacity is about 11% and 74% under saturated and unsaturated conditions, respectively. It should be pointed out that all of the previous studies on roughness effects focused on saturated conditions. This is the first study of the coupled effects of suction and roughness.

Thermal effects on the bearing capacity are also illustrated by the results in Figure 7.8. When the temperature drops from 21°C to 10°C, the bearing capacity of rough piles decreases by about 11%. In the literature, there is no study on the cooling effects on bearing capacity, but heating effects were investigated by some researchers. For example, through a series of centrifuge tests, Ng et al. (2015) measured the bearing capacity of energy piles embedded in saturated Toyoura sand. They found that when the temperature increased from 22°C to 38°C,

the bearing capacity increased by about 13%. This finding is similar to that in Figure 7.8. As observed in the previous studies (Maghsoodi et al., 2020; Di Donna et al., 2016) and this study (see Chapter 5) of soil-pile interfaces, the temperature has a negligible impact on the effective friction angle. Hence, it is postulated that the reduction of bearing capacity is due to the reduction of effective normal stress from soil to pile, which may result from the cooling-induced contraction of pile and soil. This postulation is further studied in the following section.

#### 7.6.2 Mobilization of the shaft and toe resistances

Figure 7.9 shows the axial load distributions at different loading stages of the pile load tests. The axial load distribution of the smooth pile in saturated soil was not obtained because of the damage of fiber during testing. Fortunately, the results of other tests are still sufficient to analyze the influence of suction, temperature and roughness on the axial load distribution. Based on these results, the mobilization of toe and shaft resistances is determined and shown in Figure 7.10.

Figure 7.10(a) shows the relationship between mobilized shaft resistance and pile head displacement at various test conditions. All the curves show a similar trend. The shaft resistance increases significantly at the initial stage and tends to reach a stable state. In the following paragraphs, the value of fully mobilized shaft resistance and the mobilization rate are discussed:

(1) For the fully mobilized shaft resistance, the influence of suction and roughness is obvious. With an increase in suction and roughness, the shaft resistance becomes larger. This is because the shear strength of soil-pile interfaces increases with increasing suction and

roughness, as illustrated in Chapter 5. When the temperature reduces from 21°C to 10°C, the shaft resistance decreases by about 15%. The possible reason has been discussed above: the reduction of effective normal stress from soil to pile may result from the cooling-induced contraction of pile and soil. In summary, the shaft resistance is dependent on the temperature, suction and roughness.

(2) The mobilization rate of shaft resistance is also greatly affected by the roughness and suction. At the saturated condition, the shaft resistance of rough piles is fully mobilized at a displacement of about 1.25 mm. In unsaturated conditions, the displacement required for fully mobilizing the shaft resistance is 0.3 mm for rough piles and 0.75 mm for smooth piles. These data suggest that the mobilization rate is larger at a larger suction and a higher degree of roughness. This is because the mobilization rate of shaft resistance is mainly related to the stiffness of soil-pile interfaces (Potts, 1999). The suction results in an increase in interface stiffness, as shown in Chapter 5. In addition, thermal effects on the mobilization rate of shaft resistance are not obvious.

Figure 7.10(b) presents the mobilized toe resistance – pile head displacement curves. The results suggest that the mobilization rate of the resistance and its final value are almost independent of roughness and temperature. In the ranges of temperature and roughness considered in this study, any variation in the toe resistance is less than 5%. The development of the toe resistance is strongly dependent on soil suction. When suction decreases from 90 kPa to 0, the toe resistance reduces by about 80%.

Based on the results in Figures 7.8 and 7.10, it is reasonable to conclude that temperature and roughness have a negligible influence on toe resistance. Their effects on the pile bearing capacity mainly arise from the influence of temperature and roughness on shaft resistance. On the contrary, suction show obvious effects on both shaft and toe resistances. Furthermore, suction effects on the shaft resistance seem more significant for rough piles than for smooth piles, likely because the dilatancy of soil-pile interfaces increases with increasing suction.

## **7.7 Interpretations of the results of constant-load heating and cooling tests**

### **7.7.1 Typical responses of energy pile to cyclic heating and cooling**

Figure 7.11 shows the responses of soil temperature and pile head settlement to cyclic heating and cooling. It is obtained from the test TMS0 (see Table 7.2). The results from other tests are qualitatively similar, so they are not presented here.

The results in Figure 7.11(a) demonstrate that the temperature control system is able to heat and cool the pile in a temperature range of 10 to 40°C very well. The temperatures of surrounding soils, at 2D and 4D away from the pile surface, only show small changes (less than  $\pm 5^\circ\text{C}$ ). There is a minor delay between the soil temperature and fluid temperature inside piles.

It can be seen from Figure 7.11(b) that the pile heaves at the heating stage and settles when the temperature reduces. This general trend agrees well with the observations from previous studies (Yavari et al., 2016b; Goode and McCartney, 2015; Nguyen et al., 2017).

### **7.7.2 Accumulation of irreversible pile settlement during cyclic heating and cooling**

The accumulation characteristics of irreversible pile head settlement upon thermal cycles are summarized in Figure 7.12. It should be noted that in the calculation of working loads (i.e.,  $0.3Q_{ult}$ ,  $0.5Q_{ult}$  and  $0.7Q_{ult}$ ),  $Q_{ult}$  measured at the saturated condition is used. That's to say, the applied vertical loads are independent of soil suction. The normalized settlement means the ratio of irreversible pile head displacement to pile diameter. The accumulation characteristics of irreversible pile head settlement are affected by various factors, such as soil suction, pile roughness and working load. They are analysed here in detail.

For the rough pile embedded in saturated soils, when the vertical load is  $0.3Q_{ult}$  and  $0.5Q_{ult}$ , the irreversible pile head settlement accumulates with the number of thermal cycles, but at a decreasing rate. At each level of working load, the accumulation rate becomes negligible when the number of thermal cycles reaches five. This is probably related to the thermal deformation of surrounding soils during heating and cooling (Agar et al., 1986; Kwok and Bolton, 2010). The thermal contraction of soils may happen at the early stage of heating and cooling, depending on the initial density and stress, and then the soils reach a stable state. The results in Chapter 5 can be also used to explain the results. When the soil-pile interface is subjected to cyclic heating and cooling at the constant-stress condition, irreversible relative movement between the soil and counterface occurs. The accumulation rate of irreversible movement reduces with the number of cycles. When the working load increases to  $0.7Q_{ult}$ , the pile shows a continuous settlement with thermal cycles. The pile cannot reach a stable state within five cycles, and the accumulated irreversible settlement is around  $1.5\%D$ . This observation implies that the thermally induced irreversible pile head settlement could be critical

at a larger vertical load, which should be more carefully considered in the design of energy piles.

Regarding the rough pile in unsaturated soil, the pile head settlement accumulated during the 15 thermal cycles is about only 0.2%D, which is much smaller than that in the saturated condition (i.e., about 1.5%D). Moreover, pile responses to cyclic thermal cycles can reach a stable state even when the working load is  $0.7Q_{ult}$ . The observed suction effects are mainly because a suction increment is able to increase the bearing capacity.

Upon the completion of 15 cycles of heating and cooling, the irreversible settlement of a smooth pile in unsaturated soil is about 0.7%D, much larger than that of the rough pile (i.e., about 0.2%D). This is likely because, for the smooth pile, the toe resistance plays a more important role. Under cyclic heating and cooling, the pile toe continues to mobilize and results in a larger settlement.

Figure 7.12(b) compares the responses of rough piles embedded in unsaturated soil to two different thermo-mechanical paths. One pile was firstly subjected to five thermal cycles under  $0.3Q_{ult}$  vertical load. Then, the vertical load was increased to  $0.5Q_{ult}$  and five more thermal cycles were applied. The other pile was directly subjected to  $0.5Q_{ult}$  vertical load and 15 thermal cycles. In the figure, the initial settlement (i.e., the value at zero thermal cycles) is induced by previous thermo-mechanical loads. As expected, the initial settlement is larger for the former case. However, during the subsequent cyclic heating and cooling, the irreversible settlement accumulates at a higher rate in the latter case. The settlement after five thermal

cycles is larger in the latter case. This finding implies that some prior thermal cycles at a smaller working load may be able to reduce the long-term settlement of energy piles.

### 7.7.3 Distribution of soil temperature

Figures 7.13(a) and (b) show the soil temperature distribution surrounding energy piles during the heating and cooling phases, respectively. The results at the 5<sup>th</sup> heating and 5<sup>th</sup> cooling are presented, and the results from other stages are similar. The temperature profiles, at the soil-pile interface, 2D and 4D away from the interface, are measured.

At the end of the 5<sup>th</sup> heating (see Figure 7.13(a)), the temperature at the soil-pile interface is around 36°C in the saturated condition, while it is about 38°C in unsaturated conditions. Similarly, the unsaturated soil has a higher temperature at 2D from the pile surface than the saturated soil, although the difference is only about 1°C. In contrast, the soil temperature at the 4D location is lower in unsaturated conditions than that in the saturated condition. The above data confirms that the temperature distribution is affected by soil suction. Saturated soil has a higher thermal conductivity than unsaturated soil, as shown in Chapter 3. At the saturated condition, heat would be transferred at a larger rate from the soil-pile interface to the far-field ground (Cui et al., 2022; Lu and Dong, 2015). Hence, the saturated condition has a smaller temperature in the near-field ground but a higher temperature in the far-field ground, as compared to the unsaturated condition. This observation is also consistent with the numerical results in Chapter 4.

Although the temperature variation along the depth is within 1°C, the temperature at the soil-pile interface shows a slightly decreasing trend in the vertical direction, as shown in

Figure 7.12(a). Inversely, the temperature increased with soil depth at the 2D location. This could be partially related to the thermal conductivity characteristics of soils. The thermal conductivity increases with increasing stress and depth, according to the findings in Chapter 3. The results in Figure 7.13(b) also present the same trend at the cooling stage. With a higher thermal conductivity at the larger depth, heat would be transferred from the soil-pile interface to far-field ground more quickly, as discussed above.

From the temperature distribution measured at the end of the 5<sup>th</sup> cooling, similar conclusions about the effects of suction and depth can be drawn. As compared to the temperatures in the saturated condition, the temperature in unsaturated conditions is lower in the near-field ground but higher in the far-field ground. Therefore, the results in Figure 7.13(b) are not described in detail.

### 7.7.4 Thermal effects on the axial load distribution and neutral plane

The axial load at any depth of pile can be calculated by multiplying Young's modulus of aluminium (i.e., 69 GPa) with the mechanical strain measured through TM-fibers. The results of axial load distribution are summarized in Figure 7.14. A positive value in the abscissa means compressive force, while a negative value means tension. The neutral plane of the pile is defined as the location where the relative movement between pile and soil is zero. At the neutral plane, the slope of the axial force-depth changes its sign.

The results of rough piles embedded in saturated soil are presented in Figures 7.14(a) and (d). During the heating phase, negative skin friction occurs when the working load is  $0.3Q_{ult}$ . The neutral plane is located at the depth of 0.33 m. This is because, upon the thermal

elongation of piles, the pile has an upward movement with reference to the ground. When the working load increases to  $0.5Q_{ult}$  and  $0.7Q_{ult}$ , however, no obvious negative skin friction is observed. This is likely because when the vertical load is larger, the initial upward friction from soil to pile is higher, and it cannot be fully reversed by the relative movement between soil and pile during heating. This observation is consistent with the results of saturated centrifuge tests by Ng et al. (2015). They reported that with increasing vertical load, the neutral plane shows an upward shift, meaning that the heating-induced negative skin friction takes place within a smaller portion of piles and even disappears.

The results from Figure 7.14(d) indicate that during cooling, the axial load reduces in the upper part of the pile because of skin friction. However, it increases with depth in the lower part, because the cooling-induced contraction of piles alters the direction of relative movement between pile and soil (Amatya et al., 2012; Bourne-Webb et al., 2009). Negative skin friction happens at the low part of the pile and the toe resistance is zero, which could induce significant pile head settlement (see Figure 7.12). Pile responses to the cooling should be carefully considered in the practical design. Furthermore, the locations of the neutral plane at various vertical loads ( $0.3Q_{ult}$ ,  $0.5Q_{ult}$ ,  $0.7Q_{ult}$ ) fall in a narrow range of 0.3 m to 0.35 m. The increase of vertical load results in a downward slight movement of the neutral plane. This is different from the heating case, where the neutral plane tends to move upwards as the vertical load increases.

Figures 7.14(b) (c) (e) and (f) show the axial load distributions of rough and smooth piles in unsaturated soil. The results in these two cases are qualitatively similar to those in

Figures 7.14(a) and (d). To analyze the influence of suction and roughness on the neutral plane at a quantitative level, the locations of the neutral plane at various test conditions are summarized in Figure 7.15.

With an increase in suction, the neutral plane in the heating phase moves down, particularly when the vertical load on the pile head is relatively large. The suction effects may arise from different mechanisms. Firstly, the temperature variation at the soil-pile interface is larger in unsaturated conditions, as illustrated in Figure 7.13. The heating-induced elongation of piles is larger, resulting in a larger portion of negative skin friction. Secondly, under unsaturated conditions, the applied vertical load normalized by its bearing capacity is relatively smaller, so the neutral plane is deeper. At the cooling phase, however, suction effects on the neutral plane are very minor. Any change induced by suction is less than 0.02 m. This is most probably because, during cooling, the pile contraction could reduce the end constraint. The neutral plane tends to the midpoint of piles, according to the theoretical framework of energy piles (Bourne-Webb et al., 2013).

Regarding the effects of roughness on the neutral plane, it is negligible at the low vertical load (i.e.,  $0.3Q_{ult}$ ). When the vertical load increase to  $0.5Q_{ult}$  and  $0.7Q_{ult}$ , the roughness increment results in a slight downward movement of the neutral plane at both the heating and cooling stages. This is likely related to the mobilization of shaft resistance. When the vertical load increases, the mobilized shaft resistance increases and plays an increasing role in the load transfer process.

#### 7.7.5 Effects of suction and roughness on the thermally induced axial load

Figure 7.16 shows the thermally induced axial load at different suctions and degrees of roughness. It is calculated by the following equation (Stewart and McCartney, 2014):

$$\Delta\sigma_T = E \cdot (\varepsilon_{T-free} - \varepsilon_{T-M}) \cdot A \quad (7-2)$$

where  $\Delta\sigma_T$  is the thermally induced axial load;  $\varepsilon_{T-free}$  is the thermal strain corresponding to the free expansion or contraction, which can be determined based on the measurement of T-fibers;  $\varepsilon_{T-M}$  is the measured strain by TM-fibers, considering the mechanical restraint;  $E$  is Young's modulus of aluminium;  $A$  is the cross-section area of model piles. Heating induces compressive force (i.e., an increase in axial load) due to the development of negative skin friction, and cooling results in tensile force (i.e., a reduction of axial load). This is consistent with the data reported in Figure 7.14.

A comparison between Figures 7.16(a) and (b) suggests that when a rough pile is heated, the maximum value of the thermally induced axial load is around 210N in unsaturated conditions, but it is only 18N in the saturated condition. At the saturated condition, the measured 18N is around 35% of the working load (i.e., 53N) on the pile, which is close to previous results (Bourne-Webb et al., 2009; Ng et al., 2015). At unsaturated conditions, the obtained 210N is around four times the working load. The suction effects are because the stiffness of the soil-pile interface is higher in unsaturated conditions. The influence of suction on the axial force distribution can be also observed during the cooling phase. When a rough pile is cooled, the results from Figures 7.16(d) and (e) indicate that the thermally induced axial load can be up to 75N for the unsaturated condition and 18N for the saturated condition.

The results in Figures 7.16(c) and (f) present the results of a smooth pile embedded in unsaturated grounds. During heating, the thermally induced axial load is much smaller than that of the rough pile. During cooling, however, the roughness effects on the thermally induced axial load are insignificant. This observation agrees well with the observations in Figure 7.14. This finding implies that the roughness plays an important role in the heating phase but not in the cooling phase. This conclusion is obtained through limited small-scale physical model tests. It should be applied with caution.

#### 7.7.6 Axial displacement of piles subjected to heating and cooling

The axial displacement of energy piles can be calculated from the measured pile head settlement and axial strain distribution. The results of different test conditions are shown in Figure 7.17. It can be concluded that when the pile is subjected to heating, the upper part heaves and the lower part settles. On the contrary, when the pile is subjected to cooling, the upper part settles and the lower part heaves. These two different trends are closely related to thermally induced elongation/contraction of piles.

For the rough pile in unsaturated rough soil, Figures 7.17(b) and (e) show that the axial displacement decreases along piles at a slower rate when the vertical load is larger. This is likely because the mobilized shaft resistance increases with the increasing vertical load, resulting in more constrain on pile movement. However, the curves in Figures 7.17(a), (c), (d) and (f) show a negligible effect of vertical load on the pile axial displacement. This is likely because these two cases involve either smooth or saturated conditions, and the shaft resistance is smaller.

To further analyze the effects of suction and roughness on pile head and toe displacements, the results are summarized in Figure 7.18. It can be observed from Figures 7.18(a) and (c) that compared to the results in unsaturated conditions, the pile head and toe displacements are consistently smaller in saturated conditions, during either heating or cooling. This is mainly because the thermal conductivity of saturated soil is higher. The change in pile temperature is lower, as illustrated in Figure 7.13, leading to less significant elongation/contraction of piles.

Regarding the influence of roughness on pile head displacement, it is almost negligible. However, the pile toe displacement induced by both heating and cooling is consistently larger when the pile roughness is smaller. This is because, with a smaller roughness, the stiffness of the soil-pile interface is smaller. Hence, the thermally induced axial load is smaller (see Figure 7.16) and the constraint of ground to pile expansion is smaller.

### **7.8 Summary**

In this chapter, a small-scale physical model was developed for investigating the thermo-mechanical behaviour of energy piles in saturated and unsaturated soils. Two series of model tests were conducted. The constant-temperature pile load tests were carried out to investigate the bearing capacity of energy piles. The constant-load heating and cooling tests were conducted to study the settlement behaviour of energy piles under working conditions. The data are helpful for improving the understanding of the effects of suction and roughness on the thermo-mechanical behaviour of energy piles. Based on the experimental results, some conclusions may be drawn:

(1) The bearing capacity of energy piles increases with increasing suction and roughness. For the suction effects, they are attributed to the increase in both shaft and toe resistance, due to the increase in the strengths of soils and soil-pile interfaces. However, the roughness only affects the shaft resistance. A temperature decrement results in a reduction of bearing capacity. This is probably because cooling induces smaller normal stress from soil to pile.

(2) During cyclic heating and cooling, the irreversible pile head settlement shows two different responses. When the working load is relatively small (less than  $0.5Q_{ult}$  in this study), for both saturated and unsaturated conditions, the settlement increases with the number of thermal cycles, but at a decreasing rate. When the working load is relatively large ( $0.7Q_{ult}$  in this study), the pile settlement does not reach a stable state in the saturated condition. Taking the rough pile as one example, the settlement included by 15 thermal cycles is around  $1.5\%D$  in the saturated condition, but it is only  $0.2\%D$  in unsaturated conditions. In addition, roughness decrement would induce more accumulated pile settlement, due to the reduction of pile shaft resistance.

(3) When a pile is subjected to heating, the temperature at the soil-pile interface is higher in unsaturated soil than that in saturated soil, because the thermal conductivity of surrounding soil is larger in the saturated condition. The soil temperature at the far-field ground is lower in unsaturated conditions.

(4) The location of the pile neutral plane moves downward with increasing suction when the pile is subjected to heating. This is because the larger temperature increment at

unsaturated conditions induces a larger constraint at the pile toe. However, when the pile is subjected to cooling, suction effects on the locations of the neutral plane are negligible. For the roughness effects, the pile neutral plane moves upwards with decreasing roughness, since less constraint arises from pile toe.

Table 7.1. Summary of constant-temperature pile load tests.

Series ID	Pile roughness	Compaction water content (%)	Initial suction (kPa)	Temperature (°C)	Loading sequence
MS0	Rough	13.8	0	21	M
	Smooth	13.8	0	21	M
MS90	Rough	13.6	90	21	M
	Smooth	13.6	90	21	M
MS90-T	Rough	13.6	90	10	T → M

Table 7.2. Summary of constant-load heating and cooling tests.

Series ID	Pile roughness	Compaction water content (%)	Initial suction (kPa)	Vertical load	Number of thermal cycles at a given vertical load
TMS0	Rough	12.8	0	$0.3Q_{ult} \rightarrow 0.5Q_{ult} \rightarrow 0.7Q_{ult}$	5
TMS90	Rough	12.6	90	$0.3Q_{ult} \rightarrow 0.5Q_{ult} \rightarrow 0.7Q_{ult}$	5
	Smooth	12.6	90	$0.3Q_{ult} \rightarrow 0.5Q_{ult} \rightarrow 0.7Q_{ult}$	5
TMS90-C	Rough	12.6	90	$0.5Q_{ult}$	15

Note: at each condition of suction and vertical load, the model pile is subjected to five thermal cycles; the thermal loading for one cycle:  $21^{\circ}\text{C} \rightarrow 40^{\circ}\text{C} \rightarrow 21^{\circ}\text{C} \rightarrow 10^{\circ}\text{C} \rightarrow 21^{\circ}\text{C}$ ; for the S90TMR-C test, the model pile is subjected to fifteen thermal cycles at  $0.5Q_{ult}$  vertical load.

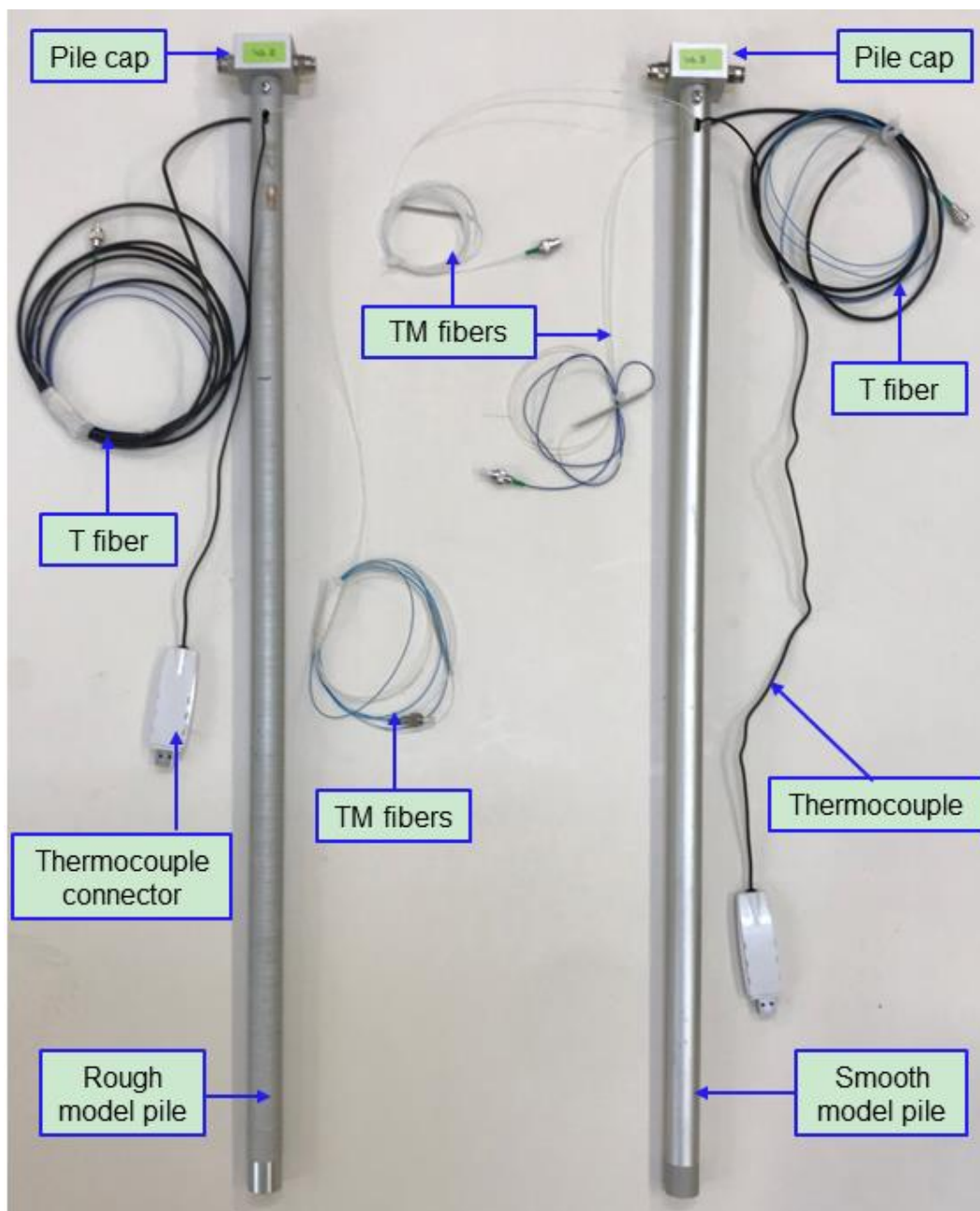


Figure 7.1. Model piles with different degrees of roughness.



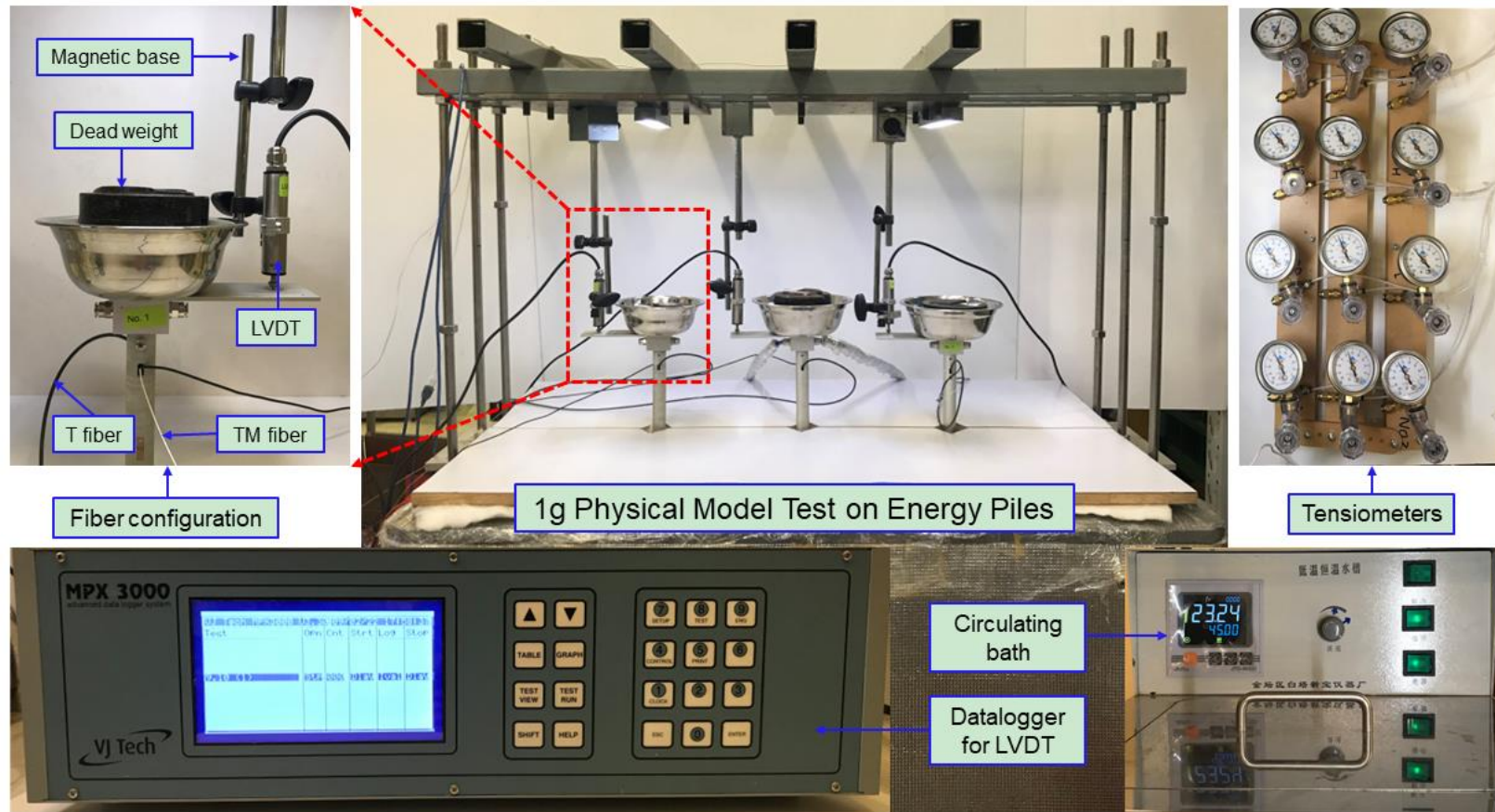


Figure 7.3. Layout of the physical model test.

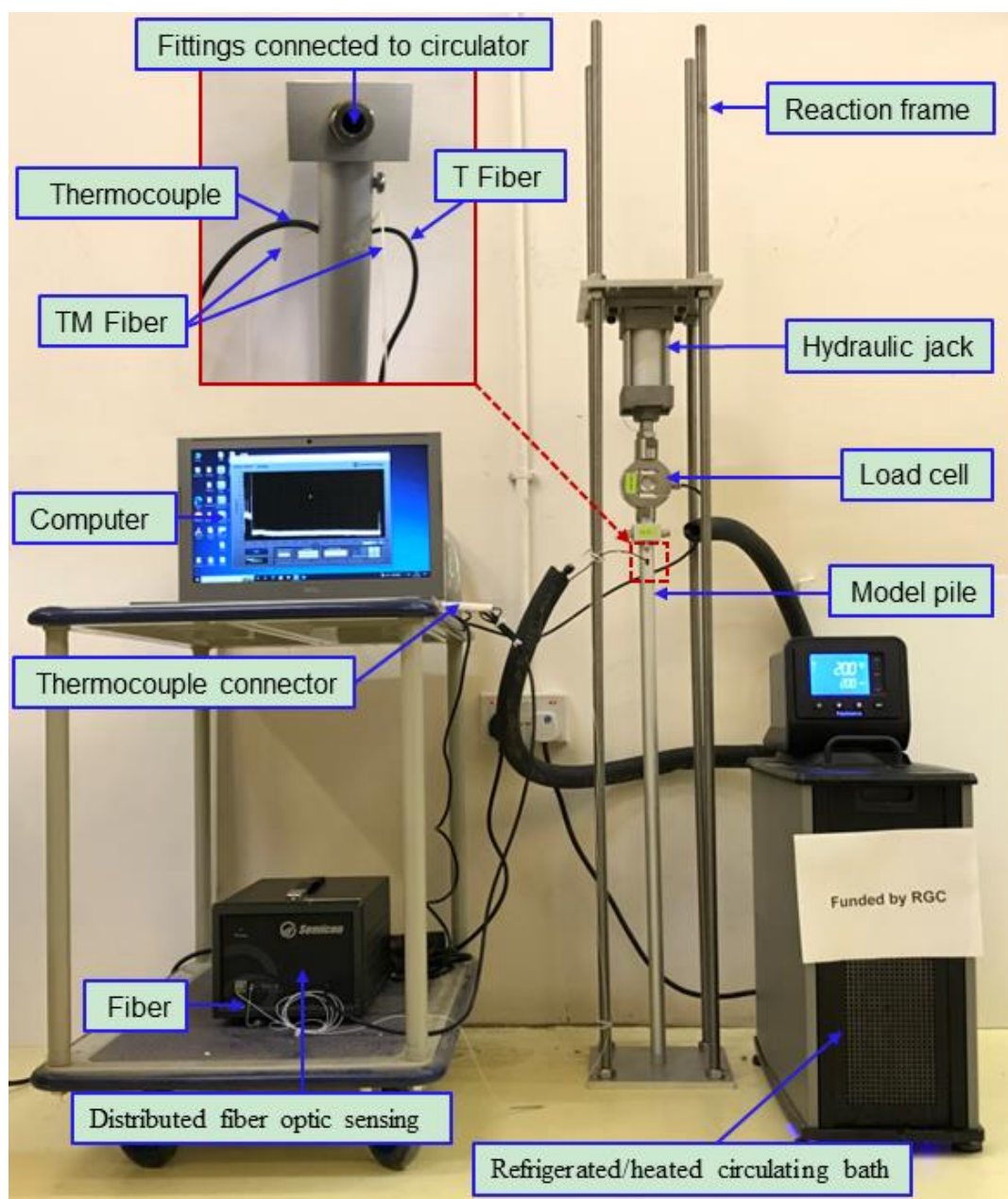
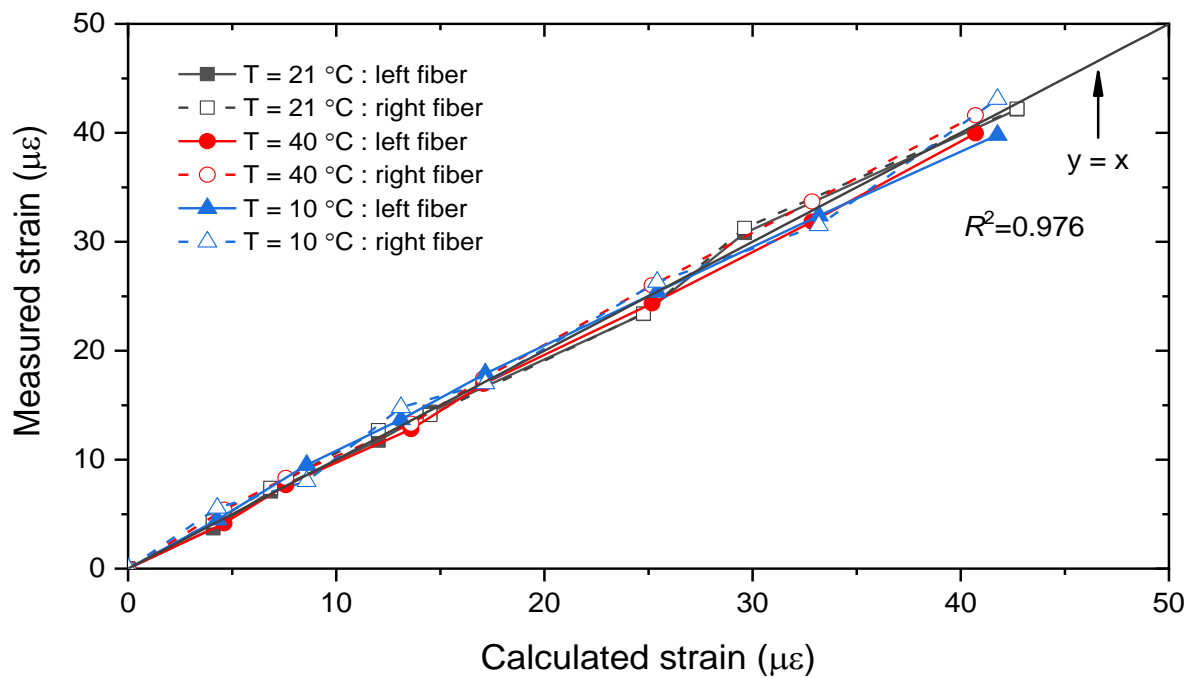
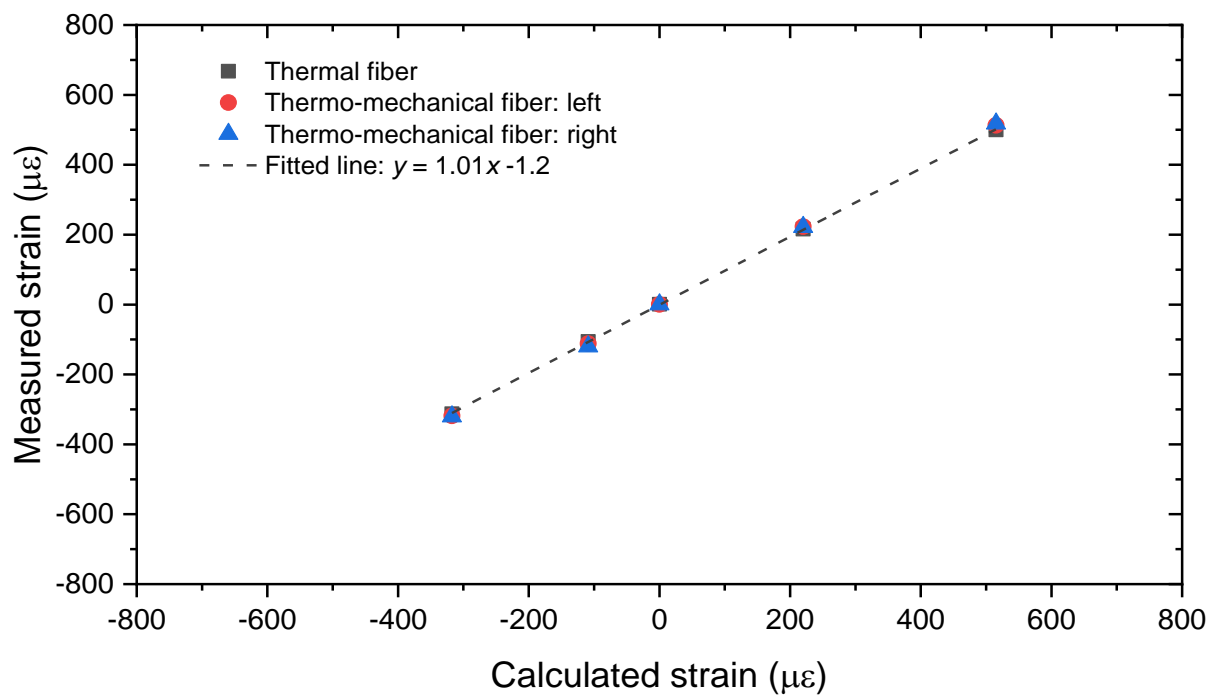


Figure 7.4. Overview of the calibration tests.



(a)



(b)

Figure 7.5. Calibration results of the fibers at different thermo-mechanical loading paths: (a) mechanical loading at different temperatures; (b) thermal loading without mechanical loads.

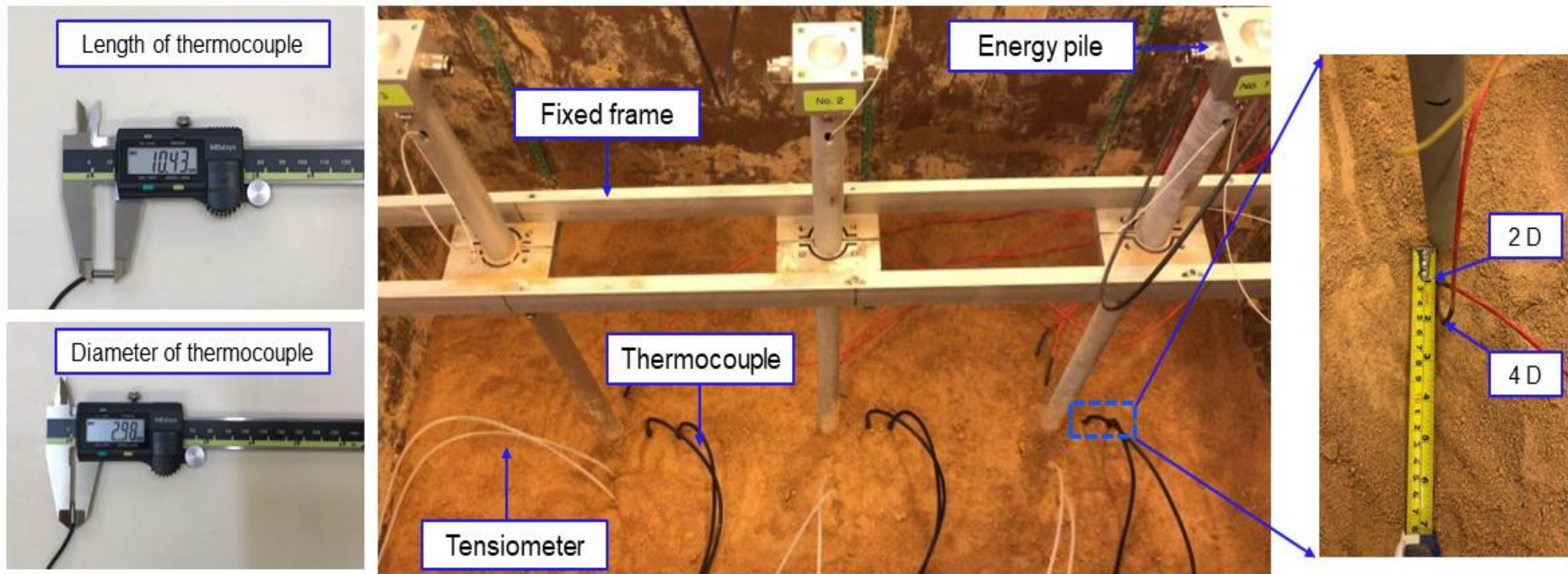
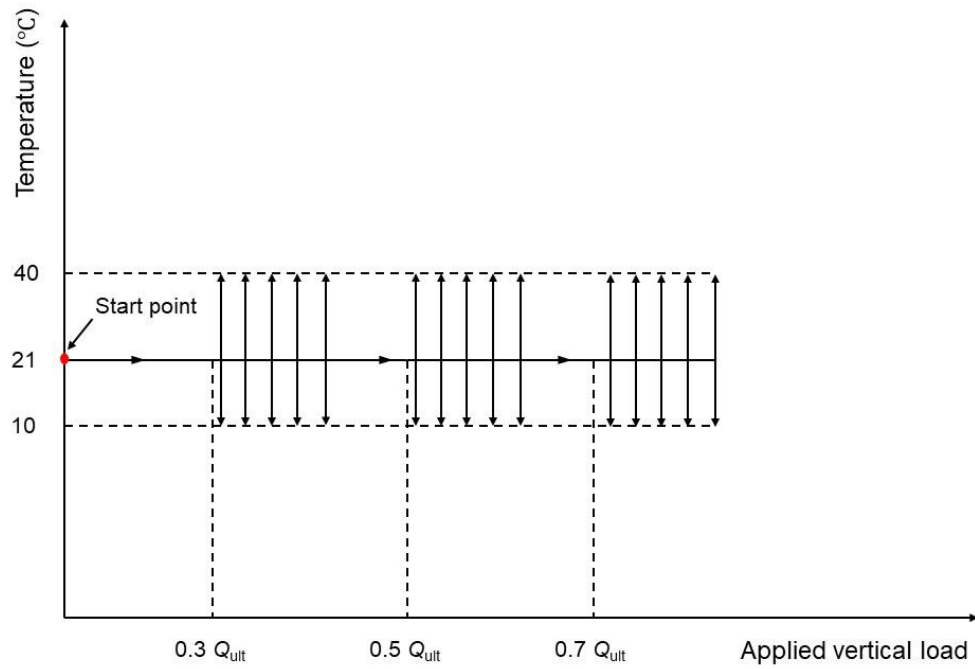
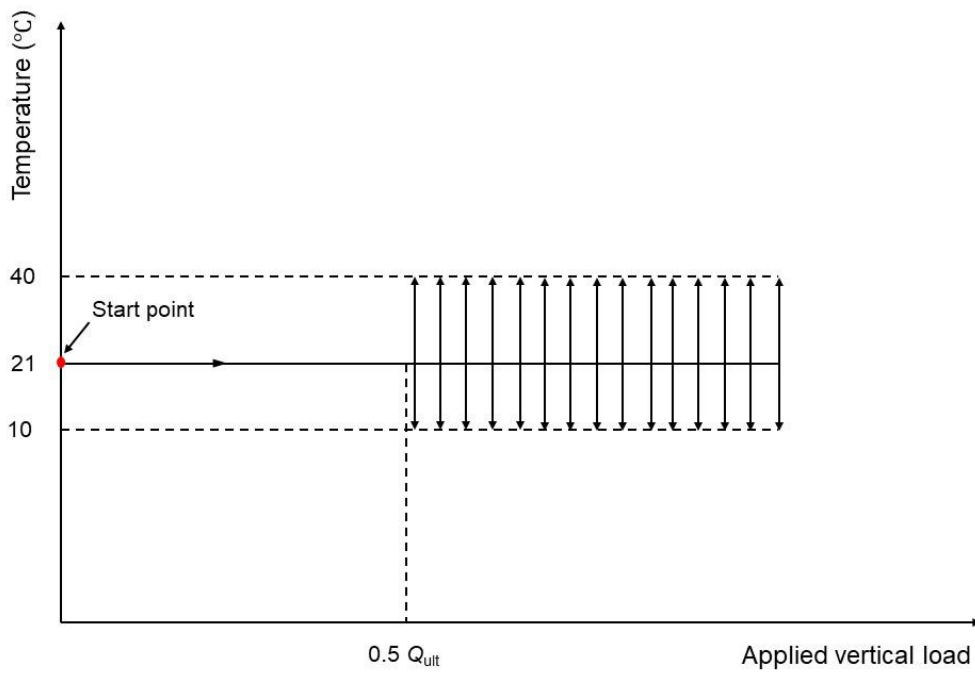


Figure 7.6. Installation of thermocouples and tensiometers.



(a)



(b)

Figure 7.7. Thermo-mechanical loading paths for constant-load heating and cooling tests.

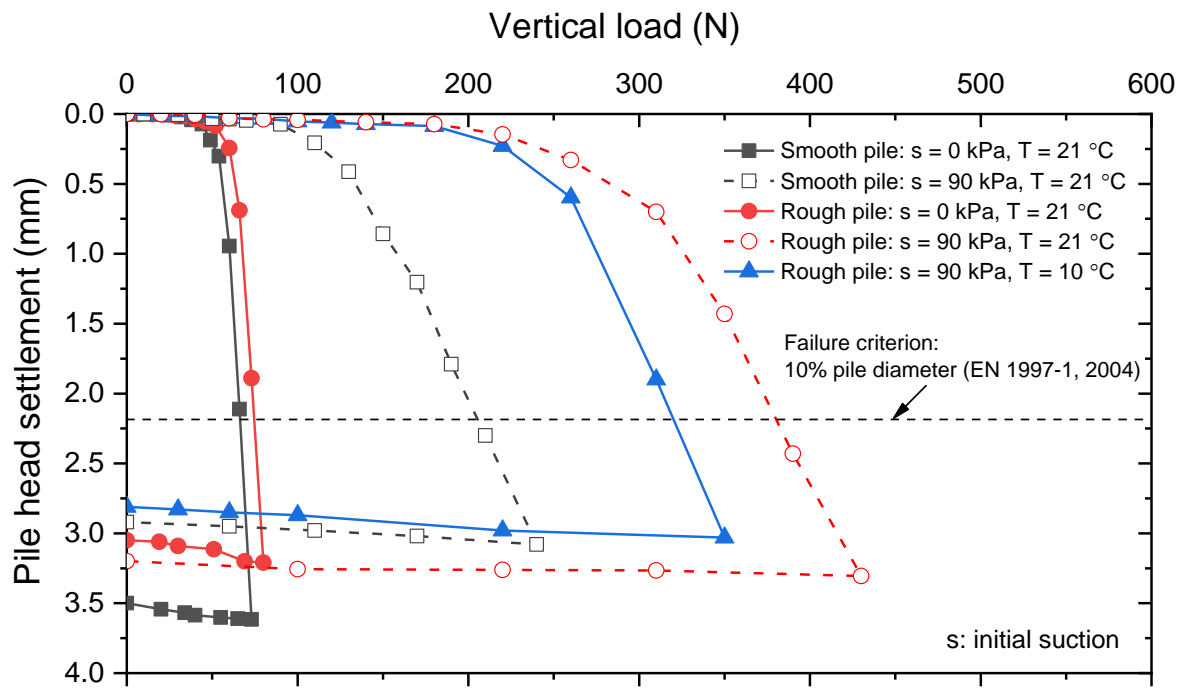


Figure 7.8. Load-settlement relationships of model piles at various conditions of suction, temperature and roughness.

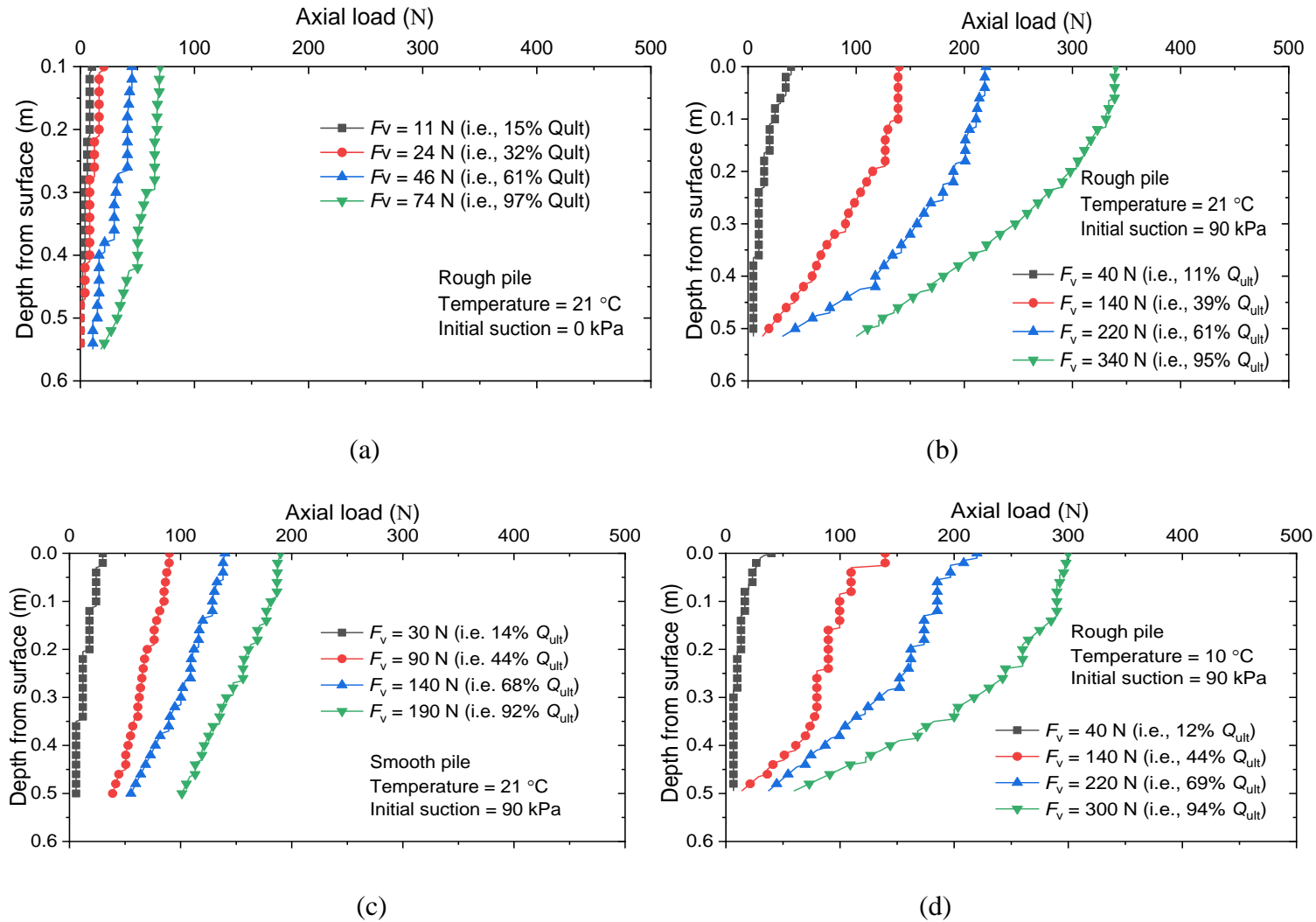
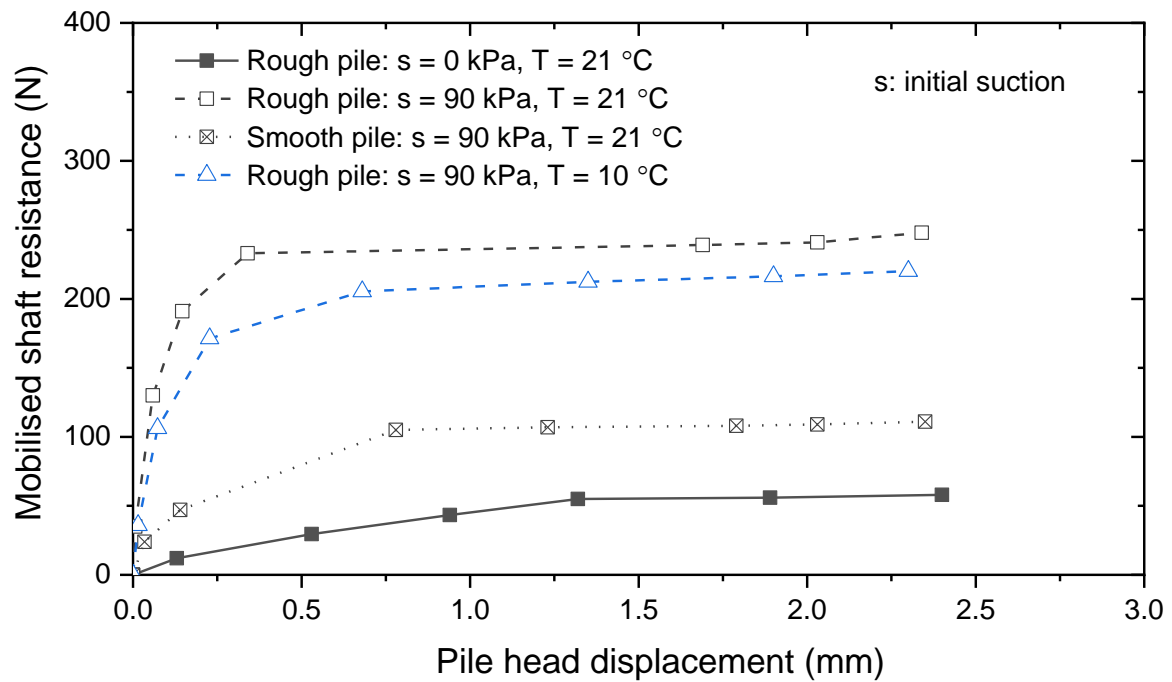
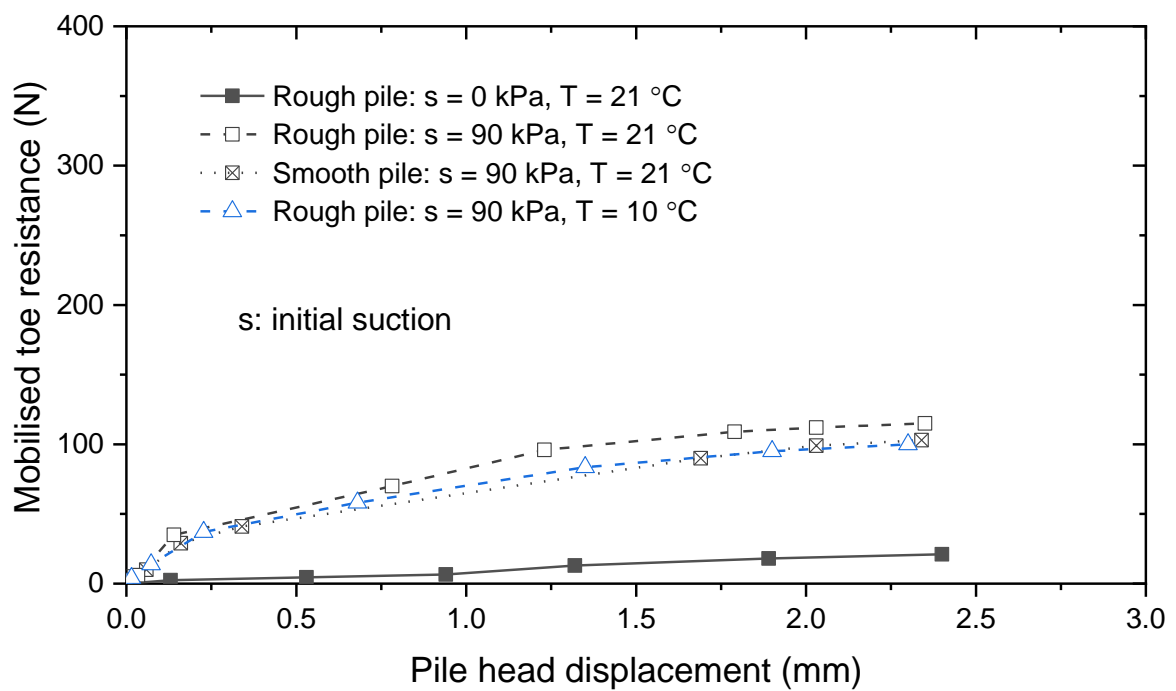


Figure 7.9. Evolution of axial load distributions during the loading process at various suctions, temperatures and degrees of roughness.

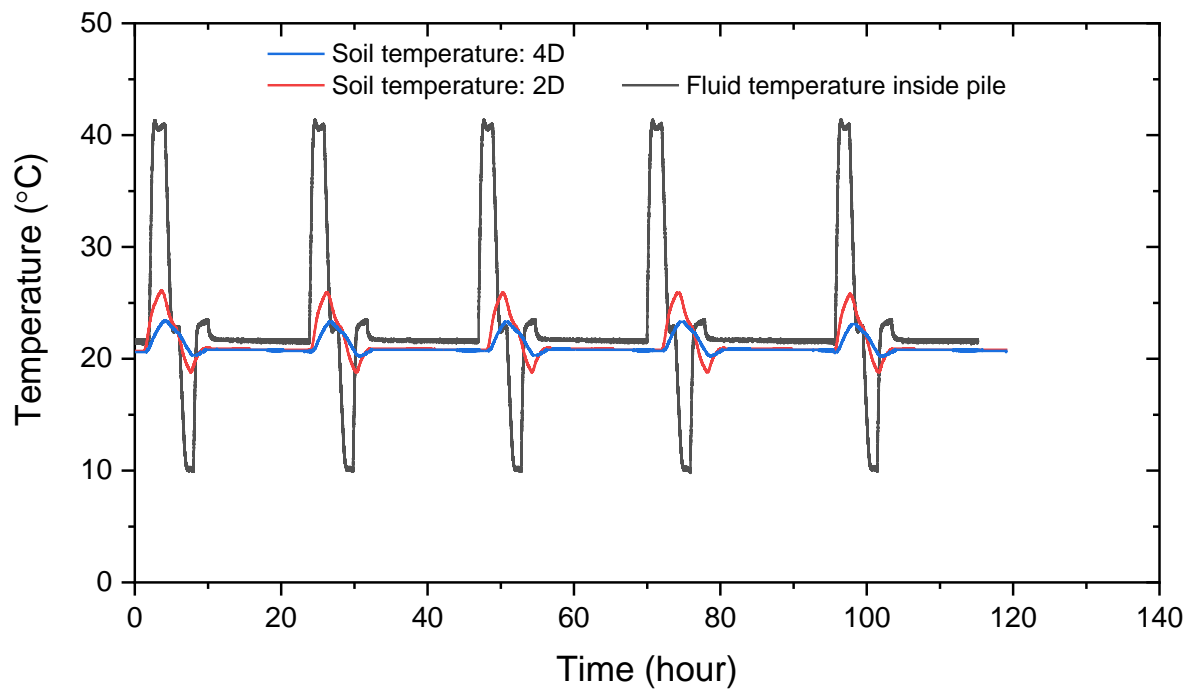


(a)

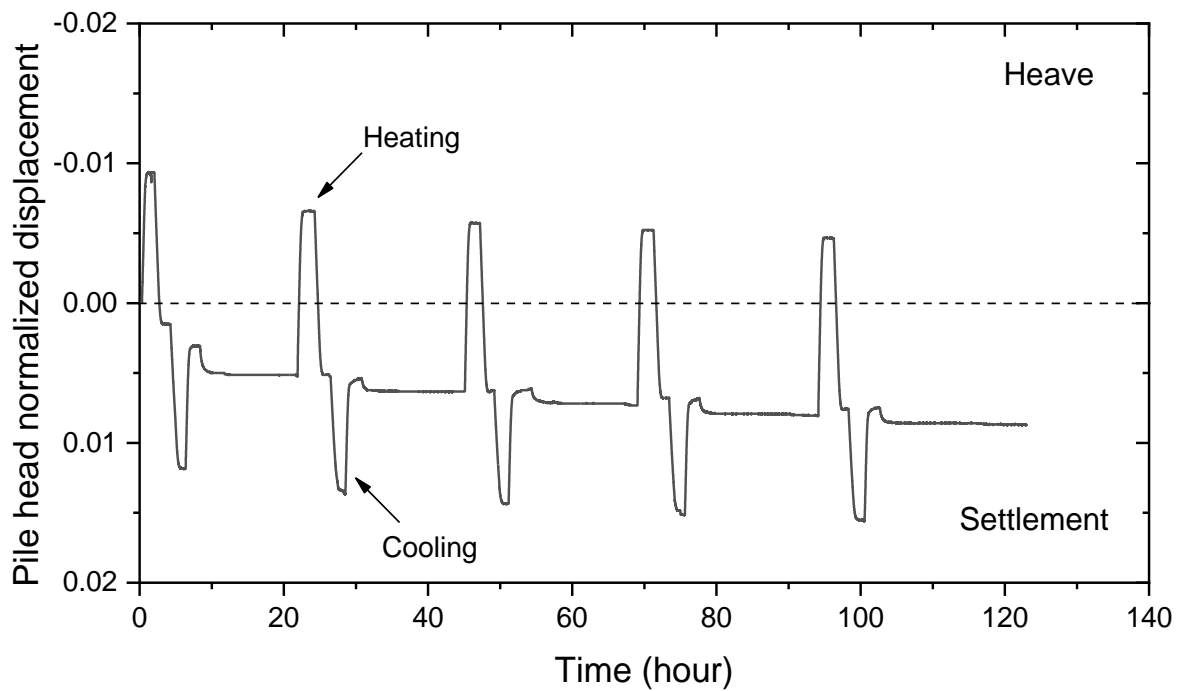


(b)

Figure 7.10. Evolution of shaft resistance and pile toe resistance at various suctions, temperatures and degrees of roughness.

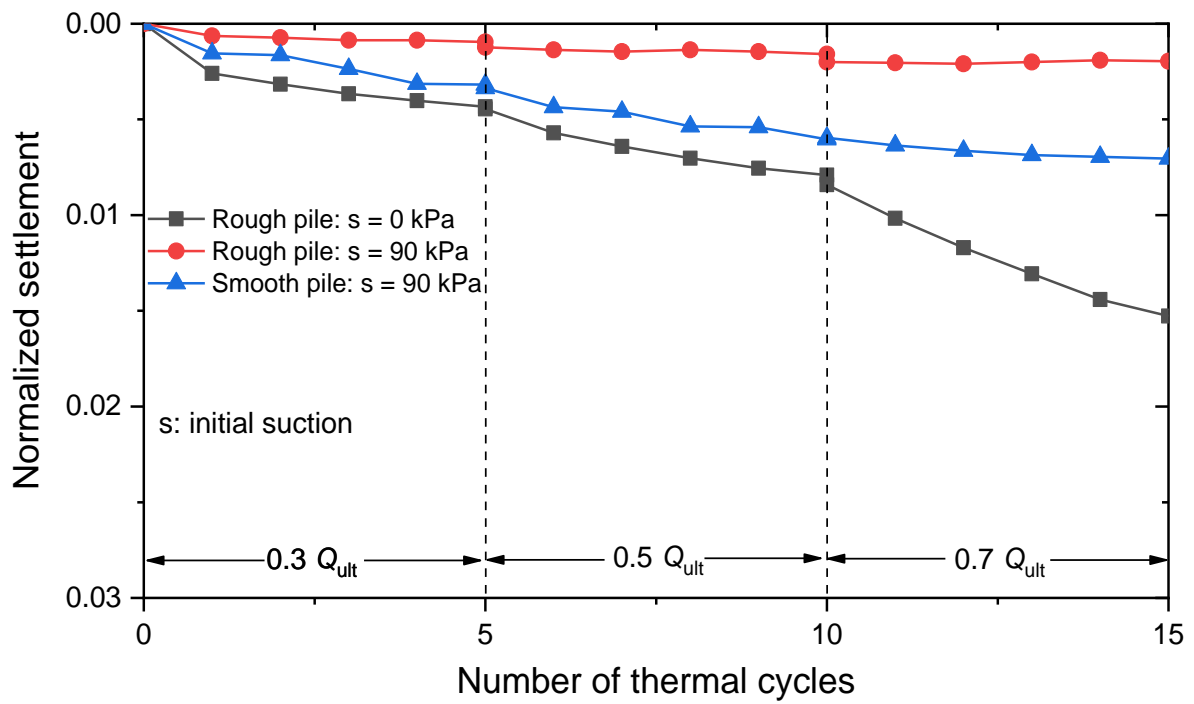


(a)

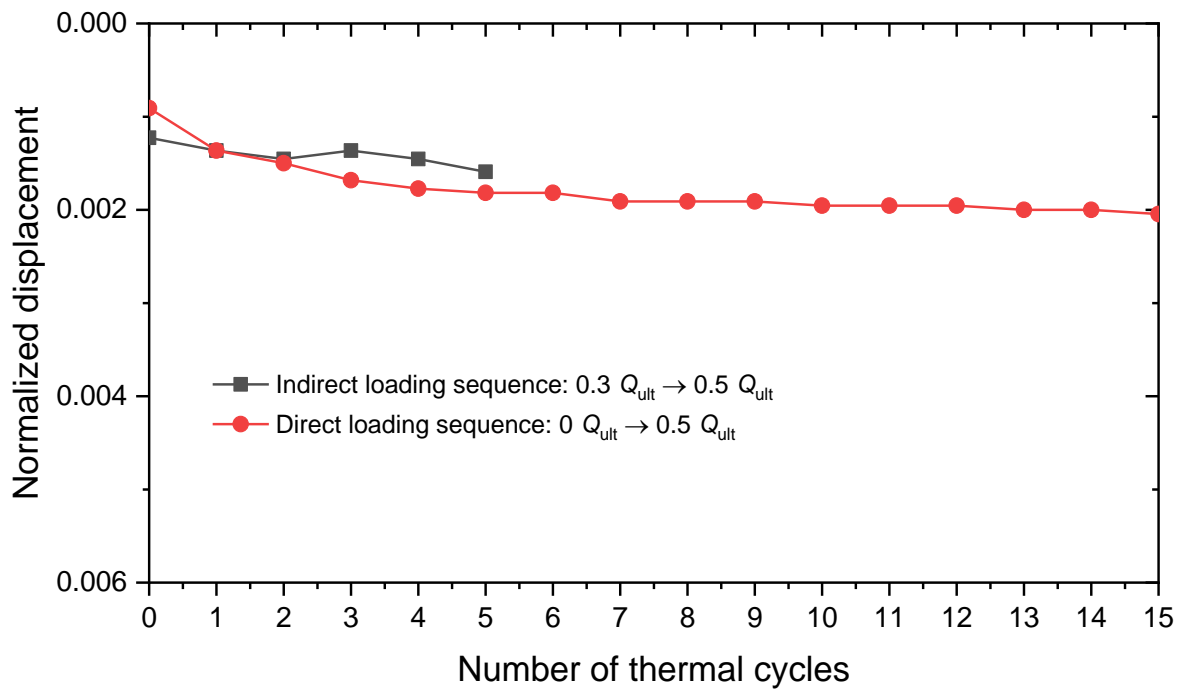


(b)

Figure 7.11. Typical response curves: (a) fluid temperature inside piles and soil temperature; (b) pile head settlement during heating and cooling.

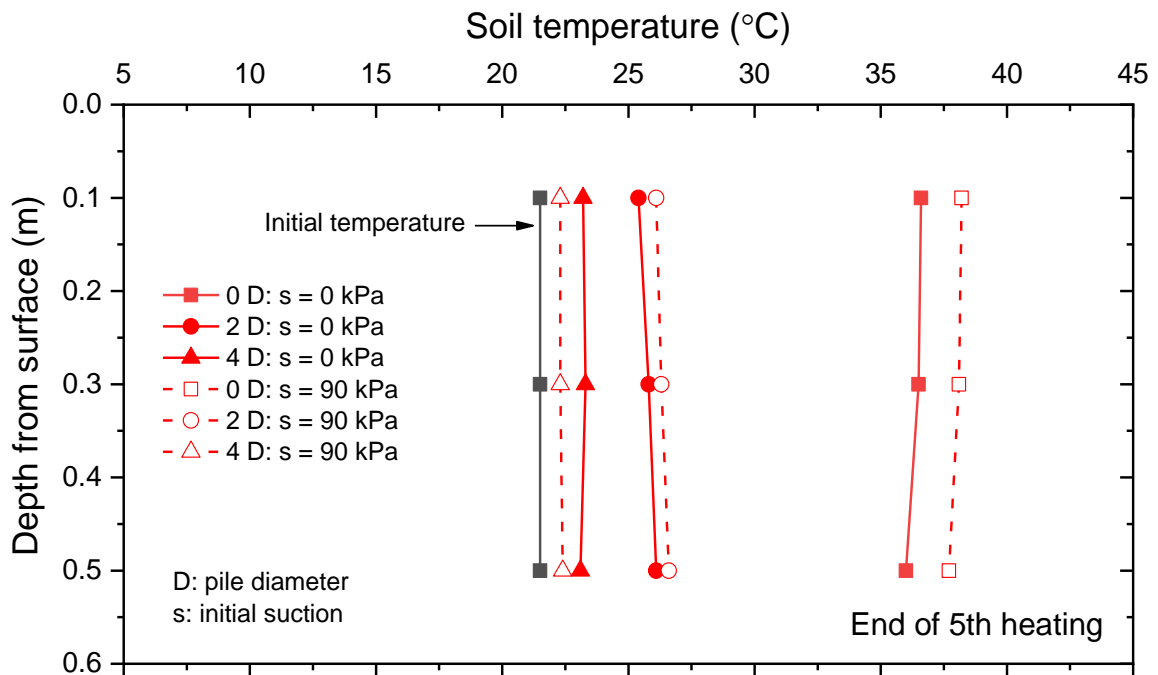


(a)

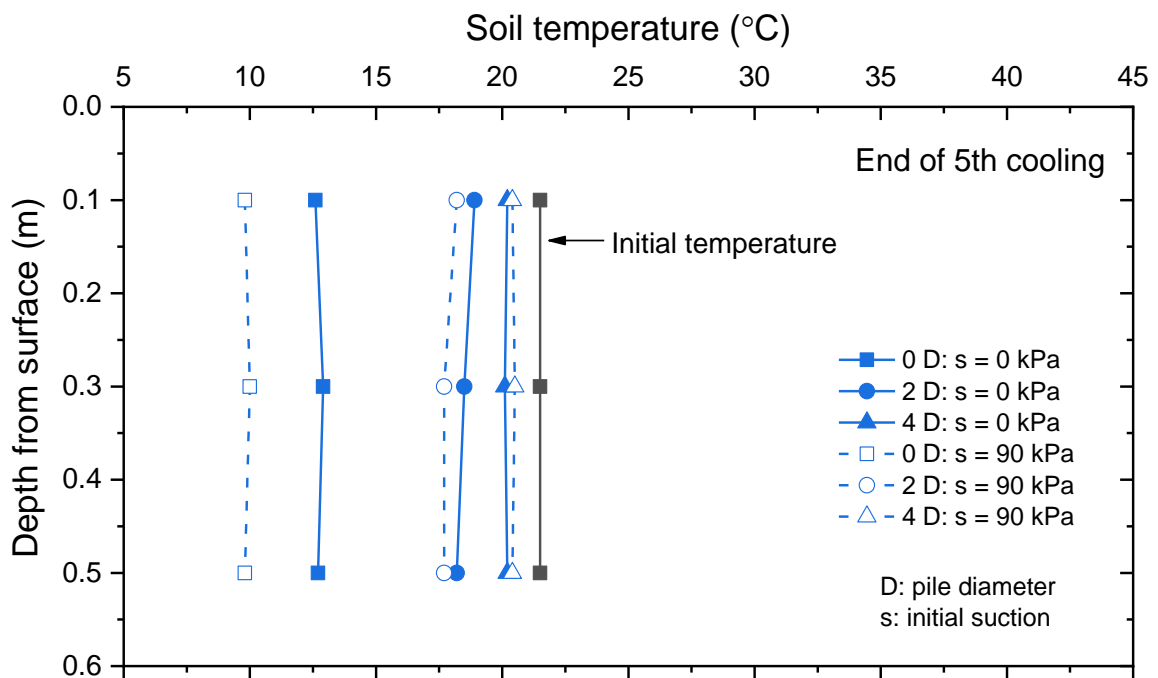


(b)

Figure 7.12. Pile head displacement during thermo-mechanical loads: (a) effects of suction, roughness and working load; (b) effects of thermo-mechanical paths.



(a)



(b)

Figure 7.13. Measured soil temperature at different suctions: (a) heating phase; (b) cooling phase.

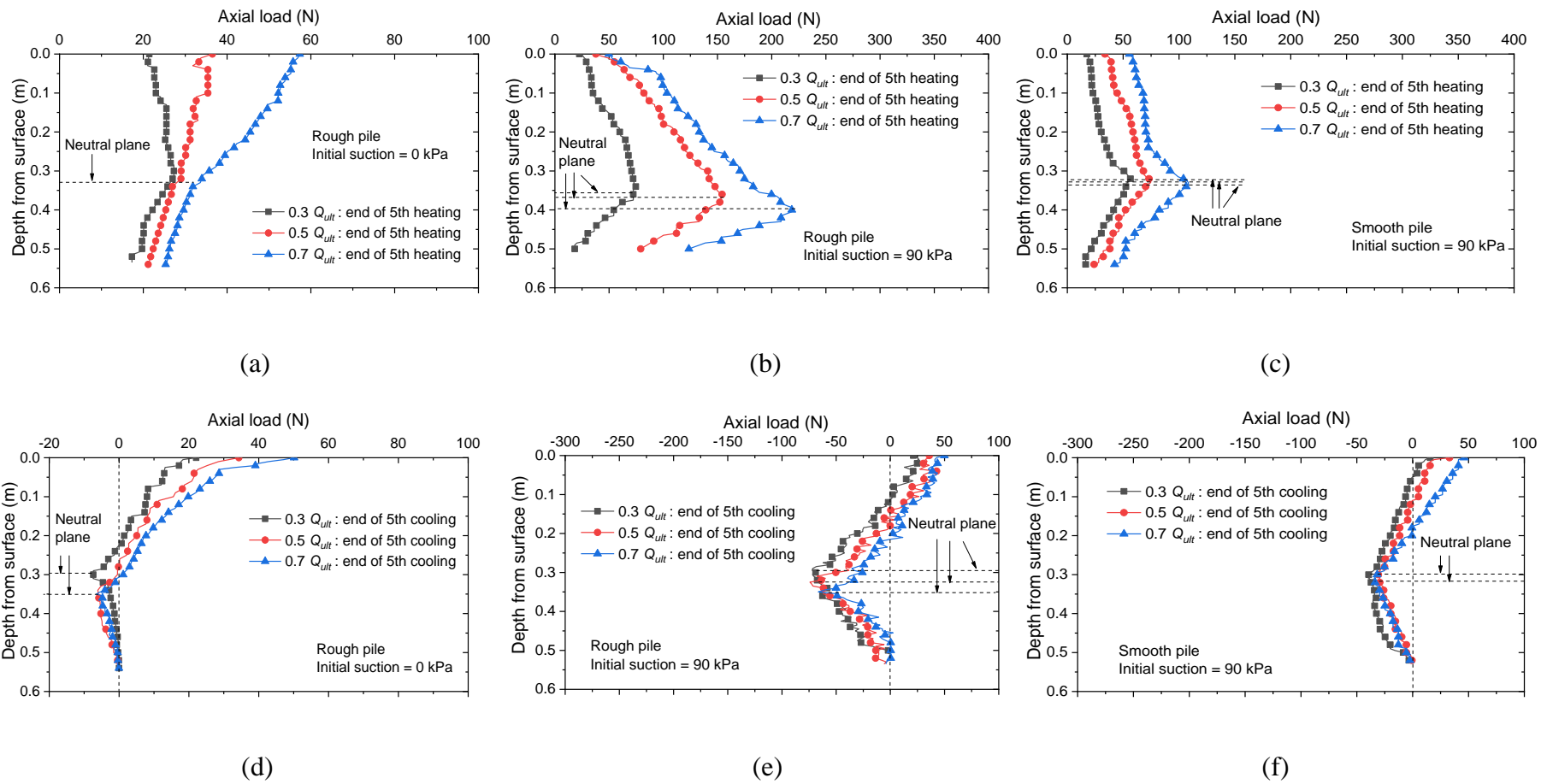
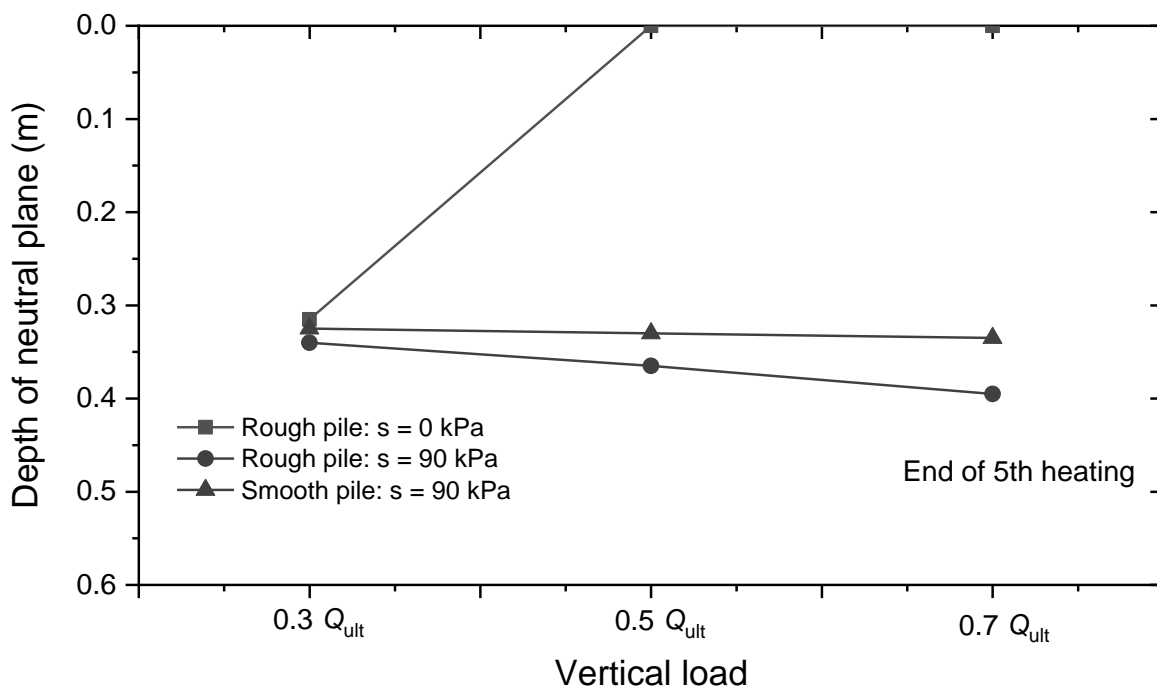
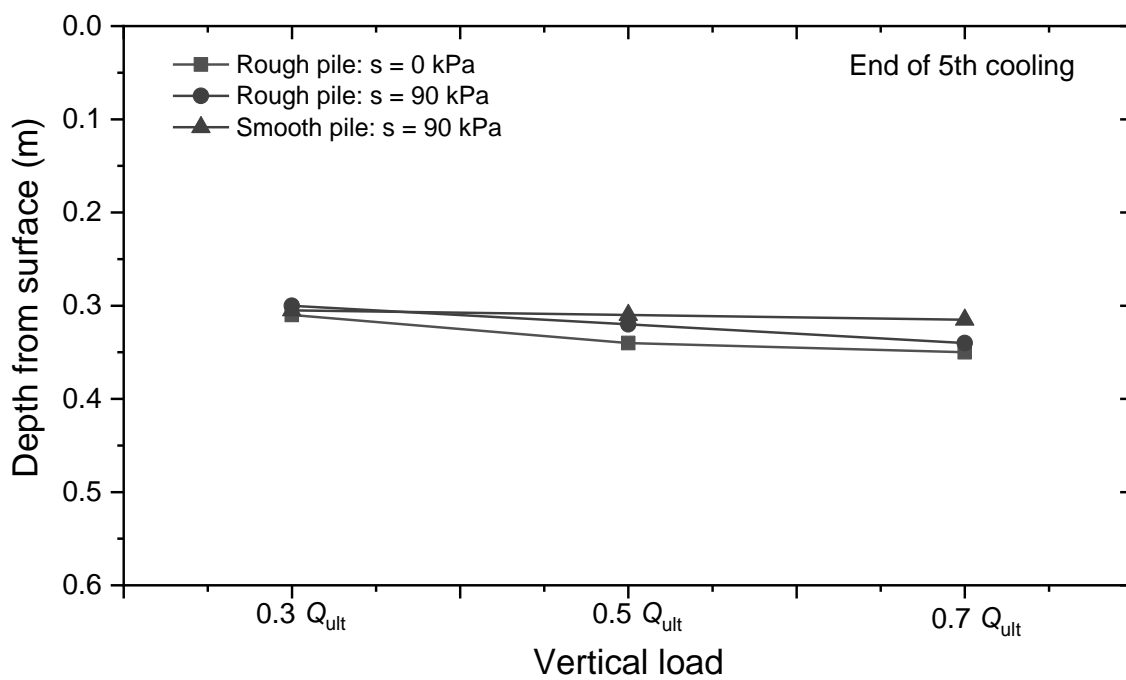


Figure 7.14. Axial load distributions at various stress levels and suctions: (a), (c), (e) heating phase; (b), (d), (f) cooling phase.



(a)



(b)

Figure 7.15. Variations of neutral plane locations: (a) at end of 5<sup>th</sup> heating; (b) at end of 5<sup>th</sup> cooling.

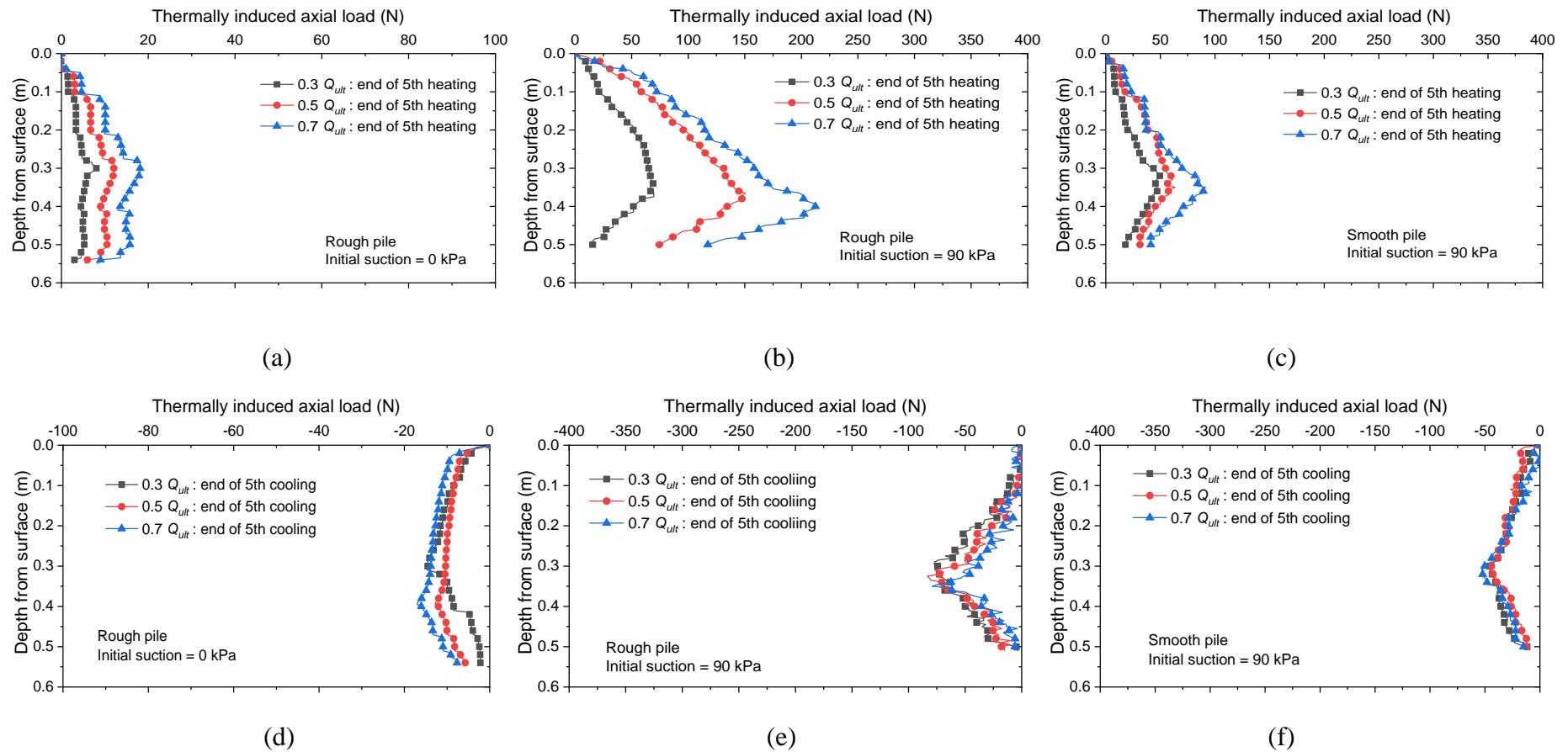


Figure 7.16. Thermally induced axial load: (a), (b), (c) heating phase; (d), (e), (f) cooling phase.

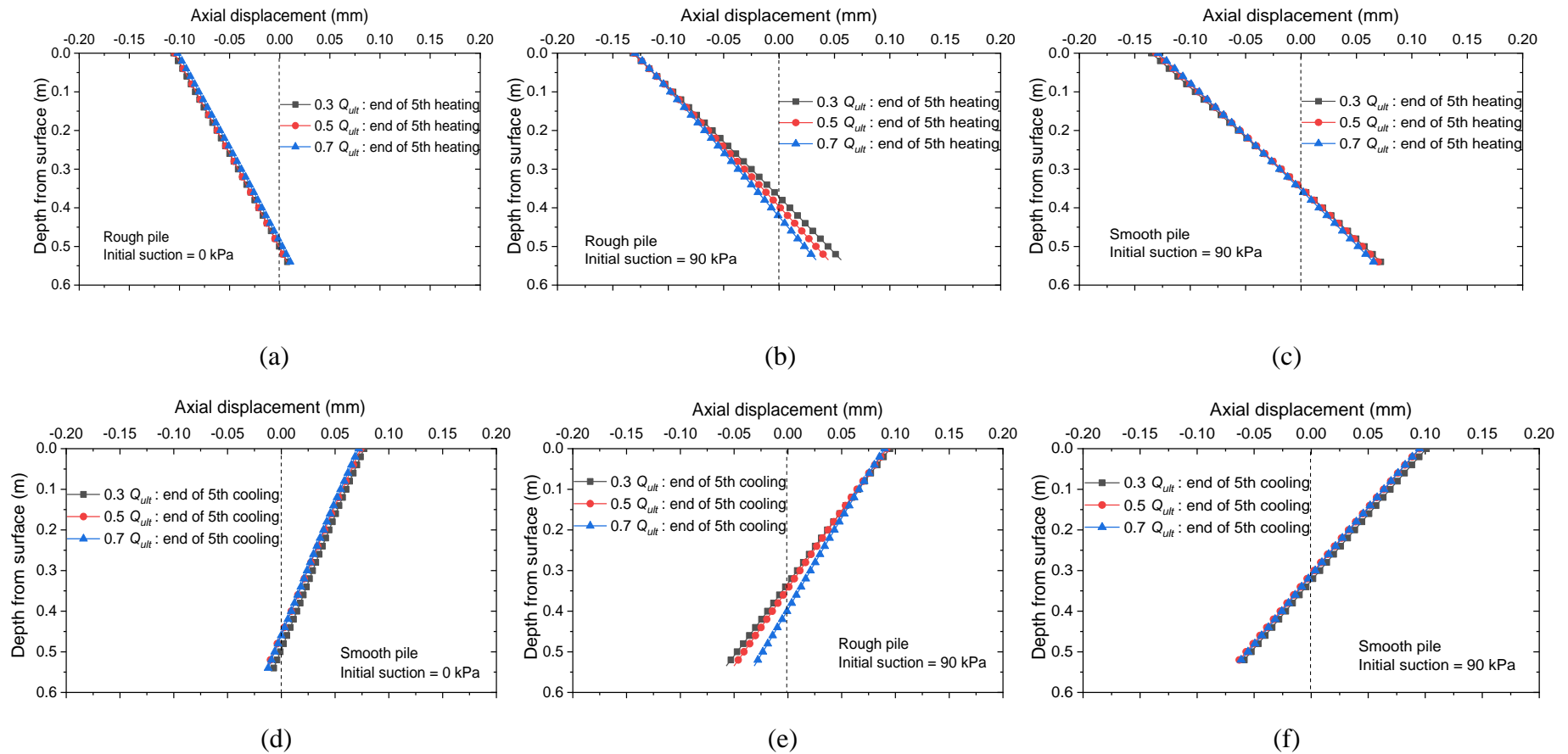


Figure 7.17. Axial displacement of model piles at various stress levels and suctions: (a), (b), (c) heating phase; (d), (e), (f) cooling phase.

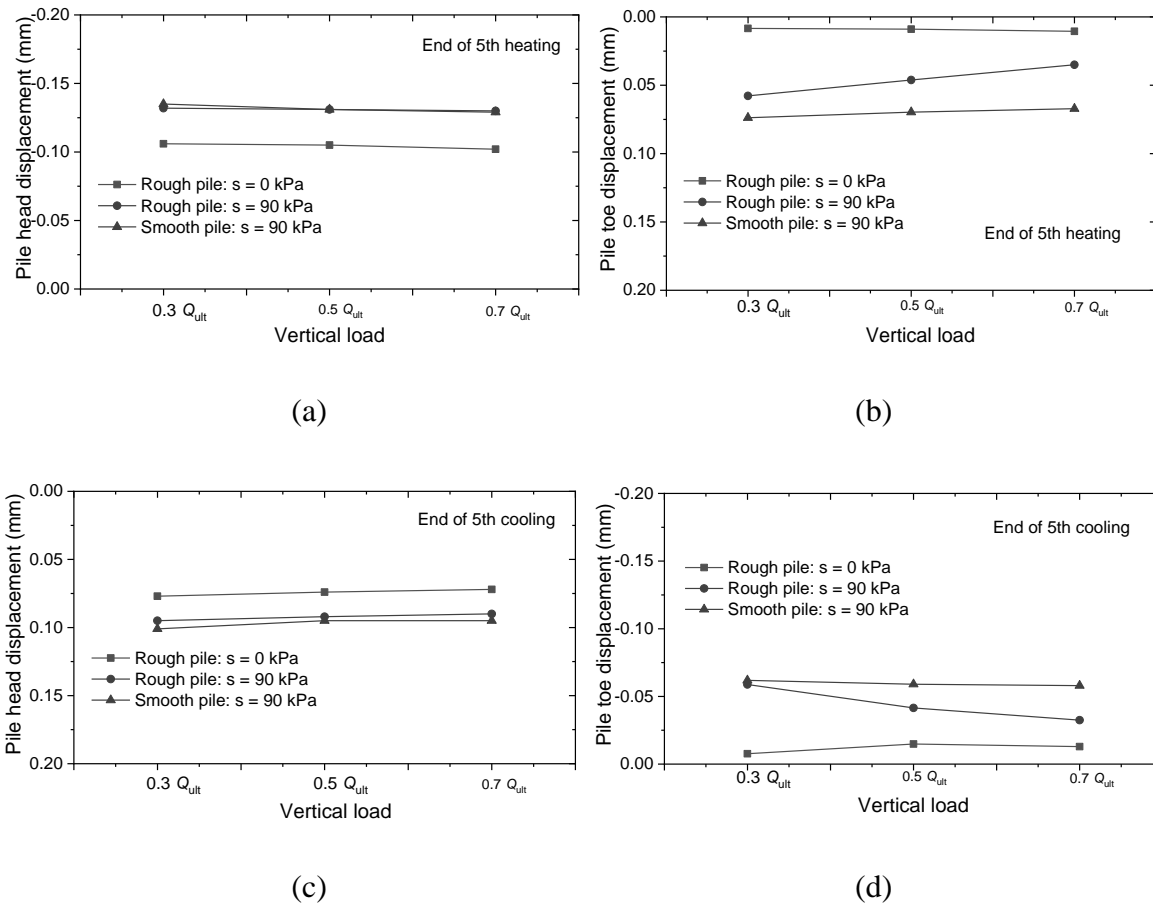


Figure 7.18. Axial displacement distributions of piles head and toe at various suctions, temperatures roughnesses and vertical loads: (a), (b) heating phase; (c), (d) cooling phase.

## CHAPTER 8: Conclusions and Future Work

The major conclusions from the experimental and theoretical investigations are summarized in this chapter. In addition, some suggestions for future work are given.

### 8.1 Major conclusions

#### 8.1.1 State-dependent thermal conductivity of soil

Stress effects on the thermal conductivity are more significant when the soil specimen is more compressible. With a stress increase from 0 to 1200 kPa, the thermal conductivity increases by 60% for the clay, 25% for the silt with 85% DOC, 20% for the silt with 95% DOC, 10% for the sand with an initial void ratio of 0.76 and 7.5% for the sand with an initial void ratio of 0.60. The observed increase in thermal conductivity is attributed to different mechanisms, including a reduction of the void ratio and a change in inter-particle contact. These two mechanisms are relatively more important for clay and sand, respectively.

Stress effects are more significant in the drier condition, where heat transfer is governed by inter-particle contacts. Taking the sand-rubber mixture as one example, at degrees of saturation of 0%, 50% and 100%, the thermal conductivity increase by about 30%, 17% and 19%, respectively, when the stress increases from 0 to 600 kPa.

The  $\lambda - \ln \sigma$  relation shows a clearly bilinearity, which is mainly attributed to the yielding. During a loading and unloading cycle, there is an obvious hysteresis for the relationship between stress and thermal conductivity, due to the elastoplastic behaviour of soil specimen. At the same stress, soil specimen has a larger thermal conductivity along the

unloading path than that along the loading path. This is most probably because loading-induced plastic deformation increases the average contact area between soil interparticle.

### 8.1.2 A new model for the soil thermal conductivity and its application in the analysis of pile thermal performance

The existing equations for soil thermal conductivity in the literature are able to well capture void ratio effects but underestimate stress effects by at least 50%. The newly proposed semi-empirical equation has greatly improved the predictions, mainly because it explicitly considers stress effects on the void ratio and inter-particle contacts of soils.

The heat exchange rate between energy pile and soil is higher when stress effects on the thermal conductivity of soils are considered. This suggests the previous methods may have underestimated the thermal efficiency of energy piles. The degree of underestimation is generally higher (i.e.,  $Q_{\text{stress}}/Q_0$  is larger) under the conditions of a larger pile aspect ratio, higher soil compressibility and deeper groundwater table. The ratio of  $Q_{\text{stress}}/Q_0$  is not sensitive to the variation of pile diameter and inlet temperature. In addition, with an increase in water flow rate inside pipes,  $Q_{\text{stress}}/Q_0$  firstly increases and then shows a minor reduction.

### 8.1.3 Shear behaviour of saturated and unsaturated interfaces at different temperatures

The friction angle  $\delta'$  of the tested CDG-structure interface slightly decreases with increasing temperature since temperature elevation results in an increment of void ratio in the shear zone. Furthermore, the shear strength of the unsaturated interface increases nonlinearly with increasing suction, and the incremental rate is dependent on temperature and stress. At net normal stress of 50 kPa, heating the interface reduces this rate. This is because heating could reduce the surface tension coefficient and the degree of saturation at a given suction. In

contrast, this rate increases at a net normal stress of 150 kPa with the same temperature increment. This is probably because the heated specimen has more small-size pores due to thermal strain and more menisci water lenses, whose influence outweighs the effects of surface tension.

For the shear-induced deformation of interfaces, the results indicate that a higher suction resulted in more dilative deformation. For example, saturated and unsaturated interfaces at net normal stress of 50 kPa exhibit contractive and dilative behaviour, respectively. Furthermore, temperature elevation would reduce shearing-induced contraction, which is at least partially attributed to the reduction of interface roughness with heating.

Under constant net normal stress and shear stress conditions, the relative movement at the soil-pile interface reduces slightly during heating but increases significantly during cooling. The cooling-induced forward movement is most likely due to the thermally induced contraction of soil particles and hence the collapse of force chains. Furthermore, the thermally-induced relative movement is dependent on the net normal stress and shear stress but not sensitive to suction. The relative movement is larger under lower net normal stress and higher shear stress conditions, under which the role of temperature variation is relatively more important. Furthermore, the relationship between relative movement and stress ratio (i.e., the ratio of shear stress to effective normal stress) is bilinear with a critical stress ratio of 0.5. To minimize the settlement of energy piles, it may be necessary to keep the stress ratio at soil-pile interfaces between this critical value.

### 8.1.4 Constitutive modelling of thermo-mechanical behaviour of unsaturated interface

A new constitutive model for the thermo-mechanical behaviour of saturated and unsaturated interfaces was proposed. This is the first model with consideration of suction and temperature effects on unsaturated interfaces.

To verify the model, it was firstly used to simulate the suction- and stress-control direct shear tests at isothermal condition. The suction effects on the shear strength at the peak and critical state are well captured in the new model. Moreover, the dilatancy can be also accurately predicted. Then, the new model was applied to simulate temperature- and stress-controlled direct shear tests on saturated interfaces. Both the increment and decrement of interface shear strength are well captured. The good consistency between the computed and measured volumetric deformations is also obtained. This comparison implies that the new model is applicable to a wide range of interface types at various temperatures. Finally, the experimental results in Chapter 5 were used to calibrate the new model. The computed results are well matched with the measured data. The coupled effects of suction, temperature and net normal stress can be well captured by this new model.

### 8.1.5 Physical modelling of energy piles in saturated and unsaturated silts

The bearing capacity of energy pile increase with increasing suction and roughness. For the suction effects, they are attributed to the increase in both shaft and toe resistance, due to the increase in the strengths of soil and soil-pile interface. However, the roughness only affects the shaft resistance. A temperature decrement results in a reduction of bearing capacity. This is probably because cooling induces smaller normal stress from soil to pile.

During cyclic heating and cooling, the irreversible pile head settlement shows two different responses. When the working load is relatively small (less than  $0.5 Q_{ult}$  in this study), for both saturated and unsaturated conditions, the settlement increases with the number of thermal cycles, but at a decreasing rate. When the working load is relatively large ( $0.7 Q_{ult}$  in this study), the pile settlement does not reach a stable state at saturated condition. Taking the rough pile as one example, the settlement included by 15 thermal cycles is around  $1.5\%D$  at saturated condition, but it is only  $0.2\%D$  at unsaturated condition. In addition, roughness decrement would induce more accumulated pile settlement, due to the reduction of pile shaft resistance.

When pile is subjected to heating, the temperature at the soil-pile interface is higher in unsaturated soil than that in saturated soil, because the thermal conductivity of surrounding soil is larger at saturated condition. The soil temperature at the far-field ground is lower at unsaturated condition.

The location of pile neutral plane decreases with increasing suction, when the pile is subjected to heating. This is because the larger temperature increment at unsaturated condition induces a larger constrain at pile toe. However, when the pile is subjected to cooling, suction effects on the locations of neutral plane are negligible. For the roughness effects, the pile neutral plane moves upwards with decreasing roughness, since less constraint arises from pile toe.

## **8.2 Future work**

### 8.2.1 Suggestions for experimental work

As discussed in Chapter 5, the shear behaviour of soil-structure interfaces is dependent on the soil type. In the saturated condition, temperature elevation shows a negligible influence on sand-structure interfaces and could result in either an increment or a decrement in the shear strength of clay-structure and silt-structure interfaces. In unsaturated conditions, there is no data about the thermo-mechanical behaviour of interfaces in the literature and the current study only tested a silt-structure interface. More laboratory tests on different interfaces (e.g., clay-structure interface and sand-structure interface) are recommended to be conducted at different temperatures and suctions. The additional data can help better reveal the mechanisms of temperature and suction coupling effects. Furthermore, these experimental results can be used to verify constitutive models in the future.

Some other kinds of thermo-mechanical stress paths are also recommended for interfaces. For example, the constant-stress heating and cooling tests and constant-temperature cyclic shearing should be meaningful. The data can give more insights into the thermo-mechanical behaviour of interfaces.

### 8.2.2 Suggestions for constitutive modelling

The newly developed model in Chapter 6 is able to provide improved predictions of interface behaviour at various temperatures, net normal stresses and suctions. In the future, it could be coupled with a soil water retention curve. It should be noted that temperature and void ratio can influence the degree of saturation by changing capillarity and adsorption (Cai et al., 2022). Although the thermally-induced changes in the degree of saturation for CDG are very minor, the consideration of temperature effects on SWRC for other soils should be necessary.

The memory bonding surface is assumed to be independent of temperature, based on the measured data in the constant stress heating and cooling tests in Chapter 5. This assumption needs to be verified by more experimental data in the future. Then, the model should be further modified to capture the accumulation of irreversible tangent movement at the soil-structure interface during cyclic heating and cooling.

### 8.2.3 Suggestions for numerical simulation

In Chapter 4, the numerical study on the thermal efficiency of energy piles in the unsaturated ground did not consider the water-vapour heat transport in the hydraulic field, since the temperature gradient between initial temperature and inlet temperature is relatively small (i.e., 10°C). However, based on the previous studies (Başer et al., 2018; Leung et al., 2020), the larger soil temperature variations could probably result in some water phase changes and vapour diffusion. In the future, the heat exchange between soil and energy pile should be simulated by incorporating the water-vapour heat transfer, with considering larger temperature gradients.

A new numerical code needs to be developed for back-analysing the test results in Chapter 6, considering the thermo-mechanical behaviour of soils and interfaces. The interface model proposed in Chapter 6 and the thermal conductivity equation in Chapter 4 could be applied. By applying the new code, parametric studies could be carried out to investigate the thermo-mechanical behaviour of energy piles in various unsaturated soils.

## Appendix: some formulations for the model in Chapter 6

### Elastic moduli

Similar to the model of Liu et al. (2006) for saturated interfaces, the stiffness parameters  $D_n$  and  $D_t$  are calculated using the following formulations (Lade and Nelson, 1987):

$$D_t = D_{t0} \frac{1+e}{e} \left[ \left( \frac{\sigma_n^*}{p_{atm}} \right)^2 + R \left( \frac{\tau}{p_{atm}} \right)^2 \right]^{0.5} \quad (\text{A-1})$$

$$D_n = D_t R \quad (\text{A-2})$$

where  $D_{t0}$  is a parameter depending on the inherent property of an interface;  $R$  is the ratio of elastic normal modulus to elastic shear modulus.

### Plastic modulus

This equation can be used to determine the loading index  $\Lambda_t$  in equation (6-15). During primary shearing, a state-dependent plastic modulus is adopted here:

$$K_t^p = \frac{D_t h}{M_m} (M_b - M_m) \quad (\text{A-3})$$

where  $h$  is a positive model parameter.

### Dilatancy

Li and Dafalias (2000) developed the theory of state-dependent dilatancy, which was then extended by Chiu and Ng (2003) from saturated to unsaturated conditions. During the shearing, the dilatancy is expressed as:

$$d_t = \frac{d_0}{M} \left( M_d - \frac{\tau}{\sigma_n^*} \right) \quad (\text{A-4})$$

$$M_d = M \exp(n_d \psi) \quad (\text{A-5})$$

where  $d_0$  is a soil parameter;  $n_d$  is a soil parameter which generally takes a positive value;  $M_d$  is the stress ratio at which phase transformation occurs.

## References

- Abdelaziz, S. L. a. M. (2013) Deep energy foundations: geotechnical challenges and design considerations.) Virginia Polytechnic Institute and State University.
- Agar, J. G., Morgenstern, N. R. & Scott, J. D. (1986) Thermal expansion and pore pressure generation in oil sands. *Canadian Geotechnical Journal* **23(3)**:327-333.
- Akrouch, G. A., Sánchez, M. & Briaud, J.-L. (2014) Thermo-mechanical behavior of energy piles in high plasticity clays. *Acta Geotechnica* **9(3)**:399-412.
- Akrouch, G. A., Sánchez, M. & Briaud, J.-L. (2016) An experimental, analytical and numerical study on the thermal efficiency of energy piles in unsaturated soils. *Computers and Geotechnics* **71**:207-220.
- Al-Khazaali, M. & Vanapalli, S. K. (2019) Experimental Investigation of Single Model Pile and Pile Group Behavior in Saturated and Unsaturated Sand. *Journal of Geotechnical and Geoenvironmental Engineering* **145(12)**:4019112.
- Alonso, E. E., Gens, A. & Josa, A. (1990) A constitutive model for partially saturated soils. *Géotechnique* **40(3)**:405-430.
- Alonso, E. E., Pereira, J. M., Vaunat, J. & Olivella, S. (2010) A microstructurally based effective stress for unsaturated soils. *Géotechnique* **60(12)**:913-925.
- Alonso, E. E., Pinyol, N. M. & Gens, A. (2013) Compacted soil behaviour: Initial state, structure and constitutive modelling. *Géotechnique* **63(6)**:463-478.
- Alsherif, N. A. & McCartney, J. S. (2015) Thermal behaviour of unsaturated silt at high suction magnitudes. *Géotechnique* **65(9)**:703-716.
- Amatya, B. L., Soga, K., Bourne-Webb, P. J., Amis, T. & Laloui, L. (2012) Thermo-mechanical behaviour of energy piles. *Géotechnique* **62(6)**:503-519.
- Asadi, I., Shafigh, P., Abu Hassan, Z. F. B. & Mahyuddin, N. B. (2018) Thermal conductivity of concrete – A review. *JOURNAL OF BUILDING ENGINEERING* **20**:81-93.
- Association, G. (2012) Thermal pile design, installation and materials standards. *Ground Source Heat Pump Association, Milton Keynes* **82**:484.

- Astm (2014) Standard Test Method for Determination of Thermal Conductivity of Soil and Soft Rock by Thermal Needle Probe Procedure, American Society of Testing and Materials (ASTM), West Conshohocken, PA, USA.
- Astm (2015) C127 Standard Test Method for Relative Density (Specific Gravity) and Absorption of Coarse Aggregate.
- Barnard, A. C. L., Hunt, W. A., Timlake, W. P. & Varley, E. (1966) A Theory of Fluid Flow in Compliant Tubes. *Biophysical journal* **6(6)**:717-724.
- Başer, T., Dong, Y., Moradi, A. M., Lu, N., Smits, K., Ge, S., Tartakovsky, D. & McCartney, J. S. (2018) Role of Nonequilibrium Water Vapor Diffusion in Thermal Energy Storage Systems in the Vadose Zone. *Journal of Geotechnical and Geoenvironmental Engineering* **144(7)**.
- Bear, J. (1972) *Dynamics of fluids in porous media*. New York, American Elsevier Pub. Co.
- Bear, J. (1979) *Hydraulics of groundwater*. New York, McGraw-Hill, Inc.
- Been, K. & Jefferies, M. G. (1985) A state parameter for sands. *Géotechnique* **35(2)**:99-112.
- Bishop, A. W. (1959) The principle of effective stress. *Teknisk ukeblad* **39**:859-863.
- Borana, L., Yin, J.-H., Singh, D. N., Shukla, S. K. & Tong, F. (2018) Direct Shear Testing Study of the Interface Behavior between Steel Plate and Compacted Completely Decomposed Granite under Different Vertical Stresses and Suctions. *Journal of engineering mechanics* **144(1)**:4017148.
- Borana, L., Yin, J. H., Singh, D. N. & Shukla, S. K. (2016) Interface Behavior from Suction-Controlled Direct Shear Test on Completely Decomposed Granitic Soil and Steel Surfaces. *International journal of geomechanics*. **16(6)**:D4016008.
- Bosscher, P. J., Edil, T. B. & Kuraoka, S. (1997) Design of Highway Embankments Using Tire Chips. *Journal of Geotechnical and Geoenvironmental Engineering* **123(4)**:295-304.
- Bourne-Webb, P. J., Amatya, B. & Soga, K. (2013) A framework for understanding energy pile behaviour. *Proceedings of the Institution of Civil Engineers. Geotechnical engineering* **166(2)**:170-177.

- Bourne-Webb, P. J., Amatya, B., Soga, K., Amis, T., Davidson, C. & Payne, P. (2009) Energy pile test at Lambeth College, London: Geotechnical and thermodynamic aspects of pile response to heat cycles. *Géotechnique* **59(3)**:237-248.
- Brandl, H. (2006) Energy foundations and other thermo-active ground structures. *Géotechnique* **56(2)**:81-122.
- Bristow, K. L., Dane, J. H. & Clarke Topp, G. (2002) 5.3 Thermal Conductivity. *Methods of soil analysis*. **5**:1209-1226.
- Cai, G., Liu, Y., Zhou, A., Li, J., Yang, R. & Zhao, C. (2022) Temperature-dependent water retention curve model for both adsorption and capillarity. *Acta Geotechnica*.
- Casagrande, A. (1936) The Determination of the Pre-consolidation Load and Its Practical Significance. In *Proceedings of Proceedings, 1st International Conference on Soil Mechanics and Foundation Engineering (ICSMFE)* vol. 3, pp. 60-64.
- Caulk, R., Ghazanfari, E. & McCartney, J. S. (2016) Parameterization of a calibrated geothermal energy pile model. *Geomechanics for Energy and the Environment* **5**:1-15.
- Cecinato, F. & Loveridge, F. A. (2015) Influences on the thermal efficiency of energy piles. *Energy (Oxford)* **82**:1021-1033.
- Cekerevac, C. & Laloui, L. (2004) Experimental study of thermal effects on the mechanical behaviour of a clay. *International Journal for Numerical and Analytical Methods in Geomechanics* **5(8)**:209-228.
- Chen, K., Cole, J., Conger, C., Draskovic, J., Lohr, M., Klein, K., Scheidemantel, T. & Schiffer, P. (2006) Packing grains by thermal cycling. *Nature (London)* **442(7100)**:257-257.
- Chen, S. X. (2008) Thermal conductivity of sands. *Heat and mass transfer* **44(10)**:1241-1246.
- Chen, X., Zhang, J., Xiao, Y. & Li, J. (2015) Effect of roughness on shear behavior of red clay – concrete interface in large-scale direct shear tests. *Canadian Geotechnical Journal* **52(8)**:1122-1135.
- Chiu, C. F. & Ng, C. W. W. (2003) A state-dependent elasto-plastic model for saturated and unsaturated soils. *Géotechnique* **53(9)**:809-829.

- Choi, J. C., Lee, S. R. & Lee, D. S. (2011) Numerical simulation of vertical ground heat exchangers: Intermittent operation in unsaturated soil conditions. *Computers and Geotechnics* **38(8)**:949-958.
- Choo, J., Kim, Y. J., Lee, J. H., Yun, T. S., Lee, J. & Kim, Y. S. (2013) Stress-induced evolution of anisotropic thermal conductivity of dry granular materials. *Acta Geotechnica* **8(1)**:91-106.
- Churchill, S. W. (1997) Friction factor equation spans all fluid-flow regimes. *Chemical Engineering* **84(24)**:91-92.
- Clauser, C. & Huenges, E. (1995) Thermal Conductivity of Rocks and Minerals.) American Geophysical Union, Washington, D. C, pp. 105-126.
- Clough, G. W. & Duncan, J. M. (1971) Finite Element Analyses of Retaining Wall Behavior. *Journal of the Soil Mechanics and Foundations Division* **97(12)**:1657-1673.
- Comsol (2015) Finite element analysis and engineering simulation software (Version 5.0), User's Guide. *Heat Transfer Module, Chapters 2&7: Conjugate Heat transfer Branch.*
- Côté, J. & Konrad, J.-M. (2005) A generalized thermal conductivity model for soils and construction materials. *Canadian Geotechnical Journal* **42(2)**:443-458.
- Council, I. C. (2014) *2015 IBC® International Building Code®*. Country Club Hills, Ill, International Code Council.
- Cui, S.-Q., Zhou, C. & Zhang, J.-H. (2022) Experimental Investigations on the State-Dependent Thermal Conductivity of Sand-Rubber Mixtures. *Journal of Materials in Civil Engineering* **34(3)**.
- Cui, S. Q. & Zhou, C. (2022) Coupled effects of stress state and void ratio on thermal conductivity of saturated soils. *Géotechnique Letters* **12(2)**:1-6.
- Dafalias, Y. F. (1986) Bounding Surface Plasticity. I: Mathematical Foundation and Hypoplasticity. *Journal of engineering mechanics* **112(9)**:966-987.
- Dafalias, Y. F. & Manzari, M. T. (2004) Simple Plasticity Sand Model Accounting for Fabric Change Effects. *Journal of engineering mechanics* **130(6)**:622-634.

- Day, R. W. (2010) Foundation engineering handbook : design and construction with the 2009 international building code. *Foundation engineering handbook* :.
- De Moel, M., Bach, P. M., Bouazza, A., Singh, R. M. & Sun, J. O. (2010) Technological advances and applications of geothermal energy pile foundations and their feasibility in Australia. *Renewable & sustainable energy reviews* **14(9)**:2683-2696.
- Dejong, J. T., Frost, J. D. & Cargill, P. E. (2001) Effect of Surface Texturing on CPT Friction Sleeve Measurements. *Journal of Geotechnical and Geoenvironmental Engineering* **127(2)**:158-168.
- Demars, K. & Charles, R. (1982) Soil volume changes induced by temperature cycling. *Canadian Geotechnical Journal* **19(2)**:188-194.
- Department, B. (2017) Code of practice for foundations 2017.) The Government of SAR Hong Kong.
- Desai, C. S. & Ma, Y. (1992) Modelling of joints and interfaces using the disturbed-state concept. *International Journal for Numerical and Analytical Methods in Geomechanics* **16(9)**:623-653.
- Di Donna, A., Ferrari, A. & Laloui, L. (2016) Experimental investigations of the soil–concrete interface: physical mechanisms, cyclic mobilization, and behaviour at different temperatures. *Canadian Geotechnical Journal* **53(4)**:659-672.
- Dong, Y., McCartney, J. S. & Lu, N. (2015) Critical Review of Thermal Conductivity Models for Unsaturated Soils. *Geotechnical and Geological Engineering* **33(2)**:207-221.
- Duc Cao, T., Kumar Thota, S., Vahedifard, F. & Amirlatifi, A. (2021) General Thermal Conductivity Function for Unsaturated Soils Considering Effects of Water Content, Temperature, and Confining Pressure. *Journal of Geotechnical and Geoenvironmental Engineering* **147(11)**.
- En1997-1 (2004) Eurocode 7 Geotechnical Design—Part 1: General Rules.) European Committee for Standardization (CEN) Brussels, Belgium.
- Fadejev, J., Simson, R., Kurnitski, J. & Haghghat, F. (2017) A review on energy piles design, sizing and modelling. *Energy (Oxford)* **122**:390-407.

- Faizal, M., Bouazza, A., Haberfield, C. & McCartney, J. S. (2018) Axial and Radial Thermal Responses of a Field-Scale Energy Pile under Monotonic and Cyclic Temperature Changes. *Journal of Geotechnical and Geoenvironmental Engineering* **144(10)**:4018072.
- Faizal, M., Bouazza, A., McCartney, J. S. & Haberfield, C. (2019a) Axial and radial thermal responses of energy pile under six storey residential building. *Canadian Geotechnical Journal* **56(7)**:1019-1033.
- Faizal, M., Bouazza, A., McCartney, J. S. & Haberfield, C. (2019b) Effects of Cyclic Temperature Variations on Thermal Response of an Energy Pile under a Residential Building. *Journal of Geotechnical and Geoenvironmental Engineering* **145(10)**:4019066.
- Fakharian, K. & Evgin, E. (2000) Elasto-plastic modelling of stress-path-dependent behaviour of interfaces. *International Journal for Numerical and Analytical Methods in Geomechanics* **24(2)**:183-199.
- Fioravante, V. (2002) On the Shaft Friction Modelling of Non-Displacement Piles in Sand. *Soils and Foundations* **42(2)**:23-33.
- Gajo, A. & Muir Wood, D. (1999) Severn-Trent sand: A kinematic-hardening constitutive model: the q-p formulation. *Géotechnique* **49(5)**:595-614.
- Gallage, C., Dareeju, B., Dhanasekar, M. & Ishikawa, T. (2016) Effects of Principal Stress Axis Rotation on Unsaturated Rail Track Foundation Deterioration. *ADVANCES IN TRANSPORTATION GEOTECHNICS III* **143**:252-259.
- Gallipoli, D. (2012) A hysteretic soil-water retention model accounting for cyclic variations of suction and void ratio. *Géotechnique* **62(7)**:605-616.
- Gallipoli, D., Gens, A., Sharma, R. & Vaunat, J. (2003) An elasto-plastic model for unsaturated soil incorporating the effects of suction and degree of saturation on mechanical behaviour. *Géotechnique* **53(1)**:123-135.

- Gan, J. K. M. & Fredlund, D. G. (1994) *Direct shear and triaxial testing of a Hong Kong soil under saturated and unsaturated condition*. Geotechnical Engineering Office, H. K., Report GEO Reort No. 46.
- Gao, J., Zhang, X., Liu, J., Li, K. & Yang, J. (2008) Numerical and experimental assessment of thermal performance of vertical energy piles: An application. *Applied energy* **85(10)**:901-910.
- Garrett, D. & Ban, H. (2011) Compressive pressure dependent anisotropic effective thermal conductivity of granular beds. *Granular Matter* **13(5)**:685-696.
- Gauthier, C., Lacroix, M. & Bernier, H. (1997) Numerical simulation of soil heat exchanger-storage systems for greenhouses. *Solar energy*. **60(6)**:333-346.
- Gennaro, V. D. & Frank, R. (2002) Elasto-plastic analysis of the interface behaviour between granular media and structure. *Computers and Geotechnics* **29(7)**:547-572.
- Gens Solé, A. (2009) Some issues in constitutive modelling of unsaturated soils. In *4th Asia-Pacific Conference on Unsaturated Soils*.) Taylor & Francis, pp. 613-626.
- Georgiadis, K., Potts, D. M. & Zdravkovic, L. (2005) Three-Dimensional Constitutive Model for Partially and Fully Saturated Soils. *International journal of geomechanics* **5(3)**:244-255.
- Ghavam-Nasiri, A., El-Zein, A., Airey, D. & Rowe, R. K. (2019) Water retention of geosynthetic clay liners: Dependence on void ratio and temperature. *Geotextiles and Geomembranes* **47(2)**:255-268.
- Ghionna, V. N. & Mortara, G. (2002) An elastoplastic model for sand-structure interface behaviour. *Géotechnique* **52(1)**:41-50.
- Gnielinski, V. (1976) New equations for heat and mass transfer in turbulent pipe and channel flow. *International Journal of Chemical Engineering* **16(2)**:359-368.
- Goode, J. C. & McCartney, J. S. (2015) Centrifuge Modeling of End-Restraint Effects in Energy Foundations. *Journal of Geotechnical and Geoenvironmental Engineering* **141(8)**:4015034.

- Gori, F. & Corasaniti, S. (2002) Theoretical Prediction of the Soil Thermal Conductivity at Moderately High Temperatures. *Journal of heat transfer* **124(6)**:1001-1008.
- Grant, S. A. & Salehzadeh, A. (1996) Calculation of Temperature Effects on Wetting Coefficients of Porous Solids and Their Capillary Pressure Functions. *Water resources research* **32(2)**:261-270.
- Gui, M., Bolton, M., Garnier, J., Corte, J., Bagge, G., Laue, J. & Renzi, R. (1998) Guidelines for cone penetration tests in sand. In *Centrifuge*.) Balkema Rotterdam, vol. 98, pp. 155-160.
- Haigh, S. K. (2012) Thermal conductivity of sands. *Géotechnique* **62(7)**:617-625.
- Hamid, T. B. & Miller, G. A. (2008) A constitutive model for unsaturated soil interfaces. *International Journal for Numerical and Analytical Methods in Geomechanics* **32(13)**:1693-1714.
- Hamid, T. B. & Miller, G. A. (2009) Shear strength of unsaturated soil interfaces. *Canadian Geotechnical Journal* **46(5)**:595-606.
- Han, C. & Yu, X. (2018) An innovative energy pile technology to expand the viability of geothermal bridge deck snow melting for different United States regions: Computational assisted feasibility analyses. *Renewable Energy* **123**:417-427.
- Han, Z. & Vanapalli, S. K. (2016) Stiffness and shear strength of unsaturated soils in relation to soil-water characteristic curve. *Géotechnique* **66(8)**:627-647.
- Hannawi, K., Kamali-Bernard, S. & Prince, W. (2010) Physical and mechanical properties of mortars containing PET and PC waste aggregates. *Waste management (Elmsford)* **30(11)**:2312-2320.
- Hertz, H. R. (1881) Über die Berührung fester elastischer Körper (On Contact Between Elastic Bodies). *Journal für die reine und angewandte Mathematik* **92**:156-171.
- Hilf, J. W. (1956) An investigation of pore-water pressure in compacted cohesive soils. In *United State Department of the Interior Bureau of Reclamation, Design and Construction Division*.) University of Colorado at Boulder, vol. PhD.

- Hopmans, J. W. & Dane, J. H. (1986) Thermal conductivity of two porous media as a function of water content, temperature, and density. *Soil Science* **142(4)**:187-195.
- Hossain, M. A. & Yin, J.-H. (2010) Behavior of a Compacted Completely Decomposed Granite Soil from Suction Controlled Direct Shear Tests. *Journal of Geotechnical and Geoenvironmental Engineering* **136(1)**:189-198.
- Hossain, M. A. & Yin, J.-H. (2012) Influence of Grouting Pressure on the Behavior of an Unsaturated Soil-Cement Interface. *Journal of Geotechnical and Geoenvironmental Engineering* **138(2)**:193-202.
- Hoteit, N. (1990) Contribution à l'étude du comportement d'interface sable-inclusion et application au frottement apparent.) Grenoble INPG.
- Hotz, R. D. & Ge, L. (2010) Investigation of the Thermal Conductivity of Compacted Silts and Its Correlation to the Elastic Modulus. *Journal of Materials in Civil Engineering* **22(4)**:408-412.
- Hu, L. & Pu, J. (2004) Testing and Modeling of Soil-Structure Interface. *Journal of Geotechnical and Geoenvironmental Engineering* **130(8)**:851-860.
- Hueckel, T., Francois, B. & Laloui, L. (2009) Explaining thermal failure in saturated clays. *Géotechnique* **59(3)**:197-212.
- Jacovides, C. P. & Mihalakakou, G. (1995) An underground pipe system as an energy source for cooling/heating purposes. *Renewable Energy* **6(8)**:893-900.
- Johansen, O. (1975) Thermal conductivity of soils. In *Defense Technical Information Center.*) Norwegian University of Science and Technology, vol. PhD Thesis.
- Johansen, O. (1977) *Thermal conductivity of soils.*
- Kaltreider, C., Krarti, M. & McCartney, J. (2015) Heat transfer analysis of thermo-active foundations. *Energy and buildings* **86**:492-501.
- Karube, D. (1994) An ideal unsaturated soil and the Bishop's soil. In *Proc. 13th ICSMFE.*), vol. 1, pp. 43-46.
- Kell, G. S. (1970) Isothermal compressibility of liquid water at 1 atm. *Journal of chemical & engineering data.* **15(1)**:119-122.

- Kersten, M. S. (1949) Laboratory research for the determination of thermal properties of soils.
- Khoury, C. N., Miller, G. A. & Hatami, K. (2011) Unsaturated soil–geotextile interface behavior. *Geotextiles and Geomembranes* **29(1)**:17-28.
- Kim, G., Ham, K. & Lee, J. (2020) Effects of Surface Roughness on Lateral Load–Carrying Capacities of Piles Embedded in Sand. *Journal of Geotechnical and Geoenvironmental Engineering* **146(8)**.
- Kwok, C. Y. & Bolton, M. D. (2010) DEM simulations of thermally activated creep in soils. *Géotechnique* **60(6)**:425-433.
- Ladd, R. S. (1978) Preparing Test Specimens Using Undercompaction. *Geotechnical Testing Journal* **1(1)**:16-23.
- Lade, P. V. & Nelson, R. B. (1987) Modelling the elastic behaviour of granular materials. *International Journal for Numerical and Analytical Methods in Geomechanics* **11(5)**:521-542.
- Laloui, L. (2011) In Situ Testing of a Heat Exchanger Pile. In *Geo-Frontiers 2011.*) American Society of Civil Engineers, pp. 410-419.
- Laloui, L. & Di Donna, A. (2013) *Energy geostructures: innovation in underground engineering*. Somerset, Somerset: Wiley.
- Laloui, L., Nuth, M. & Vulliet, L. (2006) Experimental and numerical investigations of the behaviour of a heat exchanger pile. *International Journal for Numerical and Analytical Methods in Geomechanics* **5(8)**:763-781.
- Lashkari, A. (2009) On the modeling of the state dependency of granular soils. *Computers and Geotechnics* **36(7)**:1237-1245.
- Lashkari, A. (2013) Prediction of the shaft resistance of nondisplacement piles in sand. *International Journal for Numerical and Analytical Methods in Geomechanics* **37(8)**:904-931.
- Lashkari, A. & Kadivar, M. (2016) A constitutive model for unsaturated soil-structure interfaces. *Int. J. Numer. Anal. Meth. Geomech* **40(2)**:207-234.

- Lashkari, A. & Torkanlou, E. (2016) On the constitutive modeling of partially saturated interfaces. *Computers and Geotechnics* **74**:222-233.
- Le Kouby, A., Canou, J. & Dupla, J. (2004) Behaviour of model piles subjected to cyclic axial loading. *Cyclic behaviour of soils and liquefaction phenomena*:159-166.
- Leung, A. K., Feng, S., Vitali, D., Ma, L. & Karimzadeh, A. A. (2020) Temperature Effects on the Hydraulic Properties of Unsaturated Sand and Their Influences on Water-Vapor Heat Transport. *Journal of Geotechnical and Geoenvironmental Engineering* **146**(4).
- Li, C., Kong, G., Liu, H. & Abuel-Naga, H. (2019) Effect of temperature on behaviour of red clay–structure interface. *Canadian Geotechnical Journal* **56**(1):126-134.
- Li, X. S. & Dafalias, Y. F. (2000) Dilatancy for cohesionless soils. *Géotechnique* **50**(4):449-460.
- Likos, W. J. (2014) Modeling Thermal Conductivity Dryout Curves from Soil-Water Characteristic Curves. *Journal of Geotechnical and Geoenvironmental Engineering* **140**(5):4013056.
- Likos, W. J. (2015) Pore-Scale Model for Thermal Conductivity of Unsaturated Sand. *Geotechnical and Geological Engineering* **33**(2):179-192.
- Lin, X. & Ng, T. T. (1997) A three-dimensional discrete element model using arrays of ellipsoids. *Géotechnique* **47**(2):319-329.
- Littleton, I. (1976) An experimental study of the adhesion between clay and steel. *Journal of terramechanics* **13**(3):141-152.
- Liu, H.-L., Wang, C.-L., Kong, G.-Q. & Bouazza, A. (2019) Ultimate bearing capacity of energy piles in dry and saturated sand. *Acta Geotechnica* **14**(3):869-879.
- Liu, H., Song, E. & Ling, H. I. (2006) Constitutive modeling of soil-structure interface through the concept of critical state soil mechanics. *Mechanics research communications* **33**(4):515-531.
- Liu, X., Cai, G., Congress, S. S. C., Liu, L. & Liu, S. (2020) Investigation of Thermal Conductivity and Prediction Model of Mucky Silty Clay. *Journal of Materials in Civil Engineering* **32**(8).

- Lloret-Cabot, M., Sánchez, M. & Wheeler, S. J. (2013) Formulation of a three-dimensional constitutive model for unsaturated soils incorporating mechanical-water retention couplings. *International Journal for Numerical and Analytical Methods in Geomechanics* **37(17)**:3008-3035.
- Losertová, M., Štamborská, M., Lapin, J. & Mareš, V. (2016) Comparison of deformation behavior of 316L stainless steel and Ti6Al4V alloy applied in traumatology. *Metalurgija* **55(4)**:667-670.
- Loveridge, F. & Powrie, W. (2013) Pile heat exchangers: Thermal behaviour and interactions. *Proceedings of the Institution of Civil Engineers. Geotechnical engineering* **166(2)**:178-196.
- Loveridge, F. & Powrie, W. (2014) 2D thermal resistance of pile heat exchangers. *Geothermics*. **50**:122-135.
- Loveridge, F., Smith, P. & Powrie, W. (2013) A review of design and construction aspects for bored thermal piles. *Ground Engineering*.
- Lu, N. & Dong, Y. (2015) Closed-Form Equation for Thermal Conductivity of Unsaturated Soils at Room Temperature. *Journal of Geotechnical and Geoenvironmental Engineering* **141(6)**:4015016.
- Lupini, J. F., Skinner, A. E. & Vaughan, P. R. (1981) The drained residual strength of cohesive soils. *Géotechnique* **31(2)**:181-213.
- Lurie, M. V. (2008) *Modeling of oil product and gas pipeline transportation*. Place of publication not identified, Wiley VCH Verlag.
- Maghsoodi, S., Cuisinier, O. & Masrouri, F. (2020) Thermal effects on mechanical behaviour of soil–structure interface. *Canadian Geotechnical Journal* **57(1)**:32-47.
- Maghsoodi, S., Cuisinier, O. & Masrouri, F. (2021) Non-isothermal soil-structure interface model based on critical state theory. *Acta Geotechnica* **16(7)**:2049-2069.
- Mašín, D. & Khalili, N. (2011) Modelling of thermal effects in hypoplasticity. In *Proceedings of the 13th international conference of the IACMAG, Melbourne, Australia.*, vol. 1, pp. 237-245.

- Mašin, D. & Khalili, N. (2012) A thermo-mechanical model for variably saturated soils based on hypoplasticity: A THERMO-MECHANICAL MODEL FOR VARIABLY SATURATED SOILS. *International Journal for Numerical and Analytical Methods in Geomechanics* **36(12)**:1461-1485.
- Mccartney, J. S. (2011) Engineering performance of energy foundations. In *Pan-Am CGS Geotechnical Conf.*
- Mccartney, J. S. (2013) Centrifuge Modeling of Energy Foundations. *Energy Geotechniques*:99-115.
- Mccartney, J. S., Jafari, N. H., Hueckel, T., Sánchez, M. & Vahedifard, F. (2019) Emerging Thermal Issues in Geotechnical Engineering.) Cham: Springer International Publishing, Cham, pp. 275-317.
- Mccartney, J. S., Sánchez, M. & Tomac, I. (2016) Energy geotechnics: Advances in subsurface energy recovery, storage, exchange, and waste management. *Computers and Geotechnics* **75(C)**:244-256.
- Mimouni, T. & Laloui, L. (2014) Towards a secure basis for the design of geothermal piles. *Acta Geotechnica* **9(3)**:355-366.
- Mimouni, T. & Laloui, L. (2015) Behaviour of a group of energy piles. *Canadian Geotechnical Journal* **52(12)**:1913-1929.
- Mitchell, J. K. & Soga, K. (2005) *Fundamentals of soil behavior*. John Wiley & Sons New York.
- Moradshahi, A., Faizal, M., Bouazza, A. & McCartney, J. S. (2021) Effect of nearby piles and soil properties on thermal behaviour of a field-scale energy pile. *Canadian Geotechnical Journal* **58(9)**:1351-1364.
- Morais, T. D. S. O., Tsuha, C. D. H. C., Neto, L. a. B. & Singh, R. M. (2020) Effects of seasonal variations on the thermal response of energy piles in an unsaturated Brazilian tropical soil. *Energy and buildings* **216**:109971.

- Mortara, G., Boulon, M. & Ghionna, V. N. (2002) A 2-D constitutive model for cyclic interface behaviour. *International Journal for Numerical and Analytical Methods in Geomechanics* **26(11)**:1071-1096.
- Murphy, K. D., McCartney, J. S. & Henry, K. S. (2015) Evaluation of thermo-mechanical and thermal behavior of full-scale energy foundations. *Acta Geotechnica* **10(2)**:179-195.
- Ng, C. W. W., Gunawan, A., Shi, C., Ma, Q. J. & Liu, H. L. (2016) Centrifuge modelling of displacement and replacement energy piles constructed in saturated sand: a comparative study. *Géotechnique Letters* **6(1)**:34-38.
- Ng, C. W. W., Shi, C., Gunawan, A., Laloui, L. & Liu, H. L. (2015) Centrifuge modelling of heating effects on energy pile performance in saturated sand. *Canadian Geotechnical Journal* **52(8)**:1045-1057.
- Ng, C. W. W. & Zhou, C. (2014) Cyclic behaviour of an unsaturated silt at various suctions and temperatures. *Géotechnique* **64(9)**:709-720.
- Ng, C. W. W., Zhou, C. & Chiu, C. F. (2020) Constitutive modelling of state-dependent behaviour of unsaturated soils: an overview. *Acta Geotechnica* **15(10)**:2705-2725.
- Nguyen, V. T., Tang, A. M. & Pereira, J.-M. (2017) Long-term thermo-mechanical behavior of energy pile in dry sand. *Acta Geotechnica* **12(4)**:729-737.
- Nield, D. A. & Bejan, A. (2013) *Convection in porous media*. 4th edn. New York, Springer.
- Nuth, M. & Laloui, L. (2008) Effective stress concept in unsaturated soils: Clarification and validation of a unified framework. *Int. J. Numer. Anal. Meth. Geomech* **5(8)**:771-801.
- Ochsner, T. E., Horton, R. & Ren, T. (2001) A New Perspective on Soil Thermal Properties. *Soil Science Society of America Journal* **65(6)**:1641-1647.
- Olgun, C. G., Ozudogru, T. Y., Abdelaziz, S. L. & Senol, A. (2014) Long-term performance of heat exchanger piles. *Acta Geotechnica* **10(5)**:553-569.
- Ozgener, L., Hepbasli, A. & Dincer, I. (2005) Energy and exergy analysis of the Gonen geothermal district heating system, Turkey. *Geothermics*. **34(5)**:632-645.

- Ozudogru, T. Y., Ghasemi-Fare, O., Olgun, C. G. & Basu, P. (2015) Numerical Modeling of Vertical Geothermal Heat Exchangers Using Finite Difference and Finite Element Techniques. *Geotechnical and Geological Engineering* **33(2)**:291-306.
- Ozudogru, T. Y., Olgun, C. G. & Senol, A. (2014) 3D numerical modeling of vertical geothermal heat exchangers. *Geothermics* **51**:312-324.
- Park, H., Lee, S.-R., Yoon, S. & Choi, J.-C. (2013) Evaluation of thermal response and performance of PHC energy pile: Field experiments and numerical simulation. *Applied energy* **103**:12-24.
- Pasten, C. & Santamarina, J. C. (2014) Thermally Induced Long-Term Displacement of Thermoactive Piles. *Journal of Geotechnical and Geoenvironmental Engineering* **140(5)**:6014003.
- Patel, G. P. & Bull, J. W. (2011) Selection of Material Used for Thermopiles for Recycling Heat within a Building. *In Advances in Geotechnical Engineering (ASCE)*:400-409.
- Pedrotti, M. & Tarantino, A. (2018) An experimental investigation into the micromechanics of non-active clays. *Géotechnique* **68(8)**:666-683.
- Plevova, E., Vaculikova, L., Kozusnikova, A., Ritz, M. & Simha Martynkova, G. (2015) Thermal expansion behaviour of granites. *Journal of thermal analysis and calorimetry* **123(2)**:1555-1561.
- Plum, R. & Esrig, M. (1969) *Some temperature effects on soil compressibility and pore water pressure*. Washington, Report Special report, Report 103.
- Potts, D. M. (1999) *Finite element analysis in geotechnical engineering: Volume One - Theory*.
- Pra-Ai, S. & Boulon, M. (2017) Soil–structure cyclic direct shear tests: a new interpretation of the direct shear experiment and its application to a series of cyclic tests. *Acta Geotechnica* **12(1)**:107-127.
- Ravera, E., Sutman, M. & Laloui, L. (2021) Cyclic thermomechanical response of fine-grained soil–concrete interface for energy piles applications. *Canadian Geotechnical Journal* **58(8)**:1216-1230.

- Romero, E., Gens, A. & Lloret, A. (2003) Suction effects on a compacted clay under non-isothermal conditions. *Géotechnique* **53(1)**:65-81.
- Roshankhah, S., Garcia, A. V. & Carlos Santamarina, J. (2021) Thermal Conductivity of Sand–Silt Mixtures. *Journal of Geotechnical and Geoenvironmental Engineering* **147(2)**.
- Roshankhah, S. & Santamarina, J. C. (2014) Engineered granular materials for heat conduction and load transfer in energy geotechnology. *Géotechnique Letters* **4(2)**:145-150.
- Rotta Loria, A. F. & Laloui, L. (2018) Group action effects caused by various operating energy piles. *Géotechnique* **68(9)**:834-841.
- Salager, S., François, B., Youssoufi, M. S. E., Laloui, L. & Saix, C. (2008) Experimental Investigations of Temperature and Suction Effects on Compressibility and Pre-Consolidation Pressure of a Sandy Silt. *Soils and Foundations* **48(4)**:453-466.
- Samtani, N. C., Desai, C. S. & Vulliet, L. (1996) AN INTERFACE MODEL TO DESCRIBE VISCOPLASTIC BEHAVIOR. *International Journal for Numerical and Analytical Methods in Geomechanics* **20(4)**:231-252.
- Sani, A. K. & Singh, R. M. (2020) Response of unsaturated soils to heating of geothermal energy pile. *Renewable Energy* **147**:2618-2632.
- Sani, A. K., Singh, R. M., Amis, T. & Cavarretta, I. (2019) A review on the performance of geothermal energy pile foundation, its design process and applications. *Renewable & sustainable energy reviews* **106**:54-78.
- Sawhney, R. L. & Mahajan, U. (1994) Heating and cooling potential of an underground air-pipe system. *International journal of energy research* **18(5)**:509-524.
- Sekine, K., Ooka, R., Yokoi, M., Shiba, Y. & Hwang, S. (2007) Development of a ground-source heat pump system with ground heat exchanger utilizing the cast-in-place concrete pile foundations of buildings. *ASHRAE Transactions* **113(1)**:558-566.
- Shahrour, I. & Rezaie, F. (1997) An elastoplastic constitutive relation for the soil-structure interface under cyclic loading. *Computers and Geotechnics* **21(1)**:21-39.
- Sivakumar, V. (1993) A critical state framework for unsaturated soil.) University of Sheffield.

- Smits, K. M., Sakaki, T., Limswat, A. & Illangasekare, T. H. (2010) Thermal Conductivity of Sands under Varying Moisture and Porosity in Drainage-Wetting Cycles. *Vadose zone journal* **9(1)**:172-180.
- Stewart, M. A. & McCartney, J. S. (2014) Centrifuge Modeling of Soil-Structure Interaction in Energy Foundations. *Journal of Geotechnical and Geoenvironmental Engineering* **140(4)**:4013044.
- Stutz, H., Masin, D., Wuttke, F. & Pradel, B. (2016) Thermo-mechanical hypoplastic interface model for fine-grained soils. In *1st International Conference on Energy Geotechnics (ICEGT)*., Univ Kiel, Kiel, GERMANY, pp. 351-357.
- Sultan, N., Delage, P. & Cui, Y. J. (2002) Temperature effects on the volume change behaviour of Boom clay. *Engineering geology* **64(2)**:135-145.
- Suryatriyastuti, M. E., Mroueh, H. & Burlon, S. (2012) Understanding the temperature-induced mechanical behaviour of energy pile foundations. *Renewable and Sustainable Energy Reviews* **16(5)**:3344-3354.
- Tai, P., Zhou, C., Zhou, Y. & Cui, S. (2020) Thermal conductivity of Toyoura sand at various moisture and stress conditions In *Proceedings of E3S Web of Conferences*. EDP Sciences vol. 205, pp. 04010.
- Takada, N. (1993) Mikasa's Direct Shear Apparatus, Test Procedures and Results. *Geotechnical Testing Journal* **16(3)**:314-322.
- Tang, A.-M., Cui, Y.-J. & Le, T.-T. (2008a) A study on the thermal conductivity of compacted bentonites. *Applied clay science* **41(3)**:181-189.
- Tang, A. M., Cui, Y. J. & Barnel, N. (2008b) Thermo-mechanical behaviour of a compacted swelling clay. *Géotechnique* **58(1)**:45-54.
- Tarnawski, V. R. & Leong, W. H. (2012) A Series-Parallel Model for Estimating the Thermal Conductivity of Unsaturated Soils. *International Journal of Thermophysics* **33(7)**:1191-1218.

- Tarnawski, V. R., Momose, T. & Leong, W. H. (2011) Thermal Conductivity of Standard Sands II. Saturated Conditions. *International Journal of Thermophysics* **32(5)**:984-1005.
- Tarnawski, V. R., Momose, T., Leong, W. H., Bovesecchi, G. & Coppa, P. (2009) Thermal Conductivity of Standard Sands. Part I. Dry-State Conditions. *International Journal of Thermophysics* **30(3)**:949-968.
- Tehrani, F. S., Han, F., Salgado, R., Prezzi, M., Tovar, R. D. & Castro, A. G. (2016) Effect of surface roughness on the shaft resistance of non-displacement piles embedded in sand. *Géotechnique* **66(5)**:386-400.
- Terzaghi, K. (1943) *Theoretical soil mechanics*. New York, Wiley.
- Thomas, H. R. & King, S. D. (1994) A non-linear, two-dimensional, potential-based analysis of coupled heat and mass transfer in a porous medium. *International journal for numerical methods in engineering* **37(21)**:3707-3722.
- Thomas, H. R. & Rees, S. W. (2009) Measured and simulated heat transfer to foundation soils. *Géotechnique* **59(4)**:365-375.
- Tovar-Valencia, R. D., Galvis-Castro, A., Salgado, R. & Prezzi, M. (2018) Effect of Surface Roughness on the Shaft Resistance of Displacement Model Piles in Sand. *Journal of Geotechnical and Geoenvironmental Engineering* **144(3)**:4017120.
- Tsubakihara, Y., Kishida, H. & Nishiyama, T. (1993) Friction between cohesive soils and steel. *Soils and Foundations* **33(2)**:145-156.
- Uchaipichat, A. & Khalili, N. (2009) Experimental investigation of thermo-hydro-mechanical behaviour of an unsaturated silt. *Géotechnique* **59(4)**:339-353.
- Uesugi, M. & Kishida, H. (1986) Frictional resistance at yield between dry sand and mild steel. *Soils and Foundations* **26(4)**:139-149.
- Van Genuchten, M. T. (1980) A closed-form equation for predicting the hydraulic conductivity of unsaturated soils. *Soil Science Society of America Journal* **44(5)**:892-898.

- Vanapalli, S. K., Fredlund, D. G., Pufahl, D. E. & Clifton, A. W. (1996) Model for the prediction of shear strength with respect to soil suction. *Canadian Geotechnical Journal* **33(3)**:379-392.
- Vargas, W. L. & McCarthy, J. J. (2007) Thermal expansion effects and heat conduction in granular materials. *Physical Review E* **76(4)**.
- Wan, R. G. & Guo, P. J. (1998) A simple constitutive model for granular soils: Modified stress-dilatancy approach. *Computers and Geotechnics* **22(2)**:109-133.
- Wang, B., Bouazza, A. & Haberfield, C. (2011) Preliminary observations from laboratory scale model geothermal pile subjected to thermo-mechanical loading In *Proceedings of Geo-Frontiers 2011* © ASCE 2011, pp. 430-439.
- Wang, B., Bouazza, A., Singh, R. M., Haberfield, C., Barry-Macaulay, D. & Baycan, S. (2015a) Posttemperature Effects on Shaft Capacity of a Full-Scale Geothermal Energy Pile. *Journal of Geotechnical and Geoenvironmental Engineering* **141(4)**:4014125.
- Wang, C.-L., Liu, H.-L., Kong, G.-Q., Ng, C. W. W. & Wu, D. (2016) Model tests of energy piles with and without a vertical load. *Environmental Geotechnics* **3(4)**:203-213.
- Wang, J., Shang, Y., Wang, H., Zhao, Y. & Yin, Y. (2015b) Beijing's Water Resources: Challenges and Solutions. *JAWRA Journal of the American Water Resources Association* **51(3)**:614-623.
- Wang, Y., Liu, X., Zhang, M. & Bai, X. (2020) Effect of Roughness on Shear Characteristics of the Interface between Silty Clay and Concrete. *Advances in civil engineering* **2020**.
- Wang, Z.-L., Dafalias, Y. F. & Shen, C.-K. (1990) Bounding Surface Hypoplasticity Model for Sand. *Journal of engineering mechanics* **116(5)**:983-1001.
- Weidenfeld, G., Weiss, Y. & Kalman, H. (2004) A theoretical model for effective thermal conductivity (ETC) of particulate beds under compression. *Granular Matter* **6(2-3)**:121-129.
- Wheeler, S. J., Sharma, R. S. & Buisson, M. S. R. (2003a) Coupling of hydraulic hysteresis and stress-strain behaviour in unsaturated soils. *Géotechnique* **53(1)**:41-54.

- Wheeler, S. J., Sharma, R. S. & Buisson, M. S. R. (2003b) Coupling of hydraulic hysteresis and stress-strain behaviour in unsaturated soils. *Géotechnique* **53(1)**:41-54.
- Willson, C. S., Lu, N. & Likos, W. J. (2012) Quantification of Grain, Pore, and Fluid Microstructure of Unsaturated Sand from X-Ray Computed Tomography Images. *Geotechnical Testing Journal* **35(6)**:1-13.
- Woodside, W. & Messmer, J. H. (1961) Thermal conductivity of porous media. I. Unconsolidated sands. *Journal of Applied Physics* **32(9)**:1688-1699.
- Xiao, S., Suleiman, M. T. & McCartney, J. S. (2014) Shear Behavior of Silty Soil and Soil-Structure Interface under Temperature Effects In *Proceedings of Geo-Congress 2014*. eScholarship, University of California, pp. 4105-4114.
- Xiao, Y., Liu, H., Nan, B. & McCartney, J. S. (2018) Gradation-Dependent Thermal Conductivity of Sands. *Journal of Geotechnical and Geoenvironmental Engineering* **144(9)**:6018010.
- Xiao, Y., Ma, G., Nan, B. & McCartney, J. S. (2020) Thermal Conductivity of Granular Soil Mixtures with Contrasting Particle Shapes. *Journal of Geotechnical and Geoenvironmental Engineering* **146(5)**.
- Xiao, Y., Nan, B. & McCartney, J. S. (2019) Thermal Conductivity of Sand–Tire Shred Mixtures. *Journal of Geotechnical and Geoenvironmental Engineering* **145(11)**:6019012.
- Yao, J., Özocak, A., Wang, T., Likos, W. J. & Edil, T. B. (2021) Apparatus for Coupled Effects of Suction, Temperature, and Stress on Thermal Conductivity of Unsaturated Sand. *Geotechnical Testing Journal* **44(2)**:358-372.
- Yao, J., Wang, T. & Likos, W. J. (2019) Measuring Thermal Conductivity of Unsaturated Sand under Different Temperatures and Stress Levels Using a Suction-Controlled Thermo-Mechanical Method.) American Society of Civil Engineers, pp. 784-793.
- Yavari, N., Tang, A. M., Pereira, J.-M. & Hassen, G. (2014) Experimental study on the mechanical behaviour of a heat exchanger pile using physical modelling. *Acta Geotechnica* **9(3)**:385-398.

- Yavari, N., Tang, A. M., Pereira, J.-M. & Hassen, G. (2016a) Effect of temperature on the shear strength of soils and the soil–structure interface. *Canadian Geotechnical Journal* **53(7)**:1186-1194.
- Yavari, N., Tang, A. M., Pereira, J. M. & Hassen, G. (2016b) Mechanical behaviour of a small-scale energy pile in saturated clay. *Géotechnique* **66(11)**:878-887.
- Yazdani, S., Helwany, S. & Olgun, G. (2019) Influence of temperature on soil–pile interface shear strength. *Geomechanics for Energy and the Environment* **18**:69-78.
- Yoshimi, Y. & Kishida, T. (1981) A Ring Torsion Apparatus for Evaluating Friction Between Soil and Metal Surfaces. *Geotechnical Testing Journal* **4(4)**:145-152.
- You, S., Cheng, X., Guo, H. & Yao, Z. (2016) Experimental study on structural response of CFG energy piles. *Applied Thermal Engineering* **96**:640-651.
- Yun, T. S. & Santamarina, J. C. (2008) Fundamental study of thermal conduction in dry soils. *Granular Matter* **10(3)**:197-207.
- Zhan, T. L. & Ng, C. W. W. (2006) Shear strength characteristics of an unsaturated expansive clay. *Canadian Geotechnical Journal* **43(7)**:751-763.
- Zhang, L. M., Xu, Y. & Tang, W. H. (2008) Calibration of models for pile settlement analysis using 64 field load tests. *Canadian Geotechnical Journal* **45(1)**:59-73.
- Zhang, N., Yu, X., Pradhan, A. & Puppala, A. J. (2015) Thermal Conductivity of Quartz Sands by Thermo-Time Domain Reflectometry Probe and Model Prediction. *Journal of Materials in Civil Engineering* **27(12)**:4015059.
- Zhang, N., Yu, X., Pradhan, A. & Puppala, A. J. (2017) A new generalized soil thermal conductivity model for sand–kaolin clay mixtures using thermo-time domain reflectometry probe test. *Acta Geotechnica* **12(4)**:739-752.
- Zhao, Q., Chen, B. & Liu, F. (2016) Study on the thermal performance of several types of energy pile ground heat exchangers: U-shaped, W-shaped and spiral-shaped. *Energy and buildings* **133**:335-344.

- Zhen, Z.-L., Ma, G.-L., Zhang, H.-Y., Gai, Y.-X. & Su, Z.-Y. (2019) Thermal Conductivities of Remolded and Undisturbed Loess. *Journal of Materials in Civil Engineering* **31(2)**:4018379.
- Zhou, A.-N., Sheng, D., Sloan, S. W. & Gens, A. (2012) Interpretation of unsaturated soil behaviour in the stress – Saturation space, I: Volume change and water retention behaviour. *Computers and Geotechnics* **43**:178-187.
- Zhou, C. & Ng, C. W. W. (2016) Simulating the cyclic behaviour of unsaturated soil at various temperatures using a bounding surface model. *Géotechnique* **66(4)**:344-350.
- Zhou, C., Ng, C. W. W. & Chen, R. (2015) A bounding surface plasticity model for unsaturated soil at small strains. *International Journal for Numerical and Analytical Methods in Geomechanics* **39(11)**:1141-1164.
- Zhou, C., Tai, P. & Yin, J. H. (2020) A bounding surface model for saturated and unsaturated soil-structure interfaces. *International Journal for Numerical and Analytical Methods in Geomechanics* **44(18)**:2412-2429.